



DOCTORAL THESIS

*Removal of microplastics by membrane
filtration and organic pollutants by UV-B and
UV-C LED based technologies for water
purification*

Author:

Angela Raffaella Pia Pizzichetti

Supervisors:

Cristina Pablos Carro
Javier Marugán Aguado
Ken Reynolds

Doctoral Programme in Industrial Technologies: Chemical, Environmental,
Energetic, Electronic, Mechanics and Materials

International Doctoral School

2023

La Dra. Cristina Pablos Carro, Profesora Titular de Universidad, y el Dr. Javier Marugán Aguado, Catedrático de Universidad, ambos del área de Ingeniería Química del Departamento de Tecnología Química y Ambiental de la Universidad Rey Juan Carlos, y el Dr. Ken Reynolds, investigador de ProPhotonix IRL., Irlanda.

CERTIFICAN:

Que el presente trabajo de investigación titulado “Removal of microplastics by membrane filtration and organic pollutants by UV-B and UV-C LED based technologies for water purification” constituye la memoria que presenta Dña. Angela Raffaella Pia Pizzichetti, para aspirar al grado de Doctor y ha sido realizada en los laboratorios del Grupo de Ingeniería Química y Ambiental del Departamento de Tecnología Química y Ambiental de la Universidad Rey Juan Carlos y en los laboratorios de ProPhotonix (Cork, Irlanda) bajo nuestra dirección.

Y para que así conste, firmamos el presente certificado en Móstoles, 30 de mayo de 2023.

Fdo. Cristina Pablos Carro

Fdo. Javier Marugán Aguado

Fdo. Ken Reynolds

Acknowledgements

This thesis has been realised as part of the European Project REWATERGY between Rey Juan Carlos University, under the directions of Javier Marugán and Cristina Pablos, and the company ProPhotonix, under the supervision of Ken Reynolds and Simon Stanley. First, I want to express my deepest gratitude to them for believing in me and choosing me to be one of the Early-Stage Researchers in the Project. Despite a pandemic, winter storms, and humanitarian disasters, they have always been there to support me the entire time. Thanks to Javier and Cristina for the technical guidance, intellectual inspiration, words of encouragement, and advice in the most challenging periods of my, not only professional life, and thanks to Ken and Simon for warmly welcoming me into the company, involving me in some technical problem solving, and to actively helping me in finding all the tools and equipment to achieve my research. Also, I wanted to thank Eric Moore for kindly including me in his group during the collaboration with University College Cork, open me the doors of the Environmental Research Institute (ERI) laboratories, and supporting the investigation during my stay there.

Completing this thesis is also largely thanks to the many wonderful people I met during the path.

I want to start by thanking the entire REWATERGY family for the science talks, the good moments, and the resilience in facing unexpected challenges during the Project. A particular thanks to the other ESRs: Adriana, Marina, Ruben, Salem, Conor, Shabila, and Adithya, for the mutual support, the good times during the shared training activities, and the personal other than technical talks.

I also want to thank my colleagues within the Chemical and Environmental Engineering Group at URJC for helping me in my research directly (a particular thanks to Mario, Cintia, and Miguel for the precious comments and feedback when exploring new research topics) and indirectly for the necessary breaks and for the encouraging words during the hard times. A special thanks to my research group, *Photoners*, my office mates, before in Laboratorio Polivalente III, and then in Antesala 116, for softening the daily workload and getting a smile out of me even in my stressful moments. To Veronica, who welcomed me since day one while my Spanish was very limited, and with Ruben, Pilar, Carmen, and Cristina R., for the beers after work and my first nights in Spain. To Pilar again, Alex, and Carlos for lightening a very tough and loaded period of my life between a padel, a ping pong match, or a sunny day in Patones. Finally, thanks to

Laura, Lalo, Clara, Oscar, Feb, Pietro, Ale and Kri for being my reference points in Madrid during the entire period.

Thanks to the amazing companion I luckily found at ERI, in particular to Nathan, Rajas, Jorge, Clara, Anga, and Shabila, for easing my very long days in the office and in the laboratory, and especially for the weekend plans; the bike trip, the Mexican dinner, the Catan games, or swimming in the Irish waters in Baltimore. To this, I add a special thanks to Shabila for teaching me so much through her stories and experiences. It has been a pleasure sharing the entire PhD experience throughout Spain and Ireland with you. Then less related to my work, but very important in my day-to-day life, I would like to thank Catarina and Alicia for being such amazing flatmates, for listening and supporting me in my good and my bad moments.

I also want to give special thanks to my lifelong friends. Starting from my friends in Rome, Beba, Leo, Ale, Giulia, Gianlu, and Nick, who always find the time to meet me while I am there and make me feel at home. To the exceptional friends I made in Turin, particularly my staggering classmates, Madda, Dario, Giovanni, Giulia, Piera, Alessio, Marti, Fabio, Ali, and Diego. We found each other among others, and even if we are now spread worldwide, we always find a way to see each other and organise more crazy adventures. I also want to thank Gabri, Dani, Andrea, and Sergio for their friendship, support, and inspiration throughout all these years. Thanks to the fantastic people I met in Stockholm, among others not mentioned already, Diego, Marc, David, Maria and Ainhoa, because thanks to them, the Erasmus experience has been such an enriching and stimulating part of my life.

Then, I want to express my heartfelt gratitude to Fede, who has been my pillar throughout my entire PhD journey, for his support during the toughest moments, for always believing in me also when I didn't, for brightening my day on countless occasions, and the unforgettable time and experiences together.

Thanks to my extended family. To my cousins, aunts, and uncles for the unique time we spent together during the holidays and the important moments. To my host family while I lived abroad, who treated me as a daughter. To Fede's family for always welcoming me in all the plans and making me feel at home. Finally, but most importantly, to my parents, for the unconditional love, guidance, support, and the opportunities they gave me to build and create my own future. Thank you.

*“We are on a highway to climate hell with our foot on
the accelerator.”*

—António Guterres

“Be the change that you want to see in the world.”

—Mahatma Gandhi

Table of contents

Resumen	vii
1 Summary	3
2 Introduction.....	9
2.1 ‘White gold’	9
2.2 Contaminants of emerging concern: CECs	10
2.3 Microplastics contamination	12
2.3.1 Microplastics: definition, analysis, and occurrence	12
2.3.2 Main technologies for microplastic removal.....	18
2.3.3 Membrane filtration.....	21
2.4 Organic micropollutants contamination	26
2.4.1 Diclofenac contamination	28
2.4.2 Main technologies for diclofenac removal.....	29
2.4.3 Light-emitting diodes (LEDs)	34
2.4.4 Environmental impact of UV treatments in water systems.....	37
2.5 Objective and aim of the investigation.....	42
3 Methodology	47
3.1 Microplastics removal	47
3.1.1 Materials.....	47
3.1.2 Characterisation techniques.....	48
3.1.3 Filtration system.....	51
3.1.4 Analysis of the removal efficiency.....	55
3.1.5 Modelling of the membrane fouling.....	57
3.2 Diclofenac removal	61
3.2.1 Chemical and materials	61
3.2.2 Photoreactor setup	61
3.2.3 Ferrioxalate actinometry	65
3.2.4 Analytical methods.....	68
3.2.5 Phytotoxicity test.....	71
3.2.6 Calculations of the degradation kinetic parameters	72
3.3 Life cycle assessment methodology	73

4	Results and discussion	79
4.1	Microplastic and membrane characterisation results	79
4.1.1	Microplastics detection and analysis	79
4.1.2	Particles size distribution	82
4.1.3	Zeta potential analysis	84
4.1.4	SEM images	86
4.1.5	Other membrane characterisations results.....	89
4.2	Membranes performance for microplastic removal	91
4.2.1	TMP and flux results	91
4.2.2	MPs removal efficiency	95
4.2.3	Overall performance evaluation	98
4.3	Membrane fouling by microplastics.....	100
4.3.1	Main successive fouling mechanisms	101
4.3.2	Kinetic analysis varying MPs load.....	104
4.3.3	Kinetic analysis varying the working pressure	108
4.3.4	Impact of MPs on the membrane fouling.....	114
4.4	UV-B and UV-C LEDs driven advanced oxidation processes	120
4.4.1	UV-B and UV-C LED lamps characterisation.....	120
4.4.2	Molar absorption coefficient	122
4.4.3	Degradation studies at different wavelengths	123
4.4.4	Rigorous kinetic modelling	128
4.4.5	Varying intensity	135
4.4.6	Dual-wavelength system	137
4.4.7	Energy consumption.....	141
4.4.8	Mineralisation.....	143
4.4.9	By-products and dimers formation.....	144
4.4.10	Phytotoxicity	148
4.5	Environmental impact assessment	150
4.5.1	Description of the case study	150
4.5.2	Goal and scope	151
4.5.3	Life cycle inventory	152
4.5.4	Life cycle impact assessment	157
4.5.5	UV-C LEDs photoreactor versus mercury lamp photoreactor.....	158

4.5.6	Comparison between UV-C, UV-C/H ₂ O ₂ , and UV-C/FC	164
4.5.7	Renewable electricity	167
5	Conclusions.....	173
	Bibliography.....	180
	List of Figures	203
	List of Tables.....	212
	List of Abbreviations.....	216
	Publications and communications to congresses	220

RESUMEN

Resumen

Antecedentes

En el gran desafío de la contaminación del agua, la presencia de contaminantes de preocupación emergente (*Contaminants of Emerging Concern*, CECs) en el agua tratada representa un riesgo para la seguridad del medio ambiente y la salud humana. Se ha demostrado que las plantas de tratamiento existentes no son adecuadas para eliminar estos CECs. Su detección en aguas residuales, entornos acuáticos y agua potable requiere la implementación de medidas adecuadas y procesos de eliminación para evitar su impacto en los seres humanos y los ecosistemas. Además, el aumento de la contaminación humana y los desastres naturales debido al cambio climático afectarán negativamente el agua disponible. La peculiaridad de estos contaminantes también radica en que no están sujetos a regulaciones específicas en agua potable y no están controlados por legislación actual; por lo tanto, se necesita más esfuerzo para prevenir y reducir su aparición. Por consiguiente, es crucial aumentar la resiliencia de los sistemas de producción de agua potable, ya sea en las plantas centralizadas de tratamiento, o directamente en los puntos de consumo. Para ello, es necesario considerar las diversas vías de entrada de estos contaminantes en los recursos hídricos, desarrollando estrategias específicas y optimizadas para la eliminación, entre otros CECs, de microplásticos (MPs) y compuestos orgánicos como productos farmacéuticos y de cuidado personal.

Los MPs se definen como partículas plásticas de menos de 5 mm y han generado gran preocupación debido a su presencia ubicua y abundante en el agua. También existe evidencia de que los MPs actúan como vectores de varios contaminantes debido a sus aditivos y su capacidad de absorber y acumular contaminantes tóxicos orgánicos e inorgánicos en su superficie. Además, debido a su naturaleza plástica, tardan mucho tiempo en biodegradarse y, debido a su pequeño tamaño, son fácilmente ingeridos. Entre las tecnologías desarrolladas para la eliminación de MPs, las membranas han recibido considerable atención gracias a su implementación sencilla y la calidad estable de su efluente. Dependiendo de las características de la membrana y la configuración, la tecnología puede ser rentable y fácilmente implementable. Entre los procesos de membrana, la tecnología de microfiltración (MF) ha ganado interés por la implementación sencilla y los costos energéticos operativos más bajos en comparación con los otros. Sin embargo, la obstrucción de la membrana debido al

ensuciamiento es una de sus principales limitaciones, y representa un problema crítico para el diseño y la operación del sistema.

Por otro lado, dentro de los CECs, los microcontaminantes orgánicos también están ganando cada vez más atención debido al riesgo asociado, hasta el punto en que la Comisión Europea decidió introducir una *lista de observación* de sustancias en los cuerpos de agua para comenzar a monitorear su presencia y desarrollar estrategias. Entre los CECs de la *lista de observación*, el diclofenaco (DCF), un antiinflamatorio no esteroideo comúnmente utilizado para el alivio del dolor, ha despertado interés debido a su conocida toxicidad hacia la vida silvestre y los posibles efectos en general en los ecosistemas acuáticos, donde se ha detectado en concentraciones de hasta $\mu\text{g L}^{-1}$. Sin embargo, DCF y en general los compuestos orgánicos, tienen tamaños más pequeños y comportamientos diferentes en comparación con los MPs, por lo que la microfiltración no es adecuada para su eliminación y solo los sistemas de membrana de alta presión serían efectivos. Alternativamente, la irradiación UV-B y UV-C ha demostrado ser un tratamiento efectivo para su degradación, además de ser efectivo para la desinfección del agua. La integración de procesos avanzados de oxidación (*Advanced Oxidation Processes*, AOPs) basados en UV permite lograr una mayor calidad del agua frente a una variedad de amenazas. Además, el uso de diodos emisores de luz (*Light-Emitting Diodes*, LEDs) en lugar de lámparas de mercurio podría llevar a avances interesantes en la eliminación de los contaminantes. Aparte de ser soluciones sin mercurio, los LEDs presentan como ventajas una longitud de onda variable, encendido y apagado instantáneo (sin tiempo de calentamiento) y una intensidad ajustable. Estas propiedades tienen un potencial increíble en la aplicación de AOPs basados en UV-B y UV-C, ya que el rendimiento general del proceso depende de la longitud de onda y la intensidad de UV. Adicionalmente, su pequeño tamaño permite una alta flexibilidad de diseño y la perspectiva de su crecimiento exponencial, de manera similar a los LEDs en el rango visible o UV-A, lo hace muy atractivos para el tratamiento de aguas. Sin embargo, de cara a su aplicación y para evaluar la competitividad del tratamiento contra las lámparas de mercurio convencionales, es importante realizar un análisis ambiental comparativas. Por lo tanto, la evaluación del ciclo de vida ambiental (*Life Cycle Assessment*, LCA) fue llevado a cabo en cuanto es el método preferido gracias a su reconocimiento internacional y uso generalizado. Al examinar los impactos ambientales potenciales durante todo el ciclo de vida y comparar vías alternativas, LCA proporciona información valiosa para

optimizar el proceso, destacando los puntos críticos y recomendando medidas adicionales para reducir la huella ambiental general.

Objetivos

Los sistemas de agua deben actualizarse mediante el empleo de tratamientos avanzados específicos y optimizados para la eliminación de los CECs. Por tanto, el objetivo de esta Tesis Doctoral es el diseño y la evaluación de tecnologías para sus eliminación, con un enfoque particular en los MPs y DCF.

Con respecto a la eliminación de MPs, se eligió la membrana de MF en configuración sin salida en cuanto es un sistema de fácil implementación en salidas de grifo y punto de uso y que no necesita ningún otro tratamiento. Para optimizar el sistema, el primer paso fue evaluar la eficiencia de varias membranas comerciales con diferentes características. En seguida, dado que el ensuciamiento de la membrana por los MPs tiene una significativa brecha de conocimiento y es clave para desarrollar apropiados procedimientos de filtración y limpieza, se investigó profundamente en la membrana que logró el mejor rendimiento general.

Por otro lado, la eliminación de DCF se exploró con tratamiento UV y UV-AOPs mediante innovadoras lámparas LED en el rango UV-B y UV-C (265, 285 y 310 nm) fabricadas por la empresa ProPhotonix IRL. Se investigó la degradación a diferentes intensidades de lámpara y la fotólisis debido a doble longitud de ondas. En seguida, se modeló mecánicamente la cinética de degradación de DCF en función de la longitud de onda y el proceso de oxidación, lo cual es muy útil para diseñar sistemas de tratamiento y optimizar las condiciones de operación. Finalmente, LCA se empleó para una evaluación integral de los impactos ambientales de los tratamientos empleados. Se comparó la innovadora lámpara LED con la lámpara de mercurio convencional para la eliminación de DCF en tratamiento de agua. Luego, se analizaron los impactos ambientales relativos al proceso de oxidación para evaluar los impactos de los oxidantes. Por último, se evaluó una situación que emplea una fuente de energía más limpia para explorar posibles mejoras.

Metodología

Para el estudio de la remoción de MPs, se trabajó con partículas de poliamida (PA) y poliestireno (PS) en el rango 20-300 μm . En el caso de PA, todas las partículas estaban por

debajo de 300 μm , mientras que las partículas de PS mayores de 300 μm se redujeron primero mediante un molino criogénico. En cuanto a las membranas, se evaluaron tres materiales comercialmente disponibles: policarbonato (PC), acetato de celulosa (CA) y politetrafluoroetileno (PTFE), todas con tamaño de poro nominal de 5 μm . Los MPs se analizaron primero con un microscopio acoplado a uno espectrofotómetro de rayos infrarrojos. También se evaluaron su distribución del tamaño de partículas dentro del rango tamizado, su potencial zeta en agua variando el pH y su morfología a través de microscopio electrónico de barrido (*Scanning Electron Microscope*, SEM). Por otro lado, las membranas fueron caracterizadas con imágenes SEM y medidas de ángulo de contacto, de dureza Shore tipo A y de rugosidad superficial. Se desarrolló en el laboratorio un sistema de filtración, al que se añadió un microcontrolador Arduino para los estudios a presión constante del modelo de obstrucción. Para ello se consideraron los cuatros mecanismos principales: filtración de torta, obstrucción completa de poros, obstrucción intermedia o parcial de poros y obstrucción estándar o interna de poros, cuya expresión matemática se basan en la ecuación de la ley de potencia de Hermia. Para la degradación del DCF, se construyó un fotorreactor en recirculación que trabaja a flujo constante. Primero el sistema se evaluó mediante actinometría química para determinar la irradiación recibida por la solución, mientras que la detección y cuantificación de DCF se realizó mediante cromatografía líquida de alta resolución. Entre los AOPs, se seleccionó aquellos basados en el uso de peróxido de hidrógeno y cloro libre (*Free Chlorine*, FC) como oxidantes. El primero porque en previos estudios ambientales resultó más respetuoso con el medio ambiente en comparación al peroximonosulfato y el persulfato, mientras que el FC se ha vuelto cada vez más popular debido a su bajo costo y porque ya se usa en agua como agente desinfectante residual contra la recontaminación. El modelo cinético mecanístico propuesto para los procesos UV/H₂O₂ y UV/FC se implementó en GNU Octave para resolver la optimización no lineal minimizando la función de error objetivo y evaluar respectivamente la cinética de segundo orden de HO[•] y Cl[•] con DCF. La efectividad del tratamiento también se evaluó con estudios de mineralización, a través de análisis de carbono orgánico disuelto, y de fitotoxicidad en semillas de tomate y rábano para asegurar la eliminación completa de los subproductos DCF más dañinos e inestables. Por último, para el análisis de LCA se siguió la metodología estandarizada por las normas ISO 14040 y 14044. Se usó ecoinvent v3.0 como

fuentes de datos secundaria para el inventario, mientras que se empleó SimaPro 9.4 para compilar el inventario y cuantificar los resultados.

Resultados

Como primera parte del estudio, se evaluó la membrana con mejor rendimiento en términos de eficiencia de eliminación de los MPs y costes operativos. Las membranas de CA lograron altas eficiencias de eliminación (por encima del 94%) en todos los casos, necesitando la menor presión transmembrana (*Transmembrane Pressure*, TMP) para trabajar y proporcionando el mayor flujo de agua, reduciendo así los costes de tratamiento. Además, la membrana de CA, debido a su menor dureza, indujo una menor descomposición de las partículas, aunque era potencialmente más propensa a la abrasión. Entonces, se investigó más a fondo la obstrucción de la membrana de CA inducida por las partículas de MPs. Los mecanismos de obstrucción se modelaron secuencialmente en obstrucción completa de poros seguida de la formación de una capa de torta. A continuación, se extrapolaron las cinéticas mediante las ecuaciones del modelo de Hermia, estudiándolas en función de la concentración de partículas en la entrada y la TMP de trabajo. Las constantes cinéticas se correlacionaron positivamente con la concentración de MPs, mientras que la comparación de los valores a diferentes TMP condujo a la determinación de las condiciones óptimas de trabajo, un compromiso entre los costes operativos y la reducción de la obstrucción. Las partículas de PA indujeron una obstrucción más elevada debido a su mayor hidrofobicidad y su tamaño más pequeño. En contraste, las partículas de PS, con sus mayores irregularidades y fuerzas electrostáticas repulsivas, indujeron una obstrucción menor pero con una abrasión visible de la membrana. Estos resultados destacan las principales interacciones entre los MPs y las membranas y ayudan a predecir el rendimiento de la membrana en presencia de otros MPs (con diferentes tamaños, formas y fuerzas electrostáticas) y diferentes condiciones operativas, con el fin último de desarrollar procedimientos de limpieza o predecir la sustitución de la membrana para mejorar la eliminación de las partículas de MPs. Además, dado que no se puede ignorar la abrasión de la membrana al filtrar partículas altamente irregulares y con punta, se recomienda su sustitución en lugar de implementar otras estrategias antiincrustantes que puedan aumentar el riesgo de contaminación secundaria por MPs.

En cuanto a la degradación de DCF, el proceso sigue una cinética de pseudo primer orden y su tendencia reflejó el patrón de los coeficientes de extinción molar del DCF y de los oxidantes.

Se encontró un factor sinérgico positivo para los AOPs basados en UV-LED en casi todos los casos, pero a pesar de las tasas de degradación más altas, la demanda total de electricidad calculada como energía eléctrica por orden (*Electric Energy per Order*, EE/O) fue similar a la de UV solo, debido al costo energético de los oxidantes que influye bastante cuando se considera solo el tiempo de contacto en el fotorreactor. Para los dos procesos, UV/H₂O₂ y UV/FC, se propusieron mecanismos rigurosos de degradación cinética a diferentes longitudes de onda donde los valores calculados para las constantes cinéticas fueron respectivamente de $k_{HO} = 9,12 \cdot 10^9 \text{ M}^{-1} \text{ s}^{-1}$ y $k_{Cl} = 1,30 \cdot 10^{10} \text{ M}^{-1} \text{ s}^{-1}$. No se encontró una sinergia estadísticamente significativa ($p > 0,05$) para el sistema de doble longitud de onda (265 + 285 nm), y las constantes basadas en el tiempo en todos los casos cambiaron linealmente con la intensidad de la lámpara. Por último, el análisis de carbono orgánico disuelto reveló una baja mineralización (alrededor del 20-30%) asociada con la formación de dímeros estables, mientras que los ensayos de fitotoxicidad mostraron una disminución de la toxicidad. En general, los resultados muestran el gran potencial de la implementación de LEDs con longitudes de onda específicas en tratamientos de agua para aumentar la eficiencia de la degradación de CECs mediante el control de la intensidad aplicada para lograr la velocidad de reacción requeridas.

Finalmente, se ha realizado la comparación del sistema basado en LED con un sistema equivalente basado en lámparas de mercurio de baja presión mediante el análisis de ciclo de vida. La unidad funcional se definió como "El tratamiento de 1 L de agua contaminada con 20 mg L⁻¹ de diclofenaco para lograr una eliminación del 90% del contaminante". Para la valoración se exploraron varios casos y se pudo concluir que la aplicabilidad de la lámpara LED UV-C es muy prometedora, mostrando menos impactos que las de mercurio, y considerando también que se espera un aumento significativo en la eficiencia energética en los próximos años, en particular, se pronostica un aumento del 20% para 2030. También se evaluó una comparación entre UV-C, UV-C/H₂O₂ y UV-C/FC utilizando la lámpara de LED UV-C de 265 nm, ya que anteriormente no se habían realizado estudios sobre la sostenibilidad del cloro como oxidante en el tratamiento de agua. Para el mismo tiempo de tratamiento, UV-C/H₂O₂ fue más sostenible que UV-C/FC. Sin embargo, en general se prefiere el tratamiento que requiere un tiempo más corto, siendo la electricidad de todos los sistemas la principal fuente de impacto. Por eso, el uso de fuentes de energía más limpias, como la energía fotovoltaica o la eólica, mejoraría en gran medida los impactos generales.

Conclusiones

Las membranas de CA lograron el mejor rendimiento considerando los valores de TMP, flujo, y retención de los MPs; por lo tanto, se eligieron entre las tres membranas testadas. Gracias al modelo de obstrucción de la membrana, se identificaron la correlación entre la concentración de MP y el grado de obstrucción, las condiciones operativas óptimas de TMP, y las principales interacciones entre las partículas y la membrana. Todo eso, ayuda a predecir los ciclos de reemplazo de la membrana, que se recomienda para evitar una contaminación secundaria por MP.

Los resultados de degradación del DCF proporcionaron evidencia de la aplicación de las lámparas LED UV-B y UV-C para el tratamiento de agua, donde se puede aprovechar de las ventajas de los LEDs, su longitud de onda e intensidad ajustable y el encendido y apagado instantáneo, para el diseño del reactor en la escala y aplicación final deseada. También según la evaluación ambiental, la aplicación de la lámpara LED UV-C para el tratamiento de agua es muy prometedora. Pero dado que la electricidad es el principal punto de contaminación ambiental, es recomendado reducir el tiempo de tratamiento mediante la adición de oxidantes como H₂O₂ y FC y optar por fuentes de energía más limpias.

1. SUMMARY

1 Summary

In the big challenge of water contamination, the presence of contaminants of emerging concern (CECs) in treated water poses a risk to the safety of the environment and the health of the human being. Existing treatment plants have been proven inadequate in removing these CECs, which are being introduced into the environment, nonetheless. Their detection in wastewater, aquatic environments, and drinking water requires implementing adequate measures and elimination processes to avoid their impact on humans and ecosystems. Additionally, the increase in human pollution and natural disasters due to climate change is negatively affecting the water available. The peculiarity of these contaminants is also that they are not subjected to specific regulations in drinking water and are not controlled by standard legislation; thus, more effort is needed to prevent and reduce their occurrence. As a result, it is crucial to increase water resilience, and it is important to act at drinking water treatment plants, if not directly at tap water, considering the several routes of these contaminants into the environment. It is also essential to develop specific and optimised strategies to remove CECs, including, among others, microplastics (MPs) and organic compounds such as pharmaceuticals and personal care products.

MPs are defined as plastic particles smaller than 5 mm and gained great concern due to their ubiquitous and abundant presence in the water. There is also evidence that MPs act as vectors of various contaminants due to their additives and ability to sorb and accumulate toxic organic and inorganic pollutants on their surface. Moreover, because of their plastic nature, they take a very long time to biodegrade, and their small size makes them easily ingested. Among the engineered technologies explored for removing MPs, membranes have received considerable attention thanks to their simple implementation and stable effluent quality. The technology can be cost-effective and easily implemented depending on the membrane characteristics and the configuration. In this work, microfiltration was selected due to its simple implementation and the lowest operational energy costs compared to the other membrane processes. However, membrane fouling is a representative problem, and its mechanism and kinetic should be evaluated to help develop appropriate filtration and cleaning procedures and increase the efficiency of MPs removal. Filling the gap would encourage and allow the safe implementation of the system in our daily water treatments, including in household systems.

On the other hand, among the CECs, organic micropollutants are also gaining increasing attention due to their associated risk, to the point that the European Commission decided to introduce a *watch list* of substances in water bodies to start monitoring their occurrence and develop strategies. Among the *watch list*, diclofenac (DCF), a nonsteroidal anti-inflammatory drug commonly used for pain relief, has captured the interest for the known toxicity towards wildlife and the potential ecosystems effects in water bodies, where it was detected up to $\mu\text{g L}^{-1}$. However, DCF, and in general organic compounds, have smaller sizes and different behaviours compared to MPs, and therefore microfiltration is unsuitable for their removal, where only high-pressure membrane systems would be effective. Alternatively, UV-B and UV-C irradiation has proven to be an effective treatment for their degradation, other than being effective in water disinfection. By integrating a UV-based advanced oxidation processes (AOPs) system, higher water quality can be achieved on a variety of threats. Furthermore, using light-emitting diodes (LEDs) instead of mercury lamps could lead to interesting breakthroughs in removing contaminants. Among the major advantages of the LEDs, besides being mercury-free solutions, they have a tuneable wavelength, instant on-off (no warm-up time), and adjustable intensity. These characteristics have incredible potential in UV-B and UV-C-based AOPs since the overall performance of the process depends on UV wavelength and intensity. In addition, their small size allows for high design flexibility and the perspective of their exponential growth, similar to the LEDs in the visible or UV-A range, makes them very attractive for the design of any water treatment. Finally, in support of the achievements, environmental analyses were conducted to study the overall impacts. Thanks to these studies, the aim is to increase the perspective of increasing water quality from CECs and cope with water scarcity, anthropogenic disasters, and natural calamities that could prevent or damage safe water supply.

In the first part of the study, the MPs particles (polyamide (PA) and polystyrene (PS) in the range of 20-300 μm) and the membranes selected (polycarbonate (PC), cellulose acetate (CA), and polytetrafluoroethylene (PTFE) having the same nominal pore size of 5 μm) were characterised. Next, the best performing membrane in terms of MPs removal efficiencies and operational costs was evaluated. While high removal efficiencies (above 94%) were achieved for all cases, CA membranes needed the lowest transmembrane pressure (TMP) and allowed the highest water flux, decreasing overall treatment costs. Furthermore, given its lowest hardness, the CA membrane induced less breaking down of the particles, although

it was potentially more prone to abrasion. Membrane fouling induced by the PA and the PS particles was further investigated for the CA membrane. The studies were conducted at constant pressure, and the kinetics were extrapolated using Hermia's model equations and studied as a function of the particle concentration in the inlet and working TMP. The fouling mechanisms were sequentially modelled into complete pore blocking followed by cake layer formation. The kinetic constants were positively correlated with the MPs loading, whereas comparing the values at different TMP led to an optimum working condition, a compromise between operational costs and fouling alleviation. PA particles induced higher fouling due to the higher hydrophobicity and the smaller particles' size. In contrast, PS particles' higher irregularities and repulsive electrostatic forces induced less fouling but visible membrane abrasion. These results highlight the main MPs-membrane interactions and help to predict the membrane performance under the presence of other MPs (with different sizes, shapes, and electrostatic forces) and different operating conditions, with the final scope to develop cleaning procedures or predict the membrane replacement to enhance MPs removal. Furthermore, since membrane abrasion cannot be neglected when filtering highly irregular and spiky particles, the replacement is recommended over implementing other antifouling strategies that can increase the risk of secondary MPs pollutions.

Regarding the degradation of DCF, the application of UV-B and UV-C (265, 285, and 310 nm) LEDs alone and in combination with hydrogen peroxide (UV/H₂O₂) and free chlorine (UV/FC) was evaluated. Where H₂O₂ was chosen for being more environmentally friendly than peroxymonosulfate, and persulfate, while FC has become increasingly popular since low-cost and is already used in water as a residual disinfection agent against recontamination. The degradation of DCF followed a pseudo first-order kinetic, and their trend reflected the pattern of the molar absorption coefficients of the DCF and the oxidants. A positive synergistic factor was found for the UV-LED driven AOPs in almost all cases, but despite the higher degradation rates, the overall electricity demand was similar to UV alone due to the oxidants' energy cost when only the photoreactor contact time is considered. The rigorous kinetic degradation mechanisms at different wavelengths were proposed for the two processes, UV/H₂O₂ and UV/FC, where the predicted values for the kinetic constants were respectively $k_{HO} = 9.12 \cdot 10^9 \text{ M}^{-1} \text{ s}^{-1}$ and $k_{Cl} = 1.30 \cdot 10^{10} \text{ M}^{-1} \text{ s}^{-1}$. No statistically significant synergy ($p > 0.05$) was found for the dual-wavelength system (265 + 285 nm), and the time-based constants in all cases changed linearly with lamp intensity. Finally, dissolved organic

carbon analysis revealed low mineralisation (around 20-30%) associated with the formation of stable dimers. In contrast, phytotoxicity assays on tomato and radish seeds showed a decrease in toxicity. In the main, the results show the great potential of implementing wavelength-specific LEDs in water treatments to increase the efficiency of the selected contaminant degradation and flexibility in controlling intensities and kinetic degradation rates.

Finally, the photoreactor employed was compared with a similar system using UV-C low-pressure mercury lamps through the Life Cycle Assessment (LCA) analysis. The functional unit was defined as “The treatment of 1 L of polluted water with 20 mg L⁻¹ of diclofenac to achieve a 90% removal of the contaminant”. Several cases were explored, and overall, the applicability of the UV-C LED lamp looks very promising, showing less or similar potential impacts than the mercury lamps in the 16 environmental categories selected from the Environmental Footprint method. A comparison between UV-C, UV-C/H₂O₂, and UV-C/FC while employing the 265 nm UV-C LEDs lamp was also assessed since no studies were previously conducted on the sustainability of FC as oxidant in water treatment. For the same treatment time, UV-C/H₂O₂ was more sustainable than UV-C/FC; however, the treatment requiring a shorter time is generally preferred because electricity was the main source of impact. In this regard, employing cleaner energy sources such as photovoltaic or wind energy would greatly improve the overall impacts; and, therefore, highly encouraged.

2. INTRODUCTION

2 Introduction

2.1 ‘White gold’

Water is an essential resource for life and health, and providing safe drinking water is important in both industrialised and developing countries. "There is no life without water. It is a treasure indispensable to all human activity". This sentence opens the European Water Charter, approved in 1968 [1]. Water is the main chemical, together with oxygen, that humankind uses to live. It forms most of the Earth's surface and represents approximately 60% of the human body weight. Despite its abundance, clean and safe water is a precious and limited resource, and access to it is becoming increasingly difficult in many parts of the world. It is often defined as ‘white gold’ because of its value and importance.

Water scarcity is caused by several factors, such as population growth, urbanisation, increased demand for water for agriculture and industry, and progressive desertification of the planet caused by climate change. The latter is strongly correlated to the water crisis [2]. Extreme weather, such as severe floods, long droughts, and rising sea levels, are indeed making water scarcer and the quality more unpredictable.

Water contamination is also a growing concern, as water is increasingly polluted by a variety of sources, including agricultural runoff, industrial discharge, and an increase in human activity and human waste. These harmful substances in surface water, such as chemical contaminants and microorganisms, can cause gastrointestinal illness, skin infections, developmental problems in children, and chronic health problems after prolonged exposure. In addition, they can accumulate in the ecosystem, causing loss of habitats and biodiversity. All these concerns materialised in stricter regulations for the treatment of urban and industrial aqueous effluent (Directive 91/271/EEC) [3] and the need to increase the quality of water intended for human consumption (Directive 98/83/EC) [4]. Furthermore, in 2000, the European Union (EU) implemented the Water Framework Directive (WFD) 2000/60/EC [5] with the goal of promoting sustainable water management and protection of water resources across the EU. The WFD presents a breakthrough in water policy, and it requires the EU Member States to achieve a good ecological and chemical status in all inland and

coastal water bodies, surface and groundwater, by 2027 at the latest. Yet in 2018, the European Environmental Agency (EEA) reported that only 38% of surface water bodies across Europe were in “good chemical status”, where the limit was defined by the concentration of a few priority substances found across the EU, among others mercury, cadmium, brominated diphenyl ethers, and polycyclic aromatic hydrocarbons [6]. Therefore, although efforts to address water scarcity and contamination are globally underway, much work remains to be done.

2.2 Contaminants of emerging concern: CECs

Contaminants of emerging concern (CECs) represent a group of chemicals that are not commonly monitored or regulated but are of growing concern due to their potential impact on human health and the ecosystem’s lives. Their presence in the environment is not necessarily new, but the worries about their possible consequences are. Often, they are also referred to as “emerging contaminants” (ECs), “unregulated contaminants”, or simply “contaminants of concern”. They include pharmaceuticals, personal care products (PCPs), flame retardants, pesticides, endocrine disruptors, microplastics, and nanomaterials, among others, and are summarised in Table 2.1, together with the potential health effect and their occurrence in the environment. Scientists are still evaluating their associated risks, but a broad range of adverse effects have already been identified, including cancer, cardiovascular and neurological diseases [7].

Table 2.1 Overview of different categories of CECs, the associated health effects, and occurrence in the environment.

CECs group	Examples	Potential health effects	Occurrence in the environment
Pharmaceuticals	Antibiotics, painkillers, antidepressants, metformin, synthetic progestin	Bioaccumulation in tissues, genotoxicity, altered feeding and reproductive behaviour, organ damage, antibiotic resistance	Organisms, surface waters, treated wastewater, groundwater, drinking (tap) water
Personal care products	Chemicals in soaps, cosmetics, sunscreens, lotions, fragrances	Cytotoxicity, genotoxicity, reduced reproduction, growth rates, and survival, bioaccumulation in tissues	Organisms, surface waters, treated wastewater, groundwater, drinking (tap) water, biosolids, sediment

Micro- and nanoplastics	Plastic particles with size smaller than 5 mm, found in several forms: film, fragments, foam, fibre, beads	Reduced feeding ability, growth, reproduction, and survival, endocrine disruption	Organisms, surface waters, treated wastewater, groundwater, drinking (tap and bottled) water, beer, seas salt, sediments, air
Pesticides	Chemical substances that kill, incapacitate, or prevent pests from causing damage	Reduce survival and reproduction, immunosuppression, endocrine disruption	Organisms, surface waters, treated wastewater, groundwater, drinking water, precipitation, sediment
Flame retardants	Classes of materials that inhibit or resist the spread of fire, such as polybrominated diphenyl ethers (PBDEs)	Bioaccumulation in tissues, decreased reproductive success, neurobehavioural effects, endocrine disruption	Organisms, surface water, sediment
Plasticisers	Chemical additives to increase plasticity, such as phthalates and bisphenol A	Bioaccumulation in tissues, cytotoxicity, genotoxicity, endocrine disruption, metabolic disruption, altered general behaviour	Organisms, surface water, treated wastewater, biosolids, sediment
Disinfection by-products (DBPs)	Chemical substances resulting from the interaction of organic matter with disinfection agents such as chlorine during the water treatment process	Cytotoxicity, genotoxicity, carcinogenesis	Treated wastewater, drinking water
Nanomaterials	Materials in the nanoscale with unique optical, electronic, thermo-physical or mechanical properties, such as titanium dioxide, zinc oxide, or carbon nanotubes	Cytotoxicity, altered diversity, impaired feeding ability, reduced survival, growth rate and reproductive failure	Organisms, surface water, treated wastewater, sediments

On the one hand, the increase in population and the disasters caused by climate change have helped the presence and abundance of these CECs in water bodies. On the other hand, the improvements in analytic techniques with greater sensitivity allowed their detection and quantification even at trace levels, permitting the identification of these compounds in many more matrices, including drinking water. Even if their concentration is relatively low, in the range of ng L^{-1} to $\mu\text{g L}^{-1}$, long-term exposure can still cause broad detrimental effects on human bodies and aquatic ecosystems. Notwithstanding, they are not subjected to specific regulations or controlled by standardised legislation [8]. The extensive presence of these

contaminants in surface water, groundwater, and drinking water also confirms that conventional treatments in wastewater treatment plants (WWTPs), as well as drinking water treatment plants (DWTPs), are not suitable for their complete removal, and there is the need of innovative strategies to prevent, reduce, or remove the CECs presence in water bodies. Among CECs contamination, microplastics and organic compounds received significant attention in recent years due to their abundance and potential impacts on the environment and human health. However, these two categories of contaminants present different challenges for their removal strategy due to their differences in size and behaviour in water environments.

2.3 Microplastics contamination

2.3.1 Microplastics: definition, analysis, and occurrence

Plastic has become an integral part of modern society, with its usage increasing exponentially in recent years. It is lightweight, versatile, and durable, making it an ideal material for a wide range of applications, from packaging to construction to medical devices. Worldwide, plastic production has almost reached 370 million tonnes [9], with around 55 million tonnes produced in Europe, where of the total plastic waste, only one third is recycled, around 40% is sent to energy recovery operations and over 23% is still to date sent to landfill. Therefore, the growing demand for plastic and its poor management have led to its accumulation in the environment, including oceans, rivers, and soils [10]. Furthermore, plastic items can take time to decompose, from 20 to 500 years, depending on the material's structure and the degrading conditions, making this type of contamination quite persisting in the environment. As a consequence, microplastics (MPs), defined as plastic particles smaller than 5 mm, were found ubiquitously and abundantly in many water bodies and became a widespread environmental challenge. They have recently gained a lot of interest since the situation is expected to worsen in the near future and entered into the list of contaminants of emerging concern [11], even if they are bigger in size compared to the rest of the pollutants. Indeed, MPs are usually considered particles above the micrometre size where the nanoplastics (NPs) range begins [12], even if the exact definition is still controversial [13].

Although they are very much correlated, MPs and NPs differ in the number of studies available, their possibility of being detected, and the technology to employ for their removal. Therefore, for the scope of this work, MPs are primarily discussed due to their greater detectability, as well as the availability of more research studies conducted to investigate their impacts.

Among MPs, an important categorisation is between primary and secondary [14]. Primary MPs are originally manufactured to have a size less than 5 mm; they are found in textiles, medicines, and PCPs, such as skin exfoliators and shower gels, while secondary MPs are derived from the fragmentation of larger plastic items due to mechanical and photo-degradation generated by the natural wave action and UV irradiation [15]. The shape is also an important factor that can influence their elimination efficiency and potential environmental health risks [16]. They can be the direct results of the manufacturing or degradation process and be in the form of fragments, fibres, microbeads, films and sheets, among others (Figure 2.1).

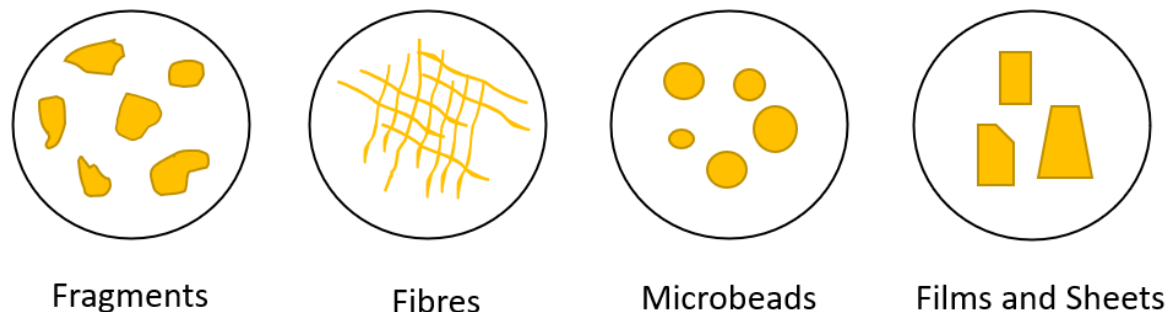


Figure 2.1. Microplastic morphology types.

Plastic particles can also have various colours if coming from textile fibres and PCPs, which can be released, for instance, through industrial discharges or domestic washing machines. It might also be transparent from the degradation of packaging products like plastic bottles, cups, and bags. Finally, to identify the source but also an efficient removal technology, it is important to identify the polymer composition. Among the main polymers detected in water bodies were polystyrene (PS), polyethylene (PE), polyethylene terephthalate (PET), polypropylene (PP) and polyamide (PA) [13,14]. To summarise, a physical characterisation,

with size, colour, and shape, and a chemical characterisation, with a clear assignment of the polymer, are usually reported when describing the occurrence of microplastic in water bodies. However, one of the main challenges in MPs and even more in NPs reports is the lack of a standardised way to identify and quantify them, which results in a large variation in concentration and particle size in the different studies. Common analytical methods are shown in Table 2.2. For quantification, the visual method and scanning electron spectroscopy (SEM) are mainly employed, while qualification is mainly done with Fourier-Transform Infrared Spectroscopy (FTIR) or Raman spectroscopy, pyrolysis coupled with gas chromatography (GC) or mass spectroscopy (MS) and finally, high-performance liquid chromatography (HPLC) [17]. When only quantification is applied, the final estimation can be greatly biased by the expertise of the observer, as plastic particles can be easily confused with other materials [18]. All methods have particle size limitations other than advantages and disadvantages. For this reason, identifying and quantifying NPs is even more challenging.

Table 2.2. Summary of the main analytical techniques for MPs analysis. Adapted from [17].

Method		Particle size	Advantages	Limitations
Visual Method	Microscopic counting	Depends on the expertise of the observer	Provide an overall picture of MPs abundance, and it is low cost	The nature of the sample cannot be determined
	FTIR	Down to 20 μm can be analysed	Non-destructive, well-established, fast and reliable	Sometimes can present difficulty in data interpretation, and it is expensive
Spectroscopic Method	Raman	> 1 μm	Low sensitivity towards water, and it analyses smaller MPs	Interference due to fluorescence. Very expensive technique
	SEM	Down to micro-scale	High-resolution image	Samples need to be coated, and there is no identification information
Chromatographic Method	Pyrolysis GC/MS	Sample sizes over 500 μm	Samples analysed together with additives, no solvents, method sensitive and reliable	Pyrolysis database available for selected polymers
	HPLC	Several mg of sample for chemical extraction	Recovery of selected polymer is high	No physical characteristics or size information. Analyse only specific polymers

Recently micro-FTIR has gained much more attention as an ideal method for quantification and qualification together [19,20]. It combines FTIR spectroscopy with microscopy, allowing the identification of the plastic particles visually and by the determination of their chemical structure. Furthermore, micro-FTIR is highly attractive since it has shown great reliability and with minimal need for sample preparation as it can be used to measure directly on the membrane filter by performing a “chemical mapping” [21]. However, limitations regarding refractive errors in the spectra of irregularly shaped particle surfaces might limit the use of the technique since the results might be hard to interpret [21]. Also, not all the filter materials are suitable for performing the chemical map, and a study should be conducted beforehand to ensure that the IR window of the filter doesn't cover the polymers' signals and that the IR spectra are clear without leading to high diffractive errors that compromise MPs identification. A further limitation is the detection limit down to 20 μm ; therefore, other techniques, such as Raman spectroscopy, should be employed to examine smaller particles.

The concern about MPs captured great attention because of their associated health impacts on the human body and the ecosystems. So far, the threats towards marine fauna have been widely reported [22–25]. Since plastics are relatively stable, they accumulate in the body and can cause long-term damage. Among the symptoms mainly reported in aquatic animals are malnutrition, inflammation, chemical poisoning, oesophagus blockage, abnormal growth, and decreased fecundity. The threat is not only connected to the plastic itself, but higher toxicity may be given by plastic additives, such as flame retardants, endocrine disruptors, and other compounds shown in Table 2.3.

Table 2.3. A list of plastic additives associated with their application.

Additive compound	Function
Plasticisers	Improve flexibility
Flame retardants	Prevent polymer ignition
Surfactants	Modify surface properties and allow emulsion with incompatible substances
Inorganic fillers	Increase stiffness and surface hardness and improve impact resistance
Pigments	Add colours to the polymer
Heat and UV resistance	Delay, slow down or stop oxidation of the polymer when heated or under prolonged sunlight exposure.
Cross-linking additives	Link together polymer chains

Some of these additives can have very strong negative effects on the human body and aquatic organisms. For example, Bisphenol A, BPA, is an endocrine-disrupting chemical that can adversely affect the entire hormones' normal operation and might have a carcinogenic, teratogenic and mutagenic effect [26].

Other than additives, MPs can carry on their surface other contaminants, also favoured by the large surface-to-volume ratio that supports chemical accumulation. For instance, due to their hydrophobic nature, they can attract on their surface other hydrophobic pollutants, such as hydrophobic persistent organic pollutants (POPs), among interaction with dichlorodiphenyltrichloroethane (DDT), polychlorinated biphenyls (PCBs), and other dioxin-like chemicals were reported [26–28]. Finally, they act as a vector of pharmaceuticals, promoting their bioaccumulation and biomagnification through the food chain [29,30], and pathogens, which can colonise the plastic particles forming successional biofilms and can infect the organisms they come in touch with [17]. Recent results have also shown that MPs in WWTPs could act as protective substrates for the microorganisms, shielding and protecting them from the disinfection treatments [15], increasing the chance of diverse contamination of drinking water. Other studies have also revealed that MPs presence might favour certain microbial communities and favour horizontal genes transfer and the increase of antibiotic-resistant bacteria [31].

To understand why the problem is so widespread, it is important to identify the main MPs' routes into the environment, which are schematically represented in Figure 2.2.

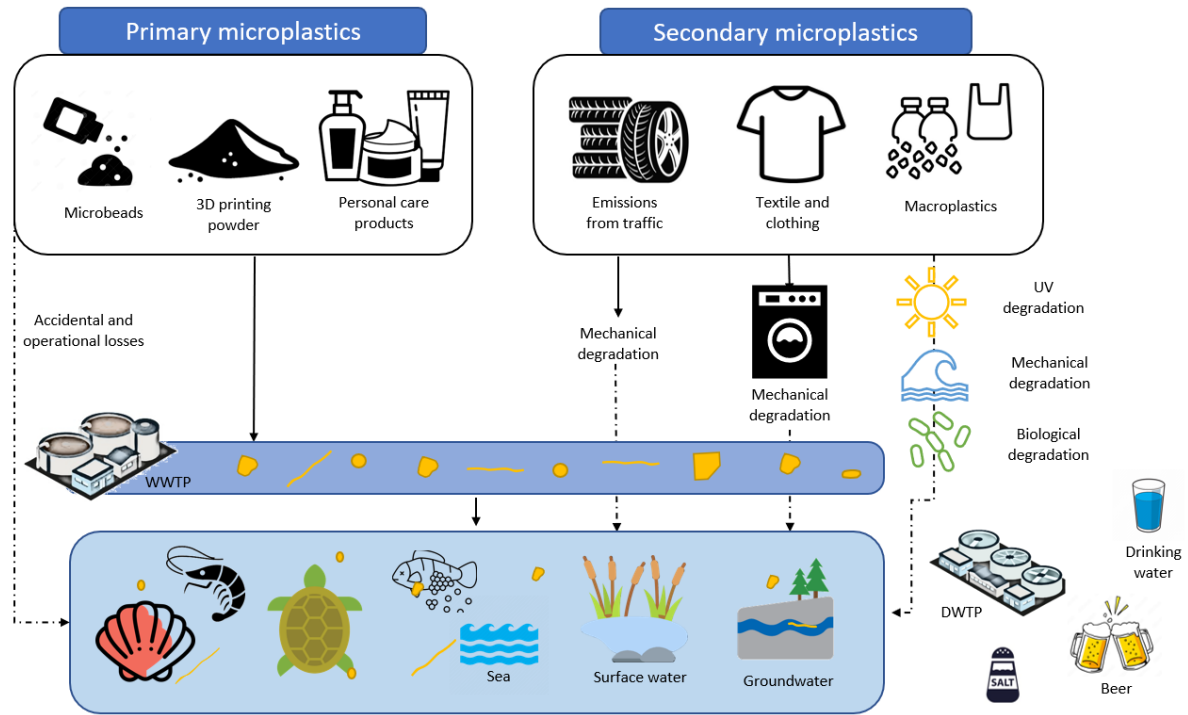


Figure 2.2. Schematic representation of the sources of MPs and plastic waste pathways.

The routes of MPs into the environment are many, and the most common is the fragmentation of macroplastic into microplastic [11]. Macroplastic are mainly in the environment due to land littering and bad waste management practices, such as poorly maintained waste collection and disposal facilities. Once in the environment, they are exposed to photo, mechanical, and biological degradation; they become brittle and easy to break into smaller particles, which are then easily transported by ocean and wind currents [18]. Washing machine effluents were also found as an important MPs contamination source, where the MPs are mainly in the form of synthetic fibres deriving from the mechanical stress of cleansing and centrifugate clothes [32]. Finally, car tyre debris, resulting from the wear and tear of the tyres as they are used on roads, are also an important point source of secondary MPs [14]. Among primary MPs, consumers' cosmetics and PCPs are probably the most

important, but accidental and operational losses from industrial manufacturing and industrial products should also be addressed [11].

A part of the MPs that enter the WWTP is successfully removed; however, WWTPs are also seen to play an important role in their release into nature, reported in several effluents with variable range size and quantities between 10^6 to 10^{10} particles per day [14]. Indeed, MPs undergo more mechanical stresses that induce further fragmentation before being discharged into water bodies or in the form of sewage sludge, which is then utilised as biofertilizers, incrementing soil pollution [14,33].

Once in the environment, microparticles can travel long distances as they can be transported by wind and water currents. This can lead to their widespread distribution throughout different ecosystems, such as oceans, rivers, lakes, and soil, and considering their role as chemicals and pathogens vectors can lead to catastrophic dispersion of species in new ecosystems [34]. In aquatic environments, MPs can be ingested by a variety of organisms, from plankton to fish and other aquatic species, causing their death and disease. Due to the accumulation of the MPs in their body, they pass them on to their predators, and so they enter the food chain and transfer bottom up along all the levels. The presence of MPs in food and beverages has been observed worldwide. Most published studies have identified drinking water, bottled water, beer, salt, honey, seafood, and even air as relevant dietary sources of MPs for humans [35–38].

2.3.2 Main technologies for microplastic removal

Despite the abundant detection and potential threat, to date, no legislation is in place to limit their presence in WWTPs effluents and the MPs content in drinking water [39]. However, some attention has been given to their fate, and some engineered technologies have been explored for their removal [13,40–44]. Figure 2.3 depicts the main processes explored for MPs removal for water treatment and the corresponding pros and cons.

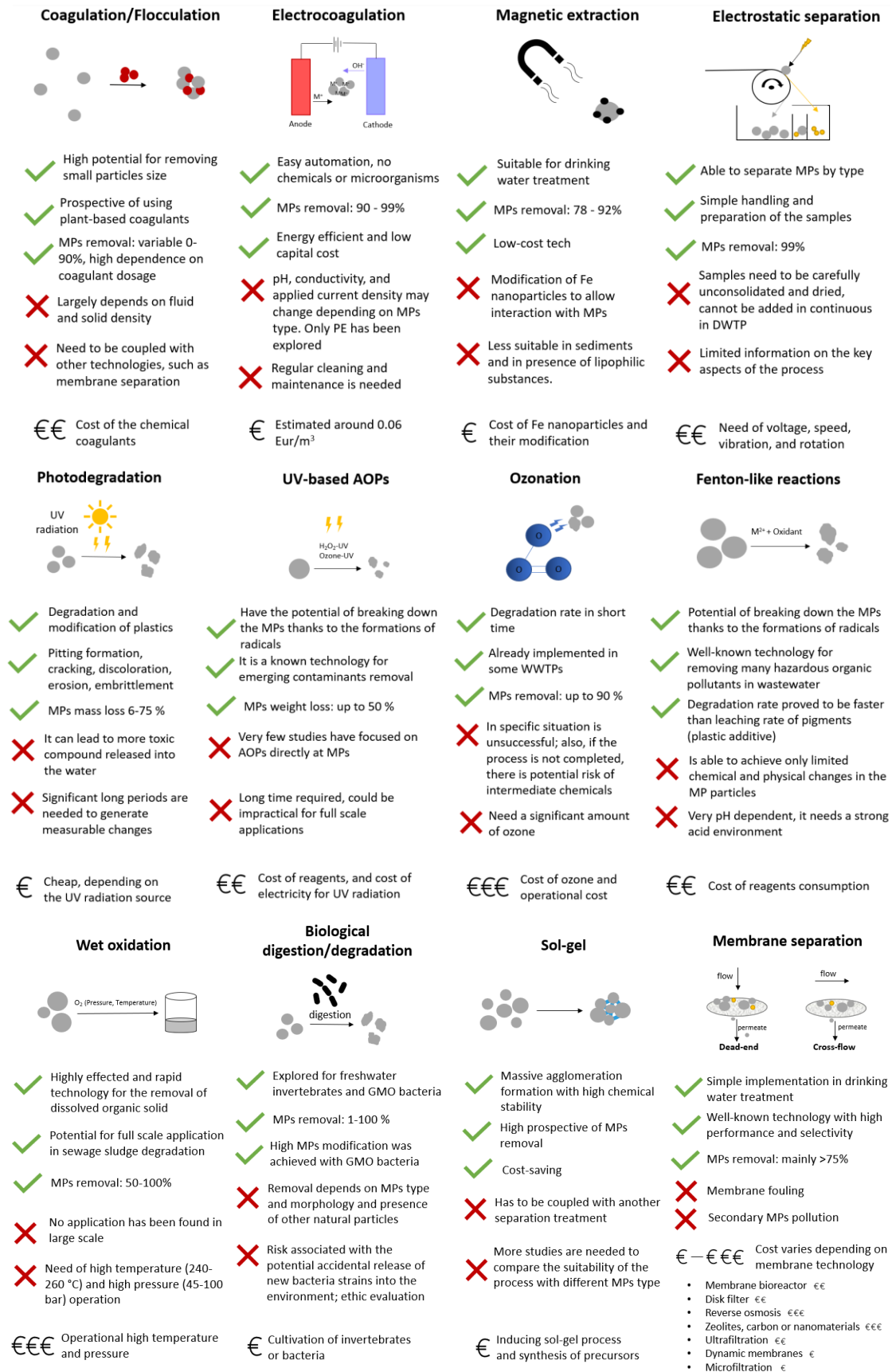


Figure 2.3. Main engineered technologies for MPs separation and degradation in water treatments.

Among them, coagulation and flocculation followed by membrane separation have been investigated by Ma et al. [45,46] in a couple of studies. They showed it has a high potential to remove small particles of MPs since the coagulants enable them to bind together, creating larger aggregates which are easier to separate; however, the chemicals added would negatively influence the following indispensable membrane process, by increasing the pressure needed for the flux to pass through. Electrocoagulation [47], magnetic extraction [48,49], and electrostatic separation [50] are interesting options recently explored for MPs removal. The former consists of the addition of the coagulants, which this time is followed by applying an electric charge to water to separate the agglomerations. Magnetic extraction is based on the addition of hydrophobic iron nanoparticles, which bind to plastic and allow their recovery by applying a magnetic field. Finally, electrostatic separation takes advantage of the different electrostatic behaviour of the plastic particles and separates MPs by type, but in dried and unconsolidated samples.

Photodegradation has also been explored for MPs degradation, mainly by direct sunlight exposure; however, it was very slow and inefficient, depending on the MPs' size [51,52]. Recently, advanced oxidation processes (AOPs) are receiving increasing attention thanks to their potential to degrade many water pollutants [53]. They refer to a set of chemical treatments consisting of highly reactive species used for the oxidative degradation of target pollutants. Among the AOPs, the combination of UV radiation with oxidants [53], ozonation [54–56], Fenton-like reactions [40,57], and wet oxidation [40] were investigated for MPs degradation. The first two processes were found to decompose some types of MPs successfully, but the decomposition mostly only occurred on the surface of the particles. The treatments' cost was variable but ranged from medium to high since also long treatment times were needed for MPs removal. Wet oxidation is a form of hydrothermal treatment consisting of oxidising suspended components in water using oxygen; however, the critical points were the high temperature and pressure necessary for the reaction. MP degradation was also studied through biological digestion [58,59], but very variable MPs structure modification was observed. The greatest efficiency was observed when engineered bacterial strains were employed, but the risk of accidental uncontrol release of genetically modified organisms (GMOs) into the environment is a potentially significant drawback [40].

Both photo-oxidation and biological degradation treatments simulate and accelerate the natural degradation processes, inducing fracture and crack on the plastic surface and increasing the decomposition rate. Therefore, the risk is that these processes only lead to higher fragmentation of larger MPs into smaller ones, which are more easily transported by wind and water and can enter more easily into the organisms. However, the potential of these treatments can be seen in the overall reduction of MPs and NPs when complete removal is achieved, especially for the latter, since other methods might fail and the treatment time required to complete the degradation is smaller.

Finally, sol-gel (alkoxy-silyl) induced cluster reactions, similar to coagulation and flocculation, have also been studied as a potential method for MPs removal [60]. In this process, the particles form larger agglomerates which can be more easily separated since they float on the water's surface. However, a separation system must be coupled with the treatment, and typically, driven-pressure membrane filtration is employed. The latter has captured significant attention combined or not with aggregation substances, thanks to the simple operation, high efficiency, and high treating volumes. However, the treatment costs can vary significantly depending on the membrane properties and the transmembrane pressure (TMP) necessary for the flow to pass [61].

2.3.3 Membrane filtration

Among the main engineering technology explored, membranes generated considerable interest and can play a fundamental role in tackling the problem of MPs [62]. They have already been extensively used for advanced drinking water treatments, and, depending on the membrane and feed suspension properties, they can be specific to intercept different pollutants. By now, several membrane processes have been explored for microplastic removals, such as micro (MF), ultra (UF) and nano-filtration (NF), reverse osmosis (RO), and dynamic membrane (DM) [63,64]. Figure 2.4 shows the main pressure-driven membrane processes. The pressure is imposed on the feed side to separate water into the permeate, the purified water, and the retentate, which is the concentrated solution with the removed pollutants to be discarded. Depending on the suspended size of the particles, and the membrane pore size and material, the costs and the applied pressures can differ.

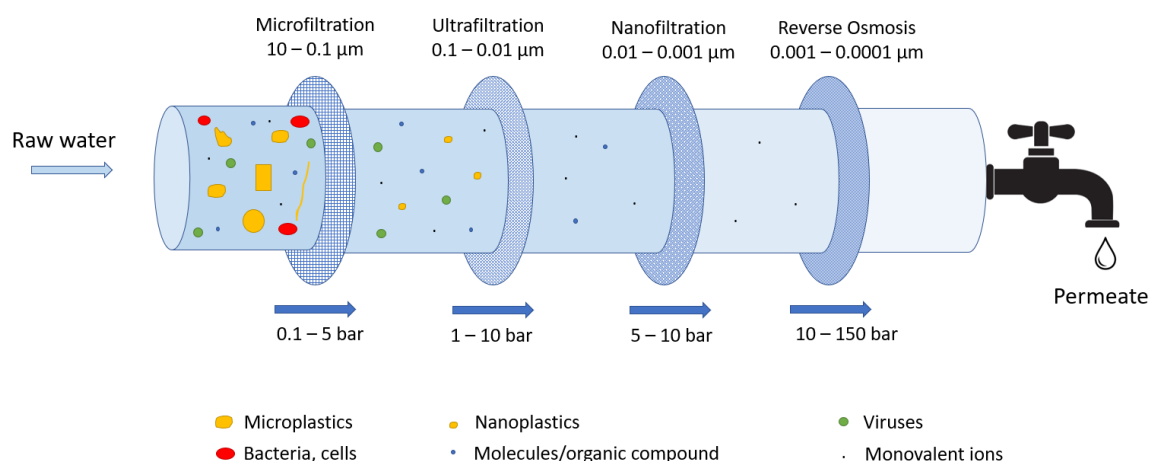


Figure 2.4. Schematic of the main pressure-driven membrane processes for water treatment technologies. Adapted from [65,66].

MF permits to obtain good water quality economically thanks to low energy consumption, high separation efficiency and compact plant size. MF is a low-pressure process, in the range of 0.1-5 bar, and membranes with pore size in the 0.1-10 μm range. UF has smaller pore sizes (10-100 nm), in which the liquid is forced through the membrane by applying a higher TMP. UF membranes are usually used in WWTPs for removing bacteria, colloids, and viruses. NF takes the lower end of UF and the upper end of RO. NF membranes are usually employed to remove colour, taste, odour and trace organic contaminants; however, they require higher operations costs. RO is able to separate up to ions and works by applying TMP in the range of 10-150 bar. It is currently mainly applied to desalination or where high purity of water is needed, such as in biopharmaceutical manufacturing. Finally, DM is an emerging filtration mechanism based on the formation of a cake layer which acts as the barrier for the pollutant if it is not too dense. Among the advantages are low TMP required for the operation, compact systems with higher permeation flux, relatively low-cost filtration materials, and no extra chemicals need; however, the removal efficiency is not high, and it mainly relies on the cake layer formation. Membrane bioreactor (MBR), disk filters (DF), and zeolites/carbon or nanomaterial are among other membrane technologies recently explored for MPs removal. MBR consists of a separation process (usually UF and MF membrane) promoted by biological catalysts, which help decrease the solution complexity

by biodegradation of the organic matter in the MPs solution. Although it is a promising technology for reducing MPs in WWTP effluent, it is not optimised for that scope, and the cost of operation and maintenance can be prohibitive in some applications due to the regular replacement of membranes needed and intensive energy inputs for aeration and pumping. DF include several woven filters meshed, which help reduce the MPs occurrence, used mainly as a final polishing step in WWTPs. However, studies showed that DF's main drawback is secondary microplastic contamination, which refers to MPs re-entering water streams due to membrane breakage. Furthermore, pore-clogging makes it necessary to operate frequent backwashes, which increases the MPs leakage. Finally, filtration with zeolites, carbon, or nanomaterials was mainly developed for other purposes but has also been explored for MPs. However, they are expensive operations and show technical problems such as low-flow water, limited sample volume capacity, and frequent clogging that limit the use of these technologies in real scenarios [67].

Overall, a literature review has shown the need for ad hoc designed microplastic separation solutions. Among the membrane processes, MF could be a good compromise between the operational costs and the removal efficiency if the target is mainly MPs with a size above the nanometre range. The main factors influencing the performance of membrane processes for MPs removal are summarised in Table 2.4 and depend on both the membrane and MP properties.

Table 2.4. Factors affecting the MPs removal by membrane processes.

	Influencing factors	Filtration process parameters
Membrane	Material	<ul style="list-style-type: none"> - Filtration mode - Flux - Transmembrane pressure - Filtration time - Mass removal - Particle number removal - Fouling mechanisms - Fouling degrees
	Pore size	
	Surface properties	
Microplastics	Shape	
	Size	
	Mass	
	Chemical composition	
	Concentration	
	Surface properties	
	Source of polluted water	

It is important to point out the inexistence of standardised protocols to measure the final removal since it has led to information not being directly comparable. For instance, the MPs removal was often reported in different units, such as mass and particle number removal efficiency [68]. Therefore, the importance to define both in the filtration process parameters. Another important distinction to make is the filtration mode, which can be in dead-end and cross-flow. In the former, the fluid flow direction is the same as the filtering direction, while for cross-flow processes, the flow is tangential to the membrane surface. Usually, in cross-flow configuration, the liquid that does not pass through the membrane is directed back into the system to increase the overall efficiency. Dead-end MF has been mostly used for small-scale operations; it has a simpler operation compared to a cross-flow configuration, needs a lower capital cost and allows an easier recovery of the highly concentrated feed which accumulates on the membrane surface. In contrast, cross-flow MF has the advantage of working with higher flow rates, therefore suitable for larger scale applications, and it has a reduced risk of fouling and membrane clogging; however, the capital costs are higher, and the operation and maintenance are more complex [69].

Since there is a need to implement a relatively low-cost and efficient strategy to limit MPs occurrence at the drinking water level, the dead-end configuration is an interesting option that can also be easily implemented for household system applications. This would also allow recollection of the MPs removed and further proper disposal. However, the major challenge in membrane processes, particularly in dead-end configuration, is the reduction of filtration capacity over time due to fouling given by the accumulation of suspended particles on the membrane surface or within the pores. Fouling can impose economic and operational issues if not appropriately controlled, and by knowing the mechanisms and the kinetics, it is possible to develop efficient strategies for minimising it and optimising MP removal. However, even if membrane technologies captured significant attention for MP remediation and fouling represents a critical problem for the design and operation of the system, there is a considerable knowledge gap on membrane fouling by MPs and the impacts and interactions between them [64]. In this regard, only five studies were found and listed in Table 2.5, where the membranes under investigation, the filtration mode, the particle type and size, and the MPs inlet concentration were reported.

Table 2.5. Literature review on membrane fouling by MPs.

Membrane employed	Filtration mode	Particles type	Particles size	Initial MPs concentration	Ref
Polysulfone (PSF) UF membrane with MWCO of 30 kDa	cross-flow configuration at constant pressure	PE particles	range of 13-690 nm	10 mg L ⁻¹	[70]
UF polyvinylidene fluoride (PVDF) hollow fibre membrane tubes, with mean pore size of 0.03 µm	cross-flow configuration at a constant flow rate	PS particles	range of 0.1-18 µm	varying from 0.01 mg L ⁻¹ to 1 mg L ⁻¹	[71]
UF and MF PVDF membranes (respectively 0.03 and 0.2 µm)	dead-end configuration at constant pressure	PE particles directly synthesised for the study	range of 1-100 µm	concentration varying from 0.1 mg L ⁻¹ to 10 mg L ⁻¹	[72]
UF PVDF membrane with MWCO of 100 kDa	dead-end configuration at constant flow-rate	PE particles	range of 40-48 µm	1 mg L ⁻¹ (~18,000 particles L ⁻¹)	[73]
Alumina membranes of 0.2 µm pores	both in cross-flow and dead-end configuration	PS particle shape (sphere, peanut, and pear)	size below 5 µm	25-50 mg L ⁻¹ in cross-flow and 5 mg L ⁻¹ in dead-end	[74]

*where the molecular weight cutoff (MWCO) is the size of the smallest particle or molecule that can pass through the membrane

Only three different membrane materials (PSF, PVDF, and alumina) were investigated, while the MPs studied were PE and PS particles. Enfrin et al. [70] modelled the fouling mechanisms for UF PSF membrane due to PE particles in cross-flow configuration and at constant pressure. Li et al. [71] mainly looked for anti-fouling strategies for UF PVDF to filtrate PS particles by adding aluminium-based flocs or introducing module rotation. LaRue et al. [72] worked with real solution matrixes and found that the presence of PE particles greatly increased the magnitude of the flux decline in both MF and UF PVDF membranes; however, MF showed higher flux recovery when backwash was employed. Xiong et al. [73] investigated more closely the PE influence in stimulating microbial activity, which increases

the production of extracellular polymeric substances, found to affect UF PVDF membrane biofouling strongly. Finally, Tanis-Kanbur et al. [74] focused on the impact of PS particles with different shapes and surface charges on alumina membranes and found that the unmodified PS particles had the highest interaction with the membrane, hence the highest fouling performance.

As a result of the review, a significant knowledge gap is still present in understanding the main fouling mechanisms occurring with different MPs and membranes, the kinetics trend of the fouling depending on operating conditions, such as initial MPs load and the working TMP, and identify the main interactions between MPs and membrane fouling. Filling the gap is essential for the correct implementation of membrane technologies in daily water treatments, including in households, hence, the interest in its investigation.

2.4 Organic micropollutants contamination

Organic micropollutants are a broad category of contaminants that can include, among others, pharmaceuticals, pesticides, and PCPs. They are single chemical compounds, and their size makes the removal with microfiltration membrane treatment unviable.

The occurrence of these compounds in the environment is also reported in many publications during the last decades [75,76]. Like MPs, these micropollutants can follow many pathways to nature, as shown in Figure 2.5.

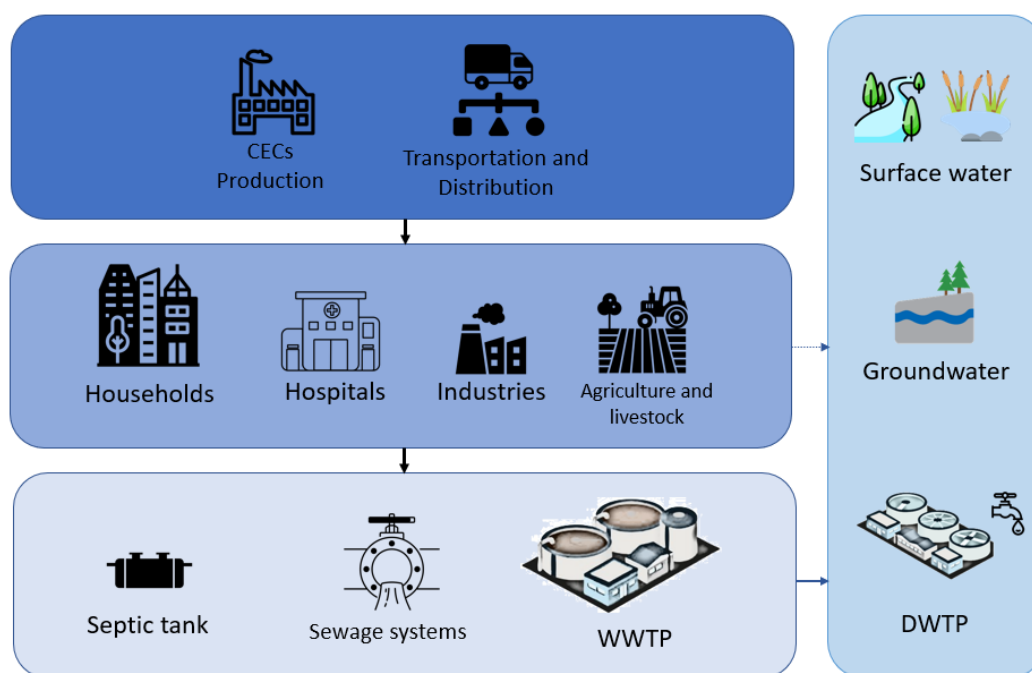


Figure 2.5. Representative sources and paths of organic micropollutants in the environment.

They can enter the environment through industrial wastewater discharge, runoff from landfills and agricultural lands, hospitals and veterinary effluents, as well as domestic wastewater discharges [77]. Other ways could be due to the leaching of septic tanks, a direct release to open waters via washing, bathing, or swimming, or contaminated discharge of industrial waste during their production or if employed in the plant. Finally, also irrigation and soil amendment with biosolids from WWTPs could help their spread in the environment [78]. A great concern is due to the consequences to humans and biota. In some pharmaceutical cases, some direct toxicity was found in aquatic organisms [79]; however, the main issues concern the recalcination of these pollutants and, therefore, the long-term exposition that can lead to serious chronic effects [80].

To date, there are no legal discharge limits also for these pollutants into the environment, but with the Decision 2015/495/EU [81], the European Commission established a *watch list* of substances for Union-wide monitoring, including 10 substances or groups of substances, for a total of 17 organic compounds listed in Table 2.6.

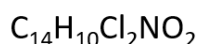
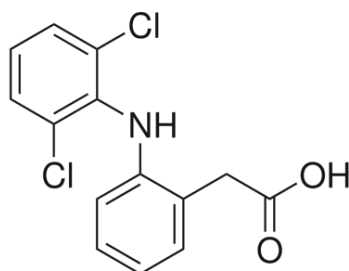
Table 2.6. List of 10 substances/groups of substances (total of 17 organic compounds) included in the first EU *watch list*.

Name of the substance	CAS number	Classification
17-Alpha-ethinylestradiol (EE2)	57-63-6	Pharmaceutical
17-Beta-estradiol (E2)	50-28-2	Natural hormone
Estrone (E1)	53-16-7	Natural hormone
Diclofenac	15307- 86-5	Pharmaceutical
2,6-di-tert-butyl-4- methylphenol	128-37- 0	Antioxidant
2-ethylhexyl-4- methoxycinnamate	5466- 77-3	UV filter
Azithromycin	83905- 01-5	Antibiotic
Clarithromycin	81103- 11-9	Antibiotic
Erythromycin	114-07- 8	Antibiotic
Methiocarb	2032- 65-7	Pesticide
Imidacloprid	138261- 41-3	Pesticide
Thiacloprid	111988- 49-9	Pesticide
Thiamethoxam	153719- 23-4	Pesticide
Clothianidin	210880- 92-5	Pesticide
Acetamiprid	135410- 20-7	Pesticide
Oxadiazon	19666- 30-9	Herbicides
Tri-allate	2303- 17-5	Herbicides

The substances were chosen for their high persistence in the environment, potential for bioaccumulation, toxicity, potential for widespread exposure, and lack of current regulation [81]. The aim of the *watch list* is to monitor them and generate high-quality data on their concentration in the aquatic environment to determine appropriate strategies and address their risk and occurrence.

2.4.1 Diclofenac contamination

Among the organic compounds reported in the first *watch list* developed according to Directive 2013/39/EU in regard to priority substances in the field of water policy [82], diclofenac (DCF) captured significant attention. It is a non-steroidal anti-inflammatory drug (NSAID) and is considered harmful to several species at environmental concentrations. In reviewed studies, DCF was reported to be ubiquitous in municipal wastewater treatment plants and aquatic environments at concentrations up to several $\mu\text{g L}^{-1}$ [76,83–85]. In Figure 2.6, it is presented its chemical formula and structure.

DICLOFENAC

2-(2-(2,6-dichlorophenylamino)phenyl)acetic acid

Figure 2.6. Diclofenac chemical formula and structure.

DCF is principally known for the dramatic decline in the population of vultures in South Asia and was recently reported to have caused death to a European vulture [86]. Among other threats, DCF has been shown to bioaccumulate in mussels and fish in relevant concentrations [84], and to be toxic to various aquatic species, causing reduced feeding activity, impaired growth, and increasing mortality rates [83].

Due to the considerable interest in both MPs and DCF, studies have also been conducted to investigate the potential adsorption of the latter onto plastic surfaces. While there are several factors affecting sorption, including environmental pH, ionic strength, salinity, the presence of other competing sorbents, as well as the type of MPs, their weathering degree, particle size, and available surface area, DCF has been found to be generally absorbed on the surface of MPs up to some mg g^{-1} [87–89]. Therefore MPs can be another source of DCF carriers in the aquatic food chain.

2.4.2 Main technologies for diclofenac removal

Traditional WWTPs and conventional DWTPs are ineffective at removing DCF. Therefore, considering the widespread presence of DCF and its associated risk, there is a need to develop new treatment strategies that can effectively remove it together with other organic contaminants.

Various new treatment technologies have been explored and tested in recent years for removing DCF from water and wastewater [85]. These include adsorption using activated carbon, membrane processes, biological treatment, photolysis, and AOPs [90]. The former employs the use of activated carbon, which is a highly porous material with a large surface area. It has been found to be quite effective for DCF removal, with an efficiency of around 90% [91]. However, the major challenge of its practical application is the environmental and economic aspects of the regeneration of the adsorbent material. Membrane separation was investigated but mainly employing high-pressure systems, which are the most suitable for the rejection of these small organic micropollutants. Indeed, MF is not appropriate in this scenario as it can only remove contaminants above 1 μm . NF and RO were the most effective for removing pharmaceuticals, reaching efficiencies $> 90\%$ [91,92], but greatly increasing the overall treatment cost, also considering the need for membrane surface modifications or additional strategies to reduce fouling. Biological processes, such as activated sludge systems, involve the use of microorganisms to degrade DCF, which can be aerobic and anaerobic. They have achieved efficiencies up to 90% in the best case [90]; however, the main drawback is the toxicity of this contaminant towards the microorganisms involved. Finally, photolysis and AOPs have also received great attention for the removal of DCF and in general, pharmaceutical and other organic compounds, achieving efficiencies above 70% in all the reviewed studies [85], even if some attention should be posed to the potential presence of harmful and unstable by-products occurring when the treatment time is incomplete [92,93].

Figure 2.7 shows a summary of the AOPs adopted for the removal of DCF. Yet, they can be categorised based on different criteria, such as the source of the hydroxyl radicals [85], non-photochemical or photochemical methods [94], and homogenous or heterogeneous phases [95]. As mentioned for the MPs removal, the term AOPs refer to a group of chemical treatment methods that generate reactive species such as hydroxyl radicals (HO^\bullet), which are capable of breaking down and removing organic pollutants from wastewater, oxidising and mineralising them into carbon dioxide, water and inorganic ions [94]. Although photolysis involves the use of light to break down the molecules and is sometimes included within AOPs, the inclusion is sometimes debated as the mechanisms of action are different from the other AOPs.

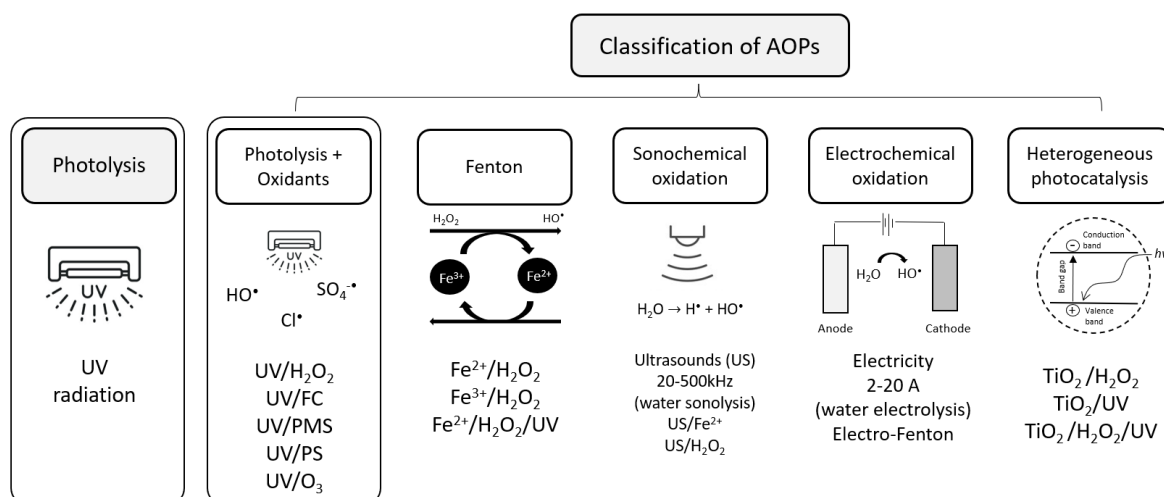


Figure 2.7. Photolysis and AOPs explored for the removal of DCF, adapted from [85]. Photolysis and Photolysis + Oxidants are boxed since chosen in this study.

During photolysis, the molecules absorb the radiation in the form of photons, which gives the energy necessary to excite specific electrons and form free radicals, which start a series of chain reactions to give the reaction products [96]. Each photon has an energy associated with it, E_λ , depending on the wavelength (λ) according to Eq. (2.1).

$$E_\lambda = \frac{h \cdot c}{\lambda} \quad \text{Eq. (2.1)}$$

Where h is Planck's constant and c is the speed of light.

Among the main factors influencing the performance of the photolysis, the most important ones are the intensity and wavelength of the radiation and the quantum yield of the compound to be eliminated. Photolysis alone has many advantages, like the absence of chemical products and low maintenance and operation costs. However, only certain pollutants are removed and to a limited extent. Moreover, the presence of turbidity can compromise the effectiveness.

To increase the effectiveness, UV radiation is often applied with oxidants to enhance the production of radicals. Together they increase the degradation rates of the parental pollutants and the potential by-products [96]. When used alone, the oxidants do not show high oxidising abilities, but the UV/oxidant system takes advantage of the synergy action given by the photolysis, the oxidant, and the photolysis of the oxidant, which help generate the

reactive species. The treatment cost should then consider the oxidants' price, offset by the typically shorter degradation times.

Fenton processes use a combination of iron catalysts and hydrogen peroxide to generate hydroxyl radicals. They are effective for a wide range of organic pollutants, have fast reaction kinetics, and can combine with other treatments; however, they have limitations, such as the presence of iron in the sludge, which causes secondary pollution and the need for an additional treatment stage, in addition to requiring acidic conditions for the reaction, which raises costs due to pH correction [97].

Sonochemical oxidation involves the use of ultrasound waves in the range of 20–500 kHz to generate reactive species, such as hydroxyl radicals, which can degrade organic pollutants. The ultrasound wave creates cavitation bubbles in the liquid, which then collapse, producing high temperatures (>5000 K) and pressures (>1000 bar), where the formation of the H^{\bullet} and HO^{\bullet} occurs. Its advantages include its ability to degrade a wide range of pollutants and its compatibility with other treatment methods. However, alone it has low efficiency; therefore, it is often used in combination with UV, O_3 , H_2O_2 or a catalyst [85]; also, it has some limitations, including the potential for reactor scaling.

Electrochemical oxidation involves the use of an electric current to generate reactive species and degrade organic pollutants. Electrochemical oxidation has several advantages, such as low energy requirements and its ability to operate at ambient temperature and pressure. Nonetheless, among the limitations are the potential for electrode fouling and the need to carefully select electrode materials and process parameters [85].

Heterogeneous photocatalysis consists of a solid phase (the semiconductor material) and a liquid phase (the contaminated water); the reactions occur on the catalyst surface, where the most used one is titanium dioxide (TiO_2). A UV source irradiates the catalyst and is typically used in combination with an oxidant to generate more reactive species. Among the advantages is the potential to selectively target specific pollutants and be low-cost, but the main difficulties faced are catalyst deactivation and recovery. Furthermore, applications on a large scale are challenging due to the ununiform distribution of radiation [85].

Among the different AOP technologies explored, Miklos et al. [98] evaluated the most efficient ones based on energy consumption, where the unit of comparison chosen was the electrical energy consumption (EE/O) first defined by Bolton et al. [99]. The EE/O describes the electric energy required to degrade the contaminant by one order of magnitude in

contaminated water, and it was chosen since electricity often represents a major fraction of the total AOP cost [98]. From the comparison, it was found that AOPs can be divided into three main groups: the first group having EE/O values below $1 \text{ kWh m}^{-3} \text{ order}^{-1}$, where there are the UV-based treatments; a second group with EE/O values ranging from $1\text{-}100 \text{ kWh m}^{-3} \text{ order}^{-1}$, among others photo-Fenton and electrochemical oxidation, and the third group with EE/O values above $100 \text{ kWh m}^{-3} \text{ order}^{-1}$ such as ultrasound and photocatalysis. Therefore for this study, the UV-based treatment and photolysis alone were selected for removing DCF in water, given their affordability and a high potential for different scale reactors and water applications. Furthermore, UV treatments, particularly with UV-C, already have broad applicability and effectiveness for disinfection purposes at the drinking water level and directly at the point-of-use, making it a very suitable technology to be explored for decontamination [100].

Among the most explored oxidants, hydrogen peroxide has commonly been employed since safe, abundant, and easy to use. It is considered one of the most viable AOPs [96], and it is already applied for full-scale application for potable water reuse integrated with other systems [98]. Other typical radical promoters are ozone, peroxymonosulfate (PMS), persulfate, and free chlorine (FC) [98]. UV-O₃ treatment covers a wide range of pollutants; however, it is not very energy efficient due to the large amount of electricity needed for both the UV lamp and the ozone generator. PMS and persulfate received great attention thanks to their high efficiency in removing a wide range of persistent pollutants [101]. Other than hydroxyl radicals, they generate sulfate radicals ($\text{SO}_4^{\cdot -}$), which have strong oxidising power and are more selective than HO^{\cdot} . Finally, FC, which refers to the sum of HOCl and OCl^- by a correlation strongly dependent on the pH [102], is a recently promising AOP, where it forms together with HO^{\cdot} reactive chlorine species (RCS) such as Cl^{\cdot} , which are more selective in oxidising the organic compounds.

However, while ozone is highly energy-expensive, PMS and persulfate were found to be less environmentally friendly than H_2O_2 . Indeed a recent study conducted by Pesqueira et al. [103] examined the life cycle assessment of UV-C combined with H_2O_2 , PMS, and persulfate by evaluating the potential impact in several environmental categories. They found that PMS and persulfate production were contributing more to the environmental footprint than the electricity employed during the process. Therefore, even if the process was effective, from the environmental perspective, their use was not recommended, while the use of H_2O_2 was

preferred to reduce the degradation times. On the other hand, UV/FC was chosen since it is an emerging AOP that has become increasingly popular since chlorine is low-cost and is already used in water as a disinfection agent against re-contamination [104,105].

2.4.3 Light-emitting diodes (LEDs)

In all the photolysis and UV-based AOPs, the irradiation source is a significant drawback of the treatment. Usually, it consists of a low-pressure (LP) mercury lamp which emits a narrow spectrum at 254 nm, and in some cases, a medium-pressure (MP) mercury lamp with a polychromatic emission spectrum in the range of 200–400 nm [96,98]. Even though MP lamps emit higher output energy than LP, the broadened wavelengths emitted from the former reduce their germicidal efficiency; therefore, most of the studies focused on LP mercury lamps. Other UV-C sources explored were excimer lamps and quasi-monochromatic light sources operating below 222 nm. In particular, excimer lamps studied were Xenon (Xe₂) and Krypton (KrCl), emitting respectively at 172 nm and 222 nm [106]. However, the mercury lamp based received greater attention so far thanks to their higher radiant power and longer lifetime [106,107].

Over the last decade, ultraviolet light-emitting diodes (UV LEDs) in the UV-B (280-315nm) and UV-C (200-280nm) range have gained attention as an alternative mercury-free UV source, which can give a major contribution to UV treatments. While also UV-A LEDs have gained interest and are widely used in water treatment [108], UV-B and UV-C bands have the potential to be more effective as they correspond to the absorption spectra of the DNA and many persistent pollutants, enhancing their elimination and degradation. LEDs are semiconductor p-n junction devices producing photons when current flows through them. The energy gap of the semiconductor determines the LED wavelengths, which corresponds to the energy of the photons when required to cross the band gap to recombine with the electron holes. The overall operating efficiency depends on several factors: the semiconductor crystal growth fabrication process, the operation design of the LED device, the packaging assembly, and finally, the full system integration. However, the three main problems currently facing are low wall-plug efficiencies, ageing of the packaging material, and thermal management issues [109].

Table 2.7 summarises the different UV sources explored for water disinfection and purification with their main characteristics.

Table 2.7. Comparisons of the UV sources for water disinfection and purification.

UV sources	UV range (nm)	Radiant power efficiency (%)	Lifetime (h)	Reference
LP-Hg	253.7	30-35	7000-12000	[106]
MP-Hg	200-400	30-35	7000-12000	
Xe₂	172	10	5000	
KrCl	222	5-8	3000-5000	
UV-C LED	265-280	5-10	>6000	[110]
UV-B LED	280-315	4-9.6	10000	[110,111]

The development since the first UV-LED shows that improvements far beyond the current state can be achieved. Furthermore, UV-B and UV-C LED are becoming increasingly relevant, especially after the outbreaks of the coronavirus disease 2019 (COVID-19)[112], for the need to sterilise and disinfect material rapidly. Therefore, a lot of attention is being posed to improving the efficiency of each step of the LED production and reducing the overall cost, with a UV market in exponential growth, hitting \$144 million in 2019 and expected to reach \$991 million by the end of 2023 [113]. The LED's efficiency is then expected to follow a similar trend, while the price is likely to follow a mirrored trend, decreasing as supplies and products increase.

LEDs offer numerous advantages, one of which is their environmental sustainability due to their mercury-free nature. Mercury is, in fact, a hazardous material, easily absorbed by the skin, respiratory tract, and digestive tract of organisms and also dangerous for the environment. Then, if the lamps are broken during installation, maintenance, or disposal, mercury vapour may enter the drinking water supply or may expose people to danger [114]. For this reason, in 2013, 127 countries signed the Minamata Convention on Mercury, named after the disaster that happened in the mid-20th century in the homonym bay in Japan, where thousands of people died of mercury-poisoned wastewater. The objective of the Convention is to reduce the overall mercury level in the environment over time [115]. In contrast, UV LEDs only contain a tiny amount of metals held within a crystalline structure and cannot leach in case of breakage or disposal [116].

Other advantages are that they allow an instant on and off, with no impact on the lamp lifetime, enhancing energy savings during the different applications, and they are compact and robust, allowing for high design flexibility. Another great advantage is that the irradiation intensities of the UV LEDs can be modulated depending on the specific application. With proper water monitoring, the voltage of the LEDs can be adjusted to reach the desired disinfection or chemical degradation with the lowest energy consumption. Finally, key aspects of UV LEDs in comparison to mercury lamps are wavelength selection that can activate the oxidants of interest and tackle specific contaminants. Indeed, the last two points have incredible potential in UV-based AOPs since the overall performance of the process is remarkably dependent on UV wavelength and intensity [96].

A comparison of the main advantages and disadvantages of the UV mercury lamps with the UV LEDs is represented in Figure 2.8.

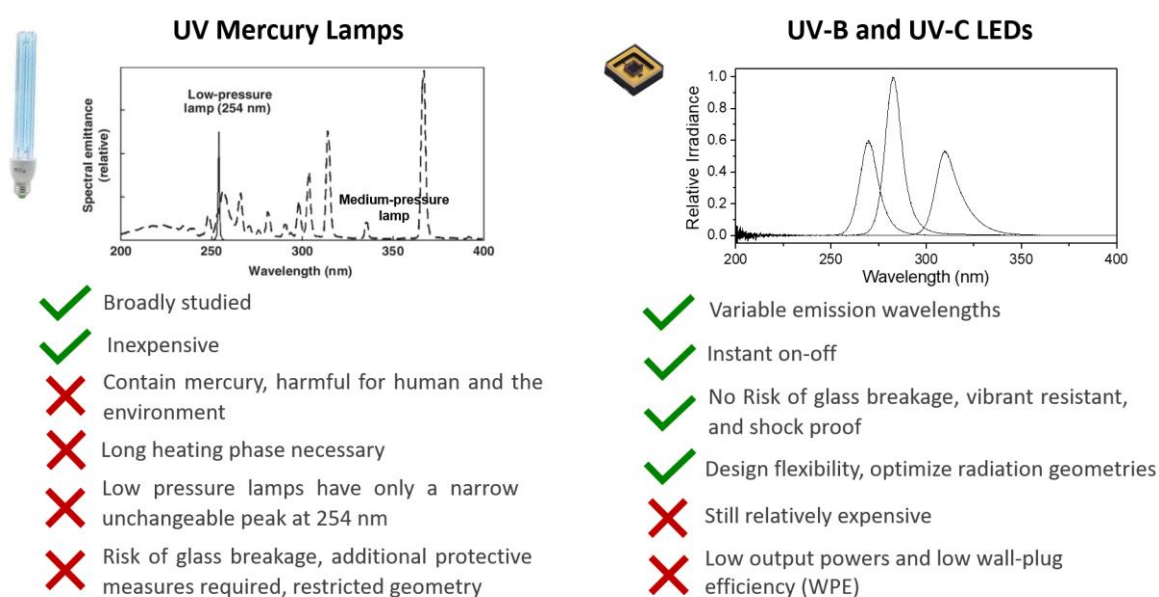


Figure 2.8. Main advantages and disadvantages of UV mercury lamps and UV-B and UV-C LEDs.

Several review papers have already identified and summarised the advances in UV-C LEDs for water disinfection purposes [117–119]. While for removing contaminants, much higher doses ($>200 \text{ mJ cm}^{-2}$) are needed [98], and therefore fewer studies have been conducted so far. However, given the need to reduce water contamination from these organic micropollutants and increase the resilience of centralised and decentralised water systems,

from large-scale to small-scale applications, LEDs can play a fundamental role with their high design flexibility. Nonetheless, more studies are needed to investigate tuneable wavelengths, intensities regulations, and dual-wavelength systems to increase the overall performance of photolysis alone or coupled with the oxidants.

2.4.4 Environmental impact of UV treatments in water systems

To assess the relative environmental impacts between UV-C LEDs and conventional UV-C mercury lamps during water purification, environmental Life Cycle Assessment (LCA) is the preferred method thanks to its international recognition and widespread use [120]. LCA considers all aspects of the life cycle, including manufacturing, distribution, use, reuse, recycling and end-of-life. In this regard, there are three main approaches: cradle-to-gate, cradle-to-grave, and cradle-to-cradle [121]. The cradle-to-gate approach considers the environmental impacts of a product or process from the extraction of raw materials to the point of leaving the factory gate, not taking into account the use phase or end-of-life impacts. Cradle-to-grave considers the environmental impacts of a product or process from the extraction of raw materials to the end of its useful life, including disposal or recycling. Finally, cradle-to-cradle is more associated with the circular economy concept; it is a closed-loop system that aims to eliminate waste by designing products and materials that can be perpetually reused or recycled without losing quality or value. By examining the potential environmental impacts over the entire life cycle and comparing alternative pathways, LCA provides valuable insights for optimising the process, highlighting the hotspots, and recommending further measures to reduce the overall environmental footprint.

LCA has been widely used in assessing the environmental impact of established technologies, but it is increasingly being applied to emerging technologies. In this context, ex-ante LCA can be used to evaluate the environmental impact of a technology in its early development stages, in an experimental proof of concept, or validation in the lab or pilot plant [122]. In relation to this, technologies are commonly characterised by the technology readiness level (TRL) indicator, a method for estimating their maturity. It was first developed by NASA but was adopted by the European Commission in 2010 and canonised by the

International Organisation for Standardisation (ISO) with the publication of ISO 16290:2013 [123]. A schematic representation of the TRL system can be found in Figure 2.9.

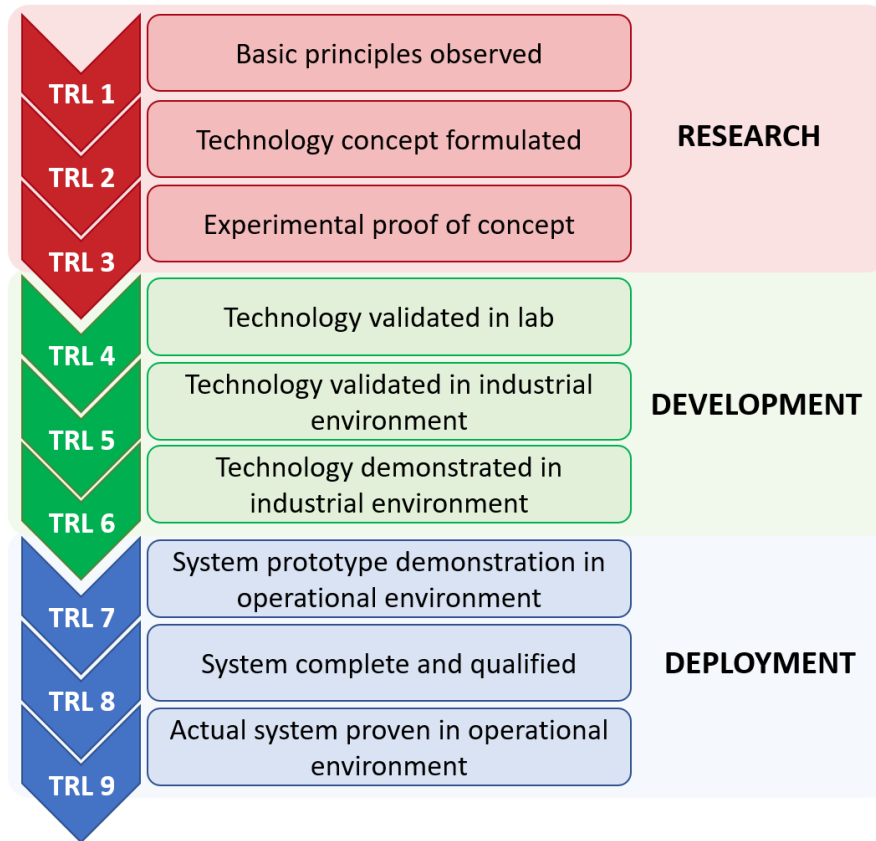


Figure 2.9. Technology readiness levels adopted by the European Commission [124].

While traditional, ex-post LCA studies usually perform assessments at the deployment stage (TRL7-TRL9), ex-ante LCA studies can be beneficial for identifying potential environmental hotspots or trade-offs associated with the new technology and opportunities to reduce its environmental impact. Ex-ante LCA consists of exploring and assessing a range of possible scenarios that define the space in which the emerging technology may operate, often compared to incumbent technologies. Contrary to ex-post LCA studies, it serves as a proactive approach to integrate environmental considerations into decision-making processes when important decisions can still be made without major disruptions, helping prevent avoidable environmental burdens and regrettable investments [122]. However, one of the main challenges of conducting LCA for emerging technologies is the availability of comprehensive data at the early stage of product development or for a novel process and

uncertainties associated with the data quality completeness, which may affect the accuracy of the assessment. Furthermore, ex-ante LCA involves making predictions based on assumptions, models, and estimation, which can affect the results once the technology is implemented, depending on the validity of the assumptions. Nevertheless, these challenges can be addressed by transparency and robustness of the assessment methodology and by acknowledging the inherent uncertainties.

Within the frame of LCA application on emerging technologies, a small review of the LCA status for UV water treatment focused on removing CECs was conducted. The SCOPUS database was employed, selecting as keywords: “life cycle assessment” and “photolysis” or “UV radiation” and “water”. Only 4 papers were selected among 9 studies on UV water treatments since the UV source was clearly specified and included in the life cycle inventory (Table 2.8).

Table 2.8. LCA studies on UV water treatments where the UV source was clearly specified in the inventory.

Year	Advanced Treatment	Functional Unit	TRL	Ref
2018	UV-A, UV-C, UV-C + H ₂ O ₂ UV-A source: Compact fluorescent lamp (Radium Ralutec, 9W/78, 350-400 nm) UV-C source: 11W LP mercury lamp (Phillips, TUV PL- S)	“The effective removal of 1 µg of 17a-ethynylestradiol (EE2) per litre of treated wastewater”	Lab scale (TRL2-TRL3)	[125]
2022	UV-C- H ₂ O ₂ , UV-C-PMS, UV-C-persulfate UV source: 16 LP mercury lamps (WEDECO ELR-30-1; 330 W)	“The treatment of 1 m ³ of urban secondary wastewater containing several micropollutants”	UWWTP (TRL5-TRL6)	[103]
2022	UV-BL/TiO ₂ versus UV-LEDs/TiO ₂ Sources: UV LP blacklight (BL) fluorescent lamp (UV-BL 354-400 nm, PLS G23, Casell Lighting) versus UV-LEDs (365 nm, LZ4-00U600, LED Engin)	“Treatment of 1 L of polluted water to remove 90% of BPA with an initial concentration of 7.5 mg L ⁻¹ ”	Lab scale (TRL2-TRL3)	[126]
2023	UV-C, UV-C + H ₂ O ₂ e UV-C + TiO ₂ UV source: LP mercury vapour lamp with a power of 280 W	“The abatement by an order of magnitude (log 10) of all persistent pollutants present in 1m ³ of wastewater to be treated in the UV-C laboratory photoreactor”	MWWTP but the photo-reactor was lab scale (TRL 3)	[127]

*Where UWWTP is urban wastewater treatment plant, and MWWTP municipal wastewater treatment plant.

Foteinis et al. [125] found that water treatment through UV-C mercury lamps was about 3 times more environmentally friendly than employing UV-A from a compact fluorescence lamp. Furthermore, the addition of H₂O₂ to the treatment decreased the total environmental impact by about 88%, calculated as a single score. As energy consumption was the main environmental hotspot, the process sustainability was inversely proportional to the treatment time and directly proportional to the treatment efficiency. By introducing renewable energy sources, they found a reduction of the single score by up to 87.5%. Pesqueira et al. [103] focused on the environmental impacts of the oxidants while using LP mercury lamps, finding that PMS and persulfate contributed more to the single score than the electricity use, unlike H₂O₂. With the latter, electricity was the main parameter, and by opting for cleaner energy sources, the impacts were highly reduced; however, the lamps heavily affected the terrestrial ecotoxicity category due to the presence of mercury, where the worst waste treatment scenario, where the mercury inside the lamps is released to the atmosphere, was considered. A direct comparison between two types of UV-A sources, the blacklight fluorescent lamp (BL), which also contains mercury, and UV-A LEDs, were investigated by McKee et al. [126] for the removal of bisphenol A, using titanium dioxide as a catalyst in a lab-scale reactor. The UV-A LED/TiO₂ treatment had a 61% lower total environmental impact, evaluated as a single score, compared to UV-A BL/TiO₂, showing great potential for the LEDs technology. In this case, the environmental hotspots were the energy consumption and the photocatalytic reactor. However, while a mix of recycled materials did not bring a significant overall impact reduction, the use of a renewable electricity mix showed a decrease of 41.5% in the case of the UV-A LEDs. Finally, Notarnicola et al. [127] compared different LP mercury lamp systems in a lab-scale reactor (UV-C, UV-C/H₂O₂, and UV-C/TiO₂). The main hotspots were the electric power consumption of the centrifugal pump for recirculation (63-64%) and the UV-C lamp (32-33%). They also confirmed that adding H₂O₂ reduced the environmental impact by 75%, while using titanium dioxide only reduced the impact by 30% compared to UV-C alone.

Considering the advantages of UV-A LEDs over BLs and the presence of mercury in conventional UV-C sources, which can also affect their implementation from full-scale reactors to household applications, it is of interest to analyse and evaluate the environmental benefits and hotspots of the innovative UV-C LED lamp, in regard of water purification treatments.

It should be considered that in all the studies mentioned, the LCA method was employed in the early development stages (TRL2-TRL6) since the application of UV photolysis and UV-driven AOPs is still under investigation for large-scale application. Also, it should be noted that UV-C LEDs are still in the research stage, and great improvements are expected in the following years. Indeed, while UV-A LED is nowadays an established technology and has seen considerable growth in the past years, and more growth is even expected as research and development in this field continue to progress, UV-C LED is a more recent technology, which is expected to follow the same growing trend [119], even if to now still has relatively low efficiency (Figure 2.10).

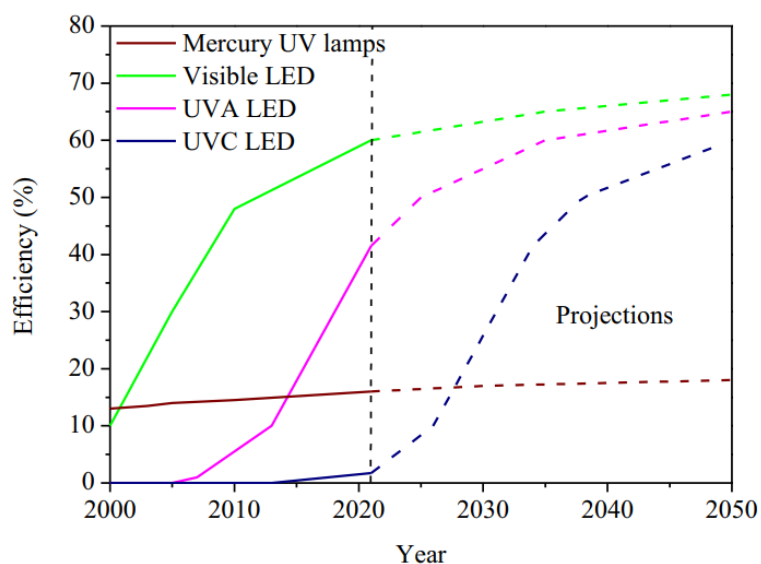


Figure 2.10. Efficiency trend and projections for LP mercury lamps, UV-A and UV-C LEDs [119].

While it is hard to draw clear conclusions for deployment-level recommendations since many factors are involved during the scale-up, studies on the novel UV-C LED lamp at an early development stage may help to identify the hotspots and strengths of the growing technology compared to the incumbent technology. With this aim, the present thesis conducts an ex-ante LCA study comparing the conventional LP mercury lamps with a UV-C LED lamp in a lab-scale reactor for water treatment purification purposes, using the degradation of diclofenac as a case study. Furthermore, the papers listed in Table 2.8 have demonstrated the efficacy of adding H_2O_2 to reduce the energy burden while revealing the inadequacy of PMS and persulfate, significantly contributing to the overall environmental

footprint even more than electricity. Therefore, this finding has sparked interest in assessing and comparing the environmental impacts attributed to the FC oxidant against H₂O₂ in water purification systems.

2.5 Objective and aim of the investigation

The previous sections have highlighted the importance of developing new strategies for removing CECs. Their abundant presence and the potential health and environmental risks associated pose serious concerns about drinking water quality, which is also affected by the increase in human pollution and general climate uncertainty. Water systems need to upgrade by employing specific and targeted advanced treatments optimised for the removal of these emerging pollutants. Therefore, the main objectives of this Doctoral Thesis are the design and evaluation of technologies for removing CECs, with a particular focus on MPs given their increasing prevalence, and DCF added to the first EU *watch list* due to the harmful effects on wildlife.

Regarding MPs removal, many technologies have been explored; however, they mainly rely on expensive operations since first developed for other purposes. Therefore, in this work to tackle the problem of MPs in drinking water, MF membrane in dead-end configuration was chosen as a simple and low-cost system that can be easily implemented to higher drinking water quality, also at point-of-use tap water locations, without any further treatments. To optimise the system, the first step was evaluating the performance of several commercial membranes with different characteristics, taking into account operational costs together with the MPs removal efficiency. Since membrane fouling by MPs has a significant knowledge gap and is key to developing appropriate filtration and cleaning procedures, it was deeply investigated on the membrane that achieved the best overall performance. Membrane fouling mechanisms were first identified, and the kinetic constants for each mechanism were studied under different working conditions, varying TMPs and MPs load in the feed. The results were finally evaluated to assess the influence of the MPs characteristics on the membrane fouling and gather insights on the best working conditions and strategies to increase MPs removal efficiency and reduce secondary MP-based pollution.

On the other hand, DCF removal was explored through UV alone, UV/H₂O₂ and UV/FC treatment by means of innovative UV-B and UV-C (265, 285 and 310 nm) LED lamps manufactured by the company ProPhotonix IRL. The photolysis of the contaminants, hydrogen peroxide, and chlorine is wavelength dependent, and therefore the interest in assessing the impact of the working wavelength, where a compromise to optimise the absorption of the DCF and the oxidant should be found. Furthermore, considering the unique characteristics of the LEDs, the two most efficient lamps were studied under different lamp intensities and combined to evaluate the effectiveness of dual-wavelength UV photolysis. Indeed, the latter has only been investigated in two other studies, showing divergent results [128,129]. The experimental data were also used to mechanistically model the DCF degradation kinetics based on the wavelength and the oxidation process. Developing the kinetic model is important to understand the main reactions involved and predict the degradation rates under different conditions, which is very useful in designing treatment systems and optimising operating conditions. In addition, the effectiveness of the treatment was also evaluated through mineralisation and phytotoxicity to ensure that the treatment was achieving the complete removal of the more harmful and unstable DCF by-products.

Finally, LCA was employed for a comprehensive evaluation of the environmental impacts of the treatments employed and to give key information to guide decision-making towards more sustainable choices. First, the comparison between the innovative UV-C LED lamp emitting at 265 nm and the conventional LP mercury lamp for the removal of DCF in a lab-scale reactor (TRL2-TRL3) was investigated, including a favourable and unfavourable case. Then the relative environmental impacts between UV alone, UV/H₂O₂ and UV/FC treatment for the UV-C LED lamp at 265 nm were analysed to evaluate the impacts of the oxidants on the process. Lastly, a situation employing a cleaner energy source was assessed to explore possible improvements.

A promising strategy for an overall increase of resilience towards CECs is a hybrid system coupling efficient processes optimised to remove targeted classes of pollutants. Given the complementary of the membrane processes with the UV-based AOPs, together they can tackle a wide variety of contaminants present in drinking water, and their integration has great potential. Thanks to the design flexibility of the LEDs, and the easy implementation of

membrane filtration systems, they are ideal treatments for small-scale applications, such as household water treatments, but also adaptable to larger scales.

The relation between the objectives and the results is schematised in Figure 2.11.

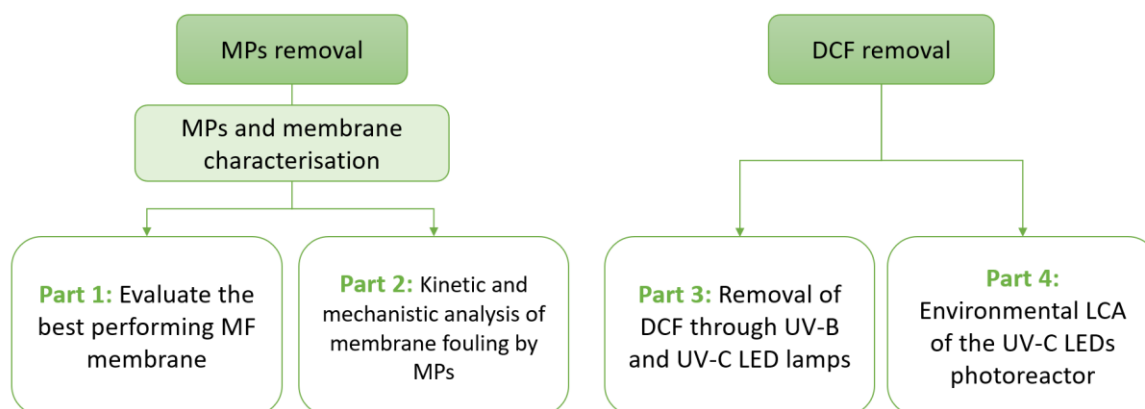


Figure 2.11. Relation between the objectives and the results.

The present doctoral thesis was developed under the framework of the Project: “REWATERGY, Sustainable Reactor Engineering for Application on the Water-Energy Nexus”, a Marie Curie European Industrial Doctorate training network funded by the European Commission within the Horizon 2020 research and innovation action (Project N. 812574).

The work was carried out in the Department of Chemical and Environmental Technology at the Rey Juan Carlos University (Móstoles, Madrid, Spain) and the Irish company ProPhotonix in Cork (Ireland), also in collaboration with University College Cork.

3. METHODOLOGY

3 Methodology

3.1 Microplastics removal

3.1.1 Materials

PA and PS particles were acquired from Goodfellow. The working particle size range was selected between 20 and 300 μm to be representative of MPs water bodies size, considering that in the literature, MPs in WWTPs effluents were on average smaller than 500 μm [14], while the smaller size was dictated by the detection limit of the analysis method [39], down to 20 μm for the micro-FTIR equipment [17]. In the case of PA, all the particles were manufactured below 300 μm , while the PS particles bigger than 300 μm were first reduced by cryogenic milling (ZM 100, Retsch) with stainless steel mortar material at a speed of 14000 rpm, and the temperature cooled down with liquid nitrogen, Figure 3.1a. Then both particles were sieved between 20-300 μm , using sieves with 300 μm , 20 μm , and a sieve pan purchased from Scharlab, Figure 3.1b.

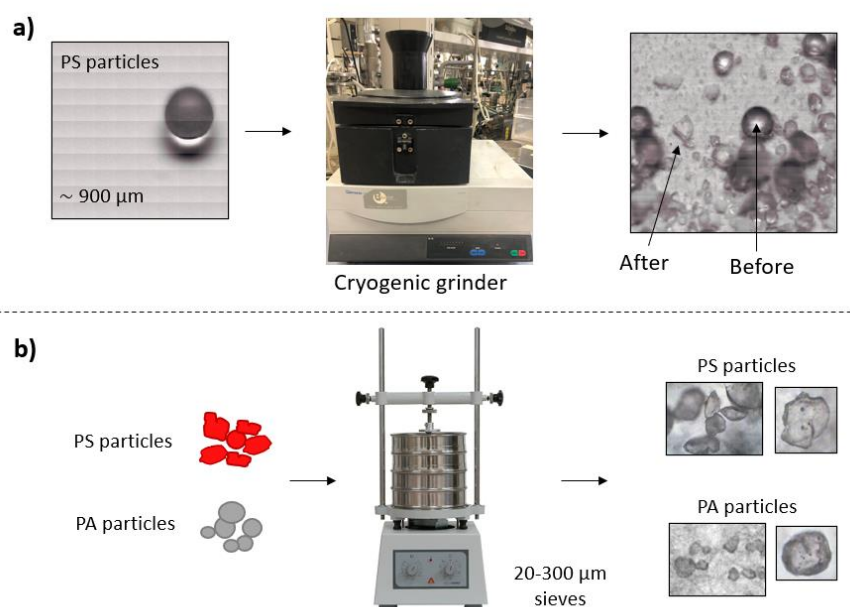


Figure 3.1. PS particles bigger than 300 μm reduced by cryogenic milling (a), PA and PS particles sieved between 20-300 μm before being employed.

Commercially available polycarbonate (PC), cellulose acetate (CA), and polytetrafluoroethylene (PTFE) membranes were purchased from Filter-Lab. All membranes had a nominal pore size of 5 μm with a diameter of 47 mm to enhance the advantages of MF while ensuring optimal removal efficiency in the MPs range selected.

3.1.2 Characterisation techniques

3.1.2.1 Reflectance micro-FTIR and attenuate total reflection-FTIR

The chemical structure of PA and PS particles on the membranes' surfaces was analysed through FTIR. The spectra were obtained in reflectance mode from a PerkinElmer Spotlight 200i microscope coupled to the FTIR Frontier Spectrometer, working at room temperature, in the wavelength range of 4000-600 cm^{-1} , with 8 cm^{-1} resolution and 30 scans. Attenuated total reflection (ATR)-FTIR spectra were obtained in the same wavelength range, resolution, and scans, with a diamond crystal as the internal reflection element.

3.1.2.2 Microplastics particle size distribution

After sieving the particles, it was still necessary to determine the particle size distribution within the selected range and identify whether particles bigger and smaller were present in the MPs feed. Indeed, smaller particles could have aggregated with others and been retained by the 20 μm sieve. On the other hand, larger irregular particles could have passed the 300 μm sieve, having one of the sizes below the value.

The particle size distribution of MP suspensions was analysed using microscopic counting and focused beam laser reflectance measurement (FBRM). Microscopic counting involved capturing images of the particles through an optical microscope (B3 Series, Motic) with an objective lens magnification of 10x and a camera (Moticam3 3.0 MP, Motic) attached to the lens. The pictures were processed with ImageJ Software, and an estimation of the distribution size of the particles was made by the results given on around 500 randomly selected particles. On the other hand, FBRM was performed using the M500LF Lasentec equipment manufactured by Mettler Toledo. The instrument scans a laser beam at a fixed speed across the particles in suspension, and the particle crossing the beam reflects part of the light [130]. The backscattered light duration is used to measure the chord length

distribution, which is the raw outcome [131]. Then, the Hukkanen and Braatz model [132] was used to convert the chord length distribution (CLD) into the particle size distribution (PSD), where the particles are assumed to be spherically shaped. The model is based on probability functions constructed for each particle size vector, \mathbf{f} , and the corresponding chord length vector, \mathbf{c} , as shown in Eq. (3.1).

$$\mathbf{c} = \mathbf{P}_{ij} \cdot \mathbf{f} \quad \text{Eq. (3.1)}$$

The elements of the matrix \mathbf{P}_{ij} are described by Eq. (3.2) when considering a midpoint distribution within the range D_j and D_{j+1} .

$$\mathbf{P}_{ij} = \begin{cases} \sqrt{1 - \left(\frac{2D_i}{D_j + D_{j+1}}\right)^2} - \sqrt{1 - \left(\frac{2D_{i+1}}{D_j + D_{j+1}}\right)^2} & i < j \\ \sqrt{1 - \left(\frac{2D_{i+1}}{D_j + D_{j+1}}\right)^2} & i = j \\ 0 & i > j \end{cases} \quad \text{Eq. (3.2)}$$

Where the j^{th} column represents the chords distribution and the i^{th} column the particle size distribution. Consequently, the inverse matrix \mathbf{P}_{ij}^{-1} allows the estimation of the particle size vector from the chord length vector. Finally, the Minitab Statistical Software was employed to identify the distribution fitting and its main parameters.

3.1.2.3 Microplastics zeta potential

In the context of membrane filtration, zeta potential (ζ) plays a critical role since it determines the surface charge of the particles and the membranes, which affects the interactions among them. Zeta potential is indeed a measure of the electrostatic potential difference between the surface of a particle or membrane and the surrounding fluid.

The NanoPlus HD sensor from Micromeritics was utilised to measure the zeta potential of PA and PS particles. A concentration of 500 mg L⁻¹ was used for both plastics, suspended in deionised water obtained from a Millipore Milli-Q system. Since the ζ -value of the particles is affected by the pH of the surrounding medium, the zeta potential was evaluated by varying

the pH of the suspensions, adjusting the amount of HCl and NaOH, respectively, for acid and basic solutions. In this way, the pH-dependent ζ -value measurements provide insights into the particles' stability and potential aggregation behaviour in different environmental conditions.

3.1.2.4 Scanning electron microscope

Scanning electron microscope (SEM) has been used to investigate the MPs particle morphology and the membrane topography. Finally, it was also employed to study the effect of the MPs fouling on the membrane surface, the possible interactions, and potential membrane abrasion. MPs' photomicrographs were obtained using SEM, XL 30 ESEM, Philips, operating in the potential range of 5 kV at 5.8 and 5.4 mm working distance for PA and PS, respectively. Membrane surface and cross-section were also analysed with the same equipment at a working distance varying from 4.5 to 6.3 mm. Finally, images after MPs filtration were obtained using a JEOL JSM 7600F Field Emission SEM at an accelerating voltage of 5kV and 8-9 mm working distance.

3.1.2.5 Water contact angle

Water contact angle (WCA) measurements were performed to evaluate the wettability and hydrophobicity on the membrane surface before and after the MPs filtration. It was carried out by the sessile drop techniques, employing the Ramé-Hart Model 200-F1 instrument. In this technique, a small droplet of distilled water is placed on the surface of the membrane, and macrographs are taken at 10, 30, and 60 s after the deposition to allow the drop to settle and ensure that it has reached an equilibrium state. Subsequently, the shape of the drop is analysed by an image analysis software using the goniometer function to determine the contact angle between the drop and the surface. At least three drops were measured for each sample.

3.1.2.6 Shore hardness, type A

The Shore hardness of the membranes was measured with a durometer (P. G. 812, Amsler W Testor), type A. The Shore hardness measures the material's resistance to indentation or deformation and is commonly used to determine the hardness of polymers. There are several scales, Shore A being the most common one. The primary distinction among the scales is

the shape of the indenter, conical in the case of type A, that is pressed into the surface of the membrane with a defined amount of force.

3.1.2.7 Membrane roughness

The roughness of a membrane surface can also influence the overall membrane's performance in many applications. It can influence permeability, selectivity, fouling behaviour, and mechanical properties. Therefore, the membranes' roughness was evaluated through a 3D optical profilometer (Zeta-20 Desktop Optical Profiler). The latter is a non-contact, non-destructive technique, which works by taking different pictures at different heights, which are used to create a 3D representation of the surface. Roughness values were evaluated before and after MPs filtration. The results show an average of ten measures for each position, where at least three sites for each membrane were evaluated.

3.1.3 Filtration system

The filtration setup system employed a glass container with a bottom exit of 5 L, where the MPs suspended in water were continuously homogenised with a magnetic stirrer at 500 rpm (Agimatic-E, J.P. Selecta). The container was connected to a centrifugal pump (model TP 78/A, Calpeda) through a needle valve, and it was constantly filled with fresh MPs solution throughout the entire run. The centrifugal pump was connected to a variable frequency drive (VFD, RS510, RS Pro) to regulate its power, and it was chosen to be able to provide a flow rate of at least 9 L min^{-1} and reach a pressure of 5 bar according to the requirements of a household system in Spain [133]. Temperature, pressure, and flow rate sensors were placed before the membrane filtration system and were monitored with online sensors coupled with a data logger (PMS-90R, Aplisens). Finally, the membranes were held in a stainless-steel filter holder of 47 mm diameter (16254, Sartorius). For the evaluation of the three membranes' performance, the initial TMP was chosen but without keeping it constant during the entire filtration. On the other hand, while studying the kinetics and mechanisms of the membrane fouling by MPs, the study was conducted at constant pressure by implementing a controller acting directly on the VFD. An Arduino Mega 2560 board was therefore integrated into the system with a keypad, an LCD monitor, and current-to-voltage converters

to read the values of the sensors from the data logger and used as input to work at constant TMP.

The filtration setup system already integrating the microcontroller is schematised in Figure 3.2 and presented in Figure 3.3 as built in the laboratory.

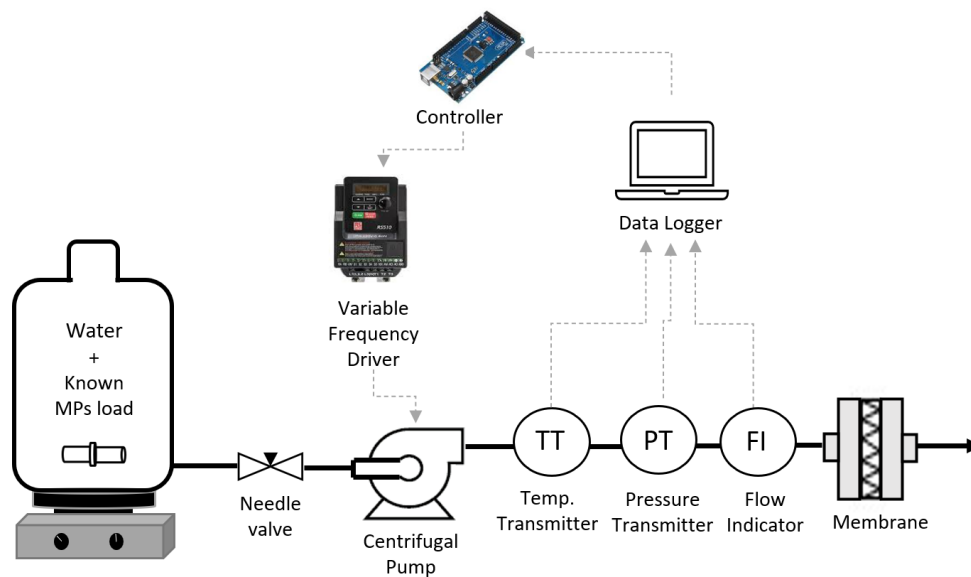


Figure 3.2. Schematic filtration setup system.

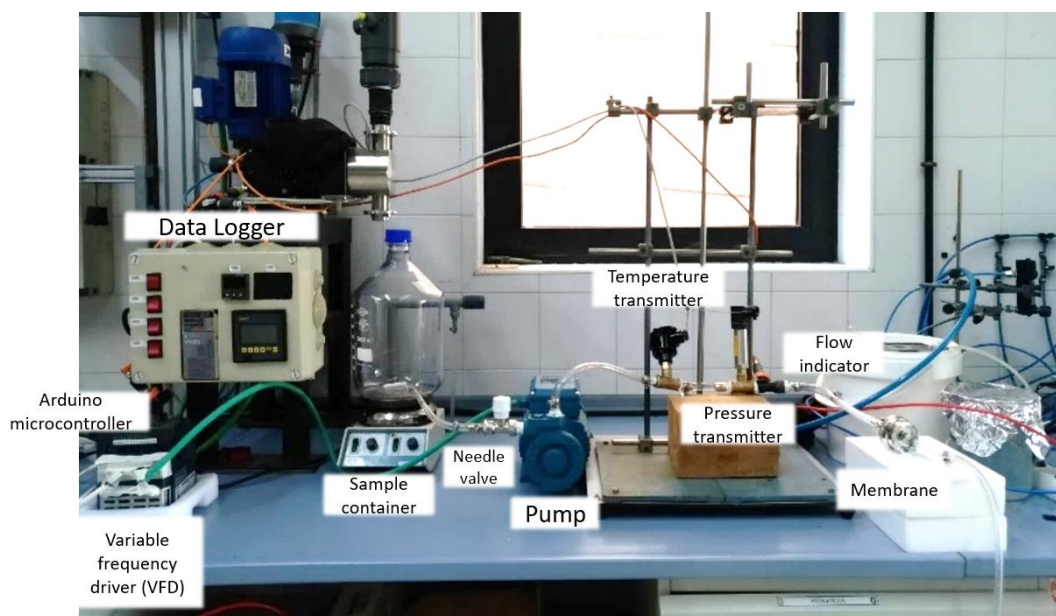


Figure 3.3. Laboratory implementation of the MPs filtration system.

The electronic sketch of the microcontroller is shown in Figure 3.4, and the Arduino code can be found in the [GitHub repository](#)¹.

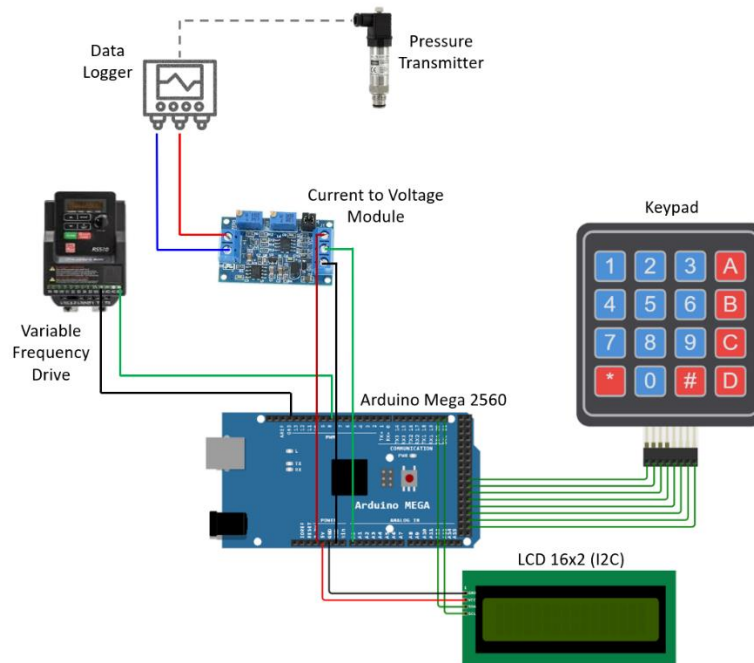


Figure 3.4. Electronic scheme to work at constant pressure using Arduino.

The microcontroller gains the information “Pressure target” directly from the user through the keypad, and it displays it on the LCD screen together with the instant pressure value, which is taken from the data logger by converting the current value into an analogue voltage input. Finally, Arduino measures the difference between the instant pressure and the user-defined “Pressure target” to act on the variable frequency drive and increase or decrease the pump outlet, as shown by the implemented logical flowchart diagram in Figure 3.5.

¹ <https://github.com/PhotonersURJC/PumpConstantPressure>

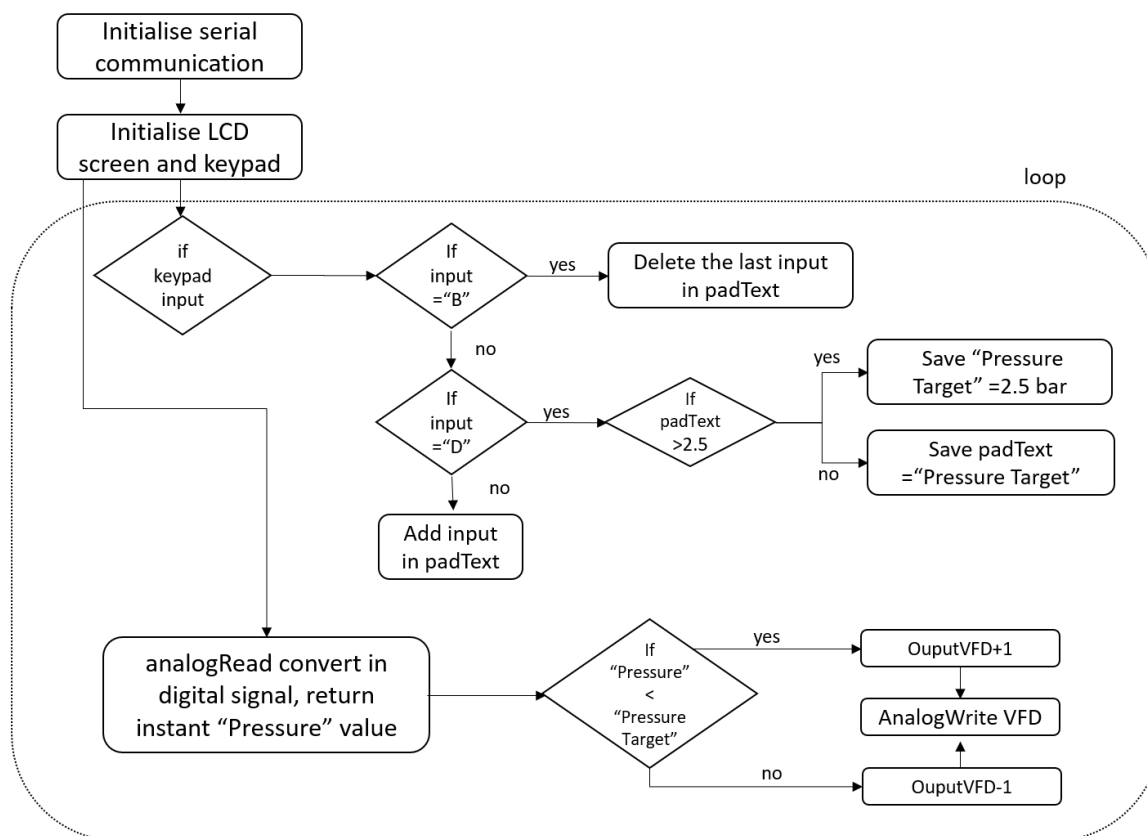


Figure 3.5 Logical flowchart diagram used in the Arduino code for the filtration system.

All the experiments were carried out at room temperature. Distilled water from Milli-Q Direct-Q® 8 UV (Merck Millipore), with a neutral pH of around 6.5, was used in all the experiments to avoid other fouling agents affecting the performance of the membrane and the fouling kinetic. It is known that other water constituents play a significant role in severe membrane fouling [72,134,135]; however, taking them into account could lead to confusing and unreliable results on the MPs' contribution since the quality of water can change substantially with time and space. Therefore, distilled water was employed to have reproducible results, identify the main MPs-membrane interactions, and address experimental variables such as particle size and shape, hydrophobicity, membrane-MPs charges, and membrane roughness.

3.1.4 Analysis of the removal efficiency

Glass microfibre filters (GFs) of $0.70\ \mu\text{m}$ provided by Filter-Lab were employed to quantify the mass removal efficiency of the different membranes tested, where the $0.70\ \mu\text{m}$ pore size was selected to ensure the complete retention of the MPs in the defined range of $20\text{--}300\ \mu\text{m}$. A volume of $1.5\ \text{L}$ was gathered from the in-line filtration and successively filtered through vacuum filtration with the GF, as represented in Figure 3.6.

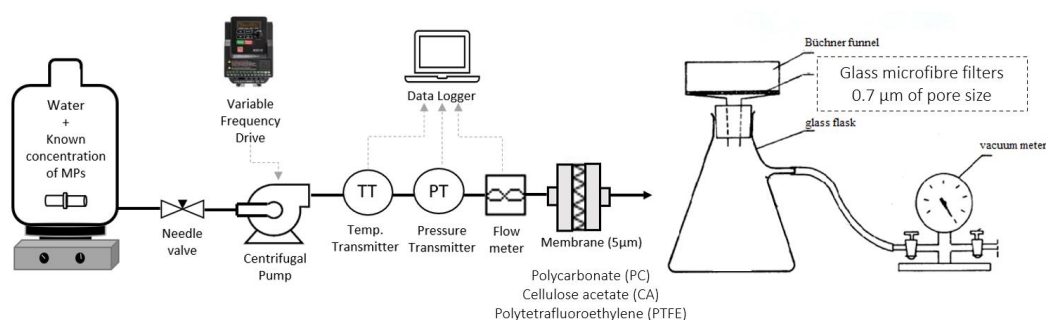


Figure 3.6. Scheme of the experimental setup coupled with the vacuum filtrations with the GFs to analyse the removal efficiencies.

An optical microscope (B3 Series, Motic) with an objective lens magnification of $10\times$ was used to study the MPs retention of the GF. With a camera attached to the lens (Moticam3 3.0 MP, Motic), pictures of the filter were obtained and then processed with the ImageJ software to identify and measure the number and the size of the MPs particles, similarly to the microscopic counting for the particles size distribution measurements. Figure 3.7 shows a schematic representation of the GF recovered after vacuum filtration of water gathered from the experiments.

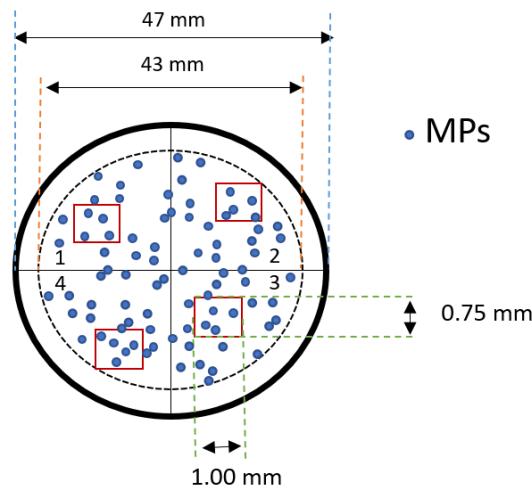


Figure 3.7. Schematic GF after vacuum filtration of the water gathered from each membrane's filtration.

A few millimetres of the filters are lost as they were used to fit the vacuum filtration system. The rest of the filter was divided into four quadrants. For each quadrant, an image of the most representative number and size of unremoved MPs was taken. From the image, MPs were counted and measured, and an average of residual particle number per litre and particle size was evaluated for the entire filter assuming homogeneous conditions. Each particle's volume was calculated from its diameter length, assuming it was spherical and considering a conservative perspective. Each particle's mass was then evaluated from the densities taken from the technical information of the producers of 1.13 g cm^{-3} and 1.05 g cm^{-3} for PA and PS, respectively. Finally, the sum of the particles' mass was used to estimate the total residual mass on the filter, Fm_{MPS} , and calculate the mass removal efficiency, $MRE\%$, as shown in Eq. (3.3).

$$MRE\% = \left(1 - \frac{Fm_{MPS}}{Im_{MPS}}\right) \cdot 100 \quad \text{Eq. (3.3)}$$

Where the initial mass of the MPs entering the system, Im_{MPS} , was known and calculated from the initial concentration of MPs in water (100 mg L^{-1}) and the total volume of water filtered in the experiment.

The same procedure was used to calculate the number of particles removal efficiency, $NpRE\%$, Eq. (3.4). This time, the number of particles in the feed, Inp_{MPS} , corresponded to

how many particles were present in 100 mg L⁻¹ of PA and 100 mg L⁻¹ or PS particles, evaluated to be 1,982,000 particles L⁻¹ and 143,000 particles L⁻¹, respectively.

$$NpRE\% = \left(1 - \frac{Fnp_{MPS}}{Inp_{MPS}}\right) \cdot 100 \quad Eq. (3.4)$$

Where Fnp_{MPS} corresponds to the number of particles that had not been removed during the filtration process.

3.1.5 Modelling of the membrane fouling

Four mechanistic models are commonly used to describe fouling phenomena; cake filtration, complete pore blocking, intermediate or partial pore blocking, and standard or internal pore blocking, as represented in Figure 3.8 with the corresponding physical meanings. Cake filtration occurs when particles accumulate at the membrane surface, forming a permeable cake that thickens over time, thereby increasing the hydraulic resistance to filtration. Complete pore blocking, on the other hand, involves the sealing of pore entrances, thereby preventing any flow through them. Intermediate or partial pore blocking results from the sealing of pore entrances by a fraction of particles, with additional particles deposited on top of the seal. Finally, standard or internal pore blocking occurs when particles accumulate on the pore walls within the membrane, ultimately reducing its permeability.

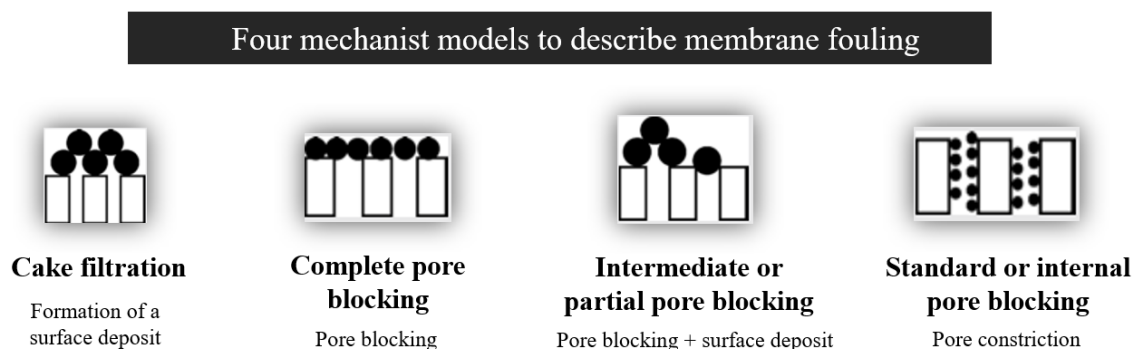


Figure 3.8. Fouling mechanisms and their corresponding physical meaning. Adapted from [136].

For dead-end filtration working at constant pressure, fouling mechanistic models have been mathematically described by Hermia's equation, Eq. (3.5) [137,138]. Hermia's blocking law defines the changing rate in the filtration resistance, $d(dt/dv)/dv$, proportional to the filtration resistance, dt/dv , raised to a power n , which depends on the filtration mechanism involved [139].

$$\frac{d^2t}{dv^2} = K_n \left(\frac{dt}{dv}\right)^n \quad \text{Eq. (3.5)}$$

Where v is the volume of filtrate per effective membrane area collected in time t , and K_n is the specific constant for the mechanism n .

Since analyses of membrane filtration are normally performed in terms of flux decline over time instead of filtration resistance, Eq. (3.5) can be rewritten in a physically more meaningful form where the filtration rate " $J=dv/dt$ " is used to represent the blocking filtration law, and the volume of filtrate depends on time and not vice versa [140], as shown in Eq. (3.6).

$$\begin{aligned} \frac{d\left(\frac{dt}{dv}\right)}{dv} &= K_n \left(\frac{dt}{dv}\right)^n \\ \frac{d\left(\frac{1}{J}\right)}{dv} &= K_n \left(\frac{1}{J}\right)^n \\ -\frac{1}{J^2} \frac{dJ}{dv} \cdot dt &= K_n J^{-n} \cdot dt \\ -\frac{1}{J^3} \frac{dJ}{dt} &= K_n J^{-n} \\ \frac{dJ}{dt} &= -K_n J^{3-n} \end{aligned} \quad \text{Eq. (3.6)}$$

Therefore, each fouling mechanism can be described mathematically using the general equation, with the specific expression depending on the n mechanism. In particular, the model for complete pore blocking is represented when n equals 2, the internal pore blocking by n equals 1.5, the intermediate pore blocking by n equals 1, and the cake filtration mechanism when n equals 0.

When $n \neq 2$, Eq. (3.6) can then be rewritten into Eq. (3.7).

$$J = J_0 \cdot (1 + (2 - n) K_n J_0^{2-n} t)^{\frac{1}{n-2}} \quad \text{Eq. (3.7)}$$

Whereas for $n = 2$, Eq. (3.6) is exponential with respect to the time.

The mathematical expressions for the four fouling mechanisms are finally summarised in Table 3.1.

Table 3.1. Fouling mechanisms for constant pressure filtrations.

Fouling mechanism	n	K_n	Flux equation	Eq. (#)
Complete pore blocking	2	K_b	$J = J_0 e^{(-K_b t)}$	(3.8)
Internal or Standard pore blocking	1.5	K_s	$J = J_0 \cdot \left(1 + \frac{K_s J_0^{0.5} t}{2}\right)^{-2}$	(3.9)
Partial or Intermediate pore blocking	1	K_i	$J = J_0 \cdot (1 + K_i J_0 t)^{-1}$	(3.10)
Cake filtration	0	K_c	$J = J_0 \cdot (1 + 2 K_c J_0^2 t)^{-\frac{1}{2}}$	(3.11)

Previous studies have highlighted that a combination of the four mechanisms usually occurs, with one of them prevailing in each filtration stage [70,136,141,142]. It has also been reported that the main fouling mechanism depends on the size of the membrane pores (d_{pore}) and the particles ($d_{particle}$), as described in Table 3.2.

Table 3.2. Effect of particle diameter versus membrane pore diameter.

Case	Main fouling mechanisms occurring
$d_{pore} > d_{particle}$	Internal pore blocking, followed by the other mechanisms once the pores reduce in size
$d_{pore} \leq d_{particle}$	Pore blocking (complete and intermediate), followed by cake filtration
$d_{pore} \ll d_{particle}$	Cake filtration

Once the dominant mechanism is identified for each filtration stage, the corresponding kinetic constants can be analysed as a function of operating factors, where other important parameters must be defined.

According to Grenier et al. [136], the kinetic constants of complete pore blocking and cake filtration are correlated respectively with the parameters η_B , blocked surface area by unit of time and surface of the membrane, and η_C , the specific resistance of the cake. The correlation between these parameters with the kinetic constants was modelled starting with the Darcy law equation, Eq. (3.12).

$$J = \frac{\Delta P}{\mu R} = \frac{\Delta P}{\mu (R_m + R_C)} \quad \text{Eq. (3.12)}$$

Where R_m is the hydraulic resistance of the membrane, R_C is the hydraulic resistance of the cake, ΔP is the pressure drop and μ the dynamic viscosity of the fluid.

$R_{m,B}$ depends, in turn, on the complete pore blocking mechanism, accordingly to Eq. (3.13).

$$R_{m,B} = \frac{R_{m,0}}{1 - \eta_B \left(\frac{V}{A_0} \right)} \quad \text{Eq. (3.13)}$$

Where $R_{m,0}$ is the clean membrane hydraulic resistance, and η_B is the mentioned parameter correlated to the kinetic constant K_b as described by Eq. (3.14).

$$\eta_B = \frac{K_b}{J_0} \quad \text{Eq. (3.14)}$$

On the other hand, the R_C depends on η_C in agreement with Eq. (3.15), and the correlation to the kinetic constant K_C is described by Eq. (3.16).

$$R_C = \frac{\eta_C}{A_0} \cdot V \quad \text{Eq. (3.15)}$$

$$\eta_C = \frac{\Delta P \cdot K_C}{\mu} \quad \text{Eq. (3.16)}$$

3.2 Diclofenac removal

3.2.1 Chemical and materials

Sodium diclofenac (>99%), acetonitrile (HPLC grade), sodium hypochlorite solution (6-14% active chlorine), sodium thiosulfate reagent plus 99%, hydrogen peroxide solution 30% (w/w), titanium sulfate solution, sodium sulfate, sulfuric acid 96%, sodium acetate, ferric sulfate pentahydrate, iron (II) sulfate heptahydrate, oxalic acid dihydrate, and 1,10-phenanthroline were all purchased by Merck, Sigma Aldrich. Finally, a Milli-Q water system supplied distilled water and deionised water employed during the study.

3.2.2 Photoreactor setup

The experiments were performed in a recirculating photoreactor system, shown in Figure 3.9. The photoreactor included a resistant plastic container of 4 L (Nalgene® round carboy with spigot, Merck), a pressure transmitter (DRTR-ED-20MA, Automation24), a flow rate sensor (YF-S201, Botnroll), and a centrifugal pump (NDP14/2, Xylem Flojet) to recirculate the content, connected to a VFD (AC10, Parker) to regulate its power. One litre of 20 mg L⁻¹ of DCF solution was prepared directly in distilled water for each experiment in order to avoid the organic solvent, which is found to possibly affect the degradation rate constants by UV-based AOPs by concurrently reacting with the oxidant radicals [143].

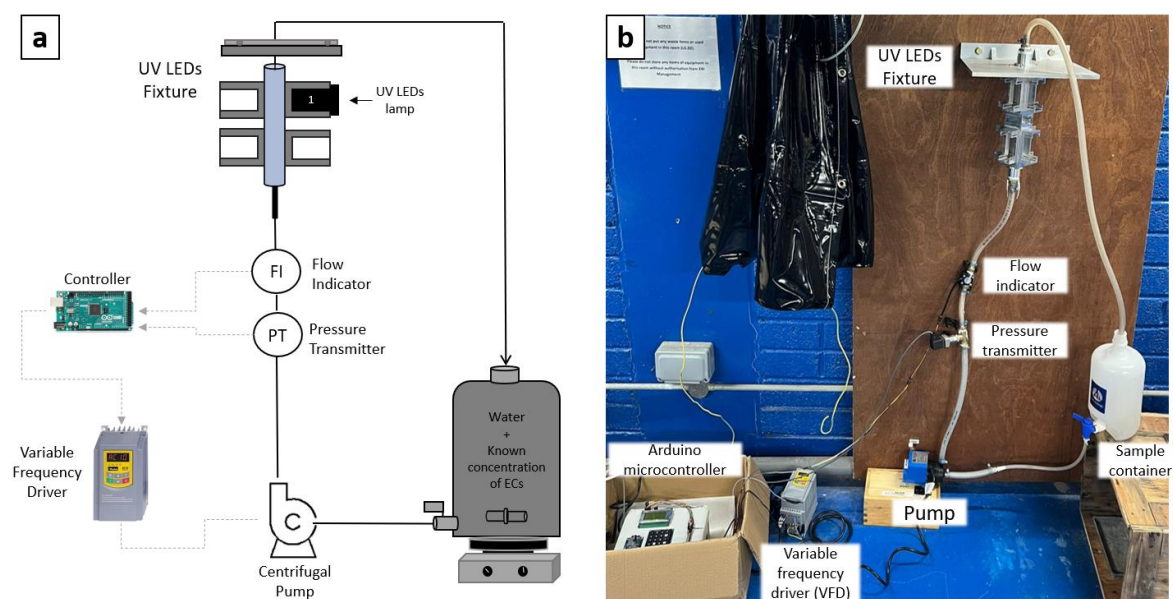


Figure 3.9. UV-B and UV-C LED photoreactor working in recirculation to evaluate DCF degradation through LED-driven AOPs. Schematic representation (a) and a picture of the photoreactor realised in the laboratory (b).

The photoreactor consisted of a quartz tube of 20 mm in inner diameter and 270 mm in length, where the LED lamps (COBRA Clean FX1, ProPhotonix IRL) were positioned at around 2 mm from the outer diameter of the quartz tube. Three lamps were employed during the study, emitting according to their data sheets at 265, 285 and 310 nm. They consisted of eight LEDs built into compact and fan-cooled devices that provide a stable light emission over time without significant changes in the temperature. Figure 3.10 shows the heads of the lamps employed during the study.



Figure 3.10. Heads of the LED lamps.

The VFD was controlled through an Arduino microcontroller. The sensors were directly connected to an Arduino Mega 2560 board, together with a keypad, an LCD monitor, and an SD memory card to read and save the data instantaneously. The electronic sketch is shown in Figure 3.11, and the implemented code is also available in the [GitHub repository](#)².

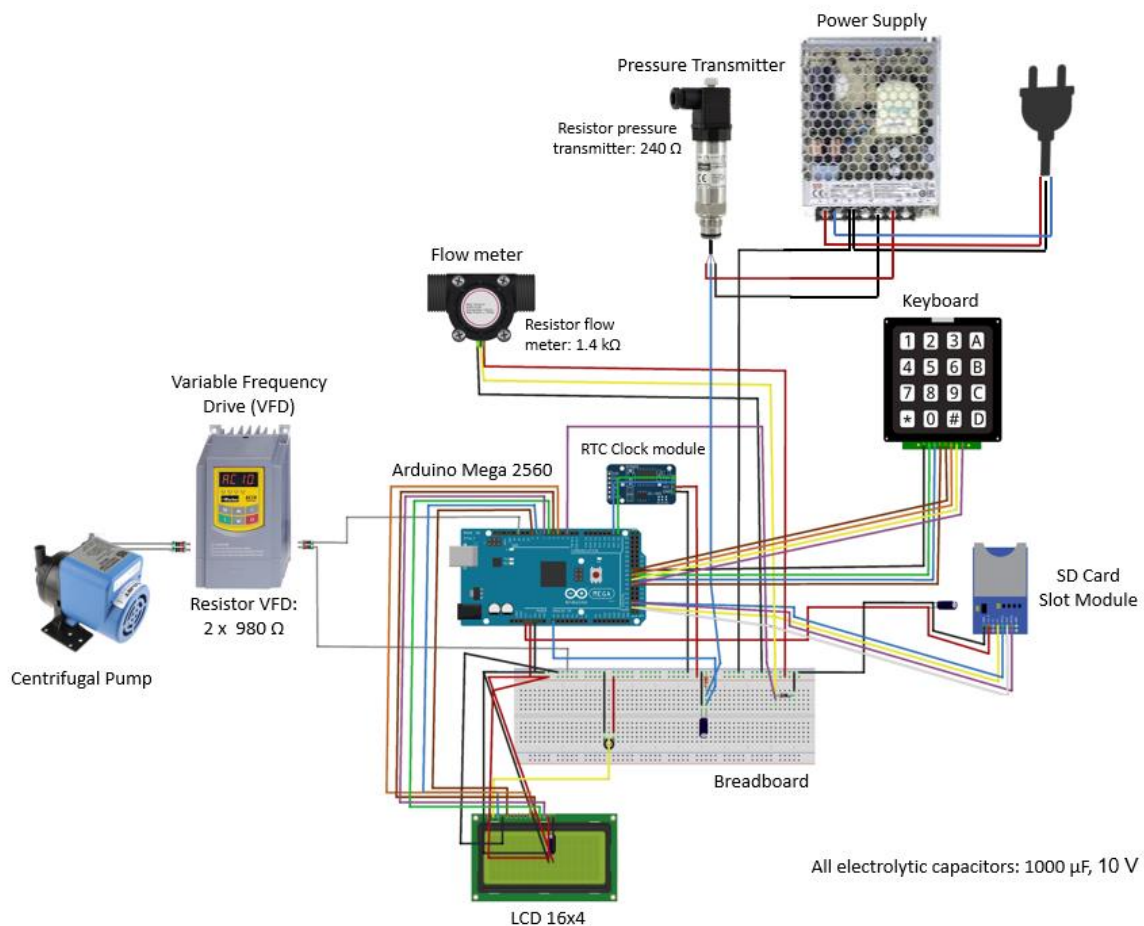


Figure 3.11. Electronic circuit implemented through Arduino Mega 2560 to work at a constant flow rate in recirculation or in the presence of external variation.

The controller gains the flow rate target value directly from the user through the keypad, and it displays it on the LCD screen, where the instant pressure value and averaged flow rate value are also reported directly from the respective sensors. Finally, a PID (Proportional-Integral-Derivative) controller was implemented in the Arduino code to reach the desired flow rate. It calculates the error value $e(t)$ as the difference between the desired target value

² <https://github.com/PhotonersURJC/PumpConstantFlowRate>

and the averaged flow rate, applying a correction based on a proportional, integral, and derivative term, reaching the desired setpoint with a minimal delay and overshoot through a feedback loop. The tuning constants “ K ” were derived experimentally and were, respectively, K_p , the proportional gain factor, which controls the output based on the error, K_i , the integral gain factor, which accounts for the past values and is able to remove the steady-state error, and K_d , the derivative gain factor, which estimates the future trend and has the effect of increasing the stability of the system, reducing the overshoot and improving the transient response. During recirculation, the flow rate chosen was 1 L min^{-1} to ensure a laminar flow rate throughout the experiments. Before uploading the final code in Arduino, the real-time clock (RTC) module was initialised to keep track of the time while saving the data as a .csv (comma-separated values) file in the SD memory card. Finally, the implemented logical flowchart is shown in Figure 3.12.

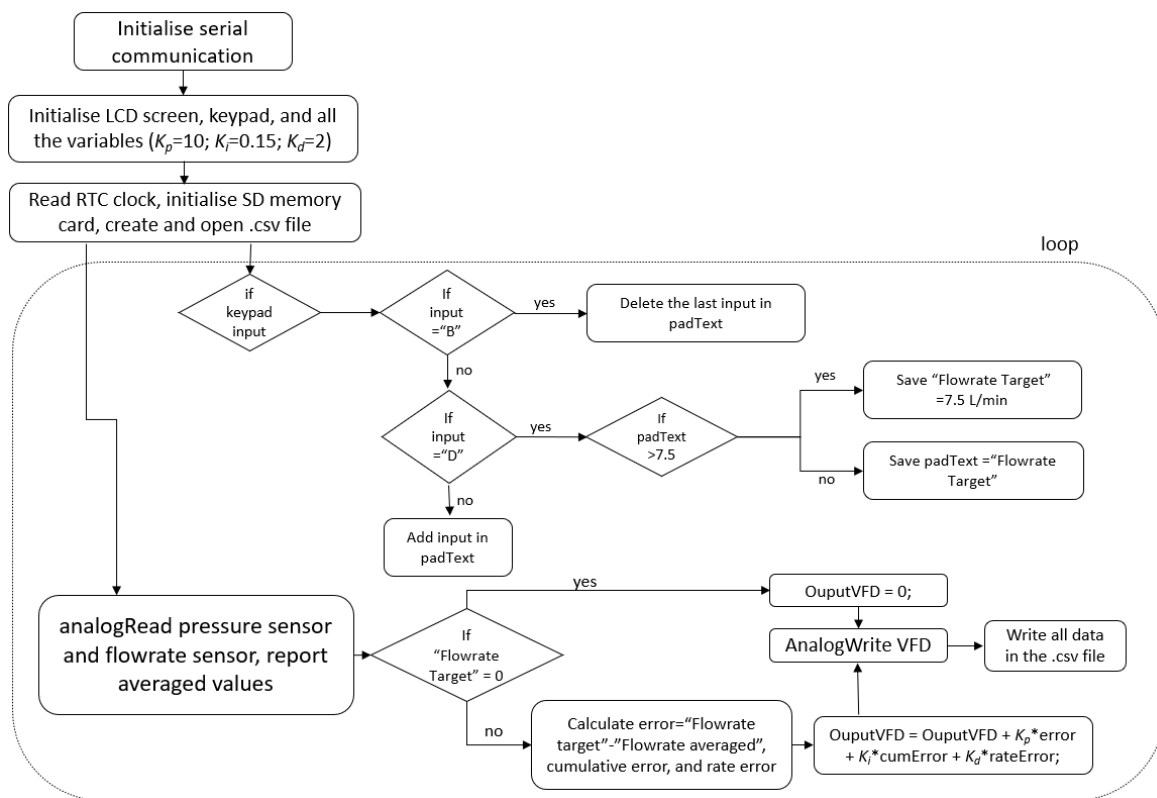


Figure 3.12. Logical flowchart diagram used in the Arduino code for the filtration system.

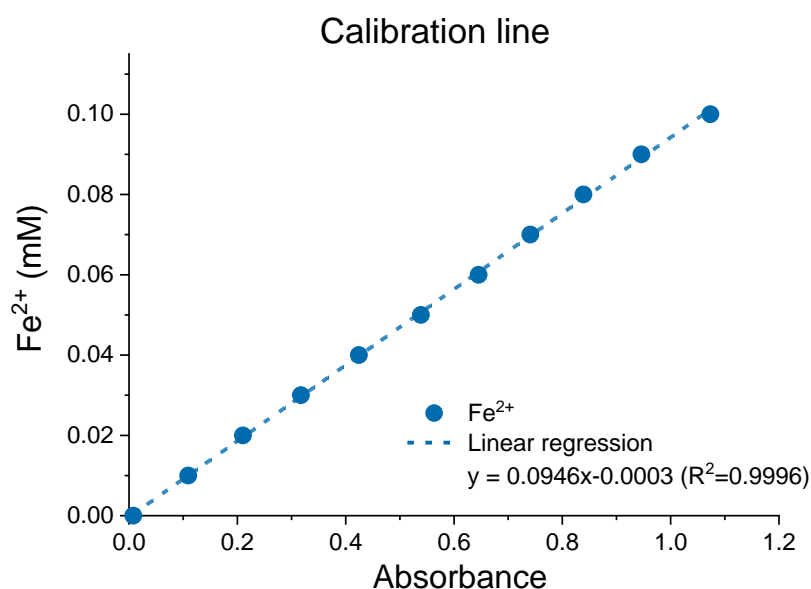
3.2.3 Ferrioxalate actinometry

Chemical ferrioxalate actinometry experiments were carried out to determine the total irradiation received by the medium in recirculation exposed to the lamps in the system [144]. Ferrioxalate actinometry was chosen over other characterisations for its high reproducibility and the economic and environmental sustainability of the materials compared to potassium iodide-iodate and uridine actinometry [144,145]. The absorption of photons by the medium solution results in the reduction of Fe^{3+} to Fe^{2+} , where the latter can be quantified using a colourimetric method based on the formation of a reaction complex with 1,10-phenanthroline, which absorbs at 510 nm, evaluated through a spectrophotometer working in the visible light, range 400-800 nm (V-3000PC, VWR). Knowing the quantum yield value, which corresponds to 1.38 in the UV-C range, and the reaction rate, by taking samples at time intervals, it is possible to calculate the number of incident photons in the reactor. First of all, all solutions were prepared accordingly to the literature [144]. A buffer solution was made of 54.18 g of sodium acetate, 5 mL of H_2SO_4 96% and milli-Q water to achieve a final volume of 500 mL. A 1,10 phenanthroline solution was made by adding 0.1 g of the compound to 100 mL of deionised water. A 0.1 N H_2SO_4 solution was made by adding 0.7 mL of sulfuric acid 96% in 250 mL of deionised water. Lastly, a 0.4 mM of Fe^{2+} solution was made by adding 27.8 mg of $\text{Fe}^{\text{II}}\text{SO}_4 \cdot 7\text{H}_2\text{O}$ and 0.7 mL of H_2SO_4 96 % in a 250 mL flask, then filled with deionised water.

A calibration line was initially measured to obtain the relation between the absorption value and known concentration of Fe^{2+} solutions prepared as presented in Table 3.3 and shown in Figure 3.13, where the data are the average of two sets of measurements.

Table 3.3. Solutions of known concentration of Fe^{2+} to obtain the calibration line.

$[\text{Fe}^{\text{II}}]$ (mM)	Fe^{II} solution (mL)	0.1 N H_2SO_4	Phenanthroline (mL)	Buffer (mL)	H_2O (mL)
0	0	5	1	2.5	1.5
0.01	0.25	4.75	1	2.5	1.5
0.02	0.5	4.5	1	2.5	1.5
0.03	0.75	4.25	1	2.5	1.5
0.04	1	4	1	2.5	1.5
0.05	1.25	3.75	1	2.5	1.5
0.06	1.5	3.5	1	2.5	1.5
0.07	1.75	3.25	1	2.5	1.5
0.08	2	3	1	2.5	1.5
0.09	2.25	2.75	1	2.5	1.5
0.1	2.5	2.5	1	2.5	1.5

Figure 3.13. Calibration line to obtain the relation between the absorption and the concentration of Fe^{2+} .

For the photoreactor, 1 L of the actinometric solution was prepared by adding 1.47 g of $\text{Fe}_2^{\text{III}}(\text{SO}_4)_3 \cdot 5\text{H}_2\text{O}$, 2.27 g of Oxalic Acid $\text{H}_2\text{C}_2\text{O}_4 \cdot 2\text{H}_2\text{O}$, and 2.72 mL of H_2SO_4 96 % in deionised water. The reactor was covered from other light sources, the solution was left recirculating at a constant flow rate, and the samples were taken at 0, 1, 2, 4, 6, 8, and 10 min. 0.25 mL of each sample was taken and added to 2.5 mL of buffer solution, 6.25 mL of H_2O and 1 mL of 1,10-phenanthroline solution and kept in the darkness for 30 min. The

absorbance at 510 nm was taken through a spectrophotometer, and through the calibration line, the absorbance value was converted into the Fe^{2+} concentration (mM). Since each sample was diluted 40 times, the resulting value was multiplied by 40 and then transformed into mEinstein (mE), divided by the quantum yield, and multiplied by the total solution volume. The representation of the incident photon flow as a function of the operation time leads to a straight line. The slope of this line corresponds to the photon-incident radiation power (mE) per unit of time (Figure 3.14).

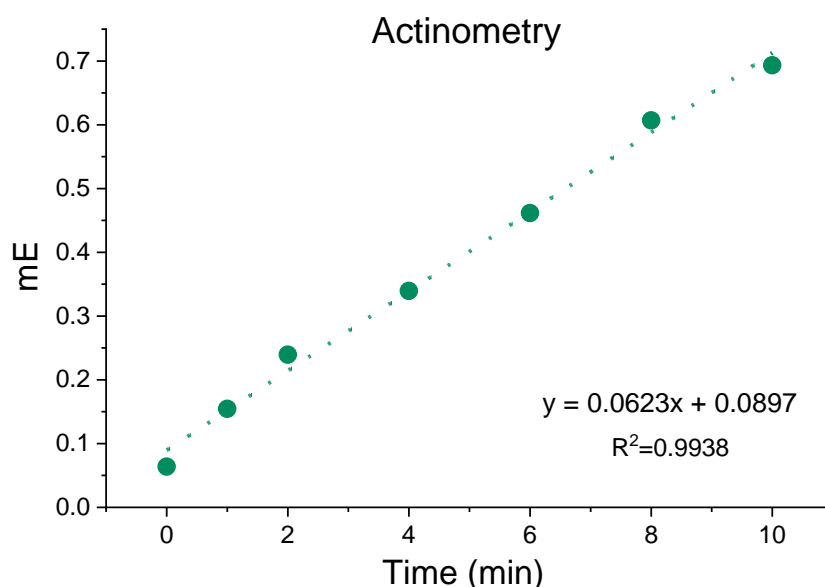


Figure 3.14. Actinometry sample, 1 L solutions irradiated by 265 nm lamp at 100% intensity.

Finally, the radiation emitted in the photoreactor by the UV LEDs lamps, I (W m^{-2}), was calculated through Eq. 3.17, where the photon energy E_p (J photon^{-1}) was calculated by multiplying the Planck constant, h (J s), by the speed of light c (m s^{-1}) and dividing by the wavelength λ (m) of the photons.

$$I = \frac{I_R \cdot E_p \cdot N_A}{A_{\text{irradiated}}} \quad \text{Eq. (3.17)}$$

Where I_R is the radiation flow (E s^{-1}), $A_{\text{irradiated}}$ the emission area (m^2), and N_A the Avogadro constant expressed in number of photons per Einstein, considering that one Einstein is, by definition, one mole of photons.

The intensity and the spectra of the UV-LED lamps were also measured by an ILT spectroradiometer (2003357U1, ILT), which proved to work well in the UV range considered [146]. It is worth mentioning that the area considered in the chemical actinometry corresponds to the part of the plane crossing the middle of the quartz tube irradiated from the lamps (108 mm · 20 mm). On the other hand, the radiometer was measured at 13.5 mm away, which was the distance from the mentioned plate to the light source, as shown in Figure 3.15.

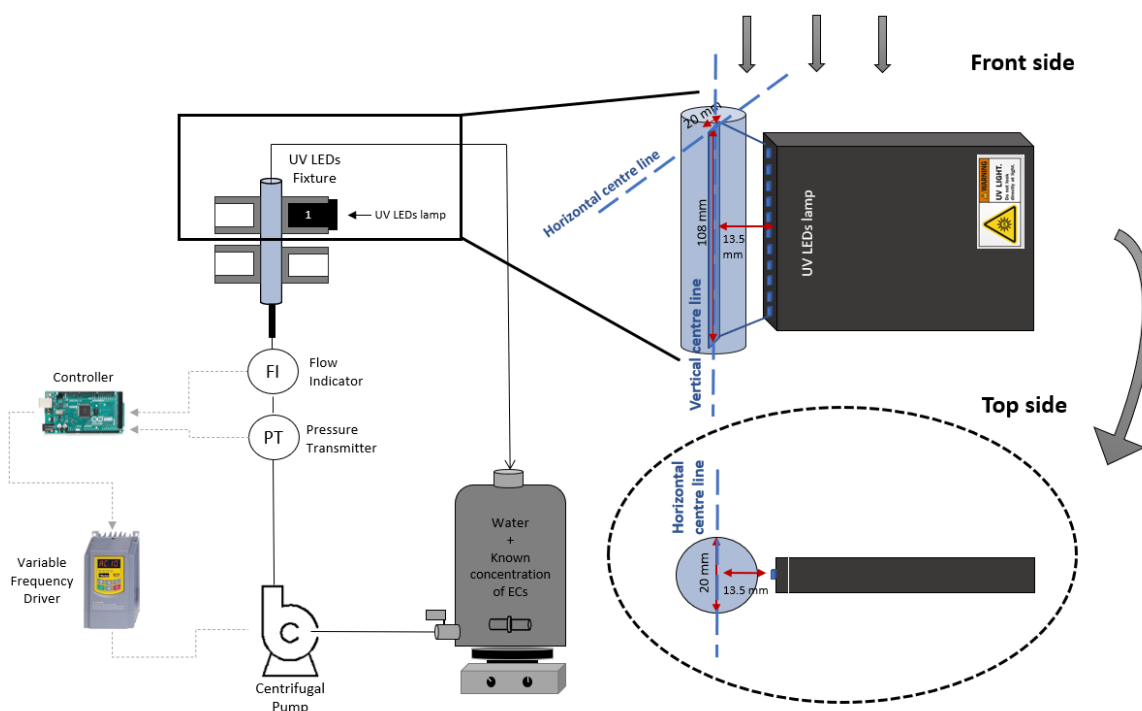


Figure 3.15. Details of the experimental setup for the chemical actinometry measurement.

3.2.4 Analytical methods

The detection and quantification of sodium diclofenac were conducted through HPLC with a reverse C18 column and equipped with a diode array detector (1200 Series, Agilent Technology). The optimised mobile phase was acetonitrile and 25 mM phosphate acetate buffer (pH 3) in a ratio of 80:20 v/v. The flow was set to 1 mL min^{-1} and the injection volume to $5 \mu\text{L}$. Finally, the pressure was constant at 45 bar, the thermostat was at $25 \text{ }^\circ\text{C}$, and the detection wavelength was set at 210 nm. The samples for the calibration were prepared in

half water and half mobile phase to best represent the sample from the experiments, which were diluted 1:1 in mobile phase before quantification. DCF calibration is shown in Figure 3.16, and the method was validated in terms of specificity (no interference was observed with the peaks of interest), linearity (the calibration curve had a linear correlation coefficient $R^2 > 0.99$), precision and accuracy (determined by intra-day and inter-day repeatability). The limit of detection (LOD) and quantification (LOQ) were defined by the signal/noise ratio, at least 3:1 for LOD and 10:1 for LOQ and were found to be 0.25 and 1 mg L⁻¹, respectively.

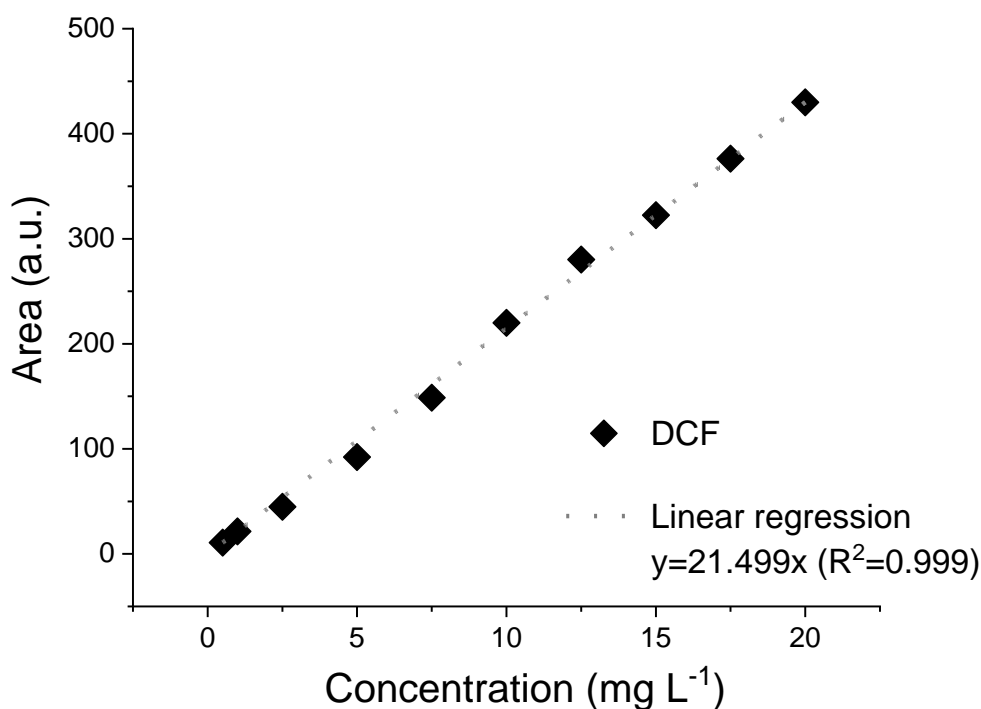


Figure 3.16. Diclofenac calibration line.

To evaluate the concentration of hydrogen peroxide in the UV-LED/H₂O₂ experiments, a titanil sulfate solution was employed [147]. The latter forms yellowish complexes with H₂O₂ due to the formation of pertitanic acid, detectable at 410 nm and quantifiable through the spectrophotometer. Firstly, a calibration line (Figure 3.17) was measured to obtain the relation between the absorption value and the concentration of H₂O₂.

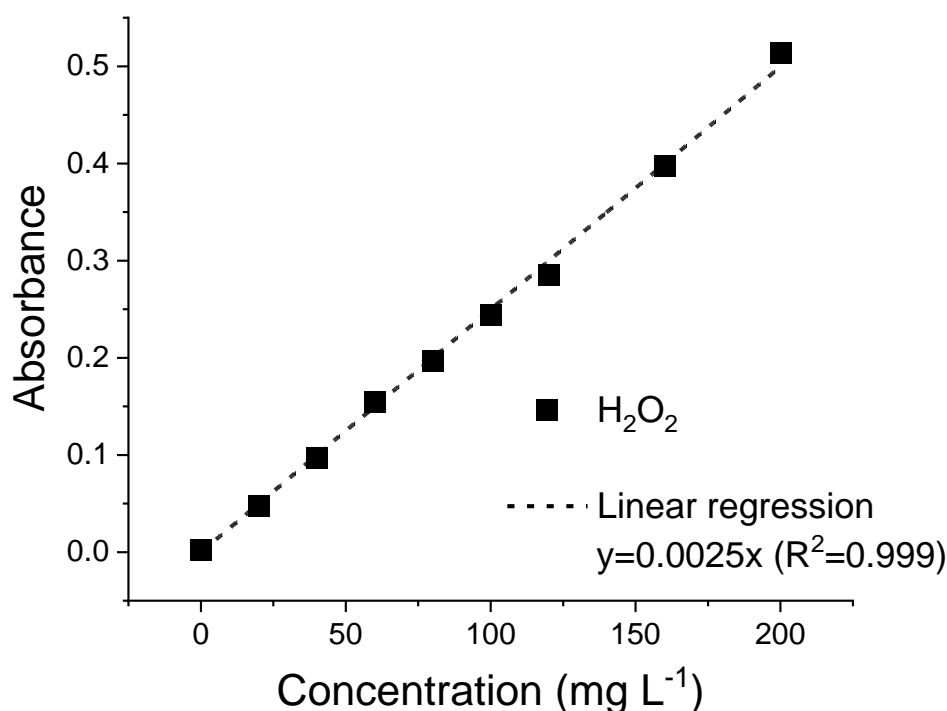


Figure 3.17. Calibration line for the quantification of H₂O₂.

Each analysis was prepared with 0.5 mL of sample, 4.5 mL of deionised water, and 0.5 mL of titanil sulfate. A blank consisting of 5 mL of deionised water and 0.5 mL of titanil sulfate was also prepared for each experiment. A control check was finally performed through H₂O₂ quantification strips ranging from 0 to 100 ppm.

The concentrations of FC in the sample from UV-LED/FC experiments were determined using the Hanna Instrument kit with the portable photometer (HI97734, Hanna Instrument) and the corresponding reagents (HI93734, Hanna Instrument). Because of the upper limit of 10 mg L⁻¹, the sample was diluted before the measurement with deionised water when higher concentrations were expected. When sodium hypochlorite is added to water, hypochlorous acid (HClO) is formed, which is one of the species with the greatest disinfectant power. Depending on the pH of the water [102], this compound dissociates, forming hydrogen ions (H⁺) and hypochlorite ions (ClO⁻). FC includes hypochlorous acid and hypochlorite ion, while total chlorine is the sum of FC and combined chlorine, which is produced when FC reacts with ammonia dissolved in the water, forming chloramines: monochloramines,

dichloramines, and trichloramines. In this case, distilled water was used in all the experiments, and only FC was evaluated since chloramines were not expected to form during the experiments.

Dissolved organic carbon (DOC) was measured with a TOC-VCPH analyser (Shimadzu), where the method described in the TOC-V CPH/CPN Total Organic Carbon Analyzer User's Manual was carefully followed.

Finally, studies of the molar absorption coefficient of the pollutant and the oxidants were evaluated through the Lambert-Beer law, Eq. (3.18), using gradient concentration solutions, measured with a UV-Vis spectrophotometer (8453, Agilent) in the UV range 200-400 nm.

$$A = \varepsilon_{\lambda} b C \quad \text{Eq. (3.18)}$$

Where A is the absorbance measured through the spectrophotometer, C is the molar concentration (M), and b is the path lengths of the quartz cuvette (1 cm).

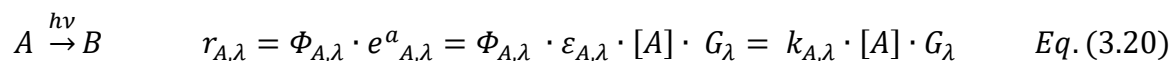
3.2.5 Phytotoxicity test

As described in the work of Ghanbari et al. [148], the germination index was used to evaluate the phytotoxicity of the treated and untreated DCF samples. Fifteen seeds of each plant, *Raphanus sativus* (radish) and *Solanum Lycopersicum* (tomato), were distributed homogenously in the Petri dish containing one filter paper of 110 mm at the bottom and one filter paper of 70 mm on top of the wet seeds (Whatman, GE Healthcare Life Sciences). 10 mL of sample was used in each test, and afterwards, all Petri dishes were incubated for 72 h at 25°C. The number of germinated seeds was measured (G_S), as well as the length of the roots (L_S), and then compared to the germinated seeds in the control condition (G_C , and L_C , respectively), where distilled water was employed. Finally, the germination index (GI) was calculated following Eq. (3.19). Each condition was performed in triplicates; therefore, the results show the average and standard deviation of three repetitions.

$$GI (\%) = \frac{G_s \cdot L_s}{G_c \cdot L_c} \cdot 100 \quad Eq. (3.19)$$

3.2.6 Calculations of the degradation kinetic parameters

A rigorous kinetic description of the model UV/H₂O₂ and UV/FC was investigated considering the wavelength dependency of the photoactivated reactions. The kinetic constants for the DCF photolysis at the wavelengths of interest were obtained from the experimental data of the present investigation, as well as the dark reactions constants. On the other hand, the rates of the elementary photo reactions for H₂O₂, HOCl, and OCl⁻ were expressed as the product of the quantum yield (Φ_λ , expressed in mol Einstein⁻¹) and the volumetric rate of photon absorption, *VRPA* (e^a , expressed in Einstein L⁻¹ s⁻¹). Where the latter can also be written as the molar absorption coefficient of the reactant (ϵ_λ , M⁻¹ cm⁻¹) multiplied by the concentration of the reactant and the irradiance (G_λ , W m⁻²), as shown in Eq. (3.20) [149].



Where k_λ is the kinetic constant (J⁻¹ m²) with respect to the concentration of the reactant and the irradiance. Each value is wavelength dependent and therefore evaluated for each lamp. The mechanisms proposals were chosen to find the best compromise between the number of reactions considered and the robustness of the results. For the selected mechanisms, the kinetic model was derived by resolving the mass balance of the different species and by applying the kinetic micro steady state approximation (MSSA) for the concentration of radicals. The second-order rate constants for the main radicals with DCF were finally estimated by minimising the normal root mean squared error (NRMSE) between the experimental and predicted concentration of DCF, H₂O₂, and FC. The sequential quadratic programming (SQP) function was implemented in GNU Octave to solve the nonlinear optimisation by minimising the objective error function, whereas the system of differential equations was solved using Euler explicit method.

3.3 Life cycle assessment methodology

The methodology standardised by the ISO was followed for the LCA analysis. The method involves four main interrelated stages, defined by ISO 14040 and 14044 series [120,150] and shown in Figure 3.18.

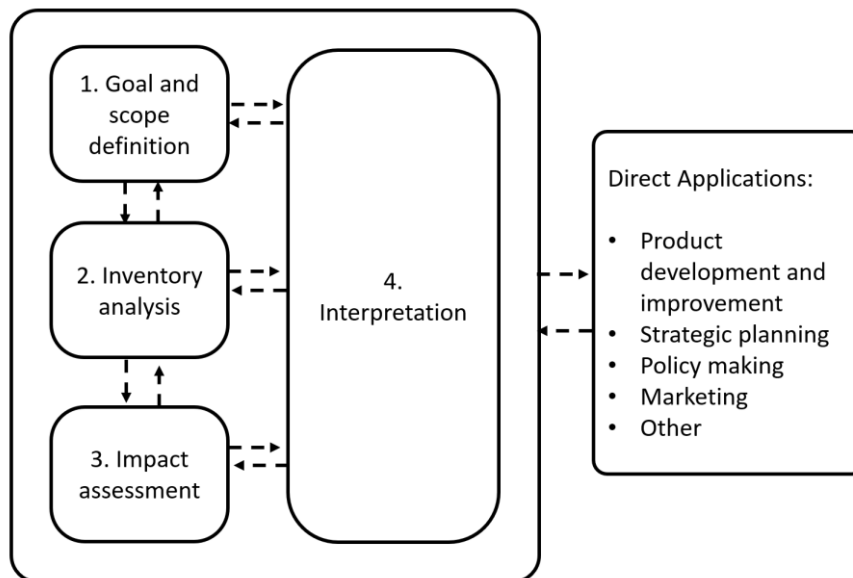


Figure 3.18. Life Cycle Assessment Framework according to ISO 14040 and 14044.

Adapted from [121].

Goal and scope

The goal and scope phase is the key step where the reasons and limitations for carrying out the study as well as the intended audience are indicated. The choices made in this step are fundamental for the rest of the study. In the first place, the functional unit (FU) is defined, which provides the reference unit and can strongly influence the conclusions. In this step, the identification of the system boundaries is also carried out, which defines the unit processes that are part of the system. Furthermore, in this phase, there are also included allocation procedures, if any, and the identification of the impact assessment method and the impact categories of interest.

Life cycle inventory

The life cycle inventory (LCI) phase involves the data collection of the inputs and outputs concerning raw material and energy, product and co-products, waste, emissions and other

environmental aspects (Figure 3.19) within the system boundaries identified in the previous phase. After the data are validated, they need to refer to the FU. Data might concern foreground processes, under the control of the decision-maker for which an LCA is carried out, and background processes, all of the indirect processes necessary to support the foreground processes but not directly part of the product or system being analysed.

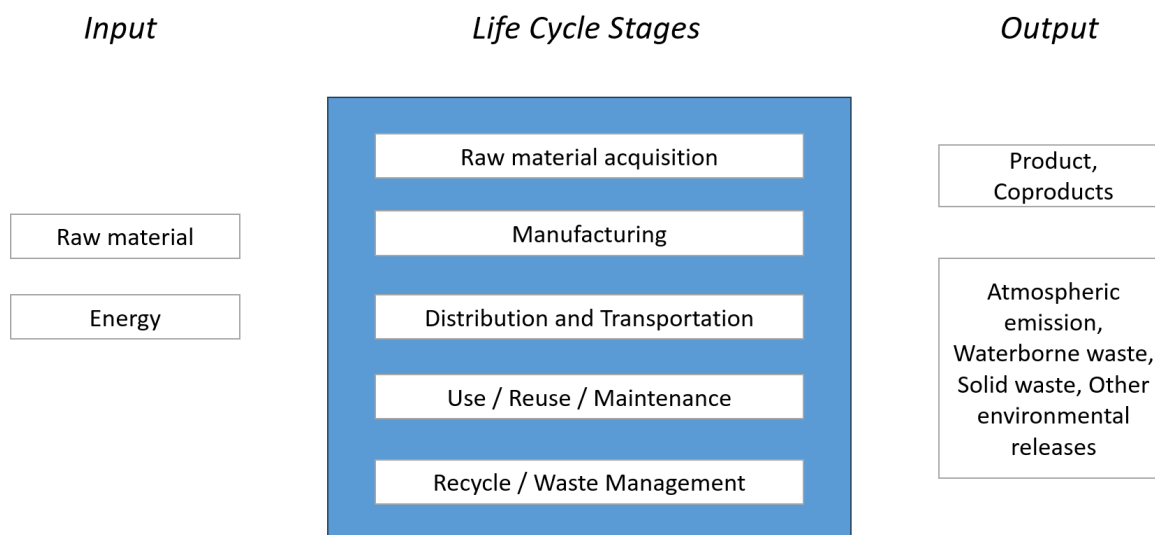


Figure 3.19. Input, output, and system boundaries of a generic product system [151].

Life cycle impact assessment

The life cycle impact assessment (LCIA) phase involves the quantification and classification of the substances of the inventory into impact categories and common units to allow comparisons. Impact methods involve results at the “midpoint level” and “endpoint level”. The former is calculated at the place where a common impacting mechanism occurs, which is associated with a high number of categories, while the endpoint is associated with three main areas of protection, which are normally “human health”, “ecosystems”, and “resources”. Optionally, the results can be normalised with respect to a reference value which provides the measure of the relative magnitude, or weighted, which refers to using numerical factors and aggregating indicators across impact categories. Weighting translates LCA results in a single score, easy to compare, but it implies subjectivity on the choice of the weighting factors.

Interpretation

The final stage of the LCA is interpretation, which involves summarising and discussing the results of the analysis. Both LCI and LCIA results are interpreted in the context of the goal and scope of the study to draw meaningful conclusions and recommendations. This phase also includes completeness, sensitivity analysis, and consistency checks. Data quality and uncertainty analysis can also be performed. As mentioned, the four stages are interrelated because LCA is an iterative procedure which leads to continuous improvements of the LCI modelling until reaching a robust conclusion and recommendation.

Although LCA is a standardised methodology, the choices on methodological aspects are quite open; therefore, to ensure that the LCA results are comparable, it is important to follow the ISO recommendations and to harmonise the methodological assumptions used in the analysis [120,150]. Methodological assumptions refer to the choices made in the LCA process, such as the functional unit, system boundaries, data sources and quality, allocation procedures, impact assessment methods, and sensitivity analysis. Small differences in these choices can significantly affect the results of the LCA and, therefore, the need to be harmonised to ensure the right comparison [152].

In this study, to compare the UV-C LEDs with an LP mercury lamps photoreactor and the sustainability of the oxidant addition (H_2O_2 or FC) in the UV-C LEDs treatments during the degradation of DCF in water, the ecoinvent v3.0 was used as a secondary data source to compile the inventory [153], while SimaPro 9.4 was employed to compile the inventory and quantify the LCA results [154].

4. RESULTS AND DISCUSSION

4 Results and discussion

4.1 Microplastic and membrane characterisation results

PA and PS particles were characterised to define the differences in shape, particle size distribution, and surface charge. FTIR analyses were also performed to evaluate their chemical structure directly on the membrane surface, where the best filter for the quantification step was selected. Finally, the chosen membranes for the filtration system were also characterised by evaluating the roughness, the Shore hardness, and the water contact angle, other than the surface morphology.

4.1.1 Microplastics detection and analysis

As mentioned, the analysis of MPs pollution in water is still one of the main challenges related to their occurrence since the microparticles can be easily confused with other materials. Within the microplastic characterisation techniques, micro-FTIR has gained a lot of attention as suitable for both quantification and qualification. However, previous studies have shown that refractive error represents a source of uncertainty when interpreting the spectra of irregularly shaped materials [19]. Consequently, ATR-FTIR measurements were performed to analyse the specific regions to identify them and identify the key characteristic peaks [155]. In the case of performing a chemical map of the MPs directly on the filter, the latter should behave as a window in the regions where the MPs characteristics peaks fall. Therefore, a study on the best choice for the filter material was also carried out.

Figure 4.1 shows the ATR-FTIR spectra of the MPs and the membranes under study. The main regions for PA and PS particles were identified as 3300-2700 cm^{-1} , corresponding to N-H and C-H stretches, and 1800-1300 cm^{-1} , which reflects the C=O stretch, N-H bend, and C-C stretch [156].

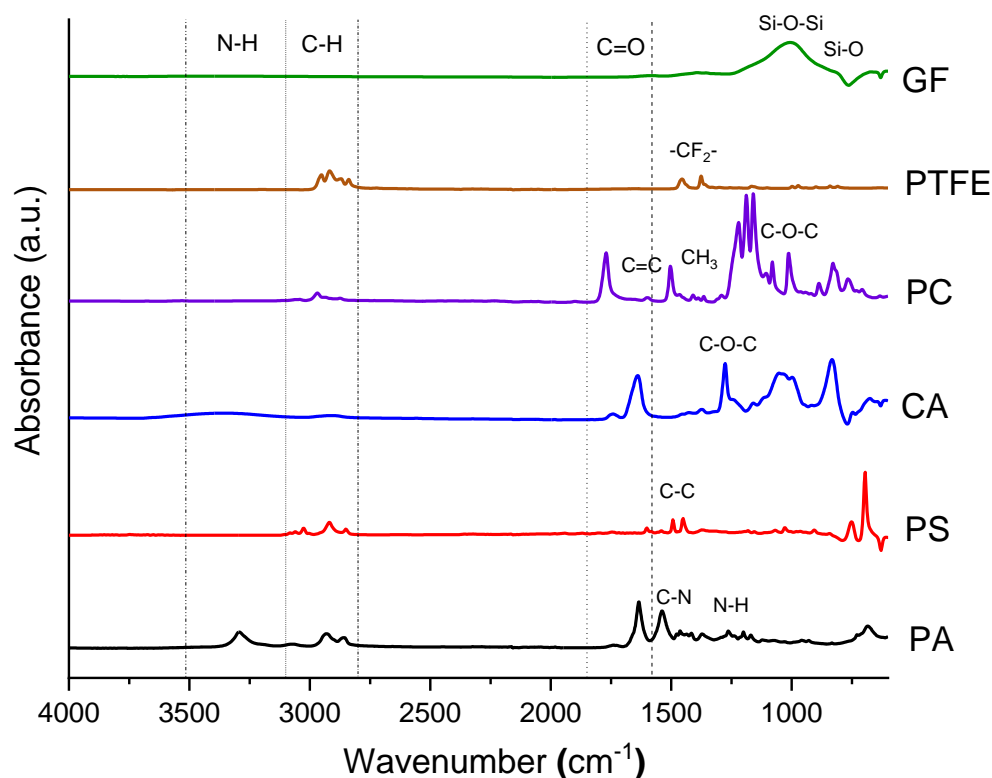


Figure 4.1. ATR-FTIR spectra of the two MPs (PA and PS) and the four membranes (CA, PC, PTFE, GF) under study.

On the other hand, the reflectance micro-FTIR spectra of the particles and the membranes are shown in Figure 4.2. As expected, the micro-FTIR spectra exhibit some distortions and baseline fluctuations attributed to refractive errors in comparison to their corresponding ATR spectra. Nevertheless, both MPs and membranes show distinctive absorbance regions related to their main stretching and bending bonds, contrary to a previous study where the spectrum of polyamide nylon-6 was unattainable in reflectance micro-FTIR [155].

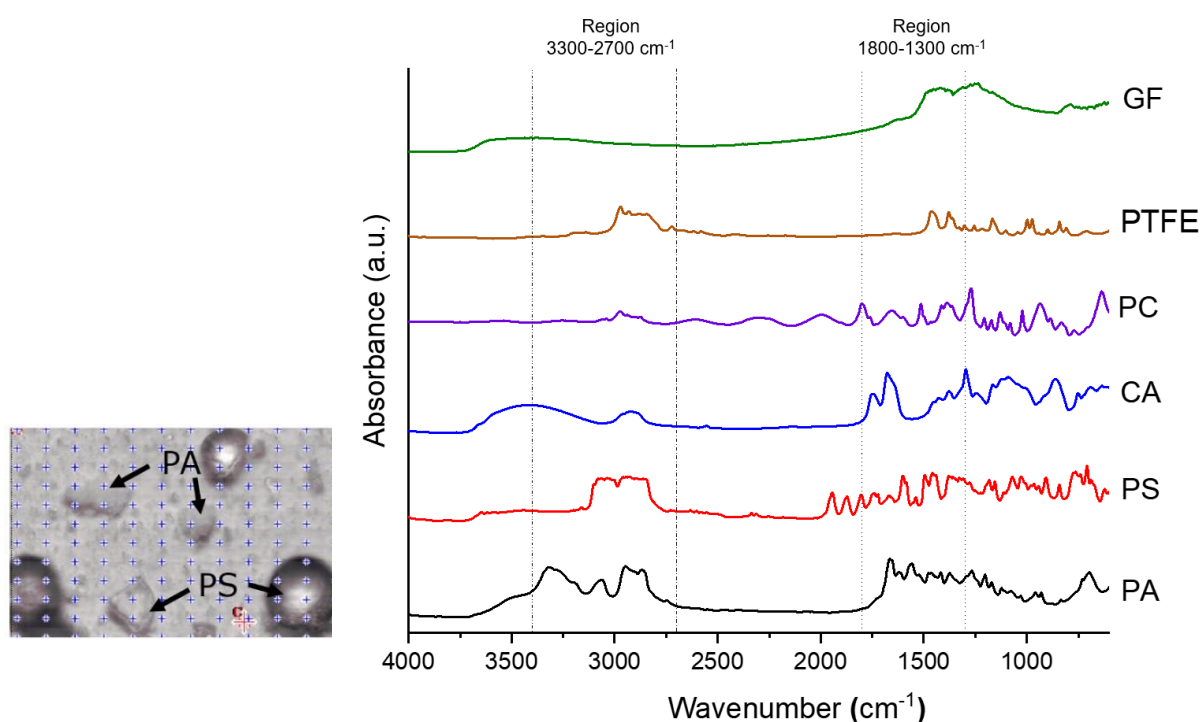


Figure 4.2. Reflectance micro-FTIR spectra of the MPs (PA and PS) and the membranes (CA, PC, PTFE, and GF).

Within the four membranes tested, GF demonstrated the highest suitability in reflectance mode since it showed a better IR window in the first region, $3300\text{--}2700\text{ cm}^{-1}$, despite exhibiting some diffractive errors and high absorbance in the second region, $1800\text{--}1300\text{ cm}^{-1}$, which could complicate MPs identification. Following in order of suitability were CA, PC, and PTFE membranes; however, all of them displayed peaks in the regions of interest that could also be problematic for identification purposes. Therefore, GFs were selected for the quantification step, while the other three membranes were explored for the removal of MPs during MF in dead-end configuration.

Prior to the removal technology study, this work was instrumental in characterising and identifying the microplastic particles of interest. The results demonstrate that micro-FTIR is suitable for identifying MPs through their main peaks directly on the membranes; however, refractive errors pose challenges, especially in more complex matrices. Additionally, a major drawback is the detection limit, which is limited to particle sizes down to $20\text{ }\mu\text{m}$, thus neglecting the identification of NPs, which are becoming increasingly prevalent.

4.1.2 Particles size distribution

Figure 4.3 and Figure 4.4 depict the particle size distribution of PA and PS particles, respectively, after being milled and sieved in the range of 20-300 μm , where the histograms represent the microscopic counting results, while the solid grey line the particle size distribution from FBRM technology. The results from the two techniques were comparable in both cases, indicating the suitability of the two measurements for quantifying the MPs size.

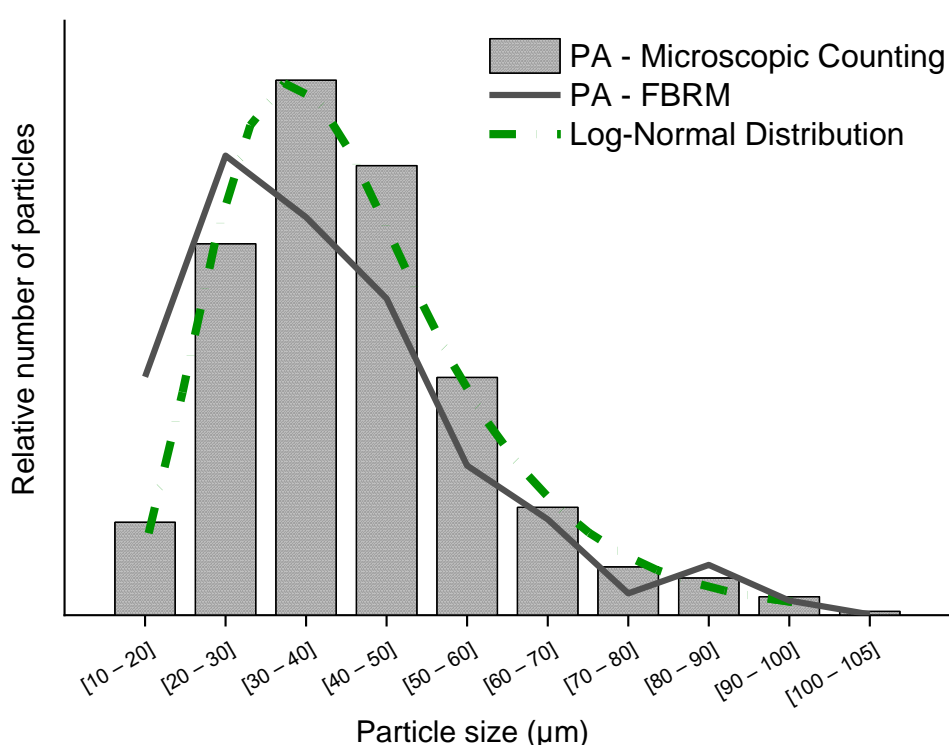


Figure 4.3. Particle size distribution of PA particles measured by microscopic counting and FBRM technology. The short-dash dot curve in green represents the log-normal distribution fitting the histogram data.

The average particle size for PA was around 40 μm , as determined by both techniques ($41 \pm 16 \mu\text{m}$ and $39 \pm 29 \mu\text{m}$ from microscopic and FBRM, respectively), while for PS particles, it was around 110 μm ($109 \pm 74 \mu\text{m}$ and $109 \pm 70 \mu\text{m}$ from microscopic and FBRM, respectively).

4.1.3 Zeta potential analysis

The zeta potential was experimentally evaluated for the two particle types in milli-Q water and shown in Figure 4.5. In general, a positive ζ -value indicates that the surface of the material has a net positive charge, a negative value indicates a net negative charge, whereas zero means a neutral surface charge. Most plastics have a relatively low zeta potential in water due to their hydrophobic nature and lack of surface charges; however, they can be modified by various functionalisation depending on the final scope of the plastic or the environmental route followed by the particles into the water. Furthermore, ζ depends on the particles' size since smaller particles have a higher surface area-to-volume ratio, increasing the available surface charges and affecting the behaviour and stability of the particles in suspension, as well as their interaction with the membrane surface [15].

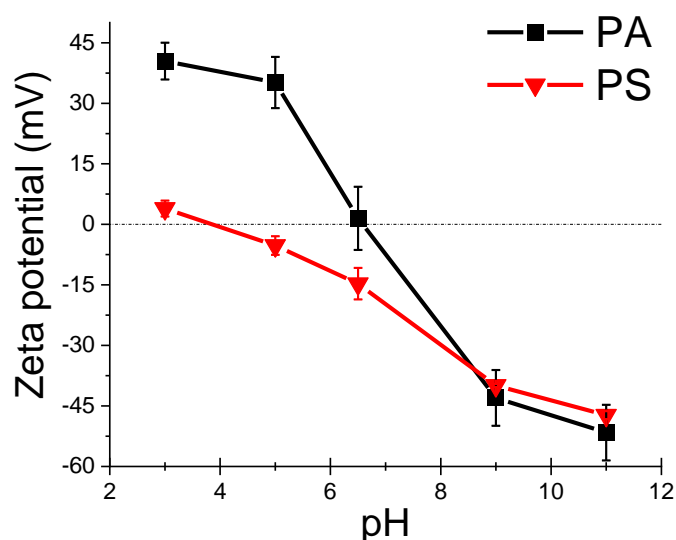


Figure 4.5. Zeta potential curves as a function of pH of 500 mg L⁻¹ of PA (black squares) and PS (red triangles) particles with sizes between 20-300 μm .

For PA and PS particles, the zeta potential changed from negative to positive when changing from basic to acid conditions. The points of zero charge for these particles were observed to be at pH 6.5 and pH 4, respectively. Hence, PA particles under neutral water conditions (considered to be at pH 6.5) displayed a high degree of aggregation and hydrophobic

behaviour. In contrast, PS particles exhibited a slightly negative ζ -value of 20 mV of magnitude, indicating incipient instability and negative surface charge.

Therefore, PA and PS, with their low ζ -value, their density (1.13 g cm^{-3} and 1.05 g cm^{-3} , respectively), and their small size, were forming unstable dispersed colloidal suspensions. Figure 4.6 shows the suspensions of 100 mg L^{-1} of PA and PS particles over time. The particles were slowly settling at the bottom of the container or on the water's surface, and for this reason, the magnetic stirrer was needed to keep the suspensions as homogeneous as possible.

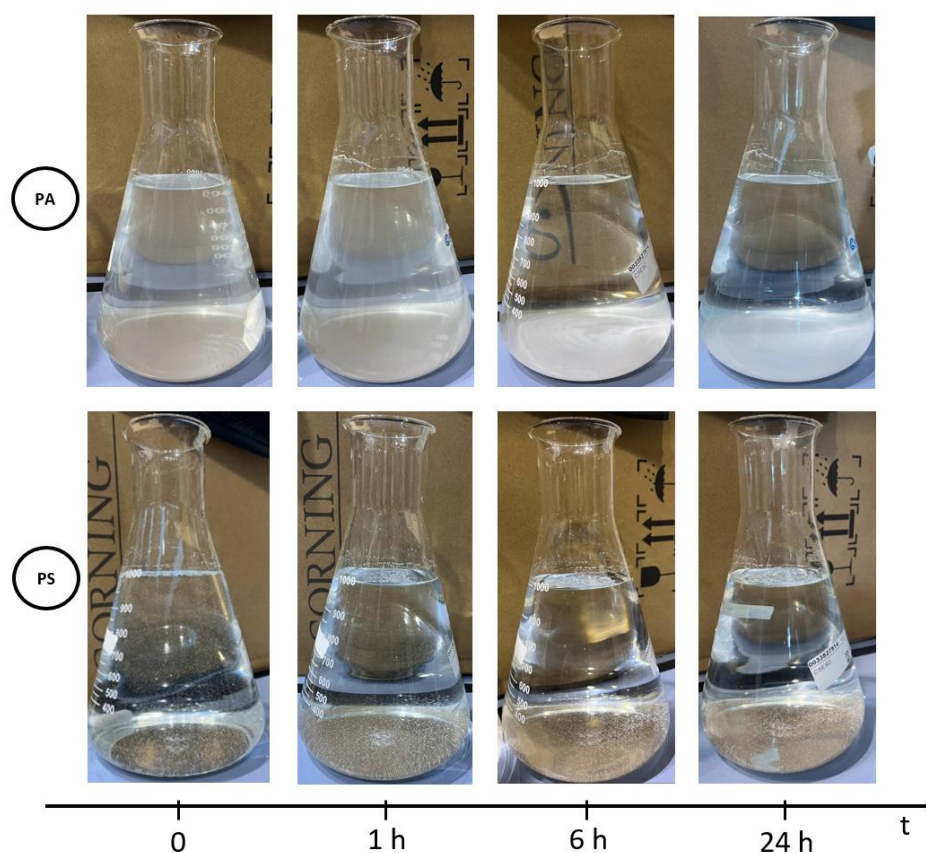


Figure 4.6. Picture of the microplastic suspensions in water over time.

The experiment also proved that using MF instead of simple decantation to separate MPs is an advantage considering a faster separation time and a higher removal efficiency; indeed, even after 24 h, some particles were still fluctuating halfway. Additionally, MF, compared to other membrane processes, only requires a small TMP (below 5 bar) to drive the flow across the membrane; therefore, it does not involve high energy costs.

Similarly, the zeta potential of the membranes plays an important role, affecting mainly the surface fouling degree and the filtration efficiency. The ζ -values of the membranes of interest were sourced in the literature. They were all negatively charged, with polycarbonate having a zeta potential of -11.5 mV at pH ~ 7.4 [157], cellulose acetate displaying a zeta potential of -35 mV at pH ~ 6 [158], and PTFE exhibiting a zeta potential of -60 mV at pH ~ 7 [159]. It is worth noting that the majority of commercially available membranes in the market possess negative charges [160]. The sole exception includes positively charged nylon membranes which were not suitable in this study as they could potentially influence the removal of the targeted MPs.

4.1.4 SEM images

MPs in the environment have diverse morphologies depending on their purpose or route of entry into water bodies. The SEM images of the MPs help identify the differences in morphology and shape irregularities between the two types employed, the synthesised PA particles and the milled PS fragments. The images are shown in Figure 4.7 and were taken at different magnifications to allow a similar representation of the particles, 2400x and 8000x in Figure 4.7a and b for PA and 300x and 1200x in Figure 4.7c and d for PS.

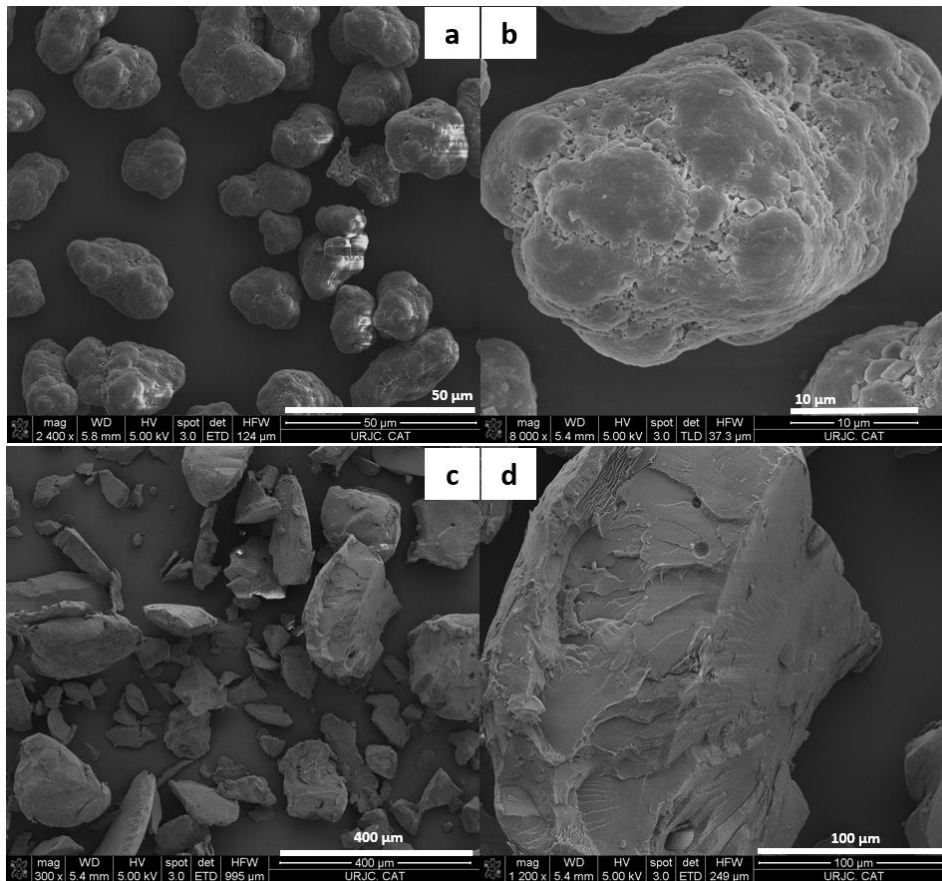


Figure 4.7. SEM images of the particles of PA (a and b, with unit distance of 50 and 10 μm) and PS (c and d, with unit distance of 400 and 100 μm).

The shape of PA particles is much more regular due to the manufacturing process, whereas the PS particles are highly irregular in size and shape as they were previously milled to attain the desired size range. Thus, it can be argued that these differences represent the disparity between primary MPs, which are directly produced as microbeads, and secondary MPs formed due to macroplastic fragmentation.

Since the morphology and structures of the membranes selected could also significantly impact MPs removal, SEM images of their surfaces were performed and shown in Figure 4.8.

4. Results and discussion

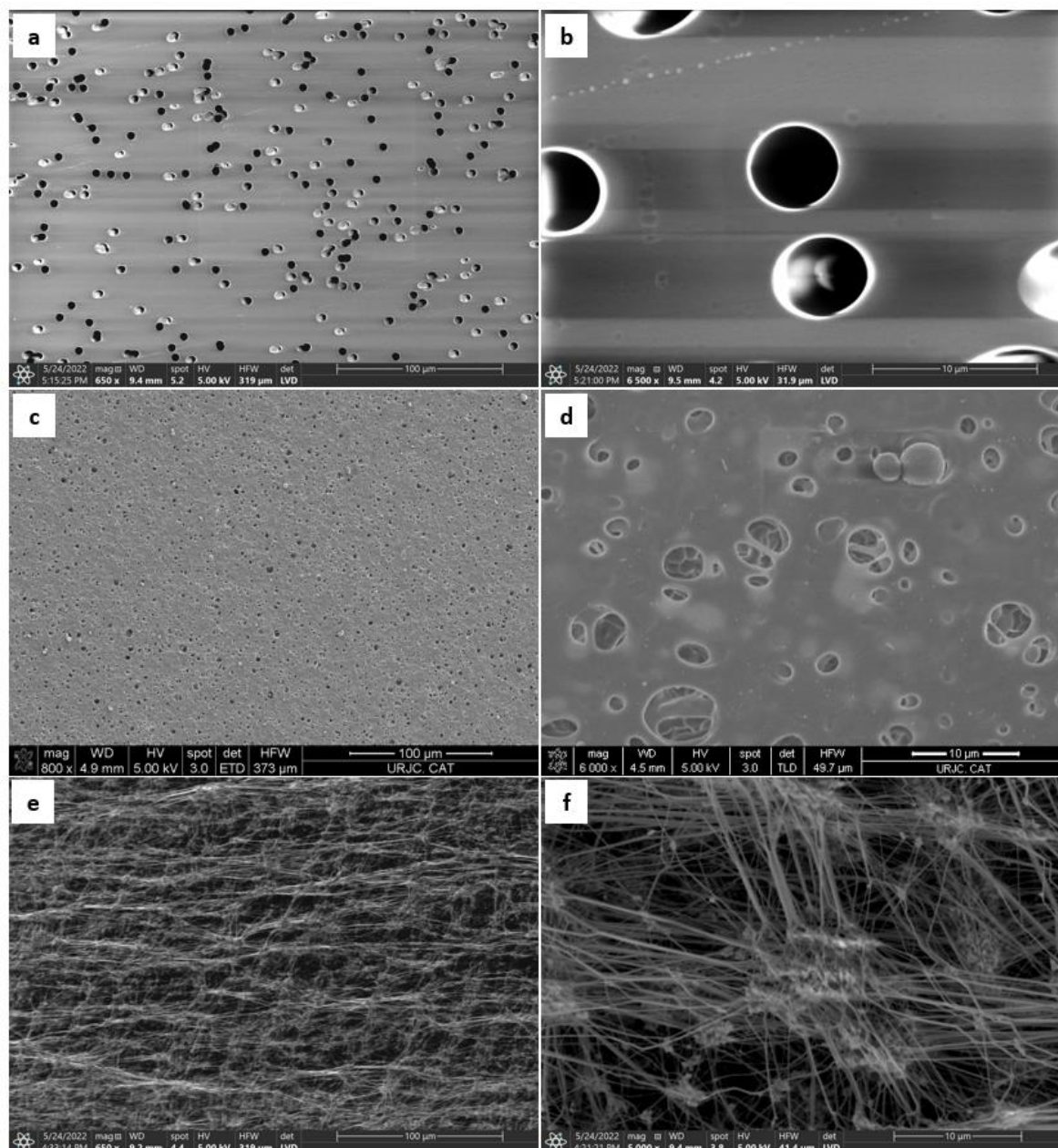


Figure 4.8. Surface morphology of the three membranes: PC (a and b), CA (c and d), and PTFE (e and f) under SEM with unit distance of 100 and 10 μ m, respectively.

The membrane pore sizes were all 5 μ m; however, differences in the manufacturing processes led to different pore sizes and shapes, which can affect the MPs removal, as highlighted in the study conducted by Cai et al. [16].

4.1.5 Other membrane characterisations results

From the WCA measurements emerged a super hydrophilicity behaviour for the CA and PC membrane, where the drop was completely absorbed as soon as it touched the surface. While for the PTFE membrane, three measures were taken at different times, but no difference was reported. Figure 4.9 shows the water drop on the PTFE membrane stable after 60 seconds, where the contact angle was measured on both sides through the goniometer function in AutoCAD®.

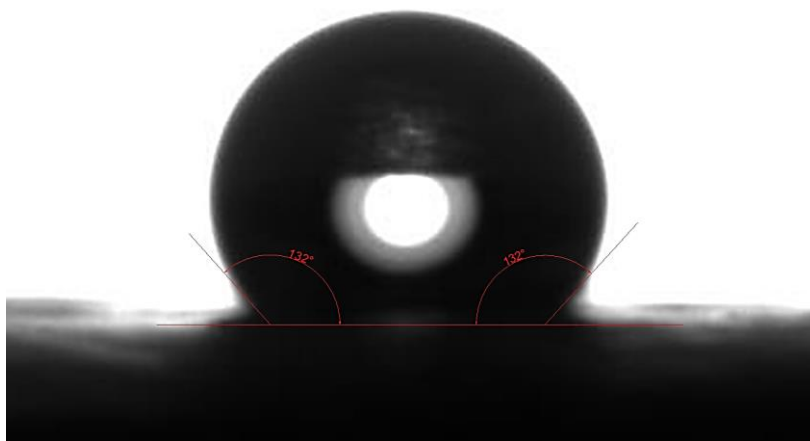


Figure 4.9. Water contact angle measured after 60 s on the PTFE membrane.




Hardness values were measured with the Shore A durometer, and the results showed that the membranes from the softest to the hardest were CA, PC, and PTFE, respectively, with 62.7, 71.0, and 76.3 in dimensionless unit of measurements in the Shore A scale.

Finally, profilometry analyses were performed. The roughness values were quite similar for the three membranes within the experimental error, ranging from 1.28 to 1.69 μm . Assessing the roughness of the membrane surface was important, as rough surfaces with irregularities and bumps could result in additional physical interactions between the MPs and the membrane. Generally, higher roughness values induce a higher fouling rate, and the main processes implied are foulant-membrane interactions, steric effects, hydrodynamic

conditions, and permeation flux [161]. However, the role of surface roughness becomes significantly more pronounced when the particles' size and shape match the membrane's valleys. Therefore, roughness is not expected to play a critical role for the three membranes since particles are substantially bigger than 10 μm . Nonetheless, the surface roughness might increase due to the formation of the cake layer, which can lead to higher fouling during the process.

In Table 4.1 all the information measured for the three membranes are summarised: WCA, Shore hardness, roughness and microscope pictures taken by the optical profilometer.

Table 4.1. Water contact angle and roughness measurement.

Membrane	PS	CA	PTFE
WCA (degree)	<5 highly hydrophilic	<5 highly hydrophilic	130.83 ± 1.33 hydrophobic
Shore Hardness (Type A)	71.0 ± 2.7	62.7 ± 0.6	76.3 ± 3.2
Roughness (μm)	1.407 ± 0.183 	1.2824 ± 0.307 	1.691 ± 0.424 

4.2 Membranes performance for microplastic removal

In this section, the evaluation of the selected membranes' performance in removing MPs within a simple dead-end filtration system was conducted, and the optimal membrane material in terms of water flux, TMP, and MPs removal efficiency was identified.

4.2.1 TMP and flux results

The membranes' performances were studied as a function of time and with a known concentration of initial MPs (100 mg L^{-1}). At the beginning of each experiment, the pump was manually set to start at 0.5 bar of TMP. However, for the PTFE membranes, the initial working pressure was set to 1.5 bar due to their high hydrophobicity; indeed, at 0.5 bar, the flux was negligible. The filtration data were taken for 10 min, and for each membrane, at least five replicates of the filtration experiments were performed to evaluate the experimental errors. A representative curve of TMP and flow rate trend during PA and PS filtration for the three membranes is shown in Figure 4.10, and for each experiment, the membrane flow rate when filtering distilled water without any particles was also shown at the set TMP.

The temperature was also monitored during the experiments; however, it is not shown as it was constant at room temperature the whole time.

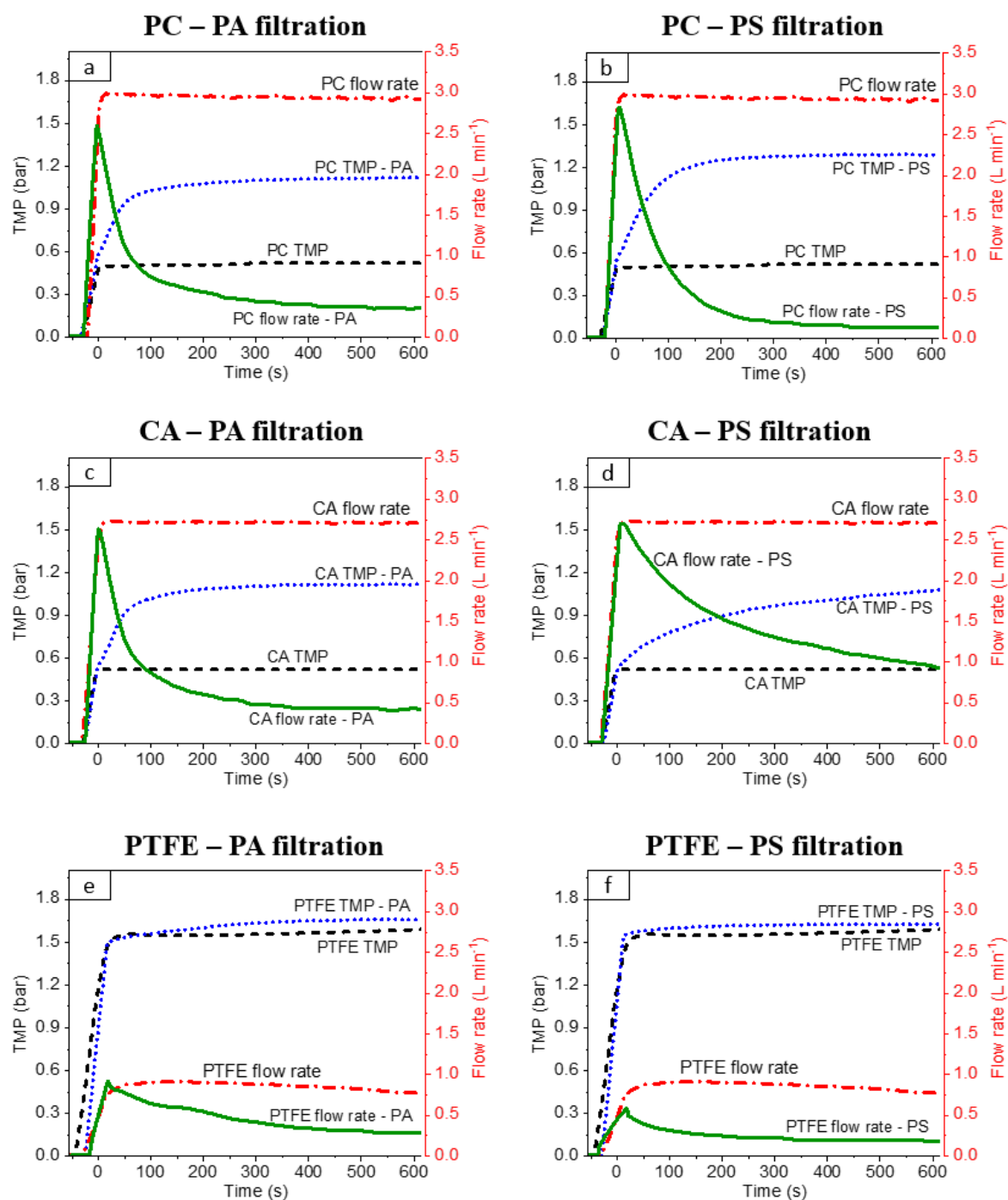


Figure 4.10. Results of TMP and flow rate for PC (a and b), CA (c and d), and PTFE (e and f) during the filtration of PA and PS, respectively. The black dash-dash curve for TMP and the red dash-dot curve for the flow rate represent the behaviour of the membranes when filtering distilled water. On the other hand, the blue dot-dot and green straight-line curves represent the membrane's TMP and flow rate when filtering water containing 100 mg L⁻¹ of PA and PS, respectively.

Without any MPs, the membranes' TMP and the flow rate are constant during the entire 10 min, also indicating that at the pressures employed, no membrane compaction occurs when only water passes. Indeed, while it was found to affect the UF membranes' performance [70], MF seems to be less affected. When adding 100 mg L⁻¹ of PA or PS particles without controlling any operating variable, the fouling induces an increase in TMP and a decrease in flow rate. Both are important to be considered for the overall performance of the membranes since TMP leads to higher energy consumption due to the pump costs, while a fast decrease in flow rate means a more frequent membrane replacement or implementation of more robust strategies to reduce the fouling, which can increase the overall energy costs.

To be able to represent the experimental error, Table 4.2 shows the average value of TMP drop and the average value of the flux with the corresponding standard deviation after 10 min of the filtration. To calculate the filtration flux, the area of the membrane was taken without the part lost due to the filter holder.

Table 4.2. Average transmembrane pressure increase (Δ TMP) and flux (J) after 10 min of 100 mg L⁻¹ of MPs filtration of the membranes under study.

	PA filtration		PS filtration	
	Δ TMP _{10min} (bar)	J _{10min} (L s ⁻¹ m ⁻²)	Δ TMP _{10min} (bar)	J _{10min} (L s ⁻¹ m ⁻²)
PC	0.54 ± 0.09	4.70 ± 0.75	0.69 ± 0.05	1.73 ± 0.63
CA	0.51 ± 0.24	4.66 ± 1.00	0.59 ± 0.05	9.67 ± 0.20
PTFE	0.13 ± 0.07	3.17 ± 0.72	0.11 ± 0.05	1.61 ± 0.34

Clearly, the concentration of 100 mg L⁻¹ was much more than the average concentration depicted in the drinking water environments; however, it was chosen to decrease the filtration time of the experiments. According to LaRue et al. [72], the worst-case scenario of MPs concentration detected in drinking water to date was around 10 µg L⁻¹. Therefore, in a more realistic scenario and assuming a linear correlation, 10 min of operation with 100 mg L⁻¹ of MPs would correspond to around 1666 h or 69 days of continuous operation with 10 µg L⁻¹ of MPs.

According to Table 4.2, the smallest increase in TMP was recorded for the PTFE membrane; however, the starting TMP was higher to allow the flux to move, and the flux decreased from $7.30 \pm 1.67 \text{ L s}^{-1} \text{ m}^{-2}$ without MPs to $3.17 \pm 0.72 \text{ L s}^{-1} \text{ m}^{-2}$ for PA and $1.61 \pm 0.34 \text{ L s}^{-1} \text{ m}^{-2}$ for PS. Therefore, regarding the operation, PTFE membranes were undoubtedly the worst performing; however, they were chosen for their hydrophobicity and the potential of achieving higher removal efficiency for the hydrophobic interaction MPs-membrane surface, even if at the cost of higher fouling.

For completeness, Figure 4.11 shows graphically the final TMP and flux reached after 10 mins of the filtration.

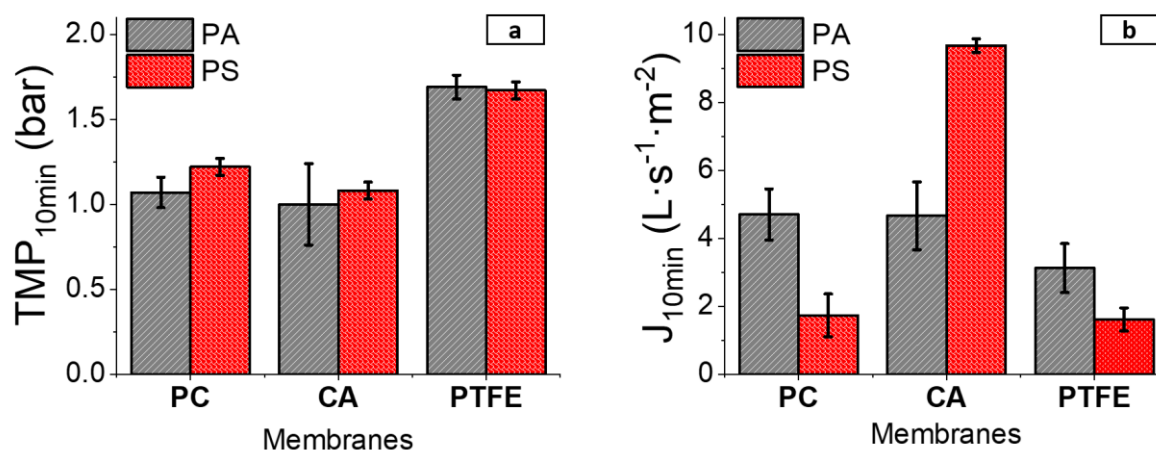


Figure 4.11. Average TMP (a) and flux (b) after 10 minutes of 100 mg L^{-1} of PA and PS filtration with the three membranes.

Among PC and CA membranes, PC suffered higher fouling with PS particles than PA particles. Whereas, in the presence of PS, the CA membrane performed much better, with the flux remaining relatively high after 10 min, around $9.67 \pm 0.20 \text{ L s}^{-1} \text{ m}^{-2}$, where the curve had not yet reached a constant value. On the other hand, the performance of the two membranes was very similar when filtering PA particles.

4.2.2 MPs removal efficiency

Simon et al. [68] pointed out the inaccuracy of reporting the MP measurements based only on particle number removal efficiency. They explained that particle number is not a conserved base quantity since they can break down during the filtration due to the mechanical impact with the membrane, and this would lead to a potential overestimation of their final amount. Indeed, several studies reported a considerable variation in treatment removal efficiencies, which could have been the direct result of the reported values other than sample collection and the analytical method for the quantification [17,162]. Mass, on the other hand, is more suited to compare independent studies on MPs, and it should be included. However, both are important considering the increasing worries of NPs in the environment. Therefore, both values, $MRE\%$ and $NpRE\%$, evaluating the mass and the particle number removal efficiency, were calculated to compare the effectiveness of the three membranes in the MPs removal with the aim to provide comparable results with other independent studies. Also, for the removal analyses, at least five replicates of the measurements were evaluated. Table 4.3 shows $MRE\%$, $NpRE\%$, together with the estimated total number of particles per litre that had not been removed by the membranes (NT_{MP}) and the particles' average diameter (D_{MP}). Whereas the number of particles (1,982,000 and 143,000 particles L^{-1} for PA and PS, respectively) and the average diameter size (40 and 110 μm for PA and PS, respectively) in the suspension feed were considered the same in all filtrations.

Table 4.3. Total number of unremoved microplastic particles per litre (NT_{MP}), average size of unremoved MPs (D_{MP}), mass removal efficiency ($MRE\%$) and particle number removal efficiency ($NpRE\%$) of each membrane when filtering water with 100 mg L^{-1} of PA and PS.

Membrane	MPs	NT_{MP} (particles L^{-1})	D_{MP} (μm)	$MRE\%$	$NpRE\%$
PC	PA	127,000	15.66	99.6 ± 0.4	93.6 ± 6.3
	PS	33,000	37.40	96.8 ± 4.5	76.9 ± 21.5
CA	PA	27,000	20.58	99.8 ± 0.1	98.7 ± 0.7
	PS	8,000	75.51	94.3 ± 5.1	94.5 ± 3.0
PTFE	PA	46,000	21.72	99.6 ± 0.3	97.7 ± 1.3
	PS	47,000	29.49	96.0 ± 4.6	66.9 ± 23.2

The results in Table 4.3 demonstrate that part of the particles could still pass through the membranes' nominal pore size even if they are bigger. A reason for this can be addressed to the membrane surface's abrasion caused by the solid particles in the flow. This phenomenon has been found to be particularly enhanced in dead-end filtration when high pressures are applied and when MPs have irregular shapes since they can more easily damage the selective layer of the membranes [11]. In this study, PS particles have higher shape irregularity than PA, but another factor that can influence the membrane abrasion degree is the hardness of the membrane, being the CA the most affected, followed in order by PS and PTFE.

On the other hand, PS particles could present internal cracks due to cryogenic fragmentation [163]. However, SEM images of the two particles, shown in Figure 4.7, revealed that even if PS particles showed some weak spots, in general, they looked more compact than PA particles. Indeed, the latter presented some smaller nanoparticles aggregated on top of bigger particles, which could disaggregate due to the impact with the membrane.

Overall, membrane abrasion and particles breaking down, shown in Figure 4.12, can be highlighted as the main phenomena potentially occurring during MF in dead-end configuration.

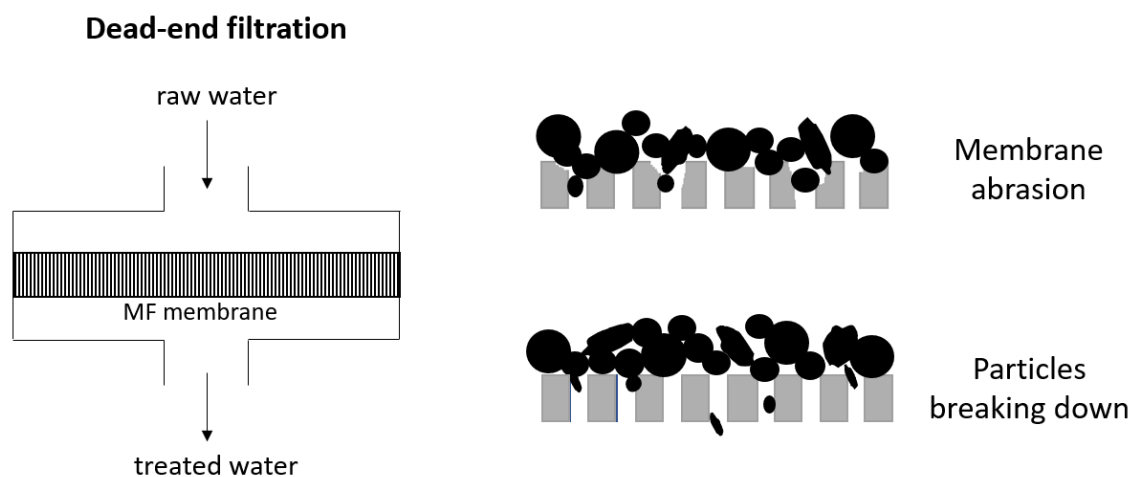


Figure 4.12. Phenomena potentially occurring during the filtration in dead-end configuration.

The water gathered from the PC membrane filtration has a substantial presence of PA particles estimated to be around $127,000 \text{ particles L}^{-1}$ but with an average size smaller than the defined range employed, $15.66 \mu\text{m}$ with a size between $2\text{-}50 \mu\text{m}$. Therefore, while some

smaller particles were part of the particle size distribution in the PA suspension feed, others have been produced due to the impact with the PC membrane. It was also the case that some PA particles bigger than the nominal pore size of the membrane could pass intact. Similarly, with the PS particles, where around 33,000 particles L^{-1} were not retained during the process, with an average diameter of around 37.40 μm , with particles in the range of 10-100 μm . In the case of PS, even bigger particles were able to pass through the membranes' pores, probably caused by a higher degree of membrane abrasion.

For CA filtrations, 27,000 PA particles L^{-1} were estimated unremoved, almost one-fifth of the amount of the PC membrane, with an average diameter of 20.58 μm , varying in the range 7-70 μm . Therefore, slightly bigger in size than the ones from PC filtration. Also, for PS, the smallest number of particles compared to the other membranes were found, 8,000 particles L^{-1} , but the filter did catch the biggest particles in comparison to the other membranes, with an average diameter of 75.51 μm , varying in the entire range of 10-300 μm . As mentioned, from the Shore hardness measure, CA membranes showed the lowest hardness value in a dry environment, which is further amplified in wet environments, making the membrane more prone to abrasion. Hence, the impact with the particles induced less breaking down of the particle but a higher degree of abrasion; therefore, the total unremoved MPs were bigger in size but less in number.

Finally, for PTFE membranes, the unremoved number of particles L^{-1} is similar for both types of MPs, and the sizes were 21.72 μm (7-90 μm) and 29.49 μm (8-220 μm) for PA and PS, respectively. As three times the initial pressure of the one used during PC and CA filtration was employed, the higher TMP was mainly responsible for both membrane abrasion and particles' breaking down in both cases, and the hydrophobicity of the PTFE did not lead to a particular higher mass removal efficiency, and instead, it also showed the worst $NpRE\%$. Figure 4.13 shows the MRE% and $NpRE\%$ of the three membranes graphically.

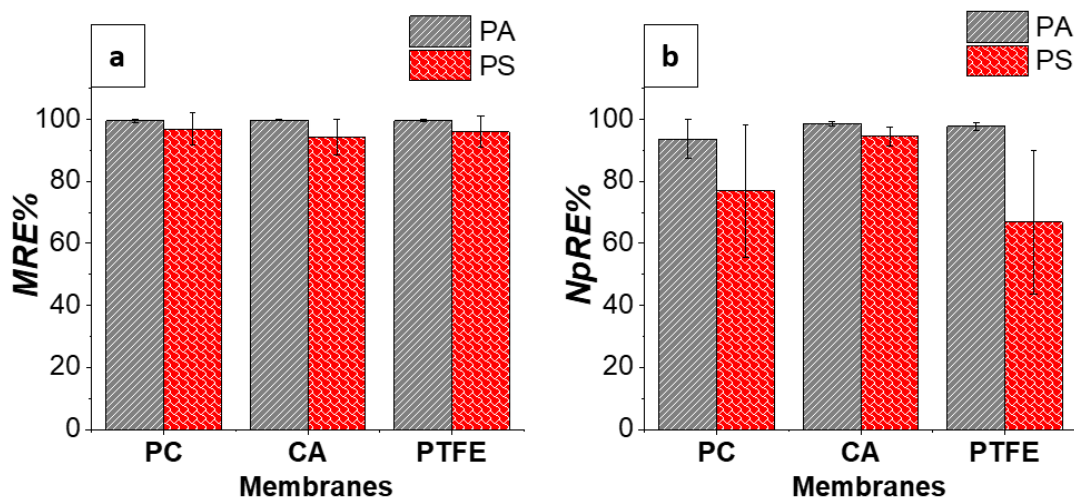


Figure 4.13. Mass removal efficiency ($MRE\%$) and particle number removal efficiency ($NpRE\%$) of each membrane when filtering water with 100 mg L^{-1} of PA and PS.

Overall, the $MRE\%$ results are quite comparable within the experimental error, showing that, in general, MF is a suitable low-cost process to employ for MPs removal. The $NpRE\%$ results showed higher differences, although the experimental error was quite big due to the estimation of the particles both in the inlet and the outlet of the filtration, especially for the PS removal due to the larger and irregular size of the particles, which led to an estimation less precise. Considering only the average values, the particle removal was overall lower than the mass removal, which is the direct result of the breaking down of the particles, according to Simon et al. [68].

4.2.3 Overall performance evaluation

Although high mass removal efficiencies were reached with all membranes for both types of MPs (above 94% for all cases), variable performances were observed as a result of differences in the MPs-membrane interaction, membrane abrasion and breaking down of the particles. PTFE, due to its hydrophobicity, requires a high working pressure, negatively affecting the pumping costs, without a tangible advantage for MPs removal. The PC and CA membranes showed a similar operating condition during PA filtration concerning TMP and flow rate. While during PS filtration, CA allowed much higher water flux. Other than higher

membrane abrasion, a second explanation could be that between the surface of CA and PS particles, higher electrostatic repulsion forces, given by a more negative CA surface compared to PC, helped create a looser cake layer, hence, allowing more flux to pass through.

Figure 4.14 shows the morphologies of the cake layer formed on the membranes after 10 min of filtration with PA and PS particles.

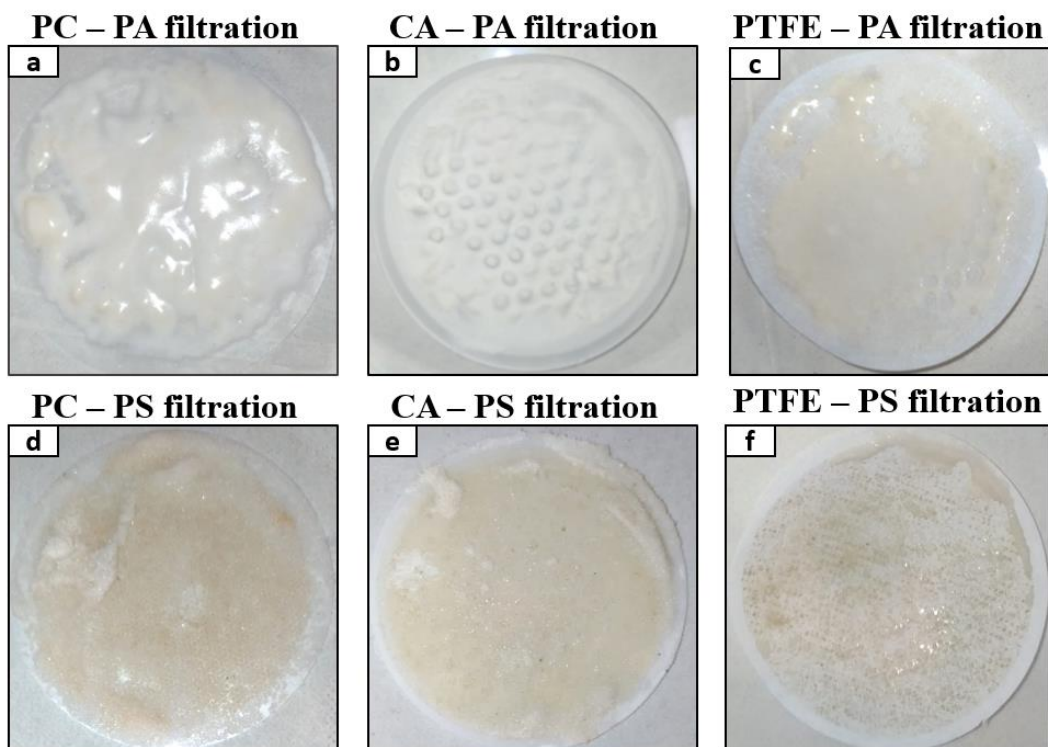


Figure 4.14. Morphology of the cake layer on PC (a and d), CA (b and e), and PTFE (c and f) after PA and PS filtration, respectively. The pictures were captured with a phone camera.

As a direct result of the zeta potential, the cake formed after PA filtration is more compact than the PS one. It is also possible to notice a minor yellowish colour after PS filtration due to small impurities coming from the grinding of the particles. However, no visible difference is shown for the PS filtration with PC and CA membranes.

The choice of membrane properties needs to compromise the risk of producing a higher amount of NPs or allowing the passage of bigger MPs particles. As the increase of NPs is of great concern, CA was evaluated as the optimal membrane material for MPs removal in this system, where the overall performance of TMP, water flux, *MRE%* and *NpRE%* were the best, or among the best, for both particles. Also, CA membranes have both negative surface charge and high hydrophilicity, which are good membrane properties to reduce fouling by MPs and increase the water flux allowed [164]. Finally, CA can be considered more sustainable and environmentally friendly compared to PC and PTFE membranes, which are synthetic polymers that can lead to further plastic contamination when breaking during filtration. In contrast, CA is a bio-based polymer derived from cellulose through acetylation of some of the hydroxyl groups. Although it may take up to 10 years to decompose, it can break down in the natural environment without causing adverse impacts. The biodecomposition of CA depends on environmental conditions, such as temperature, moisture level, and the degree of acetyl substitution [165,166]. It offers the advantage of avoiding contamination from membrane embrittlement. However, the physical and chemical cleaning of CA membranes requires extra attention as it could speed up membrane material degradation, leading to breakage and the release of micro and nano plastics, i.e., secondary pollution of MPs [64,167]. Also, cleaning procedures may increase the dimensions of the membrane's pore size through mechanical stresses and physical flushing, and chemical cleaning may introduce by-products that can be adsorbed onto the hydrophobic surface of the MPs before their release, increasing their hazard [167].

4.3 Membrane fouling by microplastics

Filling the knowledge gap on membrane fouling by MPs can encourage the use of membrane systems and implement the correct and optimised strategy for an efficient and safe operation. Since CA showed the best overall performance, it was chosen for the investigation of the fouling degree under different working conditions. The following section aims to analyse the main successive fouling mechanisms occurring during the filtration of MPs with CA membrane, find a correlation between the fouling kinetics and the operational parameters to evaluate optimal filtration settings and be able to predict membrane fouling degree in other

scenarios, other than assessing the influence of the MPs characteristics on the membrane fouling. It is also worth mentioning that due to the several difference between the two MPs employed, this study could not assess the predominant fouling factor among the MPs' variables, but the valuable results help identify the impact of each variable on the fouling behaviour.

4.3.1 Main successive fouling mechanisms

Filtrations of pure water through the membrane up to 1 bar were first performed as a control experiment to observe if it was implying changes in the permeate flux over the entire filtration run when higher pressures are employed. However, several pressures up to 1 bar were tried, and no compaction occurred (Figure 4.15).

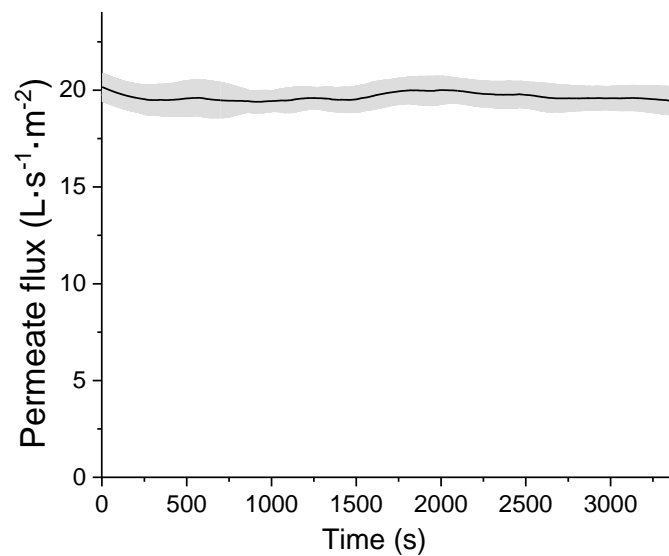


Figure 4.15. Studies on membrane compaction. No significant changes in water flux were observed after 1 h of distilled water filtration. The figure represents the filtration at 0.3 bar.

To achieve the first objective, identifying the successive prevailing mechanisms occurring during the filtration runs, $V(t)$ was evaluated from the flow meter data set. Post-processing methods have been used to attenuate the noise of the experimental data in agreement with the procedure followed by Grenier et al. [59], and the finite difference method was employed to derive the parameters d^2t/dV^2 and dt/dV . Finally, n was evaluated to identify the main

controlling fouling mechanisms as described by Hermia's model in Eq. (3.5), while the kinetic constants were assessed by the corresponding equations in Table 3.1. Figure 4.16 shows the plot of cumulative permeate volume versus time and the d^2t/dV^2 versus dt/dV plot for the evaluation of the n -mechanism for PA and PS filtrations.

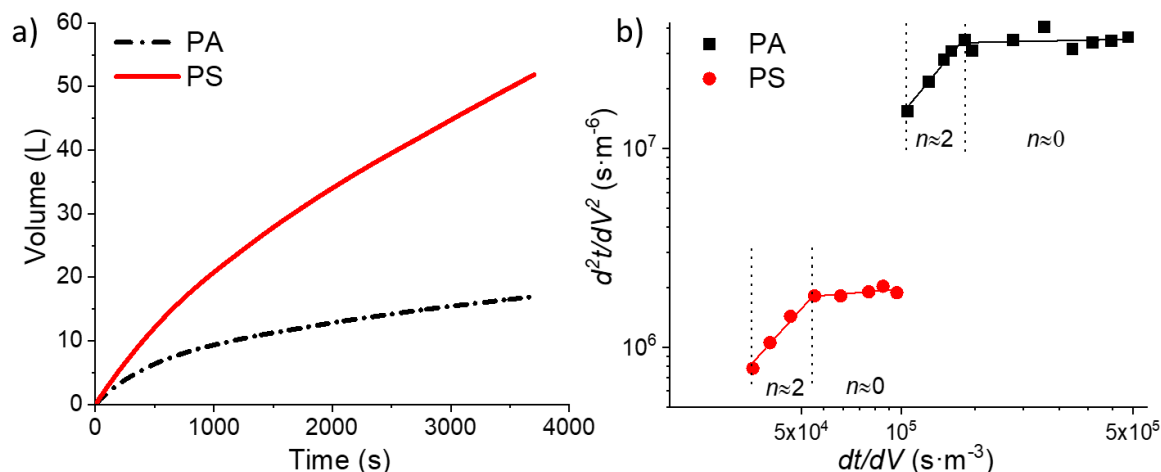


Figure 4.16. Plot of V (L) versus t (s) in black dash-dotted line for PA and in red straight line for PS (a). Plot of d^2t/dV^2 versus dt/dV for the determination of n -mechanism, black squares for PA and red dots for PS (b). Both curves refer to a representative curve at 10 mg L^{-1} and 0.3 bar .

From the d^2t/dV^2 versus dt/dV plot, considering the correlation given from Hermia's equation, it was possible to evaluate n directly. In Figure 4.16b only some experimental values are shown to highlight the two trends and facilitate the identification of the main fouling mechanisms. According to the results, the leading mechanisms were complete pore blocking (corresponding to $n \approx 2$) followed by cake formation ($n \approx 0$).

The findings are in agreement with the case where $d_{pore} \leq d_{particle}$ in Table 3.2, where the effect of complete pore coverage probably obscured the intermediate pore blocking. The internal pore blocking was not expected to occur since the membrane pore diameter was smaller than the particles size. However, since the case $d_{pore} \ll d_{particle}$ could also represent the working conditions, comparison studies with only cake formation as the controlling mechanism were also performed. Figure 4.17 represents the experimental data by fitting *model 1*, only cake formation considered through the entire run, or *model 2*, the combination

of complete pore blocking followed by cake formation. The experimental curves shown correspond to the averaged value when 10 mg L^{-1} at 0.3 bar of MPs are filtered.

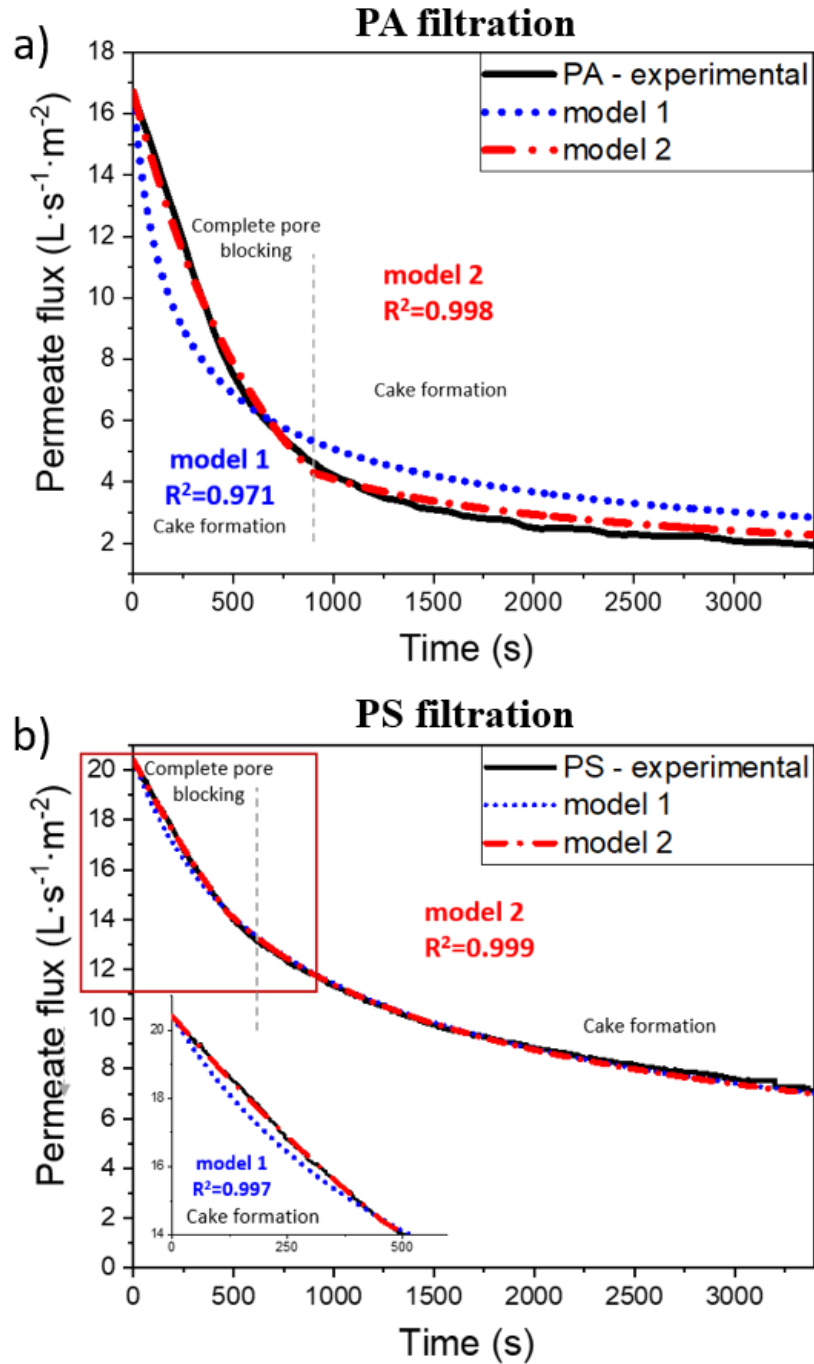


Figure 4.17. Comparison between *model 1* (when only cake formation occurs) and *model 2* (complete pore blocking followed by cake formation). The experimental curve represents the averaged value for PA filtrations (a) and PS filtration (b) at 10 mg L^{-1} and 0.3 bar.

In both cases, *model 2* fitted the data better and led to a higher coefficient of determination, R^2 . However, it was possible to notice that the difference between the models was more pronounced when higher fouling occurred; therefore, in Figure 4.17, the differences are more pronounced for PA filtration.

For the kinetic analysis, the corresponding kinetic constants for complete pore blocking and cake layer formation K_b and K_c were evaluated by fitting the equations in Table 3.1 and by minimising the sum of squared errors (SSEs) between the predicted and experimental curves using Microsoft Excel solver tool. Finally, an extra equation was added to ensure continuity passing from one mechanism to the other. K_b and K_c were studied for the two types of MPs, PA and PS, varying MPs load and operating TMP. The results are shown as an averaged value with the standard deviation error corresponding to at least five repetitions obtained for each condition.

4.3.2 Kinetic analysis varying MPs load

Figure 4.18 shows the permeate flux decline during constant pressure filtrations at different MPs loads.

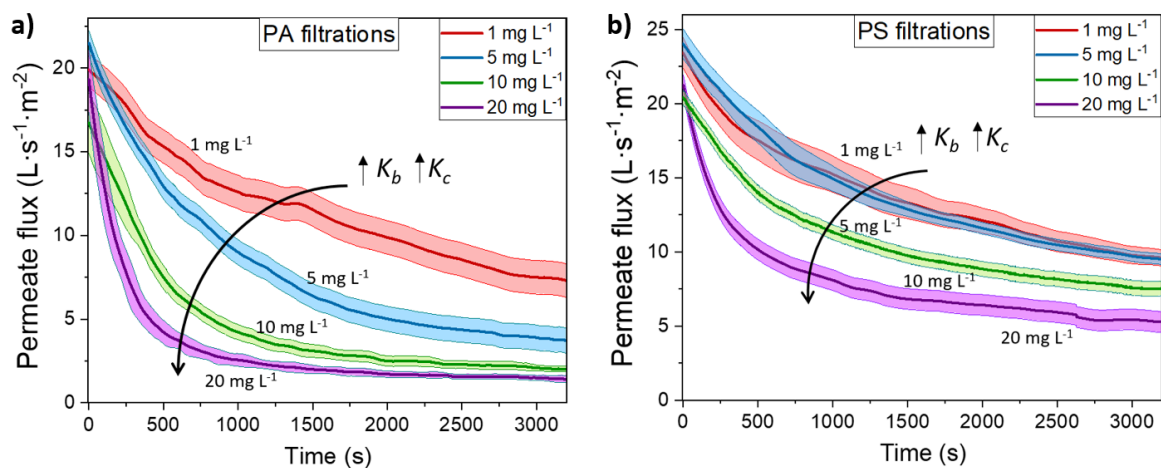


Figure 4.18. Permeate flux decline after 1 h of PA (a) and PS (b) filtrations at different MPs loads. The solid line corresponds to the average of the replicates, while the colour band around it indicates the error experienced under that operating condition.

The experimental curves were then fitted with *model 2*, which gives the results of K_b and K_c for PA and PS filtration at different MPs loads, shown in Table 4.4. To study the goodness

of the model, the coefficient of determination, R^2 , was also evaluated. Since, in all cases, R^2 was greater than 0.98, we can consider that the selected model (complete pore blocking followed by cake formation) satisfactorily represented the experimental dataset.

Table 4.4. Averaged values for complete pore blocking, K_b , cake formation, K_c , and the coefficient of determination, R^2 applied between the model and the experimental data for PA and PS filtration at different feed concentrations.

Concentration (mg L ⁻¹)	K_b (s ⁻¹)	K_c (s m ⁻²)	R^2	K_b (s ⁻¹)	K_c (s m ⁻²)	R^2
	PA	PA		PS	PS	
1	$(5.1 \pm 2.3) \cdot 10^{-4}$	2.8 ± 1.2	0.982 ± 0.016	$(7.1 \pm 3.8) \cdot 10^{-4}$	1.6 ± 0.5	0.984 ± 0.011
5	$(1.1 \pm 0.4) \cdot 10^{-3}$	12.7 ± 6.8	0.990 ± 0.008	$(5.2 \pm 1.2) \cdot 10^{-4}$	1.6 ± 0.4	0.992 ± 0.005
10	$(1.5 \pm 0.4) \cdot 10^{-3}$	30.1 ± 1.4	0.988 ± 0.008	$(7.9 \pm 1.5) \cdot 10^{-4}$	3.0 ± 0.7	0.990 ± 0.006
20	$(3.6 \pm 0.9) \cdot 10^{-3}$	80.7 ± 21.7	0.990 ± 0.005	$(2.1 \pm 0.3) \cdot 10^{-3}$	8.5 ± 1.4	0.992 ± 0.003

Figure 4.19 shows the correlation between the kinetic constants for complete pore blocking and the blocked surface area parameter with the suspension MPs type and dosage in water.

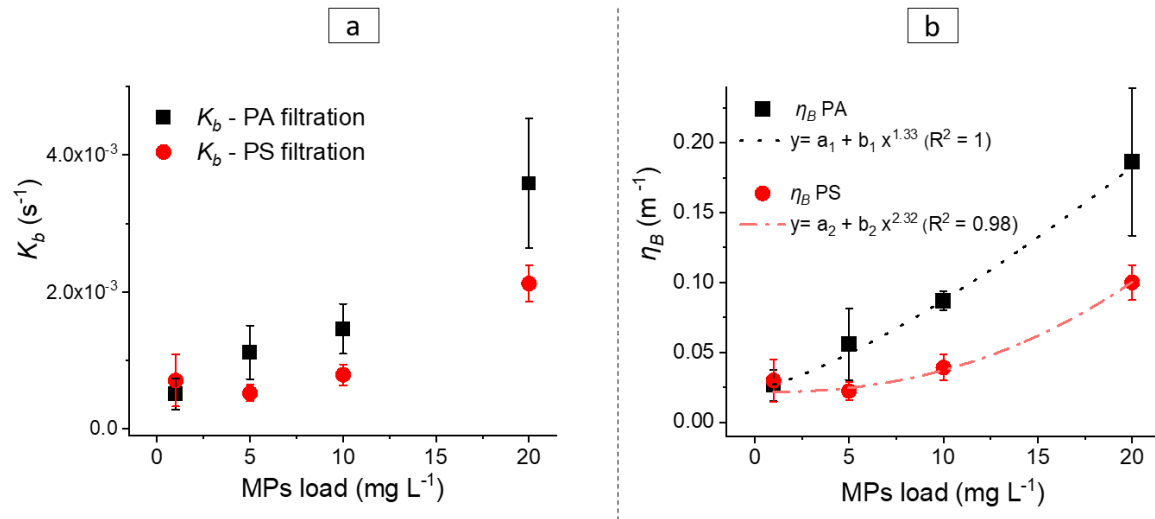


Figure 4.19. K_b (a) and η_B (b) for PA (black squares) and PS (red dots) at variable MPs load, both reported on the same scale.

The blocking parameter η_B was chosen for discussion since it also considered the initial flux, according to Eq. (3.14). On the other hand, Figure 4.20 shows the kinetic constants for cake formation in the same scale and in two scales as a function of the suspension MPs type and the dosage. Since η_C is a function of two constants, TMP fixed at 0.3 bar and the fluid viscosity, the pattern was the same as K_C and, therefore, not reported.

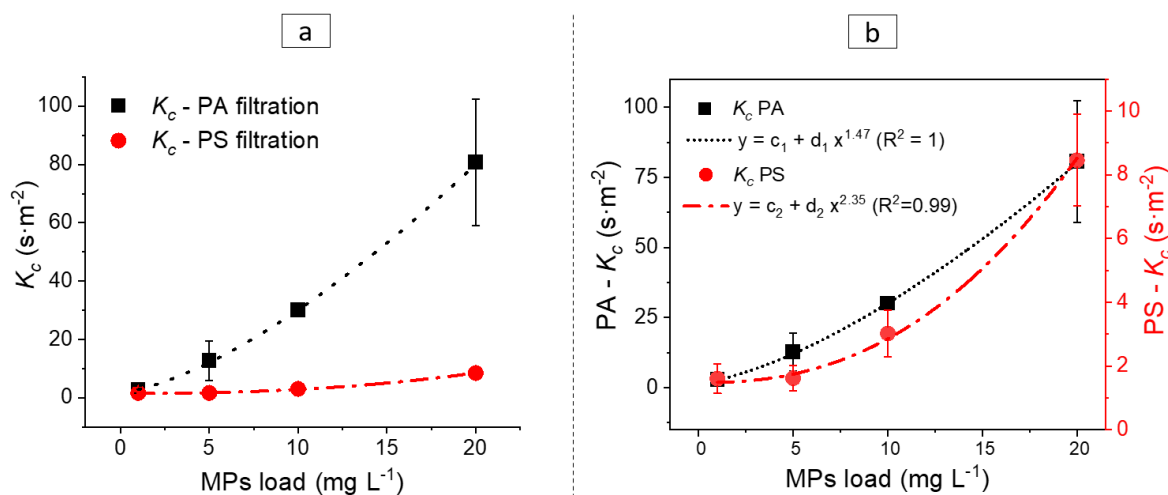


Figure 4.20. K_C as a function of MPs load for PA (black squares) and PS (red dots) in the same scale (a) and a magnification of the two trends on two scales (b).

The blocking parameter η_B and the kinetic constant K_C are strongly correlated with the MPs load. The results showed a power-law relationship between fouling and MPs concentration, with a stronger correlation observed for PS ($C^{-2.3}$) compared to PA ($C^{-1.4}$). At low MPs dosages (1-5 mg L⁻¹), fouling induced by PS did not change significantly but increased critically at higher MPs load, whereas PA-induced fouling showed noticeable differences at low dosages and increased less critically than PS at higher dosages.

Therefore, the overall increase in MPs concentration induces higher fouling than a linear correlation between the two. The power-law relationship can be attributed to an increase in steric obstacles at the pore entrance and to an intensification of interactions in the presence of a higher number of particles. This also explains the higher dependence on MPs load in the case of PS particles since they have a greater averaged diameter compared to PA particles.

Besides the trend, the values of η_B and K_c are much higher after PA filtration than PS, indicating a higher level of fouling in the former. This suggests that there is a greater level of interaction between the MPs particles and the membrane in the case of PA, which lead to higher fouling. Indeed, a denser cake layer was formed due to the hydrophobic interaction among the PA particles. In contrast, PS particles are charged, which could lead to intermolecular repulsion between the particles and the membrane, both of which are negatively charged. This repulsion may increase the cake layer's porosity and prevent the formation of a thick and compact layer.

Figure 4.21 shows the cake appearance only for the chosen CA membrane after 1 h of MPs filtration with an initial concentration of 10 mg L^{-1} and working at 0.3 bar.

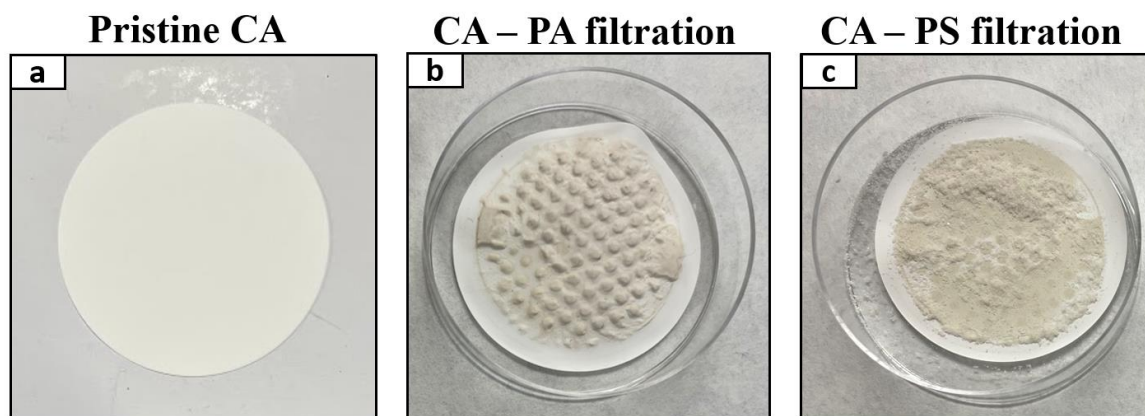


Figure 4.21. Images of the CA pristine membrane (a) and after 1 h filtration of 10 mg L^{-1} of PA (b) and PS (c) particles at 0.3 bar.

In the case of PA filtration, the cake layer formed a cohesive and dense structure on the membrane surface, while for PS filtration, the particles showed a tendency to detach more readily from the membrane.

Additionally, the size distribution and shape of the particles might also play a significant role in the extent of fouling. Two previous studies by Li et al. [71,168] found that MPs in the range size of $1.0\text{-}2.7 \mu\text{m}$ caused more fouling due to their ability to act as binders and form a denser layer. It has also been reported that non-spherical particles induce less fouling as they allow for the formation of a looser cake layer due to the varied particle orientations [74].

Therefore, the smaller size distribution of PA particles may have contributed to the compactness of the cake layer, while the irregular shapes of PS particles have helped its looseness. Furthermore, as already discussed, the sharp-cornered PS particles coming from cryogenic milling could have also caused a higher degree of membrane abrasion. Although membrane abrasion is undesirable not to favour MPs secondary contamination, it leads to larger pore diameters and higher membrane porosity, allowing more flux to pass through. Finally, the major interactions discussed at the interface MPs-CA membrane are summarised in Figure 4.22.

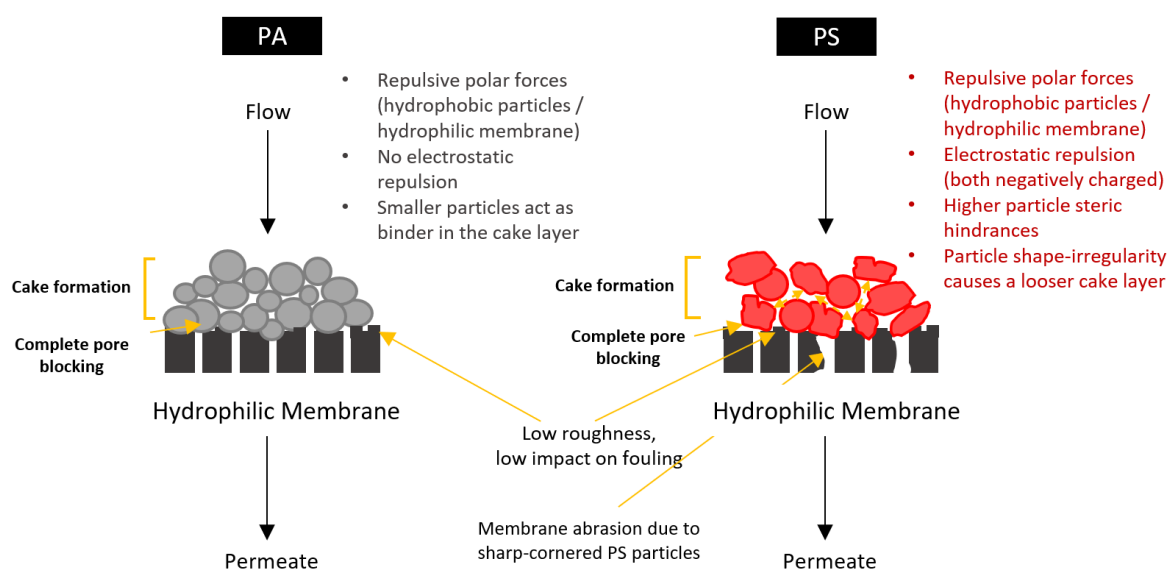


Figure 4.22. Main interactions occurring between MPs and MPs-membrane and affecting the fouling kinetic.

4.3.3 Kinetic analysis varying the working pressure

Figure 4.23 shows the permeate flux decline at different transmembrane working pressure which was kept constant during the entire filtration.

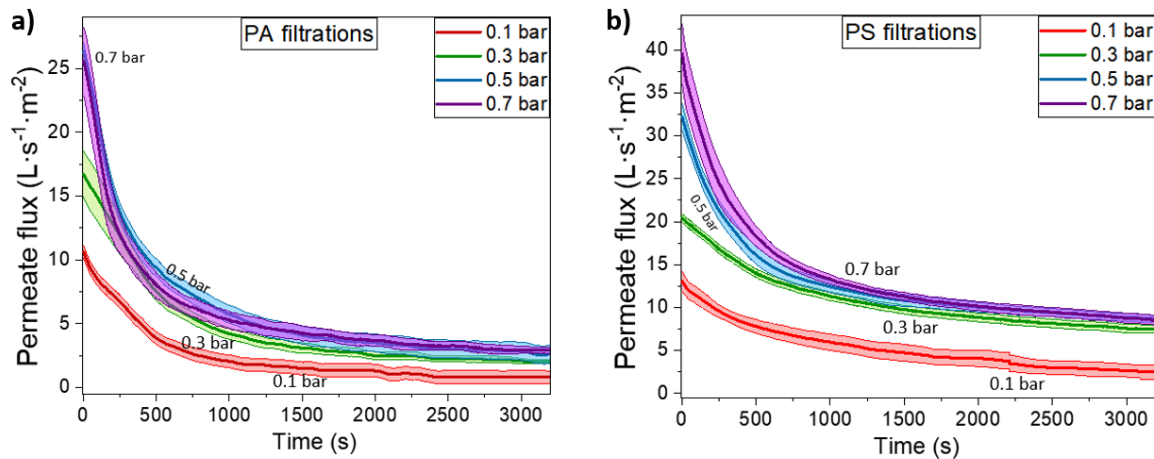


Figure 4.23. Permeate flux decline after 1 h of PA (a) and PS (b) filtrations at different working TMP. The solid line corresponds to the average of the replicates, while the colour band around it indicates the error experienced under that operating condition.

The experimental curves were then analysed and fitted with *model 2*. The resulting K_b and K_c for PA and PS filtration varying TMP from 0.1 bar up to 0.7 bar are shown in Table 4.5.

Table 4.5. Averaged values for complete pore blocking, K_b , cake formation, K_c , and the coefficient of determination, R^2 applied between the model and the experimental data for PA and PS filtration at different TMP.

TMP (bar)	K_b (s^{-1})	K_c ($s\ m^{-2}$)	R^2	K_b (s^{-1})	K_c ($s\ m^{-2}$)	R^2
	PA	PA		PS	PS	
0.1	$(2.1 \pm 0.5) \cdot 10^{-3}$	100.8 ± 17.2	0.985 ± 0.014	$(1.1 \pm 0.2) \cdot 10^{-3}$	10.4 ± 1.5	0.980 ± 0.011
0.3	$(1.5 \pm 0.4) \cdot 10^{-3}$	30.1 ± 1.4	0.988 ± 0.008	$(7.9 \pm 1.5) \cdot 10^{-4}$	3.0 ± 0.7	0.990 ± 0.006
0.5	$(2.5 \pm 1.0) \cdot 10^{-3}$	16.9 ± 7.1	0.994 ± 0.004	$(1.5 \pm 0.1) \cdot 10^{-3}$	3.0 ± 0.4	0.991 ± 0.006
0.7	$(3.3 \pm 1.2) \cdot 10^{-3}$	16.7 ± 5.9	0.997 ± 0.001	$(2.1 \pm 0.5) \cdot 10^{-3}$	2.8 ± 0.6	0.995 ± 0.003

Also in this case, R^2 was greater than 0.98 under all circumstances, and Figure 4.24 and Figure 4.25 show the correlation between the kinetic constants and the parameter η_B and η_C with the MPs type and the working TMP. This time, the cake specific resistance η_C , which

is dependent on the pressure drop as per Eq. (3.16), was also reported as it shows a distinct pattern compared to K_c .

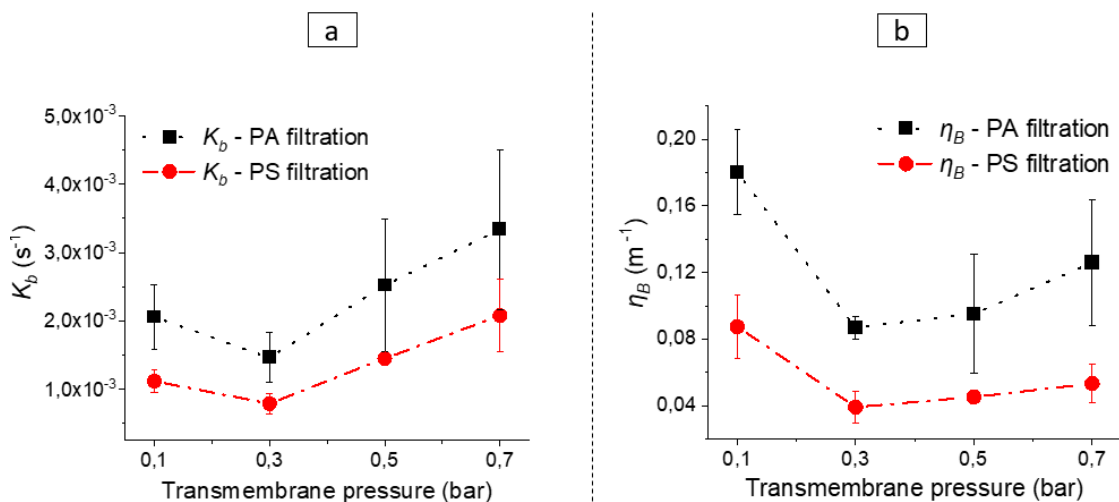


Figure 4.24. K_b (a) and η_B (b) for PA (black squares) and PS (red dots) as a function of TMP, represented on the same scale.

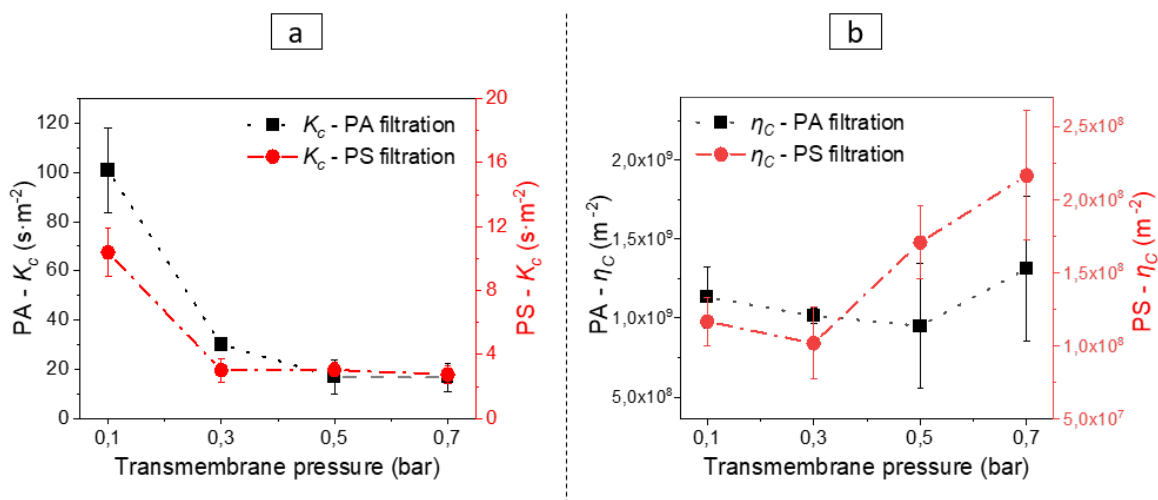


Figure 4.25. K_c (a) and η_C (b) for PA (black squares) and PS (red dots) as a function of TMP, represented on two different scales to appreciate the trends.

By increasing the TMP, the K_c values decreased until they reached a constant value within the experimental error. This occurred at a threshold pressure that corresponded to a value between 0.3 and 0.5 bar for PA and 0.3 bar for PS filtration.

Similarly, K_b , η_C , and η_B showed a minimum in correspondence of the same TMP value. At lower pressures, the particles have a higher tendency to stick to the membrane. However, as the pressure increases to the threshold value, the shear stress at the pore entrance becomes sufficient to dislodge the particles captured at the membrane surface pore or the cake layer. This process leads to the liberation of some previously obstructed pores and results in a decrease in the cake's density, ultimately resulting in weaker fouling [136]. The shear stress is an important factor in the fouling of membranes, as it influences the three main resistances: $R_{m,0}$, $R_{m,B}$, and R_C , and is mathematically linked to the lift force that can displace the particle from the membrane surface [169]. It is often manipulated to regulate and mitigate membrane fouling, although the properties of the foulants play a crucial role in this potential mitigation. Li et al. [71] have demonstrated in their study that increasing the wall shear stresses by applying rotation or helical rotation is an effective fouling alleviator for PS particles. Alternatively, Enfrin et al. [170,171] showed the efficacy of periodic gas scouring, which generates higher shear forces with the gas bubbles, in reducing the fouling by PE nano/microparticles and PET nanofibers on hydrophobic PSF membranes.

Nevertheless, working at higher TMP and higher shear stresses is not always optimal as it would lead to increased operational costs and energy consumption without any significant advantages for membrane fouling. In theory, for rigid foulants, the stronger the shear stress, the weaker the fouling [169]. However, MPs cannot be considered rigid foulants since they are susceptible to mechanical impacts during filtration [163], which causes their breakage. Also, an increase in TMP leads to higher membrane abrasion and particle breakup. The former results in larger membrane pores and reduced MPs removal, whereas the latter leads to higher NPs contamination and can cause more severe fouling due to their interstitial effects [169,172]. As a result, the best working conditions are those corresponding to the threshold pressure value, where kinetic constants reach their minimum or constant value. To evaluate the differences among the MPs types, the wall shear stress occurring during the filtrations at the beginning of complete pore blocking, $\tau_{w,0}$, and at the transition from complete pore blocking to cake formation $\tau_{w,b \rightarrow c}$. were evaluated according to Eq. (4.1).

$$\tau_w = -\mu \left. \frac{du}{dr} \right|_{r=R} = 4\mu \frac{\bar{u}}{R} = 8\mu \frac{\bar{u}}{d_{pore}} \quad \text{Eq. (4.1)}$$

Where u is the flux velocity and r is the radius of the membrane pore.

Furthermore, also the Reynolds number, Eq. (4.2), within the pores was calculated to determine whether the flow was in the laminar ($Re < 2300$), transient ($2300 < Re < 4000$) or turbulent ($Re > 4000$) range.

$$Re = \frac{\rho \bar{u} D}{\mu} \quad \text{Eq. (4.2)}$$

Where D is the hydraulic diameter, in this case corresponding to the pore size of the membrane where the flow channels ($d_{pore} = 5\mu\text{m} = 5 \times 10^{-6} \text{ m}$), \bar{u} is the mean velocity of the fluid in m s^{-1} , ρ is the density of the fluid (water density = 997 kg m^{-3}), and μ is the dynamic viscosity of the fluid (water viscosity = $0.00089 \text{ kg m}^{-1} \text{ s}^{-1}$).

Table 4.6 and Table 4.7 show the permeate flux, the flow velocity, the Reynolds number, and the wall shear stress at the beginning of the filtration (0) and at the transition from complete pore blocking to cake formation (b→c) for PA and PS, respectively.

Table 4.6. Permeate flux, flow velocity, Reynolds number, and wall shear stress after PA filtration at the beginning of the run, J_0 , u_0 , Re_0 , τ_0 , and at the transition from complete pore blocking to cake formation $J_{b \rightarrow c}$, $u_{b \rightarrow c}$, $Re_{b \rightarrow c}$, $\tau_{wb \rightarrow c}$.

TMP (bar)	J_0 ($\text{L s}^{-1} \text{m}^{-2}$)	u_0 (m s^{-1})	$J_{b \rightarrow c}$ ($\text{L s}^{-1} \text{m}^{-2}$)	$u_{b \rightarrow c}$ (m s^{-1})	Re_0	$Re_{b \rightarrow c}$	$\tau_{w,0}$ (Pa)	$\tau_{w,b \rightarrow c}$ (Pa)
0.1	11.35 ± 2.67	0.011	2.67 ± 0.49	0.003	0.064	0.015	16.16	3.81
0.3	16.72 ± 3.60	0.017	4.32 ± 0.65	0.004	0.094	0.024	23.81	6.15
0.5	26.33 ± 0.50	0.026	7.91 ± 1.27	0.008	0.147	0.044	37.50	11.26
0.7	25.97 ± 2.53	0.026	9.47 ± 0.79	0.009	0.145	0.053	36.98	13.49

Table 4.7. Permeate flux, flow velocity, Reynolds number, and wall shear stress after PS filtration at the beginning of the run, J_0 , u_0 , Re_0 , τ_0 , and at the transition from complete pore blocking to cake formation $J_{b \rightarrow c}$, $u_{b \rightarrow c}$, $Re_{b \rightarrow c}$, $\tau_{wb \rightarrow c}$.

TMP (bar)	J_0 (L s ⁻¹ m ⁻²)	u_0 (m s ⁻¹)	$J_{b \rightarrow c}$ (L s ⁻¹ m ⁻²)	$u_{b \rightarrow c}$ (m s ⁻¹)	Re_0	$Re_{b \rightarrow c}$	$\tau_{w,0}$ (Pa)	$\tau_{w,b \rightarrow c}$ (Pa)
0.1	13.06 ± 1.79	0.013	8.35 ± 1.18	0.008	0.073	0.047	18.60	11.88
0.3	20.42 ± 1.66	0.020	13.62 ± 1.93	0.014	0.114	0.076	29.08	19.39
0.5	32.20 ± 2.35	0.032	18.34 ± 3.10	0.018	0.180	0.103	45.85	26.11
0.7	39.55 ± 6.95	0.040	21.54 ± 4.08	0.022	0.222	0.121	56.32	30.67

In Table 4.6, it is noted that J_0 at 0.7 bar was curiously similar to the value at 0.5 bar. This observation can be justified by the fact that when the pressure approached 0.7 bar, the high fouling rate had already started to lower the flux allowed to pass through the membrane.

As the flux is higher during PS filtration, higher shear stress values are typically observed for PS particles compared to PA particles. Additionally, the differences between the shear stress values are greater when comparing the values at the transition of the mechanisms ($\tau_{w,b \rightarrow c}$) relative to the beginning of the filtration ($\tau_{w,0}$). This phenomenon is responsible for the fact that K_b and η_B could be represented on the same scale, while K_c and η_C values differed by one order of magnitude between the two MPs and thus represented on two scales. These observations suggest that cake formation is the mechanism that is most strongly influenced by the type of particle suspension.

Finally, Figure 4.26 summarises the main forces acting on the particles at the pore entrance during the filtration run.

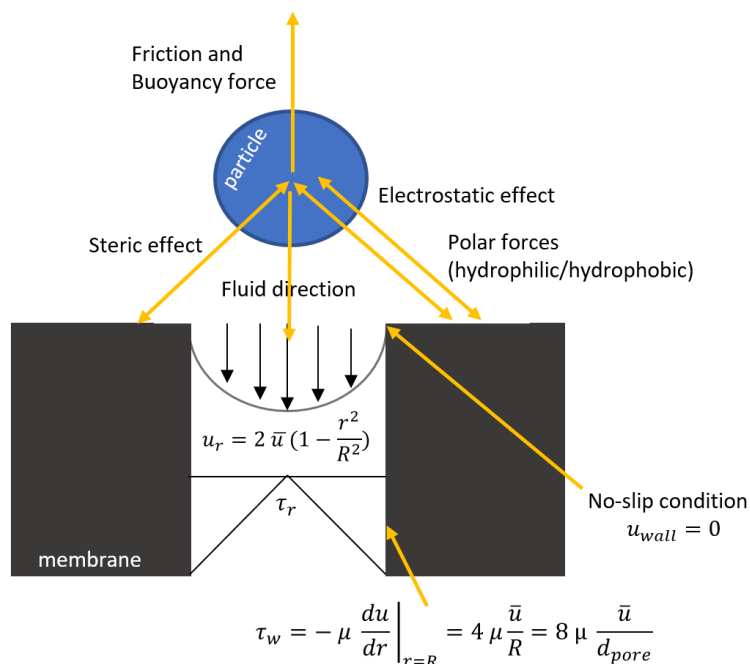


Figure 4.26. Schematic forces acting on an MP particle fouling during dead-end filtration.

4.3.4 Impact of MPs on the membrane fouling

The impact of MPs on the membrane surface was evaluated by conducting water contact angle and profilometry analysis after the MPs filtration to investigate changes in the membrane surface properties during fouling.

In the case of a pristine CA membrane, the water drop was found to spread during the contact moment, indicating complete wetting. However, after PA and PS filtration, the water contact angle greatly increased above 90° , as shown in Figure 4.27, with a spherical shape on top of the MPs cake layer, indicating incomplete wetting.

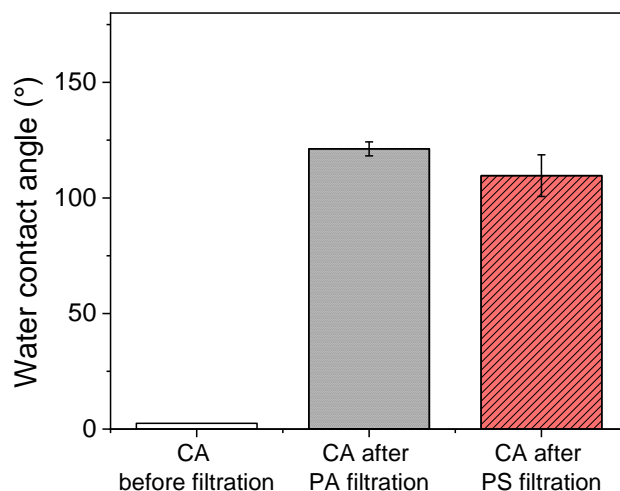


Figure 4.27. WCA measured before and after the filtration of MPs (10 mg L^{-1} at 0.3 bar).

As shown in Figure 4.28, profilometry also underwent a significant increase after 1 h of filtration. Notably, the increase was more pronounced after PA particles, which exhibited higher fouling tendencies. It is plausible that the gradual increase in hydrophobicity and roughness of the fouled membrane surface during the filtration process could have intensified the MPs-membrane surface interactions, thus contributing to further fouling.

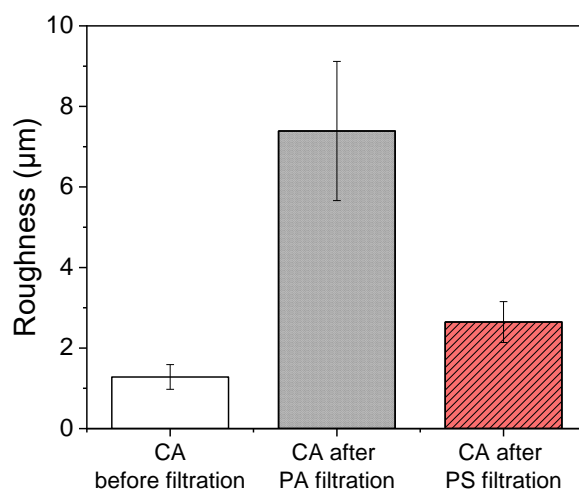


Figure 4.28. Profilometry measured before and after the filtration of MPs (10 mg L^{-1} at 0.3 bar).

However, it should be noted that the locations where large PS particles were present in the cake layer were excluded from the final roughness value calculation, as shown in Figure 4.29, due to their considerable contribution to the local roughness, which was substantially greater than the representative value.

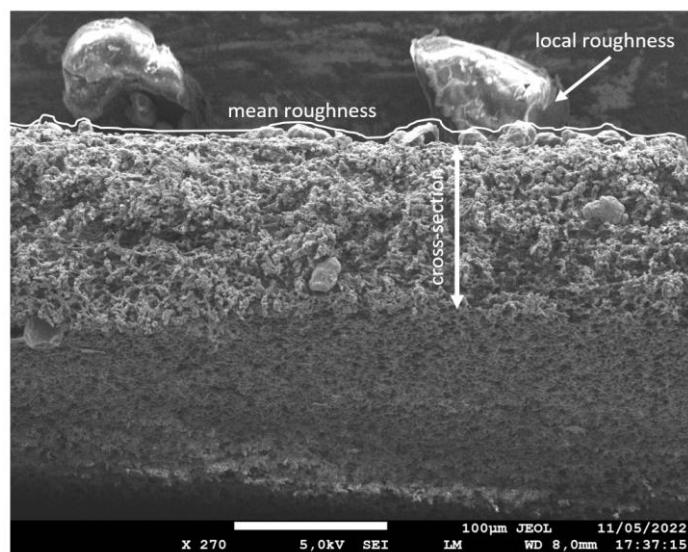


Figure 4.29. SEM image of the CA membrane after PS filtration: details of mean roughness evaluation. Unit distance of 100 μm .

While the membrane's limited roughness alone did not generate ridges and valleys to capture particles, the roughness of the cake layer plausibly created favourable voids for other particles to settle into.

Finally, SEM images were captured before and after the filtrations to investigate the abrasion degree of the CA membrane surface resulting from the exposure to regular-shaped PA particles and irregular-shaped PS particles.

First of all, Figure 4.30 shows the pristine CA membrane. There are small pellets on the surface, which probably come from the manufacturing process and can be easily distinguished, while from the cross-section image, the membrane reveals a thin dense layer of smaller pore size which makes the material selective, and under it, a highly porous structure with open channels to increase the filtration surface area and the permeate flux.

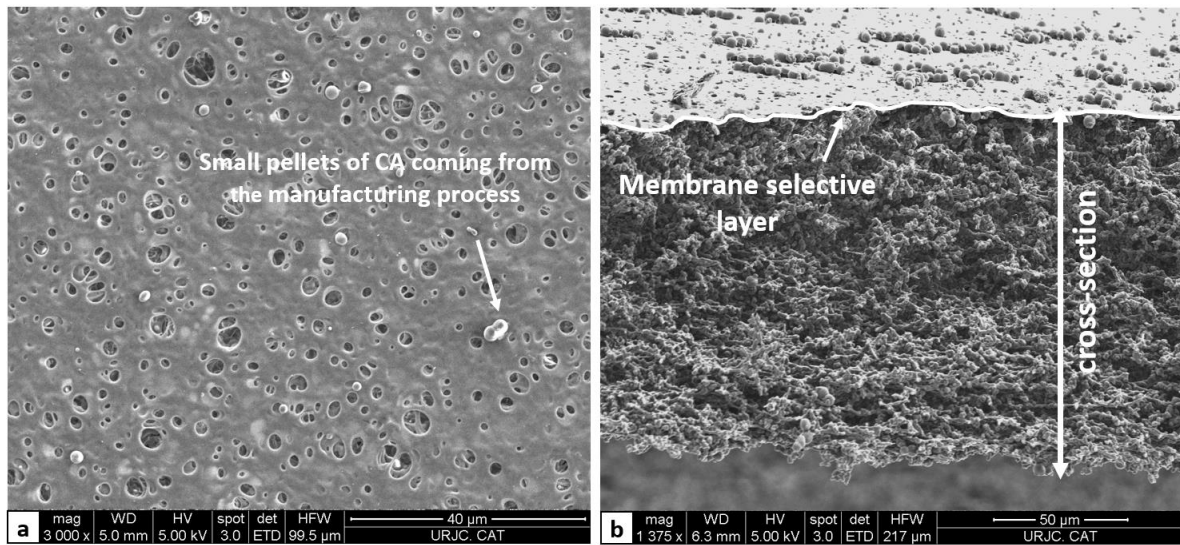


Figure 4.30. SEM images of the CA membrane surface (a) with unit distance of 40 μm and cross-section (b) with unit distance of 50 μm .

Figure 4.31 depicts SEM images after PA and PS filtration, where Figure 4.31a and c exhibit an identical magnification of 1000x, while Figure 4.31b and d differ slightly in magnification to provide an optimal representation of the cross-section, at 600x and 500x, respectively.

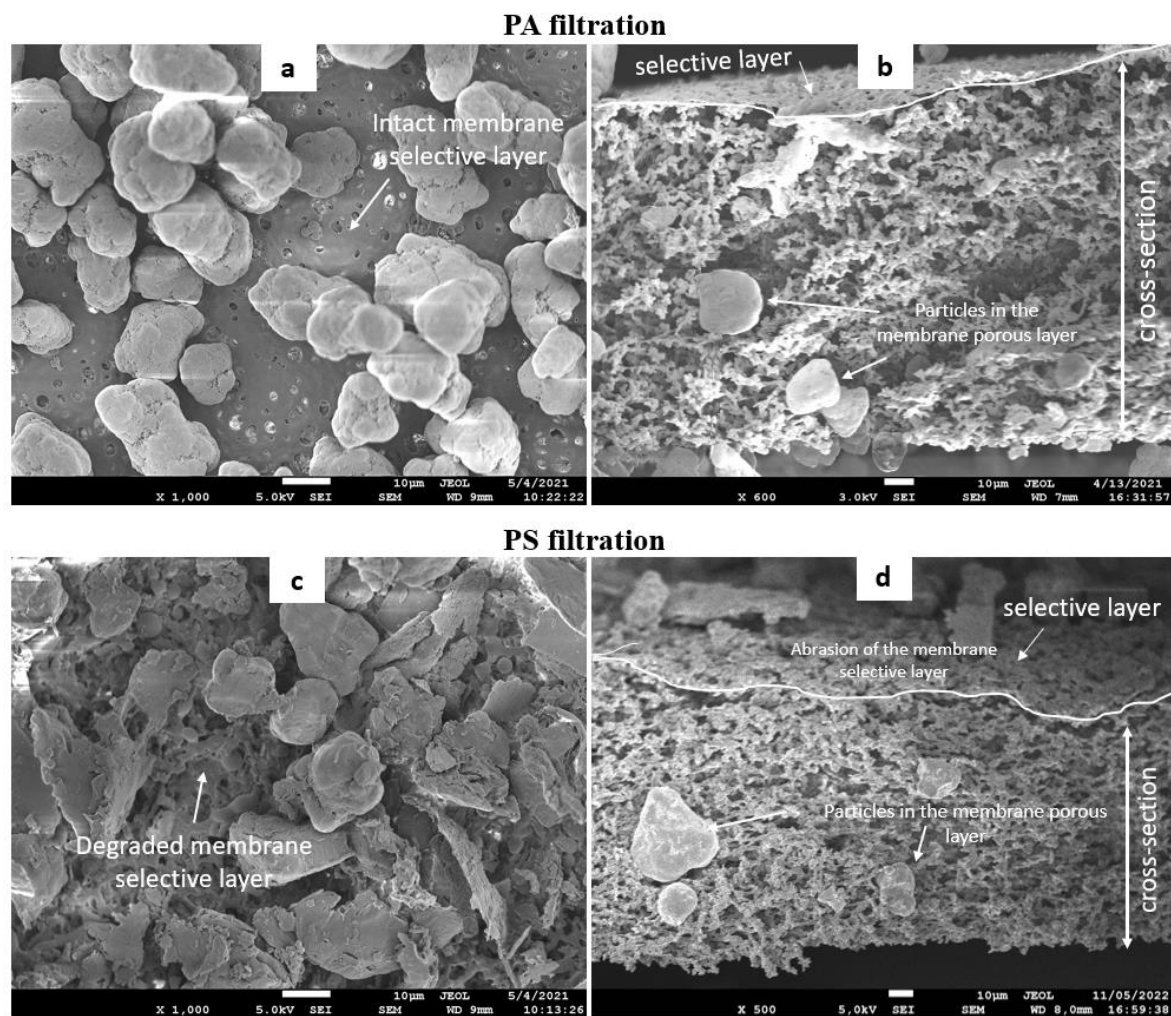


Figure 4.31. SEM images of the membrane surface (a and c after PA and PS filtration) and cross-section (b and d after PA and PS filtration). All images display a unit distance of 10 µm.

In the case of PS filtration, the sharp-cornered particles caused damage to the thin selective layer of the pristine membrane, thereby reducing the blockage of particles above the membrane's nominal pore size. On the contrary, the abrasion that occurred after PA particle filtration was significantly less severe, as the selective layer remained easily identifiable in all images. Thus, membrane abrasion cannot be neglected when filtering highly irregular and spiky particles and should be considered when implementing these membranes.

However, cross-sectional images in both cases revealed the presence of trapped MPs in the porous structure of the membrane. On the one hand, this is an indicator that MPs are capable of passing through the selective layer. On the other hand, it suggests that the porous

structures beneath the selective layer are capable of retaining MPs, which explains the high removal efficiency even in the case of PS filtration, where the selective layer is mostly gone.

Some final reflections are made regarding strategies for reducing fouling but at the same time limiting secondary MPs contamination and loss in removal efficiencies. It has been reported that backwash and other physical and chemical cleaning processes are a good solution to reduce fouling [164,170]; however, they dilute and reintroduce the MPs back into the water, not reducing the overall problem. They can also weaken the membrane surface allowing secondary MPs contamination, as observed by LaRue et al. [52], who reported visible cracks in the cake layer of backwashed membranes, which could have also caused damage to the membrane underneath. Furthermore, the use of chemical agents in conjunction with these processes may cause further abrasion or weakening of the membrane, leading to the release of MPs/NPs contaminated with these chemicals into the water. Therefore, direct membrane replacement should be considered when the membrane is cost-effective, available, and does not cause further environmental pollution. By replacing the membrane, secondary MPs contamination is limited since the membrane is not further damaged by physical and chemical stresses, but also MPs are not diluted or reintroduced into the environment. From the membrane replaced, MPs could then be recovered, recycled, and reused for further purposes. For instance, a possible approach is reheating and extruding them into new garments or degrading them into carbon dioxide and water for carbon extraction [173]. Nevertheless, replacing the membrane may only be a feasible solution for small-scale drinking water treatment plants or households where the treated water does not create excessive fouling, thus reducing the need for frequent membrane replacement. A more realistic scenario of CA membrane working time shows that every hour of 10 mg L^{-1} of MPs filtration corresponds to an underestimated time of 42 days of operation in water contaminated with $10 \text{ } \mu\text{g L}^{-1}$ that can be considered acceptable for membrane replacement.

4.4 UV-B and UV-C LEDs driven advanced oxidation processes

While from one side, it was important to find an efficient and low-cost solution for MPs removal, other CECs, together with microbiological contamination, would remain mostly untreated with the methodology proposed for the MPs. Therefore, other solutions must be coupled to the membrane system to ensure a higher quality of treated water from different pollutants. UV-C photolysis alone or coupled with oxidation processes was chosen, as it has proven to be an emerging effective technology for many CECs, and it could potentially also help the removal of unremoved NPs. However, the major drawback of these processes is the use of LP mercury lamps. UV-B and UV-C LEDs have the potential to overcome the limits of mercury lamps, allowing design flexibility, together with instant on-off, intensity regulation, and wavelength selection.

DCF was selected as a model CEC, given the worry for this compound and inclusion in the first EU *watch list*. The study was focused on the evaluation of its removal under different wavelengths and lamps intensity. Dual wavelength was also investigated since it has not been significantly examined for the degradation of the contaminants, and it is argued whether it leads to synergy or not. Given the worries of possible by-products due to incomplete treatment, mineralisation and phytotoxicity analyses were also carried out. On the other hand, this work did not assess the effects of varying initial DCF concentration, pH, scavengers and other organic matter presence, or increase of the oxidant dosage, as these factors have already been covered in other studies [93,174–176].

This part of the work was conducted in ProPhotonix, the manufacturer of the LED lamps, in collaboration with University College Cork.

4.4.1 UV-B and UV-C LED lamps characterisation

First of all, each lamp was characterised by a horizontal and vertical profile through the ILT radiometer, as shown in Figure 4.32.

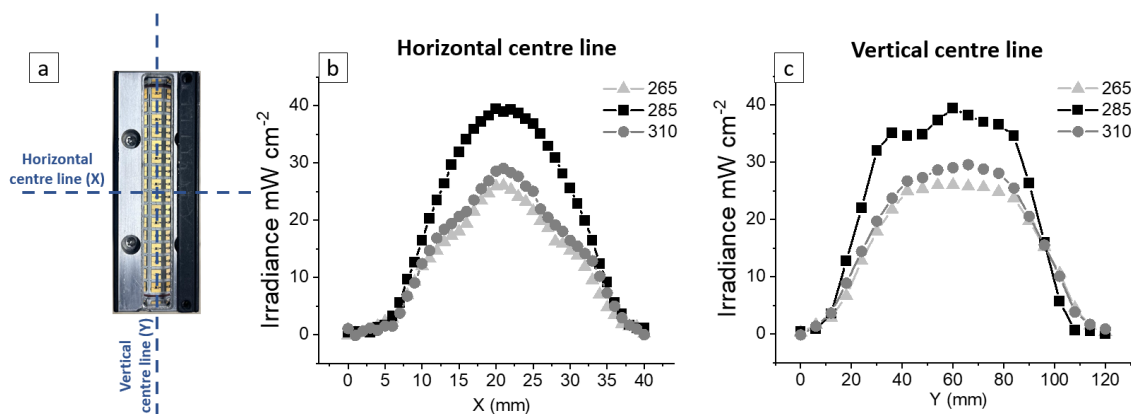


Figure 4.32. Lamps characterisation (a), horizontal (b) and vertical (c) profile.

Table 4.8 shows the values of the maximum irradiance measured by the radiometer in comparison with the chemical actinometry value for the three lamps.

Table 4.8. Lamps' characterisation through the chemical actinometry and the ILT radiometer.

Lamp wavelength (nm)	Irradiance from actinometry (mW cm ⁻²)	Max. Irradiance from ILT (mW cm ⁻²)	Current (A)	Total Electric Power (W)
265	21.98 ± 0.43	26.07	0.75	36.14
285	31.18 ± 0.06	39.44	0.97	46.56
310	27.62 ± 0.61	29.59	0.64	30.72

While the radiometer measured the value in the air, actinometry is affected by the refraction occurring in water and the losses in the quartz tube; therefore, the values from chemical actinometry were considered for the rest of the study.

Each lamp was also characterised at different intensities by regulating the voltage through a power supply. A linear relationship was confirmed with the current and the irradiation versus lamp intensity (Figure 4.33)

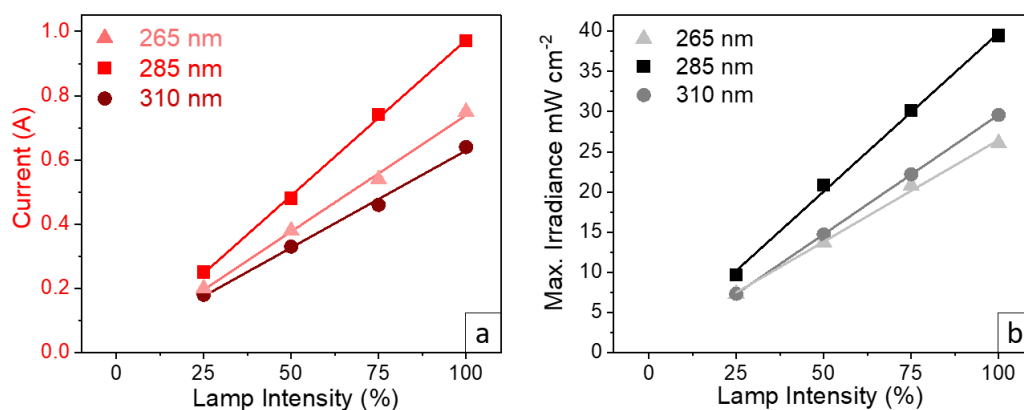


Figure 4.33. Linear correlation among the current values (a) and maximum irradiance values measured by the ILT radiometer (b) at different lamp intensities.

4.4.2 Molar absorption coefficient

The pH conditions were measured for the solutions with 20 mg L⁻¹ of DCF, 20 mg L⁻¹ of H₂O₂, and 20 mg L⁻¹ of FC. They were respectively 7.2, 6.5, and 8.5, and no further adjustment was made. The absorption spectra of the compound and the oxidants compared to the lamp's emission spectra are shown in Figure 4.34.

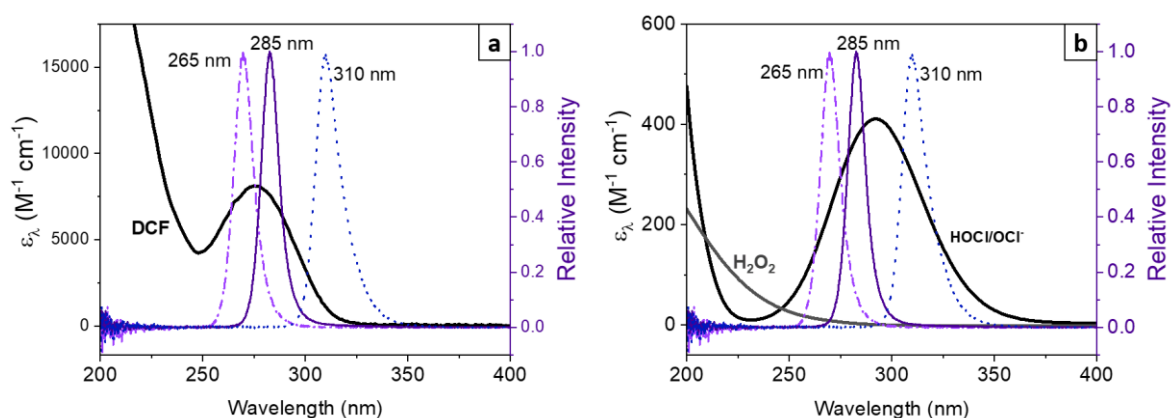


Figure 4.34. Absorbance of DCF (pH 7.2) (a), HOCl/OCl⁻ (pH 8.5), and H₂O₂ (pH 6.5) (b).

Finally, the values at the specific wavelengths of interest are reported in Table 4.9.

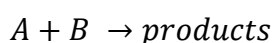
Table 4.9. Molar absorption coefficient for DCF (pH 7.2), HOCl/OCl⁻ (pH 8.5), and H₂O₂ (pH 6.5) measured in this study at the wavelengths of interest.

Compound/Oxidant	$\epsilon, \text{M}^{-1} \text{cm}^{-1}$			
	254 nm	265 nm	285 nm	310 nm
Sodium diclofenac	4740.14	7126.11	7157.93	1113.46
Hypochlorous acid and hypochlorite ion	71.49	173.86	388.75	300.52
Hydrogen peroxide	20.76	8.58	4.24	0.62

For H₂O₂, the shortest wavelength has the highest degradation efficiency and photon absorption. In contrast, FC has its peak at 292 nm, which is the maximum absorption of OCl⁻, the specie mostly present at the working pH of 8.5 [177]. Finally, the DCF absorption peak was found to be at 275 nm.

4.4.3 Degradation studies at different wavelengths

For a first approximation, the DCF degradation was described by a pseudo first-order kinetic, which is a second-order reaction that is made to behave like a first-order. This happens when one of the reactants is present in great excess, and its concentration can be considered constant compared with the other substance. Given the reaction:



The rate of disappearance of A follows Eq. (4.3).

$$\frac{d[A]}{dt} = -k^*[A][B] \quad \text{Eq. (4.3)}$$

And when $[B]_0 \approx [B]$, the reaction rate constant k^* can be rewritten, including the constant concentration of B, where $k=k^*[B]$. Therefore, the degradation of DCF can be expressed as a function of time, solving Eq. (4.3), which turns into Eq. (4.4).

$$\ln\left(\frac{C}{C_0}\right) = -k \cdot t \cdot \frac{V_R}{V_T} \quad Eq.(4.4)$$

Where C_0 is the initial concentration of DCF in the system, C is the concentration at a specific time t (min) during the operation, and k is the time-based kinetic constant (min^{-1}). V_R and V_T are, respectively, the active volume and the total volume of the reactor and were used to evaluate the photoreactor contact time of the solution to have comparable values with other studies since it is system independent. Figure 4.35 illustrates the degradation of DCF via direct photolysis, dark oxidation, UV/ H_2O_2 and UV/FC with respect to the total operation time, where 60 min represents around 2 min of photoreactor contact time. Each experiment was performed in triplicates; therefore, the average value was reported, and error bars represented the standard deviation.

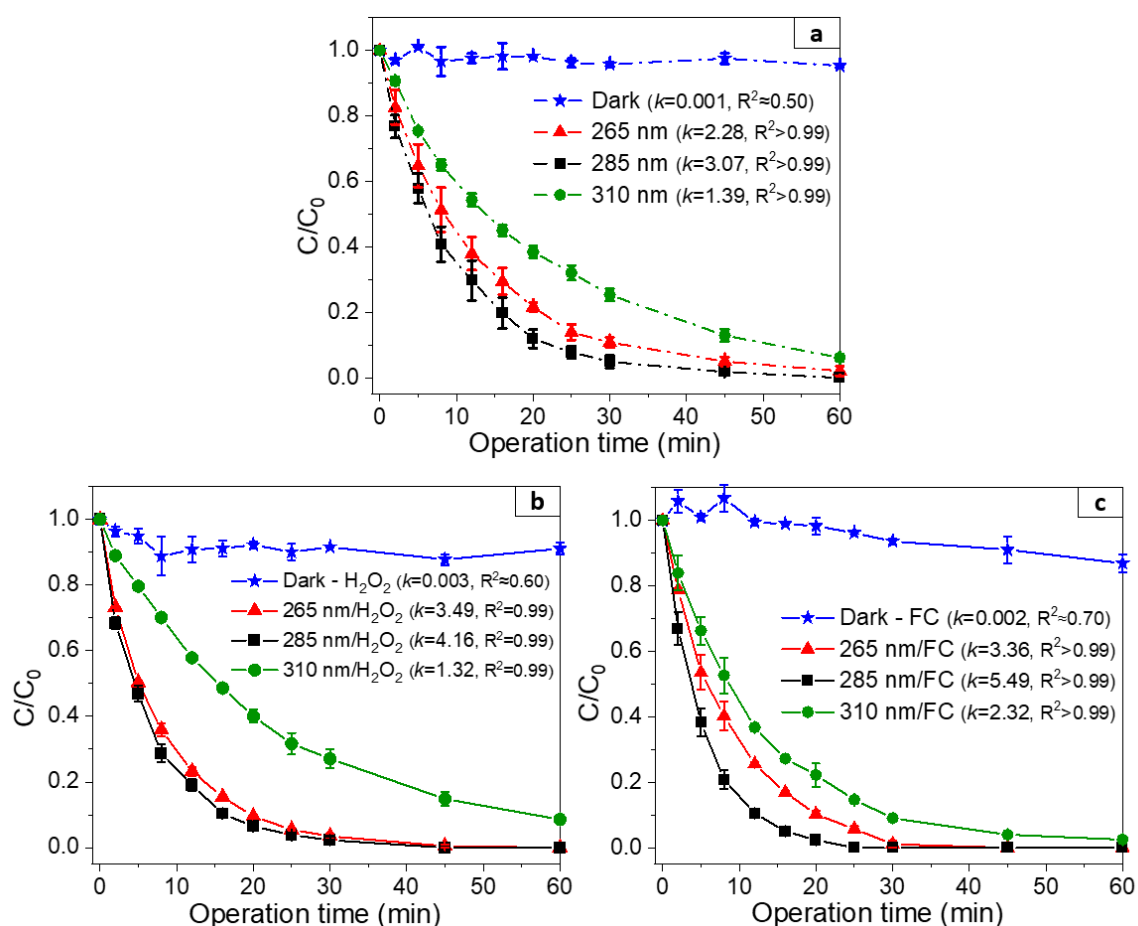


Figure 4.35. The degradation of DCF (20 mg L^{-1}) versus the total operation time through photolysis alone (a), UV/ H_2O_2 oxidation with 20 mg L^{-1} of H_2O_2 (b), and UV/FC oxidation with 20 mg L^{-1} of FC (c), where k is the time-based kinetic constant (expressed in min^{-1}).

The high correlation coefficient, R^2 , greater than 0.99 during the UV-LED processes, shows a strong linear relationship between $\ln(C/C_0)$ and the time, which was used to evaluate the kinetic constant k . Therefore, the pseudo first-order assumption reasonably approximates the DCF degradation through these processes.

Since each UV-LED lamp had a different irradiation value, it is of interest to also compare the degradation rates as a function of the UV fluence, as shown in Eq. (4.5).

$$\ln\left(\frac{C}{C_0}\right) = -k' \cdot UV_{fluence} \quad Eq. (4.5)$$

Where k' is the UV fluence-based kinetic constant ($\text{mJ}^{-1} \text{cm}^2$). Similar to Figure 4.35, Figure 4.36 illustrates the degradation of DCF via direct photolysis, dark oxidation, UV/ H_2O_2 and UV/FC with respect to the UV fluence in the active reactor.

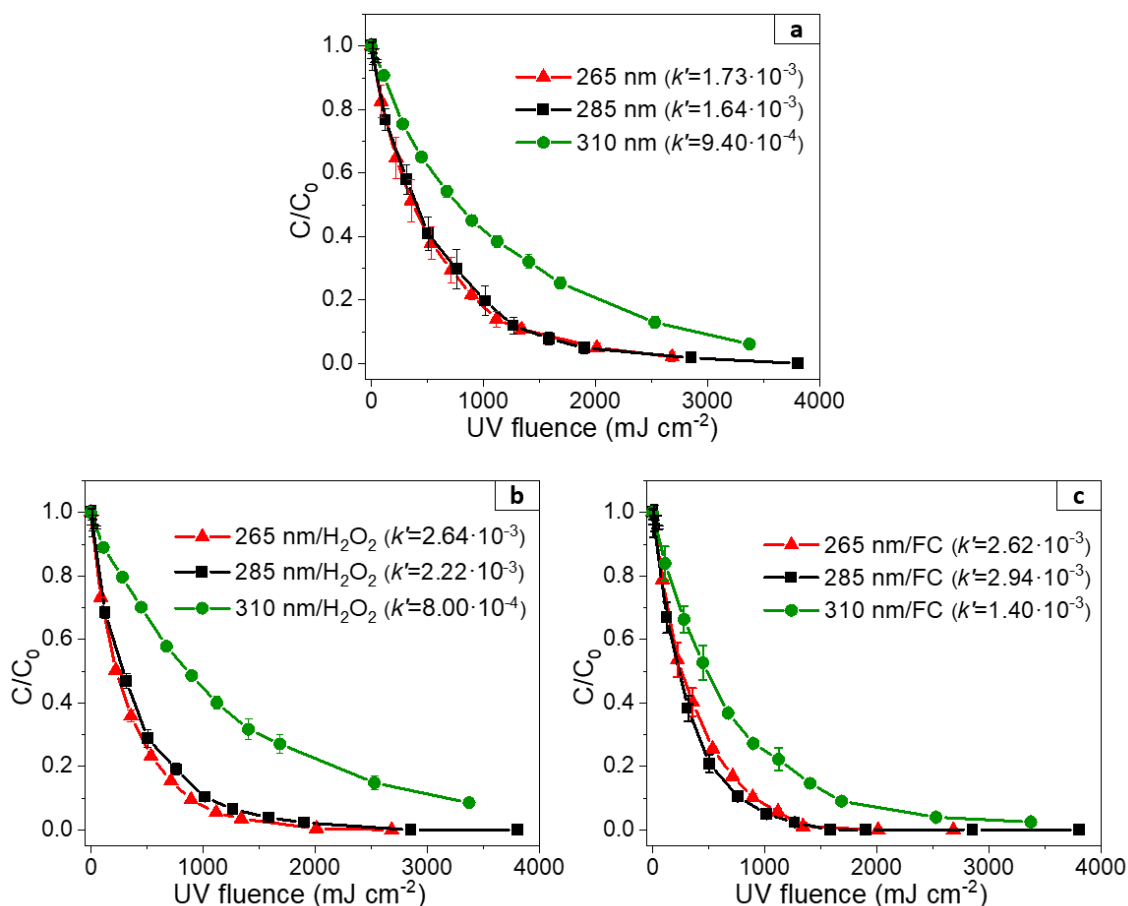


Figure 4.36. DCF degradation (20 mg L⁻¹) versus UV fluence through photolysis alone (a), UV/H₂O₂ oxidation with 20 mg L⁻¹ of H₂O₂ (b), and UV/FC oxidation with 20 mg L⁻¹ of FC (c), where k' is the UV fluence-based kinetic constant (expressed in mJ⁻¹ cm²).

A removal dependency on the wavelength was found in agreement with the absorption coefficient of the DCF and the oxidant employed. The UV fluence-based constants for 265 and 285 nm have similar values during UV photolysis alone, but it is lower for 310 nm. On the other hand, a higher k' value can be observed for 265 nm/H₂O₂, while 285 nm had the highest k' value in combination with FC. This follows the wavelength dependency of the oxidant's activation; H₂O₂ has a higher absorption at lower wavelengths, while hypochlorite ion (prevalent at pH 8.5) has a higher molar absorption coefficient at 285 nm. In all cases, the lamp at 310 nm had the lowest degradation efficiency in agreement with the DCF absorption. However, the best result with the latter was achieved with chlorine since a good activation of the oxidant was possible.

To quantify the synergistic effect of the UV-driven AOPs given by the formation of radical species through the photolysis of the oxidants, a synergy factor (F_S) was calculated according to Eq. (4.6).

$$F_S = \frac{k_{UV/oxidant}}{k_{UV} + k_{oxidant}} \quad Eq. (4.6)$$

When the value is equal to 1.0 means that the combination leads exactly to the sum of each individual contribution. On the other hand, a value greater than 1.0 means a synergistic effect when combining the two processes, whereas a factor inferior to 1.0 indicates an antagonistic effect. The values obtained are plotted against the respective process in Figure 4.37b, where the dashed line corresponds to F_S equal to 1.0, and the time-based constants shown in Figure 4.37a were considered for the calculations.

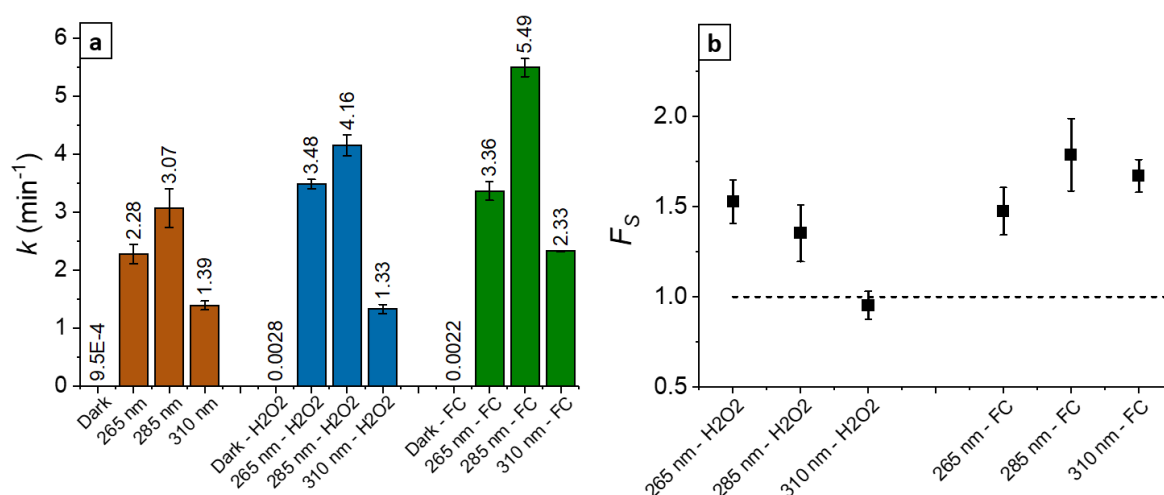


Figure 4.37. Comparison among the time-based constant k by direct photolysis, dark oxidation and UV-driven AOPs (a), and values of the synergist factor (b).

In all cases, except for the 310 nm/H₂O₂, a synergistic effect was reached when coupling the UV treatment with the oxidants. By adding H₂O₂, 265 followed by 285 nm were the wavelengths with the highest synergistic factor, while the highest synergy for the UV/FC process was reached by the 285 and 310 nm lamp, in agreement with the wavelength-dependent absorption of the species discussed earlier.

4.4.4 Rigorous kinetic modelling

In order to explain and describe rigorously the synergy during UV/H₂O₂ and UV/FC, a mechanistic kinetic model was developed, investigating the main elementary reactions of the oxidising radicals acting during the degradation of DCF. The novelty of the model is to consider the effect of the different wavelengths explored during the study. By estimating the second-order kinetic constants between DCF and the main radicals, it is possible to predict its degradation as a function of the operational conditions. The mechanisms proposed were the best compromise between simplicity and robustness of the fitting of the experimental data.

Table 4.10 shows the kinetic model proposed for UV/H₂O₂.

Table 4.10. Proposed mechanism for the UV/H₂O₂ treatment.

#	Reaction	Rate	Kinetic constant	Unit	Ref
(R1a)	$DCF + hv \rightarrow products$	$k_{f_{otolisis,\lambda}}[DCF]G_{\lambda}$	$\frac{k_{F,265} = 1.73 \cdot 10^{-4}}{k_{F,285} = 1.64 \cdot 10^{-4}} \cdot \frac{k_{F,285}}{k_{F,310} = 9.40 \cdot 10^{-5}}$	$J^{-1} \cdot m^2$	This work
(R2a)	$DCF + H_2O_2 \rightarrow products$	$k_{perox}[DCF][H_2O_2]$	$k_{perox} = 0.061$	$M^{-1} \cdot s^{-1}$	This work
(R3a)	$H_2O_2 + hv \rightarrow 2 HO \cdot$	$k_{f,H_2O_2}[H_2O_2]G_{\lambda}$	$\frac{k_{fH_2O_2,265} = 9.52 \cdot 10^{-7}}{k_{fH_2O_2,285} = 5.06 \cdot 10^{-7}} \cdot \frac{k_{fH_2O_2,285}}{k_{fH_2O_2,310} = 8.08 \cdot 10^{-8}}$	$J^{-1} \cdot m^2$	Φ_{λ} , from [178] ϵ_{λ} , from this work
(R4a)	$DCF + HO \cdot \rightarrow products$	$k_{HO}[DCF][HO \cdot]$	To estimate	$M^{-1} \cdot s^{-1}$	Determined in this work
(R5a)	$2 HO \cdot \rightarrow H_2O_2$	$k_{Recomb}[HO \cdot]^2$	$k_{Recomb} = 5.5 \cdot 10^9$	$M^{-1} \cdot s^{-1}$	[178]
(R6a)	$H_2O_2 + HO \cdot \rightarrow HO_2 \cdot + H_2O$	$k_1[H_2O_2][HO \cdot]$	$k_1 = 2.7 \cdot 10^7$	$M^{-1} \cdot s^{-1}$	[179]
(R7a)	$H_2O_2 + HO_2 \cdot \rightarrow HO \cdot + H_2O + O_2$	$k_2[H_2O_2][HO_2 \cdot]$	$k_2 = 3.7$	$M^{-1} \cdot s^{-1}$	[179]

The kinetic constants for the DCF photolysis at different wavelengths (R1a) and the dark reaction (R2a) were obtained experimentally from the experimental data. $k_{F,\lambda}$ represents the UV fluence-based kinetic constant shown in Figure 4.36, while k_{perox} is the time-based kinetic constant during the dark reaction with H₂O₂ divided by its initial concentration. Finally, both constants were converted into the units shown in the table, which were used in the code. The kinetic constants $k_{fH_2O_2}$ of reaction R3a were obtained from the H₂O₂ molar

absorption coefficient, ε_λ , calculated in this study and shown in Table 4.9, and the primary quantum yield, Φ_λ , 0.5 according to the literature [178].

$$k_{fH_2O_2} \left(\frac{m^2}{J} \right) = \Phi_{H_2O_2} \left(\frac{mol}{E} \right) \cdot \varepsilon_{\lambda, H_2O_2} \left(\frac{L}{mol \cdot cm} \right) \cdot x_\lambda \left(\frac{E}{J} \right) \cdot \frac{10^2}{1} \left(\frac{cm}{m} \right) \cdot \frac{1}{10^3} \left(\frac{m^3}{L} \right)$$

Where x_λ is the parameter to convert the energy units to photonic units, shown in Eq. (4.7)

$$x_\lambda \left(\frac{E}{J} \right) = \frac{\lambda}{h \cdot c} \left(\frac{photon}{J} \right) \cdot \frac{1}{N_A} \left(\frac{E}{photon} \right) \quad Eq. (4.7)$$

Finally, the model was derived by resolving the mass balance of the different species and by applying the kinetic MSSA for the concentration of radicals.

$$r_{HO \cdot} = \frac{d[HO \cdot]}{dt} = 2k_{fH_2O_2}[H_2O_2]G_\lambda - 2k_{Recomb}[HO \cdot]^2 - k_{HO}[DCF][HO \cdot] - k_1[H_2O_2][HO \cdot] + k_2[H_2O_2][HO_2 \cdot] \approx 0$$

Since $HO \cdot$ depends on $HO_2 \cdot$ and vice versa, to simplify the derivation, the concentration of $HO_2 \cdot$ was neglected while solving $HO \cdot$ as the relative amount is expected to be quite low [179].

$$2k_{Recomb}[HO \cdot]^2 + (k_{HO}[DCF] + k_1[H_2O_2])[HO \cdot] - 2k_{fH_2O_2}[H_2O_2]G_\lambda \approx 0$$

$$[HO \cdot] = \frac{-(k_{HO}[DCF] + k_1[H_2O_2]) \pm \sqrt{(k_{HO}[DCF] + k_1[H_2O_2])^2 - 4 \cdot 2k_{Recomb} \cdot -2k_{fH_2O_2}[H_2O_2]G_\lambda}}{2 \cdot 2k_{Recomb}}$$

Where the positive root is the only one that has physical meaning:

$$[HO \cdot] = \frac{-(k_{HO}[DCF] + k_1[H_2O_2]) + \sqrt{(k_{HO}[DCF] + k_1[H_2O_2])^2 + 4 \cdot 2k_{Recomb} \cdot 2k_{fH_2O_2}[H_2O_2]G_\lambda}}{2 \cdot 2k_{Recomb}}$$

$$r_{HO_2 \cdot} = \frac{d[HO_2 \cdot]}{dt} = k_1[H_2O_2][HO \cdot] - k_2[H_2O_2][HO_2 \cdot] \approx 0$$

$$[HO_2 \cdot] = \frac{k_1[H_2O_2][HO \cdot]}{k_2[H_2O_2]} = \frac{k_1[HO \cdot]}{k_2}$$

$$r_{H_2O_2} = \frac{d[H_2O_2]}{dt} = -k_{perox}[DCF][H_2O_2] - k_{fH_2O_2}[H_2O_2]G_\lambda + k_{Recomb}[HO \cdot]^2 - k_1[HO \cdot][H_2O_2] - k_2[HO_2 \cdot][H_2O_2]$$

$$r_{DCF} = \frac{d[DCF]}{dt} = -k_{fotolysis,\lambda}[DCF]G_\lambda - k_{perox}[DCF][H_2O_2] - k_{HO}[DCF][HO \cdot]$$

The radicals' concentration expression, together with the differential equations, were inserted in the Octave code, where the only incognito was k_{HO} , the second-order rate constant for $HO \cdot$ with DCF of reaction *R4a*. This constant was calculated by minimising the error between the experimental data for DCF and H_2O_2 at the three wavelengths with the model described. The value obtained for k_{HO} was $9.12 \cdot 10^9 \text{ M}^{-1} \text{ s}^{-1}$, which is in agreement with other values and range reported in the literature, $7.6\text{-}9.1 \cdot 10^9$ [176], $9.29 \cdot 10^9$ [180], and $1.36 \cdot 10^{10}$ [181] $\text{M}^{-1} \text{ s}^{-1}$. The model prediction based on the mechanism shown in Table 4.10 and with the estimated constant k_{HO} is shown in Figure 4.38, which satisfactorily fits the experimental data. In the latter, the x-axis represents the photoreactor contact time.

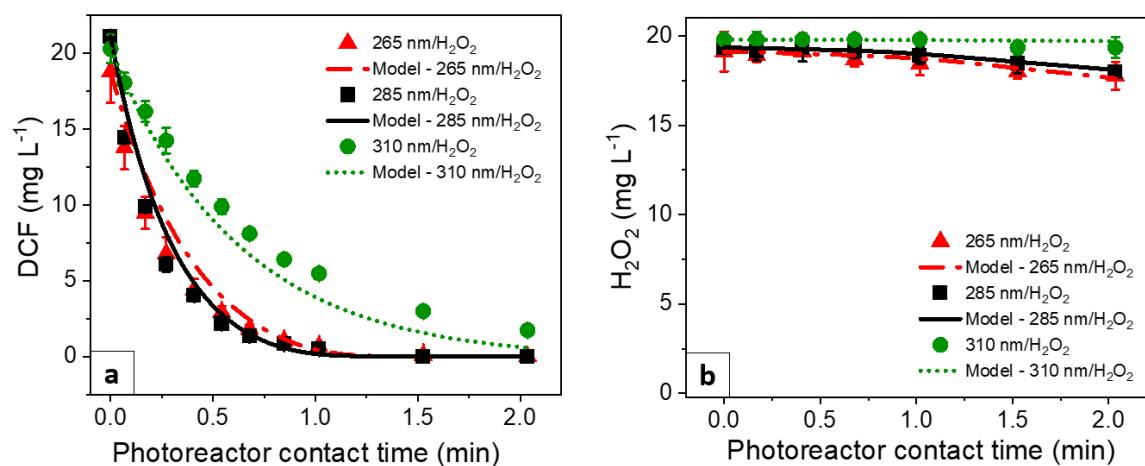


Figure 4.38. Correlation between the experimental data (red triangles, black squares, and green dots at 265, 285 and 310 nm) and model predictions (red dashed-dotted, black solid, and green dotted lines at 265, 285 and 310 nm) for DCF (a) and H_2O_2 (b).

Similarly, Table 4.11 shows the kinetic model proposed for UV/FC.

Table 4.11. Proposed mechanism for the UV/FC treatment.

#	Reaction	Rate	Kinetic constant	Unit	Ref
(R1b)	$HOCl \rightleftharpoons OCl^- + H^+$		$pKa^* = 7,5$		[102]
(R2b)	$HOCl + hv \rightarrow HO \cdot + Cl \cdot$	$k_{HOCl,\lambda}[HOCl]G_\lambda$	$k_{HOCl,268} = 7.60 \cdot 10^{-6}$ $k_{HOCl,282} = 6.25 \cdot 10^{-6}$ $k_{HOCl,301} = 6.29 \cdot 10^{-6}$	$J^{-1} \cdot m^2$	[178]
(R3b)	$OCl^- + hv \rightarrow O^- \cdot + Cl \cdot$	$k_{OCl^-,\lambda}[OCl^-]G_\lambda$	$k_{OCl^-,265} = 3.75 \cdot 10^{-5}$ $k_{OCl^-,285} = 7.61 \cdot 10^{-5}$ $k_{OCl^-,310} = 6.01 \cdot 10^{-5}$	$J^{-1} \cdot m^2$	ϕ_λ , from [178] ϵ_λ , from this work
(R4b)	$DCF + HO \cdot \rightarrow products$	$k_{HO}[DCF][HO \cdot]$	k_{HO} calculated from UV/H ₂ O ₂ kinetic	$M^{-1} \cdot s^{-1}$	This work
(R5b)	$HO \cdot + HOCl \rightarrow ClO \cdot + H_2O$	$k_{HO,A}[HO \cdot][HOCl]$	$k_{HO,A} = 2.0 \cdot 10^9$	$M^{-1} \cdot s^{-1}$	[93]
(R6b)	$HO \cdot + OCl^- \rightarrow ClO \cdot + OH^-$	$k_{HO,B}[HO \cdot][OCl^-]$	$k_{HO,B} = 8.8 \cdot 10^9$	$M^{-1} \cdot s^{-1}$	[93]
(R7b)	$DCF + Cl \cdot \rightarrow products$	$k_{Cl}[DCF][Cl \cdot]$	To estimate	$M^{-1} \cdot s^{-1}$	Determined in this work
(R8b)	$DCF + HOCl \rightarrow products$	$k_{d,HOCl}[DCF][HOCl]$	$k_{d,HOCl} = 0.0077$	$M^{-1} \cdot s^{-1}$	This work
(R9b)	$Cl \cdot + HOCl \rightarrow Cl^- + ClO \cdot + H^+$	$k_{Excess,A}[Cl \cdot][HOCl]$	$k_{Excess,A} = 3.0 \cdot 10^9$	$M^{-1} \cdot s^{-1}$	[93]
(R10b)	$Cl \cdot + OCl^- \rightarrow Cl^- + ClO \cdot$	$k_{Excess,B}[Cl \cdot][OCl^-]$	$k_{Excess,B} = 8.2 \cdot 10^9$	$M^{-1} \cdot s^{-1}$	[93]
(R11b)	$DCF + OCl^- \rightarrow products$	$k_{d,OCl^-}[DCF][OCl^-]$	$k_{d,OCl^-} = 0.0772$	$M^{-1} \cdot s^{-1}$	This work
(R12b)	$DCF + hv \rightarrow products$	$k_{fotolisis,\lambda}[DCF]G_\lambda$	$k_{F,265} = 1.73 \cdot 10^{-4}$ $k_{F,285} = 1.64 \cdot 10^{-4}$ $k_{F,310} = 9.40 \cdot 10^{-5}$	$J^{-1} \cdot m^2$	This work

As mentioned, FC refers to hypochlorous acid (HOCl) and hypochlorite ion (OCl⁻). Hypochlorous acid is a weak acid that dissociates into hypochlorite ions and protons depending on the equilibrium of the reaction *R1b*. Therefore, their concentrations are not independent but are conditioned by the pH of the medium. The lower the pH, the higher the percentage of hypochlorous acid and vice versa. From pH 5 and below, 100% of the FC is considered to be in the form of HOCl, while from pH 10, it is considered to be in the form of OCl⁻ [102]. In this study, the degradation with FC was conducted at pH 8.5; therefore, as a consequence of the equilibrium reaction, the initial amount of HOCl and OCl⁻ was evaluated as follows:

$$FC_0 = [HOCl]_0 + [OCl^-]_0$$

4. Results and discussion

$$10^{-pKa} = \frac{[OCl^-][H^+]}{[HOCl]}$$

$$[OCl^-]_0 = \frac{10^{-pKa}[HOCl]_0}{10^{-pH}} = 10^{pH-pKa}[HOCl]_0$$

$$f_{HOCl} = \frac{[HOCl]}{[HOCl]+[OCl^-]} = \frac{1}{1+10^{pH-pKa}} = 0.09$$

$$[HOCl]_0 = f_{HOCl} [FC]_0 = 0.0354 \text{ mM}$$

$$[OCl^-]_0 = 0.3536 \text{ mM}$$

Both species are capable of absorbing ultraviolet radiation, although to a different extent, as described by reactions *R2b* and *R3b*, generating hydroxyl radicals, chlorine radicals and superoxide radicals.

Their kinetic constants, $k_{HOCl,\lambda}$ and $k_{OCl^-,\lambda}$, were calculated from the molar absorption coefficient, ϵ_λ , and the primary quantum yield, Φ_λ , for HOCl and OCl⁻, respectively (Table 4.12). The values for the quantum yield were taken from the literature at a similar wavelength [177]. Also, the molar absorption coefficients for HOCl were taken from the same source; on the other hand, the molar absorption coefficient for OCl⁻ was taken from Table 4.9. Indeed, the spectra of the FC at pH 8.5 matched the spectra of OCl⁻ shown by Yin et al. [177].

Table 4.12. Apparent quantum yields and the molar absorption coefficients for HOCl and OCl⁻ at the wavelengths of interest.

Wavelength (nm)	Φ_{HOCl}^* (mol E ⁻¹)	$\Phi_{OCl^-}^*$ (mol E ⁻¹)	ϵ_{HOCl}^* (M ⁻¹ cm ⁻¹)	$\epsilon_{OCl^-}^*$ (M ⁻¹ cm ⁻¹)	Wavelength (nm)	$\epsilon_{OCl^-}^{**}$ (M ⁻¹ cm ⁻¹)
268	1.11	0.97	30.82	175.47	265	173.86
282.3	0.98	0.82	26.69	305.21	285	388.75
301.2	0.96	0.77	25.21	316.15	310	300.52

*From literature [177], **From this study

$k_{HOCl,\lambda}$, and $k_{OCl^-\lambda}$, were finally calculated as follows:

$$k_{HOCl,\lambda} \left(\frac{m^2}{J} \right) = \Phi_{HOCl} \left(\frac{mol}{E} \right) \cdot \varepsilon_{\lambda,HOCl} \left(\frac{L}{mol \cdot cm} \right) \cdot \chi_{\lambda} \left(\frac{E}{J} \right) \cdot \frac{10^2}{1} \left(\frac{cm}{m} \right) \cdot \frac{1}{10^3} \left(\frac{m^3}{L} \right)$$

$$k_{OCl^-\lambda} \left(\frac{m^2}{J} \right) = \Phi_{OCl^-} \left(\frac{mol}{E} \right) \cdot \varepsilon_{\lambda,OCl^-} \left(\frac{L}{mol \cdot cm} \right) \cdot \chi_{\lambda} \left(\frac{E}{J} \right) \cdot \frac{10^2}{1} \left(\frac{cm}{m} \right) \cdot \frac{1}{10^3} \left(\frac{m^3}{L} \right)$$

The kinetic constants for the DCF photolysis at different wavelengths (*R12b*) were the same as the previous model, from which it was also taken the value of k_{HO} in reaction *R4b*. On the other hand, the kinetic constants from the dark reactions (*R8b* and *R11b*), $k_{d,HOCl}$ and k_{d,OCl^-} , were calculated from the percentage of HOCl and OCl⁻ in the solution at pH 8.5 and the known $k_{dark,FC}$ value, which was measured experimentally adding FC in the dark with DCF, similarly to k_{perox} during the UV/H₂O₂ treatment.

$$k_{d,HOCl} = f_{HOCl} \cdot k_{dark,FC} = 0.0077 \text{ M}^{-1} \text{ s}^{-1}$$

$$k_{d,OCl^-} = (1 - f_{HOCl}) \cdot k_{dark,FC} = 0.0772 \text{ M}^{-1} \text{ s}^{-1}$$

Finally, the differential equations and the expression for the radicals' concentration were derived by resolving the mass balances of the different species and by applying the kinetic MSSA for the radicals.

$$r_{HO \cdot} = \frac{d[HO \cdot]}{dt} = k_{HOCl,\lambda}[HOCl]G_{\lambda} - k_{HO}[DCF][HO \cdot] - k_{HO,A}[HOCl][HO \cdot] - k_{HO,B}[OCl^-][HO \cdot] \approx 0$$

$$[HO \cdot] = \frac{k_{HOCl,\lambda}[HOCl]G_{\lambda}}{k_{HO}[DCF] + k_{HO,A}[HOCl] + k_{HO,B}[OCl^-]}$$

$$r_{Cl \cdot} = \frac{d[Cl \cdot]}{dt} = k_{HOCl,\lambda}[HOCl]G_{\lambda} + k_{OCl^-\lambda}[OCl^-]G_{\lambda} - k_{Cl}[DCF][Cl \cdot] - k_{Excess,A}[Cl \cdot][HOCl] - k_{Excess,B}[Cl \cdot][OCl^-] \approx 0$$

$$[Cl \cdot] = \frac{k_{HOCl,\lambda}[HOCl]G_{\lambda} + k_{OCl^-\lambda}[OCl^-]G_{\lambda}}{k_{Cl}[DCF] + k_{Excess,A}[HOCl] + k_{Excess,B}[OCl^-]}$$

4. Results and discussion

$$r_{DCF} = \frac{d[DCF]}{dt} = -k_{HO}[DCF][HO \cdot] - k_{Cl}[DCF][Cl \cdot] - k_{d,HOCl}[DCF][HOCl] - k_{d,OCl-}[DCF][OCl^-] - k_{photolysis,\lambda}[DCF]G_{\lambda}$$

$$r_{HOCl} = \frac{d[HOCl]}{dt} = -k_{HOCl,\lambda}[HOCl]G_{\lambda} - k_{d,HOCl}[DCF][HOCl] - k_{HO,A}[HO \cdot][HOCl] - k_{Excess,A}[HOCl][Cl \cdot]$$

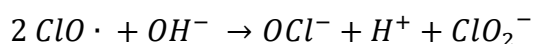
$$r_{OCl^-} = \frac{d[OCl^-]}{dt} = -k_{OCl-,\lambda}[OCl^-]G_{\lambda} - k_{d,OCl-}[DCF][OCl^-] - k_{HO,B}[HO \cdot][OCl^-] - k_{Excess,B}[Cl \cdot][OCl^-]$$

$$r_{FC} = r_{HOCl} + r_{OCl^-}$$

The resulting equations were used to evaluate the unknown kinetic constant k_{Cl} for $Cl \cdot$ with DCF of reaction *R7b*, which is the result of minimising the error among the experimental data for DCF and FC at the three wavelengths with the model described.

The reactivity of $O \cdot$ was omitted since it is known that it has low reactivity with the organic matter [93].

On the other hand, while it is well established that the role of $Cl_2 \cdot^-$ is also negligible in the UV/FC treatment [182], in some cases, the role of $ClO \cdot$ can be relevant since the reactions of $Cl \cdot$ and $HO \cdot$ with $HOCl/OCl^-$ produce a significant amount of this radical [182]. However, in this case, the $ClO \cdot$ concentration is balanced out by the recombination mechanism and the reaction with OH^- , which amount is more relevant at the alkaline working pH as shown by the following reaction:



Furthermore, in any case, the second-order reaction rate constant for $ClO \cdot$ with DCF is expected to be two or three orders of magnitude smaller than the one for $Cl \cdot$ [182] and therefore omitted in this case. The second-order rate constant k_{Cl} was estimated to be $1.30 \cdot 10^{10} \text{ M}^{-1} \text{ s}^{-1}$, which is also in agreement with the value in literature of $3.77 \cdot 10^{10} \text{ M}^{-1} \text{ s}^{-1}$ [183] and in the range of other similar contaminants such as carbamazepine $5.6 \cdot 10^{10} \text{ M}^{-1} \text{ s}^{-1}$ [184] and N,N-diethyl-m-toluamide (DEET), $6.4 \cdot 10^9 \text{ M}^{-1} \text{ s}^{-1}$ [185]. The model predictions based on the mechanism shown in Table 4.11 and with the estimated constants

k_{HO} and k_{Cl} are shown in Figure 4.39, where the curves adequately fit the experimental data. To note that the x-axis represents the photoreactor contact time, similarly to Figure 4.38.

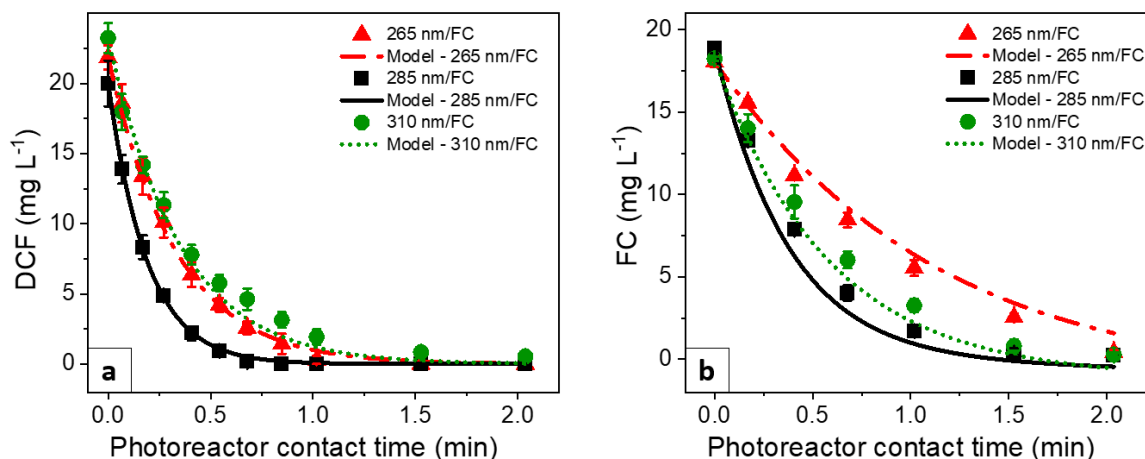


Figure 4.39. Correlation between the experimental data (red triangles, black squares, and green dots at 265, 285 and 310 nm) and model predictions (red dashed-dotted, black solid, and green dotted lines at 265, 285 and 310 nm) for DCF (a) and FC (b).

4.4.5 Varying intensity

Since another unique characteristic of the LEDs over mercury lamps is the possibility of regulating their intensity and consequently decreasing the total electric power, it is important to study the behaviour of the pollutant degradation as a function of the intensity. The results allow for choosing the best operational conditions once the photoreactor is designed. The study was performed only for the 265 and 285 nm lamps since they exhibited the best DCF degradation results, and they were evaluated working at 25%, 50% and 75% of the total intensity. Table 4.13 lists the values of current, irradiance measured through the ILT radiometer, and the resulting total electric power at different intensities.

4. Results and discussion

Table 4.13. Current, irradiance, and total electric power at different intensities of the lamp at 265 and 285 nm.

Lamp wavelength (nm)	Lamp intensity (%)	Current (A)	Max. Irradiance from ILT (mW cm^{-2})	Total Electric Power (W)
265	25	0.20	7.31	9.36
	50	0.38	13.72	18.22
	75	0.54	20.80	25.94
	100	0.75	26.07	36.14
285	25	0.25	9.60	11.76
	50	0.48	20.86	23.76
	75	0.74	30.08	35.28
	100	0.97	39.44	46.56

Figure 4.40 shows the time-based and UV fluence-based constants resulting from the two lamps at different light intensities alone or coupled with the oxidants. At least two repetitions were performed for each case, where the value reported represents the average, and the error bars the standard deviation.

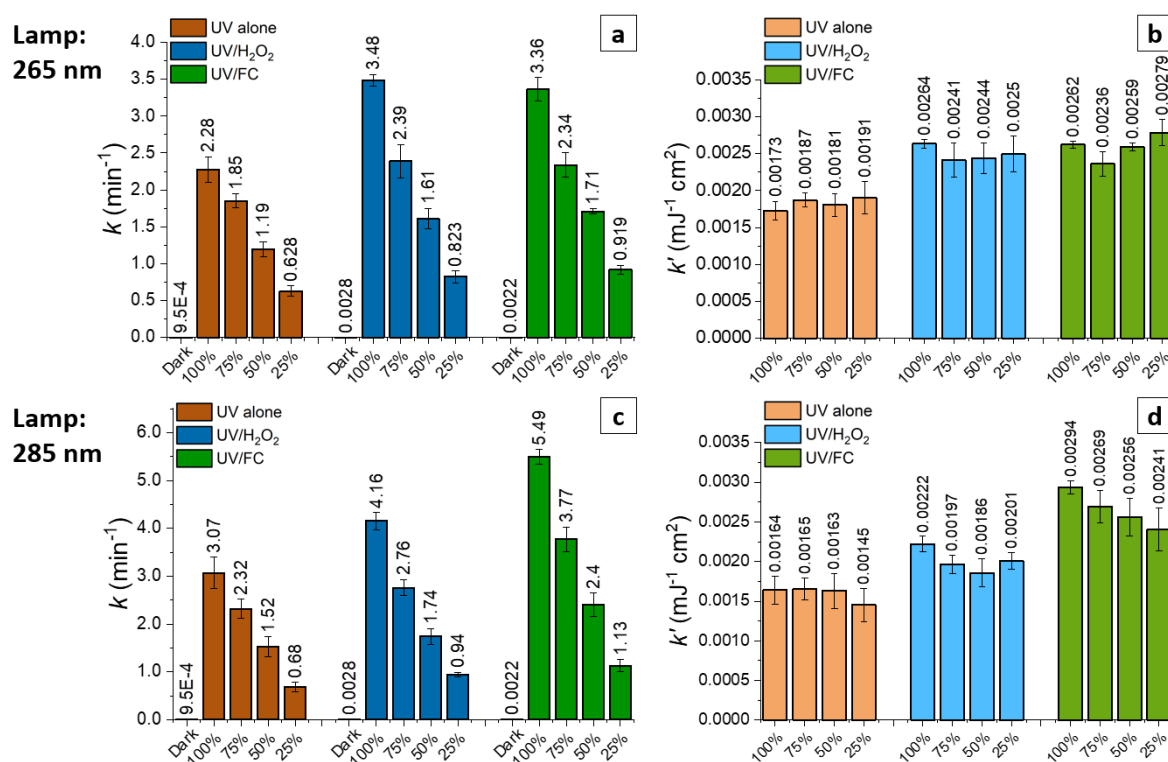


Figure 4.40. Time-based constants (a, c) and UV fluence-based constants (b, d) alone or coupled with H₂O₂ or FC at different lamp intensities.

At the selected wavelengths, the UV fluence-based constants displayed similar values for each treatment, indicating that the required UV fluence for the degradation of the compound would be consistent, irrespective of the lamp intensity. Hence, time-based constants showed a decreasing trend with a reduction in lamp intensity, as a longer time is required to attain the same UV fluence and degradation percentage. The time-based constants for both lamps were plotted against lamp intensity in Figure 4.41, and all cases exhibited a linear correlation with a high correlation coefficient of R^2 .

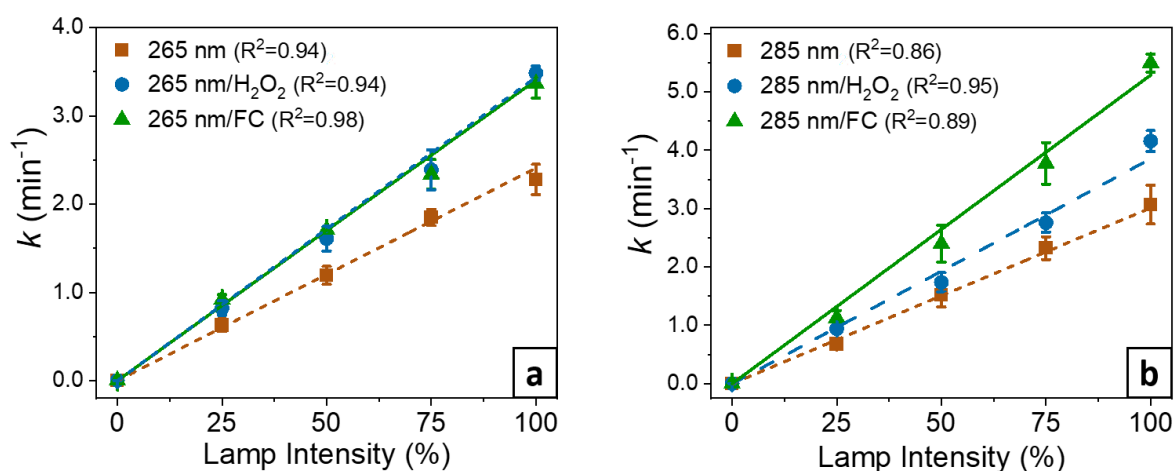


Figure 4.41. Linear correlation between the time-based constants and the lamp intensity for UV alone (brown squares), UV/ H_2O_2 (blue dots), and UV/FC (green triangles) for the two lamps: 265 nm (a) and 285 nm (b).

4.4.6 Dual-wavelength system

Dual-wavelength ultraviolet irradiation is particularly interesting in LED systems thanks to the option of having several wavelengths available. The potential synergistic effect of dual-wavelength UV photolysis on the degradation of the contaminant and the oxidant was evaluated for the 265 nm and 285 nm wavelengths. To this end, lamp 2 was incorporated into the experimental setup, as shown in Figure 4.42.

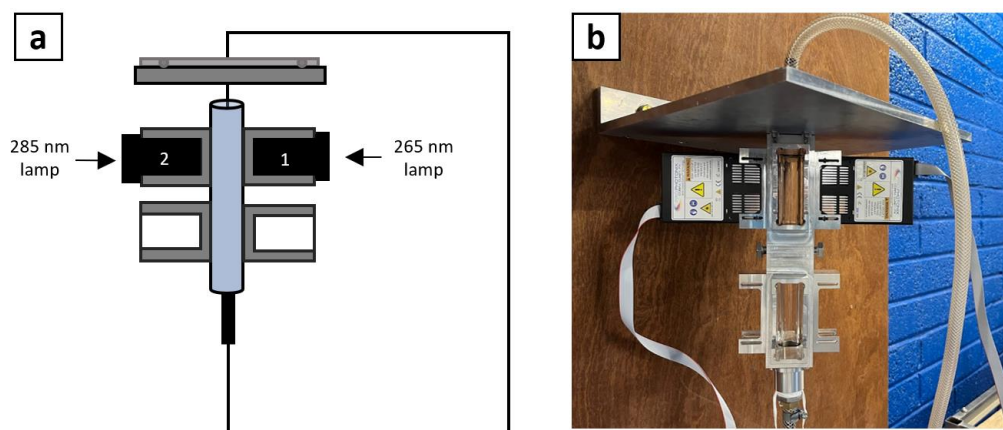


Figure 4.42. Incorporation of lamp 2 into the experimental setup, schematic representation (a) and laboratory image (b).

The total irradiance of the two lamps irradiating in parallel was measured using chemical actinometry and compared to the sum of photons when each lamp was emitting singularly. All cases were performed at 100% intensity. Table 4.14 shows the irradiance values, together with the total current and the total electric power for the two lamps working at the same time.

Table 4.14. Dual-wavelength irradiation.

Lamp wavelength (nm)	Current (A)	Irradiance from actinometry (mW cm^{-2})	Irradiance as the sum of photons (mW cm^{-2})	Total Electric Power (W)
265	0.75	21.98 ± 0.43	-	36.14
285	0.97	31.18 ± 0.06	-	46.56
265 + 285	1.72	55.42 ± 1.60	53.16 ± 0.43	82.56

The small difference between the measured value of $55.42 \pm 1.60 \text{ mW cm}^{-2}$ and $53.16 \pm 0.43 \text{ mW cm}^{-2}$ from the sum of the photons demonstrated that the lamps at the positions did not cause any extra refractions due to the opposite lamp reflectors.

The investigation was performed for UV alone, UV/H₂O₂, and UV/FC. Figure 4.43a shows the comparison among the “observed” (experimental) value where both wavelengths were irradiated at the same time and the “simulated” time-based constants, measured as the sum of the k -values evaluated for each lamp. Similarly, Figure 4.43b shows the k' -values for the “observed” and “simulated” case.

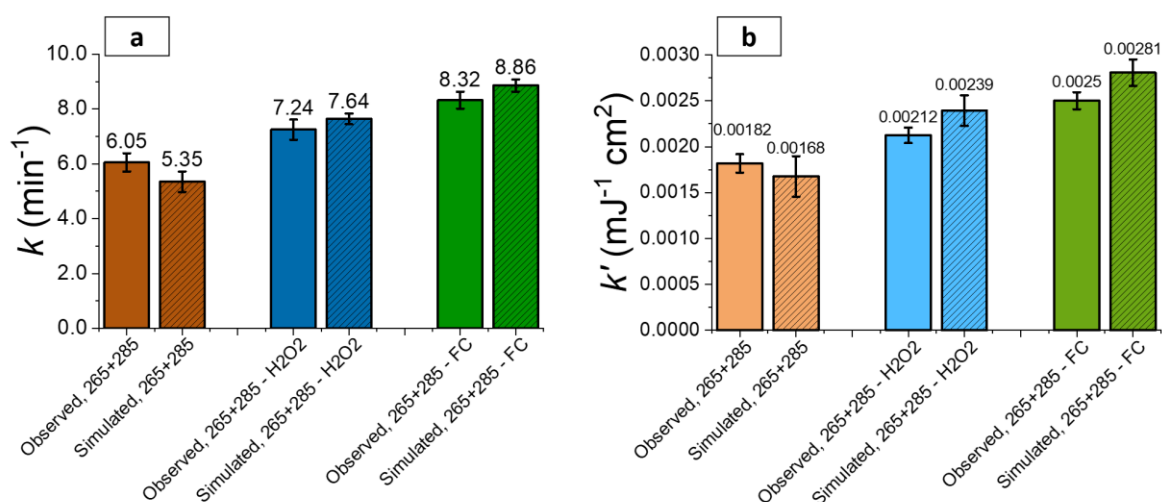


Figure 4.43. Time-based constants (a) and UV-based constants for the “observed” and “simulated” dual-wavelength irradiation.

Regarding the photolysis alone, the observed value was slightly greater than the simulated one, whereas, during UV/H₂O₂ and UV/FC treatment, an opposite trend was observed. Nevertheless, the difference between the two values was negligible due to the experimental error, which was evaluated by repeating two sets of experiments for the observed values and through uncertainty propagation for the simulated values. The synergy factor was then evaluated for the three cases and shown in Figure 4.44.

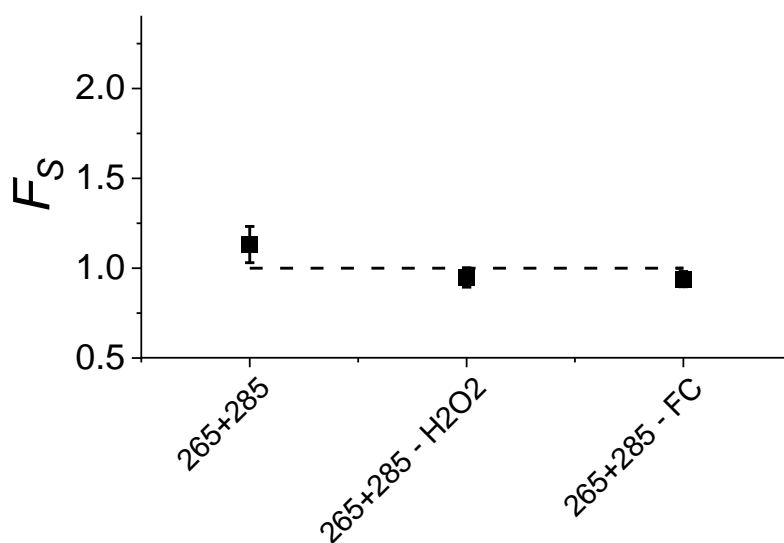


Figure 4.44. The extent of synergy during the dual-wavelength irradiation.

The synergy factor was 1.13 ± 0.1 , 0.95 ± 0.05 , and 0.94 ± 0.04 for UV photolysis, UV/H₂O₂, and UV/FC, respectively. Due to the closeness of the value to the line of no synergy, represented by the dashed line, a one-way analysis of variance (ANOVA) was also performed. ANOVA is a statistical tool to compare variances across the average of different groups. This time the two groups were formed by the two observed values and the possible combinations for the sum of the results given by the two lamps separately. To determine if the difference is statistically significant, the *p*-value was determined through the Minitab Software. If the significant level (*p*-value) is less than 0.05, the null hypothesis, which states “all means are equal”, can be rejected and conclude that there is a meaningful difference between the means. Otherwise, if the *p*-value is greater than 0.05, it means that there is not enough evidence to say that there is a statistically significant difference. In this study, the *p*-values were respectively 0.054, 0.068, and 0.061 for UV alone, UV/H₂O₂, and UV/FC; therefore, we failed to reject the null hypothesis, and we concluded that the dual-wavelength system did not exhibit any remarkable synergy. The degradation given by two wavelengths can be simply attributed to the cumulative effect of the photons generated by both lamps.

This is in agreement with Popova et al. [128], who investigated bisphenol A degradation using various wavelength combinations (222+282, 222+365, and 282+365 nm) and oxidants (potassium persulfate and H₂O₂) and observed no synergy. In contrast, Gao et al. [129] reported a statistically significant synergistic effect (*p*<0.05). They studied the degradation of iopamidol using a dual-wavelength system (265+280 nm, each lamp at 50% intensity) through direct photolysis and UV/chlorine oxidation. The synergy in direct photolysis was attributed to an increase in photon number between 265 and 280 nm, potentially inducing a higher rate to reach the excited state. The synergy in UV/FC was also supported by the promotion of chlorine photolysis and enhancement in reactive radicals production. Investigation on dual-wavelength synergy systems mainly gained interest for disinfection purposes [186–188], but more studies should clarify whether synergy might be significant during chemical degradation and, if so, an explicit explanation of the mechanisms involved.

4.4.7 Energy consumption

The electrical energy per order is defined as the electric energy in kWh required to reduce the concentration of a contaminant by one order of magnitude (90% removal) in 1 m³ of water, and it is measured in batch operations according to Eq. (4.8) [99].

$$EE/O_{UV} = \frac{P \cdot t}{V \cdot \log\left(\frac{C_0}{C}\right)} \quad Eq. (4.8)$$

Where P is the rated power or energy input (kW) of the lamp system, V (m³) is the volume of water treated in irradiation time t (h). In order to evaluate the overall estimation of the energy consumption for each UV-LED process, the electrical energy was calculated accordingly. Eq. (4.8) can be rewritten as a function of the time-based kinetic constant to Eq. (4.9) by converting the photoreactor contact time, t_{pc} , in min, the total volume, V , in litres, and considering that $\log(C_0/C) = 0.4343 \ln(C_0/C)$.

$$EE/O_{UV} = \frac{1000 \cdot P \text{ (kW)} \cdot t_{pc} \text{ (min)}}{V \text{ (L)} \cdot 0.4343 \cdot k \text{ (min}^{-1}) \cdot t_{pc} \text{ (min)} \cdot 60} = \frac{38.38 \cdot P}{V \cdot k} \quad Eq. (4.9)$$

During the UV/H₂O₂ and UV/FC treatment, the equivalent electrical energy of the oxidant, $Eq_{oxidant}$, was also considered, accordingly to Eq. (4.10) and Eq. (4.11).

$$EE/O_{oxidant} = Eq_{oxidant} \cdot \frac{[oxidant]_0}{\log\left(\frac{C_0}{C}\right)} \quad Eq. (4.10)$$

$$EE/O_{total} = EE/O_{UV} + EE/O_{oxidant} \quad Eq. (4.11)$$

The Eq to produce H₂O₂ was found in the literature to be $1.08 \cdot 10^{-5}$ kWh mg⁻¹ [189], while the energy consumption to produce chlorine was $1.16 \cdot 10^{-5}$ kWh mg⁻¹ [184].

$[Oxidant]_0$ is the initial concentration of oxidant added in mg m⁻³, while in this case, $\log(C_0/C)$ was directly considered as one, which corresponds to the reduction of one order

of magnitude of the contaminant. Table 4.15 reports the EE/O value at different wavelengths for direct photolysis, UV/H₂O₂ and UV/FC, considering the photoreactor contact time.

Table 4.15. The electrical energy per order for DCF degradation during different photolysis processes, considering the photoreactor contact time.

	Oxidant dosage (mg L ⁻¹)	EE/O _{oxidant}	EE/O _{UV} @ 100% (kWh m ⁻³ order ⁻¹)	EE/O _{total} @ 100%
UV				
265 nm	-	0.00	0.61 ± 0.05	0.61 ± 0.05
285 nm	-	0.00	0.58 ± 0.06	0.58 ± 0.06
310 nm	-	0.00	0.85 ± 0.05	0.85 ± 0.05
265+285 nm	-	0.00	0.52 ± 0.03	0.52 ± 0.03
UV/H ₂ O ₂				
265 nm	20	0.22	0.40 ± 0.01	0.61 ± 0.01
285 nm	20	0.22	0.43 ± 0.02	0.65 ± 0.02
310 nm	20	0.22	0.89 ± 0.05	1.11 ± 0.05
265+285 nm	20	0.22	0.44 ± 0.02	0.66 ± 0.02
UV/FC				
265 nm	20	0.23	0.41 ± 0.02	0.64 ± 0.02
285 nm	20	0.23	0.33 ± 0.01	0.56 ± 0.01
310 nm	20	0.23	0.51 ± 0.00	0.74 ± 0.00
265+285 nm	20	0.23	0.38 ± 0.01	0.61 ± 0.01

Although the UV-driven AOPs exhibit a higher degradation rate, the overall electricity demand is similar to photolysis alone due to the production of the oxidants. Despite the 310 nm lamp having a lower total electric power and current, the total EE/O was higher in comparison to the other cases, making it the least performing. During photolysis, the results of the other two lamps at 265 and 285 nm were comparable. However, when combined with H₂O₂, 265 nm followed by 285 nm demonstrated the highest effectiveness, while with FC, 285 nm performed the best.

The overall electrical energy consumption at different intensities for 265 and 285 nm lamps was also reported in Table 4.16, but similar results to their corresponding 100% power were obtained due to the linearity of the *k*-values with the intensity.

Table 4.16. The electrical energy per order for DCF degradation at different lamp intensities.

Oxidant dosage		EE/O _{total} @ 100%	EE/O _{total} @ 75%	EE/O _{total} @ 50%	EE/O _{total} @ 25%
(mg L ⁻¹)		(kWh m ⁻³ order ⁻¹)			
UV					
265 nm	-	0.61 ± 0.05	0.54 ± 0.03	0.59 ± 0.05	0.59 ± 0.07
285 nm	-	0.58 ± 0.06	0.59 ± 0.05	0.58 ± 0.08	0.68 ± 0.10
UV/H ₂ O ₂					
265 nm	20	0.61 ± 0.01	0.64 ± 0.04	0.66 ± 0.04	0.67 ± 0.04
285 nm	20	0.65 ± 0.02	0.71 ± 0.03	0.73 ± 0.05	0.71 ± 0.03
UV/FC					
265 nm	20	0.64 ± 0.02	0.66 ± 0.03	0.64 ± 0.01	0.63 ± 0.03
285 nm	20	0.56 ± 0.01	0.59 ± 0.02	0.60 ± 0.04	0.64 ± 0.05

4.4.8 Mineralisation

Mineralisation was evaluated through the measurement of DOC. The measures were taken at the end of the treatment, after 60 min of the operation time, and evaluated for the treatments that gave the highest performance: 265 and 285 nm alone, 265 nm combined with H₂O₂ and 285 nm with FC. Table 4.17 shows the values of DOC before the treatment for a solution of 20 mg L⁻¹ of DCF in distilled water and after the mentioned treatments. Finally, it shows the percentage of DOC removed during the degradation process.

Table 4.17. DOC value and DOC removal after the selected treatments.

Treatment	DOC (mg L ⁻¹)	DOC removal (%)
DCF in water, 20 mg L ⁻¹	10.95 ± 0.11	-
Photolysis at 265 nm	8.84 ± 0.25	19.26 ± 2.24
Photolysis at 285 nm	7.40 ± 0.35	22.39 ± 3.18
UV-driven AOPs: 265 nm/H ₂ O ₂	8.29 ± 0.20	24.29 ± 1.87
UV-driven AOPs: 285 nm/FC	8.70 ± 0.09	30.56 ± 0.78

After each treatment, the pollutant was almost completely removed, while DOC showed a partial decrease of only 20-30%, regardless of the degradation process employed. Similar

observations were made by Peng et al. [190], who studied the DCF degradation by UV-activated PMS after 2 h of irradiation and Fischer et al. [191] after 18 h of UV-A irradiation. Ardila et al. [192] also reported insignificant mineralisation after 30 min of direct photolysis or TiO₂-induced hydroxylation. Although some studies have achieved significant mineralisation with longer irradiation periods and higher oxidant amounts [192], it is possible that the degradation of DCF by-products is more recalcitrant than DCF itself. If complete degradation is possible to eventually form only H₂O, HCl and CO₂, longer exposure time and higher oxidant dosage might be needed.

4.4.9 By-products and dimers formation

During the photolysis of DCF, a visible yellowish colour appeared in all cases, as shown in Figure 4.45. According to Keen et al. [193] and Iovino et al. [194], the colour could be addressed to the formation of dimers, which are reported to be stable forms to UV irradiation. The dimers are the combination of two parent molecules or the parent and a product of the photolysis.

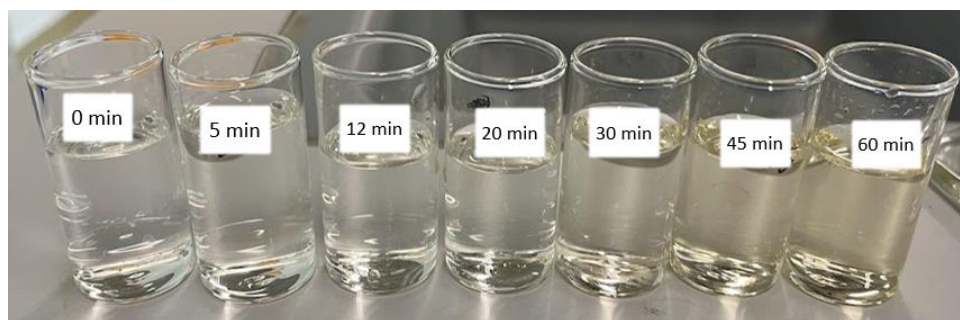


Figure 4.45. Change in colour over the treatment time. The sample in the figure represents the solution irradiated by the 265 nm lamp at 100 % intensity.

The change of colour was monitored as suggested by Keen et al. [193], visually and by measuring the absorbance at 400 nm during the treatment with 265 or 285 nm alone and after 265nm/H₂O₂ and 285nm/FC, Figure 4.46. The absorbance value increased with time until it reached a plateau value, which value and time depended upon the process, and it possibly

corresponded to the total degradation of DCF and the dimers reaching their maximum concentration.

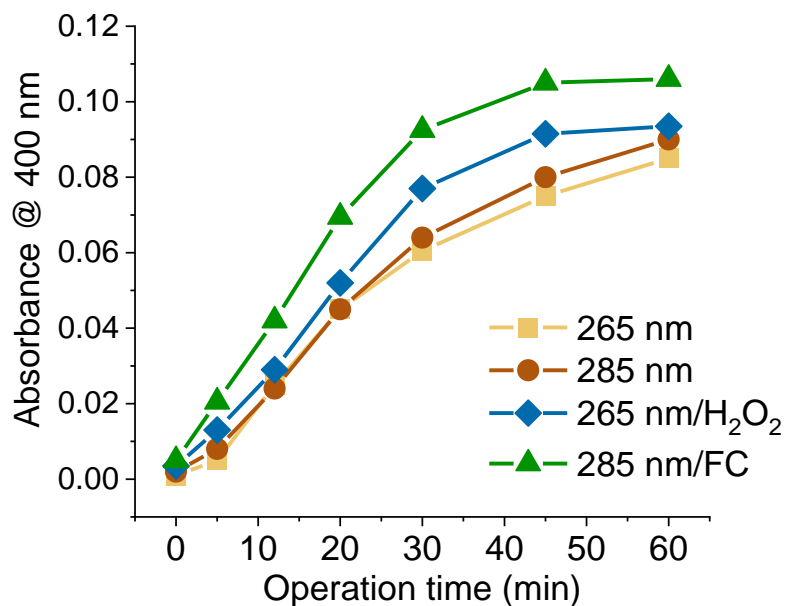


Figure 4.46. Absorbance at 400 nm versus operation time.

Finally, Figure 4.47 shows the colour at the naked eye and the absorption spectra in the UV range after 60 min of operation time.

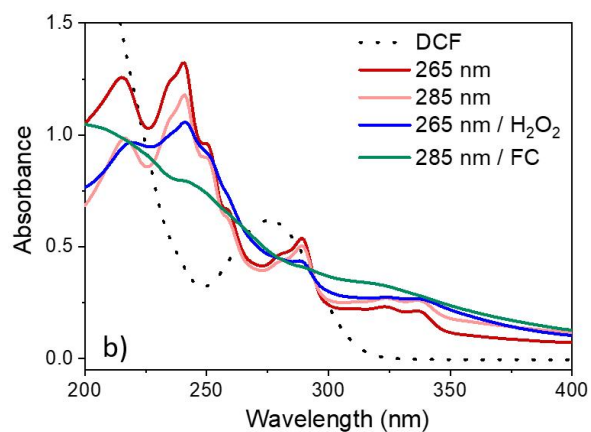
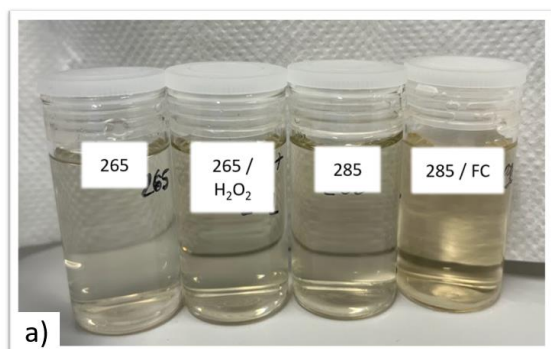


Figure 4.47. The colour at the naked eye (a) UV spectra in the range of 200-400 nm (b) after 60 min of operation time.

A second peak in the HPLC spectra is also appearing during the photolysis reaction at the retention time of 2.915 min, while the DCF retention time was at 3.236 min, as shown in Figure 4.48, where the peak at 1.863 was intrinsic to the column.

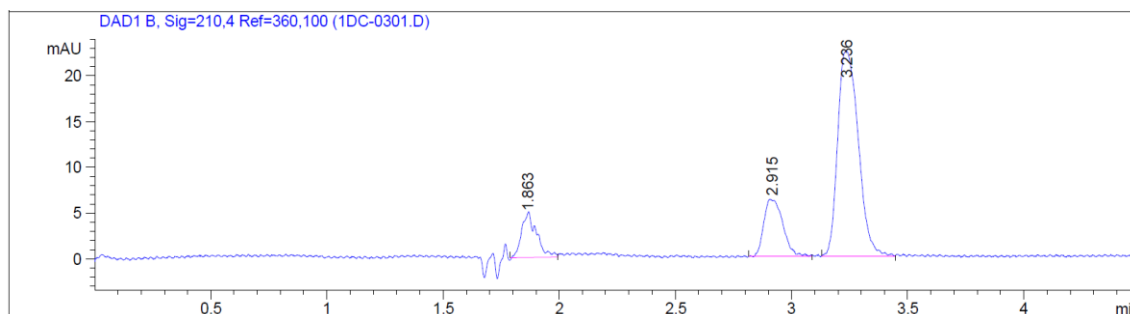


Figure 4.48. The peaks occurring during the DCF degradation. The example shown was taken after 5 min of operation time at 265 nm.

The peak at ca. 2.9 min rapidly increases during the treatment, but after reaching a maximum, it decreases much more slowly than the increase, as shown in Figure 4.49. Other studies also reported this peak, associating it with the potentially toxic and unstable by-product [195].

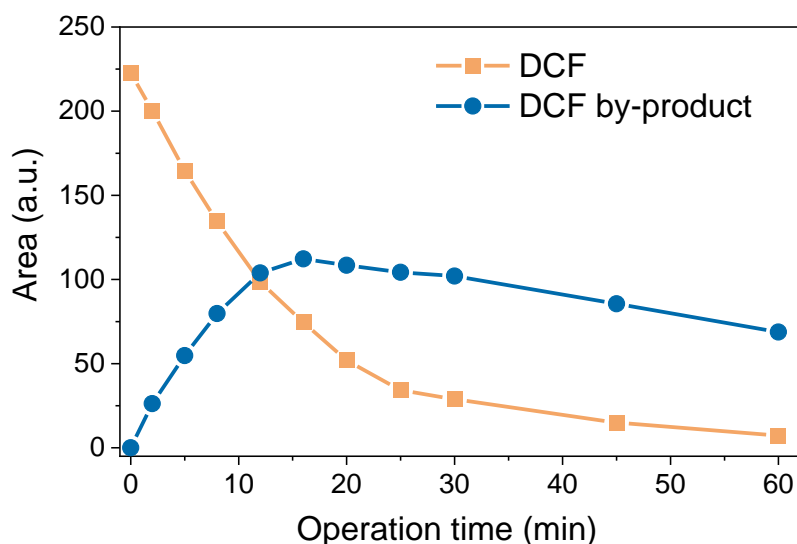


Figure 4.49. The trend of the DCF (yellow squares) and the DCF by-product (blue dots) peaks' area during the treatment. The example shown was taken for the photolysis alone at 265 nm.

Keen et al. [193] reported in detail all the degradation products during UV photolysis and proposed the chemical structures of the by-products, as shown in Figure 4.50.

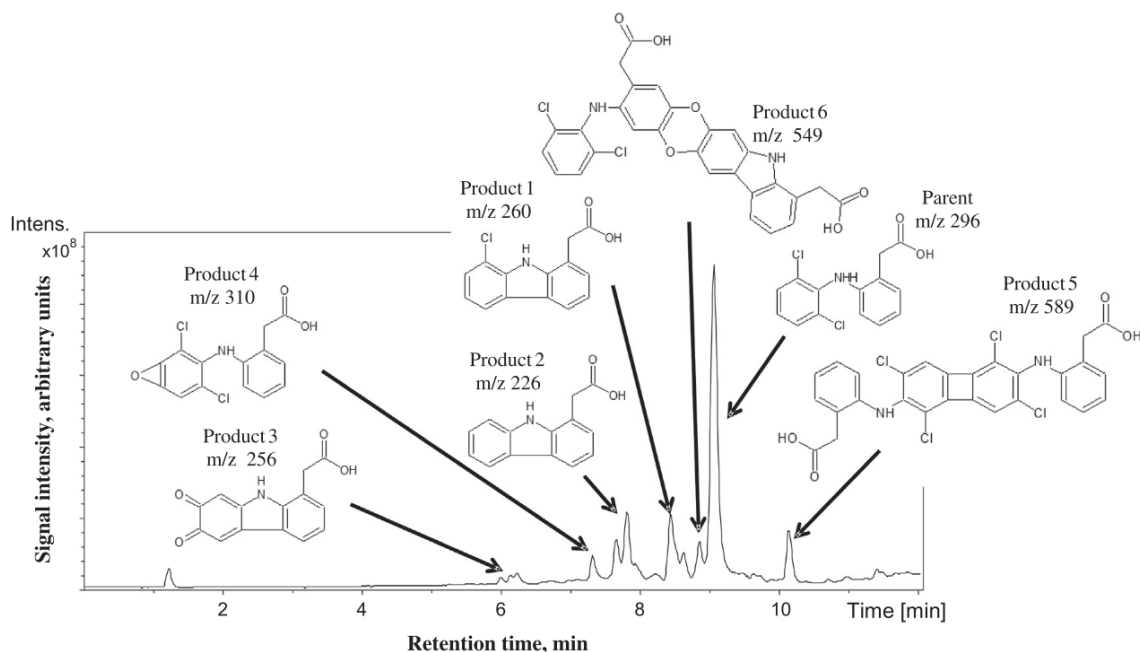


Figure 4.50. DCF degradation compounds after exposure to UV fluence at 254 nm. Proposed chemical structures of the products by Keen et al. [193].

According to their study, the HPLC peak could refer to “Product 1”, where DCF loses its first chlorine and closes the middle ring, or “Product 2”, where the second chlorine is also lost. On the other hand, the yellowish colour is due to the formation of the dimer, “Product 5”, which corresponds to the dimer with a 4-chlorine signature, or “Product 6”, the dimer with a 2-chlorine signature. Finally, their study showed that if the dimer continues to be irradiated, it loses all the chlorines, forming stable forms to additional UV degradation, which explains the low mineralisation degree. Therefore, in agreement with the DOC analysis, only a small part of the parent compound degrades, but the rest goes through condensation and forms these stable dimers, preventing further pollutant degradation. Nevertheless, the use of AOPs might help further the degradation of the by-products. However, in the UV/FC degradation process, Li et al. [93] highlighted slightly different by-products, but dimerisation still occurs. On the other hand, Lekkerkerker-Teunissen et al. [174] suggested that the influence of H_2O_2 in the degradation by-product path may be minimal and follow the same pattern as the UV direct photolysis.

4.4.10 Phytotoxicity

Finally, the phytotoxicity tests were performed after 60 min of operation time of the selected treatments: 265 and 285 nm alone, 265 nm/H₂O₂ and 285 nm/FC, as shown in Table 4.18. As mentioned in the methodology, the germination value was measured against the control condition, where distilled water without any sample was employed. A sample with a germination index below 70% is considered phytotoxic, while above 70% could be considered safe to release into the environment [148].

Table 4.18. Germination index (GI) for radish and tomato seeds after the selected treatments.

Treatment	GI (%) for radish	GI (%) for tomato
DCF in water, 20 mg L ⁻¹	39.15 ± 5.53	23.42 ± 5.16
Photolysis at 265 nm	57.56 ± 4.16	36.05 ± 4.20
Photolysis at 285 nm	60.82 ± 7.07	39.56 ± 7.75
UV-driven AOPs: 265 nm/H ₂ O ₂	71.60 ± 9.11	49.46 ± 9.98
UV-driven AOPs: 285 nm/FC	58.65 ± 3.22	47.72 ± 2.26

In both radish and tomato seeds, a GI value below 70% was observed when exposed to a sample of 20 mg L⁻¹ of DCF alone in distilled water. Tomato seeds were found to be more sensitive to toxic effluents, in agreement with previous findings by Ghanbari et al. [148]. After treatment, the GI values increased by around 20-30 percentage points in radish germination and 15-20 points in tomato plants. As expected, UV direct photolysis alone produced similar results for the two wavelengths, while among the oxidation processes, H₂O₂ might lead to higher detoxification compared to FC, in particular for the radish seeds. Nonetheless, the difference is negligible when taking into account the experimental error. In this investigation, the change in phytotoxicity was selected since there is limited research available on it [196]. Majewska et al. [196] investigated the impact of untreated DCF (32.7 mg L⁻¹) on the green alga *Chlamydomonas reinhardtii*, and observed oxidative stress and inhibition of photosynthesis. In another study, *Chichorium intybus* seedlings irrigated with DCF solution (1 mg L⁻¹) displayed a decrease in root biomass and an effect on chlorophyll biosynthesis, but also an increase in root length [197]. The phytotoxicity on *Lactuca sativa* was also explored, but neither the initial DCF solution nor the treated solution was toxic

[192]. Finally, Naddeo et al. [198] conducted a germination index study for *Lepidium sativum* (garden cress) but for a mixture of pharmaceuticals (DCF, amoxicillin, and carbamazepine with a DCF concentration of 2.5 mg L⁻¹ in the mix) treated under ultrasonic irradiation. Interestingly, the spiked WWTP effluent, compared to the non-spiked effluent, stimulated higher seed growth, attributed to the added nutrient elements resulting from the low drug concentration. Nevertheless, not all the experimental conditions led to a decrease in toxicity, and the mixture was found to be severely toxic to the microalga *Pseudokirchneriella subcapitata*. It should be noted that the concentration of the other pharmaceuticals was higher than that of DCF, which might have been less influential in the mixture.

On the other hand, several investigations have explored the toxicity of DCF by-products towards bacteria and organisms, such as *Vibrio fischeri*, *Vibrio quighaiensis*, *Photobacterium leiognathid*, *Daphnia similis*, and *Mus musculus* mice kidneys and livers. The toxicity towards *Vibrio fischeri* initially increased upon photo-transformation with UV-A irradiation, indicating that certain unstable by-products were more toxic towards those bacteria. However, toxicity decreased after 90 min of further treatment [191]. Another study investigated the toxicity towards the bacteria *Vibrio quighaiensis* by monitoring changes in their natural luminescence before and after treatment with UV/persulfate. The overall toxicity of the solution decreased, reaching a minimum of 1.5% inhibition, in contrast to the 4.5% inhibition observed for the DCF solution. Similarly, the toxicity initially increased, and after a gradual decrease, it increased again before a rapid decrease at the end of the treatment after 140 min [195]. Another study conducted by Alharbi et al. [199] reported the toxicity towards the naturally luminescent bacteria *Photobacterium leiognathid* after treatment with UV at 254 nm and after 254 nm/H₂O₂. While toxicity increased in the former case, the overall toxicity decreased below the assay's detection limit with H₂O₂.

Since the second peak in the HPLC spectra is potentially associated with a more toxic and unstable by-product [45], it is reasonable to associate it with the up-and-down toxicity behaviour encountered in the bacteria. Therefore, the treatment time and the total UV fluence must be carefully selected to avoid its presence in treated waters. In fact, while the occurrence of the dimers seems to have a small impact on toxicity, the mentioned compound is responsible for increasing toxicity until it is removed with further treatment.

Finally, research towards organisms' toxicity shows that untreated DCF were likely to cause tumours in mice livers, while no adverse effect was observed after DCF was treated by simulated solar-UV-A/ZnO/PPS [200]. In a separate study [192], a solution of 20 mg L⁻¹ of DCF was found to cause the mortality of all *Daphnia similis* organisms, while direct photolysis and TiO₂-assisted photodegradation effectively reduced the toxicity.

To conclude, UV-based treatments are effective in decreasing toxicity towards bacteria, organisms and plants, although the optimal treatment time should be chosen accurately to prevent the occurrence of toxic and unstable by-products. It should be noted that in various cases, including the current investigation, the toxicity of DCF was not diminished to levels below the established safety threshold. However, it is crucial to consider that the actual concentrations of DCF in natural water systems are significantly lower than those examined under many experimental conditions.

4.5 Environmental impact assessment

The ex-ante environmental LCA was performed to compare the innovative LED lamp to an LP mercury lamps photoreactor for their application in small-scale water treatment, using the removal of DCF as a case study for comparative purposes. Indeed, while UV-C LED lamps are a new technology with still relatively low efficiency, mercury lamps are at full growth, but the presence of mercury is highly concerning. In particular, the 265 nm lamp was chosen for the comparison in the UV-C range, but similar results can be extrapolated for the 285 nm lamp, which performed similarly in the oxidants' absence.

4.5.1 Description of the case study

Data for the UV-C LEDs system at 265 nm were collected from the experimental work carried out in this thesis. On the other hand, a similar photoreactor was chosen for the mercury lamp system (254 nm). It was considered that the two photoreactors had the same lab equipment, and they only differed on the power input, the energy emitted by the lamps at the same distance from the quartz tube, and the working wavelength. It is also important to notice that for the mercury lamp photoreactor, while the quartz tube was considered with

the same diameter of 20 mm, the height irradiated from the mercury lamp was 160 mm compared to the 108 mm irradiated from the LEDs lamp, given the different geometries of the two lamps. For simplicity and since they would be the same for the two systems, the sensors, the VFD, and the Arduino microcontroller were not considered in the lab equipment inventory. The two systems are schematised in Figure 4.51.

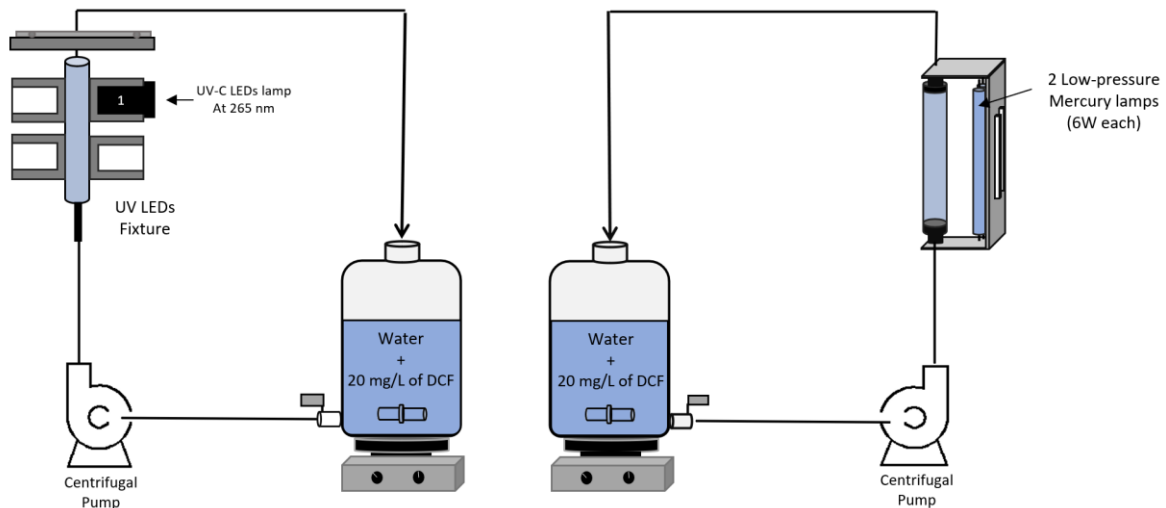


Figure 4.51. Schematic representation of the two photoreactors: UV-C LEDs lamp (to the left side) and two LP mercury lamps (to the right side).

4.5.2 Goal and scope

First of all, the FU was defined considering the main objective of the investigation. “The treatment of 1 L of polluted water with 20 mg L⁻¹ of diclofenac to achieve a 90% removal of the contaminant” was the FU chosen. The removal of 90% of contaminants is a standard approach [126]. Furthermore, the FU provides the reference unit, and 1 L of polluted water was selected, given that the final aim is water treatment application.

The system boundaries for each process were also determined and shown in Figure 4.52. The study takes into consideration the cradle-to-gate approach, similar to previous studies [5,8]. The system boundaries included the production of the two photoreactors (the UV-C lamp and the lab equipment), including resources, energy and transport of the main materials, the energy needed during the operation, and the emission to air, water and soil

during production. In contrast, the end-of-life of the photoreactors was omitted due to the uncertainty of the disposal.

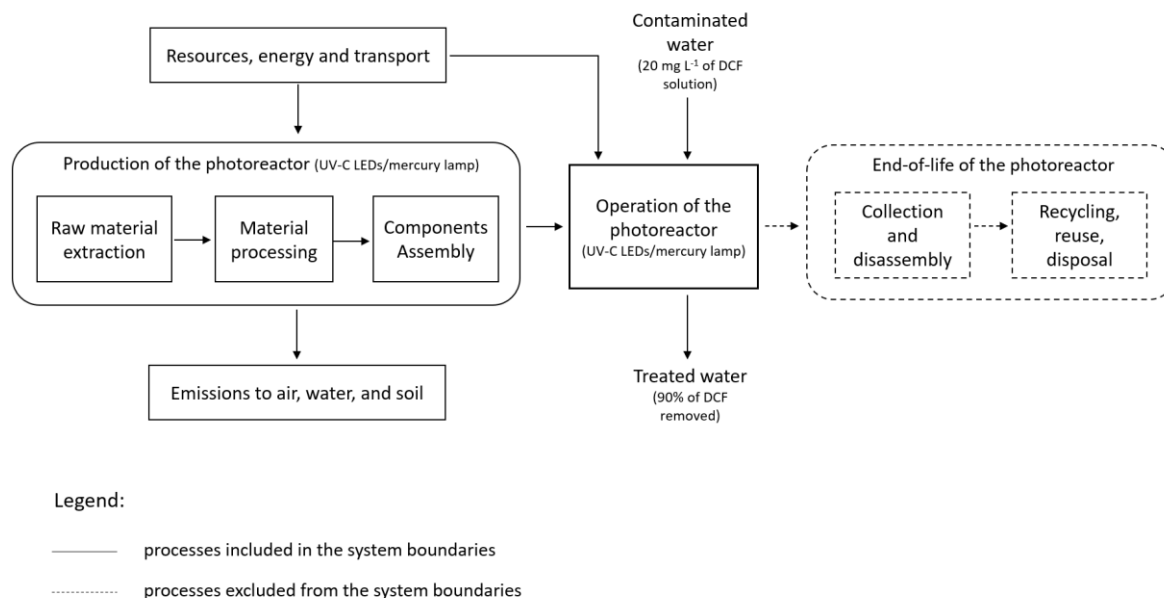


Figure 4.52. Scheme of the system boundaries for the two photoreactors.

4.5.3 Life cycle inventory

In defining the inventory, the cut-off options for the unit process were selected from the ecoinvent database. They differ from the other choices solely in the way the waste and recyclable materials are treated, which is reflected in the resulting impact scores [153].

The specific input data were collected by selecting the global market {GLO} for the material flows, which represents the consumption mix of the product and accounts for the trade between producers and consumers. The global situation is considered to measure the average distances, modes of transport required, and the product losses occurring during transport, loading, and unloading. While for the manufacturing process, the European market {RER} was selected, assuming that the production occurs in Europe once the material is available. Also, the electricity employed was selected for a small-scale application (low voltage) from the European market. The selection was made to create an average supply chain at the European level and extrapolate conclusions for all European countries.

The material and processes input for the UV-C LED lamp and each mercury lamp are shown respectively in Table 4.19 and Table 4.20. The UV-C LED lamp materials were directly quantified by opening and dissecting the lamp. In contrast, the material inputs for the mercury lamp were estimated from the ecoinvent database [153]. In this regard, a few modifications were appointed to take into account the manufacturing processes for aluminium, plastic, and steel and avoid the use of primary material such as the “Aluminium, primary, ingot”. Furthermore, the amounts were remodelled for the mercury lamp system under study by considering a mass proportion between the ecoinvent amounts (380 g) and the lamp employed of 20 g. A ballast was added to each lamp to provide the correct starting and operating voltage and current, as recommended by the lamp manufacturer. Also, in agreement with the ecoinvent database [153], silica sand was assumed to be equivalent to quartz in both lamp inventories.

Table 4.19. Raw materials and processes input for 1 unit of the UV-C LEDs lamp.

	Materials and processes	Ecoinvent dataset selected	Amount (1 unit)	Units
LED lamp 265 nm	16 LEDs	Light emitting diode {GLO} market for Cut-off, U	0.31	g
	Heatsink	Aluminium alloy, AlMg3 {GLO} market for Cut-off, U	127.59	g
	Lamp case	Aluminium alloy, AlMg3 {GLO} market for Cut-off, U	130.70	g
	Screws/spring	Aluminium alloy, AlMg3 {GLO} market for Cut-off, U	5.78	g
	Aluminium processing	Metal working, average for aluminium product manufacturing {RER} processing Cut-off, U	264.07	g
	Quartz glasses	Silica sand {GLO} market for Cut-off, U	5.42	g
	Fans	Fan, for power supply unit, desktop computer {GLO} market for Cut-off, U	23.47	g
	PLC-programmable logic controller	Printed wiring board, for power supply unit, desktop computer, Pb free {GLO} market for Cut-off, U	20	g

4. Results and discussion

Table 4.20. Raw materials and processes input for 1 unit of an LP mercury lamp of 6 W (20 g).

	Materials and processes	Ecoinvent dataset selected	Amount (1 unit)	Units
LP mercury lamp 6 W (20 g)	Aluminium parts	Aluminium, wrought alloy {GLO} market for Cut-off, U	1.72	g
		Metal working, average for aluminium product manufacturing {RER} processing Cut-off, U	1.72	g
	Mercury	Mercury {GLO} market for Cut-off, U	0.021	g
	Plastics parts	Polyethylene, high density, granulate {GLO} market for Cut-off, U	0.098	g
	Plastics parts	Polypropylene, granulate {GLO} market for Cut-off, U	2.402	g
	Plastic processing	Injection moulding {RER} processing Cut-off, U	2.5	g
	Glass	Sanitary ceramics {GLO} market for Cut-off, U	6.617	g
	Lamp quartz tube	Silica sand {GLO} market for Cut-off, U	8.858	g
	Steel parts	Steel, unalloyed {GLO} market for Cut-off, U	0.229	g
		Metal working, average for steel product manufacturing {RER} processing Cut-off, U	0.229	g
Electronics, for stabilising lamp emissions (ballasts)	Electronics, for control units {GLO} market for Cut-off, U	55	g	

While the materials and processes input for the lab equipment are shown in Table 4.21.

Table 4.21. Raw materials and processes input for the lab equipment, which are equal for the two photoreactors.

	Materials and processes	Ecoinvent dataset selected	Amount Used	Units
Lab equipment	UV Quartz tubes	Silica sand {GLO} market for Cut-off, U	130	g
	PVC tube systems	Polyvinylchloride, emulsion polymerised {GLO} market for Cut-off, U	1	kg
		Extrusion, plastic pipes {RER} extrusion, plastic pipes Cut-off, U	1	kg
	Plastic container	Polyethylene, low density, granulate {GLO} market for Cut-off, U	200	g
		Blow moulding {RER} blow moulding Cut-off, U	200	g
	Magnetic stirrer	Permanent magnet, for electric motor {GLO} production Cut-off, U	0.4072	kg
	Magnetic bar	Steel, low-alloyed {GLO} market for Cut-off, U	7.45	g
		Metal working, average for steel product manufacturing {RER} processing Cut-off, U	7.45	g
	Centrifugal pump	Pump, 40W {GLO} market for Cut-off, U	1	p
	Aluminium support base	Aluminium, wrought alloy {GLO} market for Cut-off, U	2	kg
Metal working, average for aluminium product manufacturing {RER} processing Cut-off, U		2	kg	

Lastly, it is important to define each part's lifetime: both the LED lamp and the mercury lamp photoreactors were considered with a life span of 8,000 h. The former experimentally showed a lifetime between 10,000 h to reach 80% and 6,000 h to reach 60% of the initial intensity; therefore, an average value was taken. On the contrary, for the mercury lamp, the manufacturer data was taken. Regarding the lab equipment, 15 years, which corresponds to the lowest lifetime expected for electromechanical equipment [103,127], were considered for the magnetic stirrer, the magnetic bar, the centrifugal pump, and the aluminium support base. In contrast, 3 years were considered for the quartz tube and the plastic components since they are more sensitive to breakage, and plastic could be affected by the contaminant. While the tables shown represent the construction phase, the operational phase is considered through the electricity demand of the UV source, the centrifugal pump, and the magnetic stirrer, which depends on the treatment time and, therefore, the effectiveness of the system. Data obtained from the previous section showed that the 265 nm LED lamp under only photolysis reached 90% removal of DCF after 29.8 min of the operation time, which is the time considered for the energy costs associated with the system. The mercury lamp photoreactor shown in Figure 4.51 was first characterised by chemical actinometry to experimentally evaluate the radiation emitted by the mercury lamps, which was 150.70 W m^{-2} compared to the 220 W m^{-2} of the UV-C LED lamp. Finally, to measure the 90% removal of DCF through the mercury lamp system, the UV fluence-based kinetic constant at 254 nm was evaluated from the 265 nm results ($k'_{265}=1.73 \cdot 10^4 \text{ J}^{-1} \text{ m}^2$) according to Eq. (3.19), considering the molar absorption coefficient at 254 nm and assuming the same quantum yield at the two wavelengths. From the estimation, the UV fluence-based k'_{254} was $1.10 \cdot 10^4 \text{ J}^{-1} \text{ m}^2$. Considering the mercury lamp irradiation of 150.70 W m^{-2} , the time-based constant independent on the system k_{254} was estimated as 1.00 min^{-1} in comparison with the value of 2.28 min^{-1} at 265 nm. However, to calculate the time inside the reactor, the active volume over the total volume was considered by Eq. (4.4), which reduced to Eq. (4.12).

$$\ln\left(\frac{0.1}{1}\right) = -k \cdot t \cdot \frac{V_R}{V_T} \quad \text{Eq. (4.12)}$$

Where V_T was 1 L in the two cases, while V_R of the mercury lamp photoreactor was 0.050 L against the 0.034 L of the LEDs photoreactor, given the longer size of the mercury lamp

compared to the LED lamp. Finally, the time in the mercury lamp photoreactor was evaluated to be 45.96 min.

The electrical energy consumed by the two UV photoreactors was consequently calculated from Eq. (4.8), which reduced to Eq. (4.13), considering $\log(C_0/C) = 1$ (one order of the pollutant is degraded) and a total volume of 1 L.

$$\text{Electricity consumption (Wh)} = P \text{ (W)} \cdot t \text{ (h)} \quad \text{Eq. (4.13)}$$

Where t is the total illumination time, and P is the power input of the lamps.

The centrifugal pump and the magnetic stirrer were the same for the two photoreactors, and the power inputs were taken from the manufacturer data, respectively 51 and 90 W. However, only half power was considered for the latter since the stirring was used approximately at half of the maximum rpm allowed. For the mercury lamp system, the time the lamps need to warm up (15 min as per standard procedures) was also taken into account. Table 4.22 summarises the electrical energy consumed during the operation phase for the two photoreactors, where the values in brackets indicate the percentage contribution to the total operational electricity demand. The electricity chosen from the ecoinvent database was “Electricity, low voltage {RER}| market group for| Cut-off, U”, which corresponds to the mix for the European market for households’ applications.

Table 4.22. Electricity consumption referred to the FU during the operation phase for the two photoreactors.

Energy source	Power Input (W)	Treatment time (h) UV-C LEDs photoreactor	Inputs, energy (Wh) UV-C LEDs photoreactor	Treatment time (h) Mercury lamp photoreactor	Inputs energy (Wh) Mercury lamp photoreactor
Electricity for UV-C LEDs lamp	36.14	0.50	17.95 (27%)	-	-
Electricity for the mercury lamp	12.00	-	-	0.77 + 0.25*	12.19 (14%)
Electricity for the centrifugal pump	51.00	0.50	25.33 (39%)	0.77	39.06 (46%)
Electricity for the magnetic stirrer	45.00	0.50	22.35 (34%)	0.77	34.47 (40%)

*The time spent to warm up the mercury lamps (15 min = 0.25 h) was included in the treatment time of the mercury lamp photoreactor.

According to the operation time and the lifetimes, the operation phase for the LEDs photoreactor also included $6.2 \cdot 10^{-5}$ p of UV-C LED lamp, $1.9 \cdot 10^{-5}$ p of quartz tube, plastic tubes and plastic container, and $3.8 \cdot 10^{-6}$ p of magnetic stirrer, magnetic bar, centrifugal pump, and aluminium support base. Whereas for the mercury lamp photoreactor, during the operation phase were needed $2.5 \cdot 10^{-4}$ p of LP mercury lamps, $2.9 \cdot 10^{-5}$ p of quartz tube, plastic tubes and plastic container, and $5.8 \cdot 10^{-6}$ p of the rest of the lab equipment.

4.5.4 Life cycle impact assessment

The Environmental Footprint (EF) 3.0 method was employed as it is the reference method proposed by the European Commission [201], with the scope of bringing together different methods under one. For instance, regarding toxicity, the EF method includes the USEtox model, which calculates the impacts of chemicals on ecosystems and human health [202]. The EF method assesses the environmental impacts through 16 midpoint impact categories; indeed, the midpoint level is generally considered to be more accurate than the endpoint level [203]. The methods usually differ on the characterisation factor, which is the factor that converts an elementary exchange into the reference unit, for example, kg CO₂-equivalents for the climate change category. The 16 impact categories covered in the EF method are climate change, ozone depletion, ionising radiation, photochemical ozone formation, particulate matter, human toxicity (cancer and non-cancer effects), acidification, eutrophication (freshwater, marine, terrestrial), ecotoxicity freshwater, land use, water use, and resource use (fossils, minerals and metals). Each category strongly correlates with the sustainable development goals (SDGs), as shown in Figure 4.53 [204].

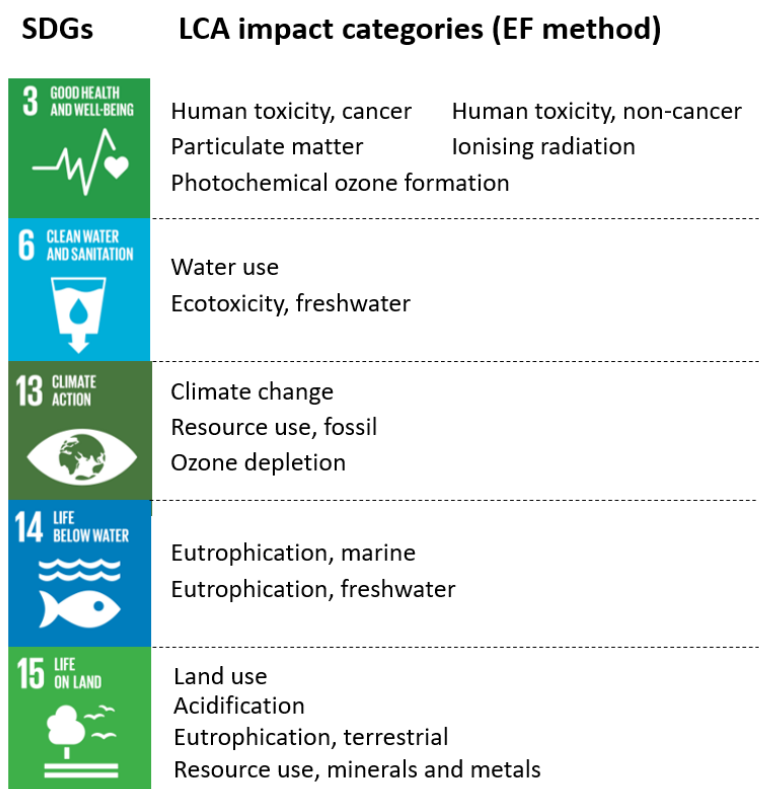


Figure 4.53. Connection between the LCIA impact categories of the EF method with the SDGs. Adapted from [204].

4.5.5 UV-C LEDs photoreactor versus mercury lamp photoreactor

LCA results were computed through the implementation of the inventory data referred to the FU in SimaPro [154] and solved through the EF method. Figure 4.54 shows the relative impacts of the two systems for the 16 midpoint categories.

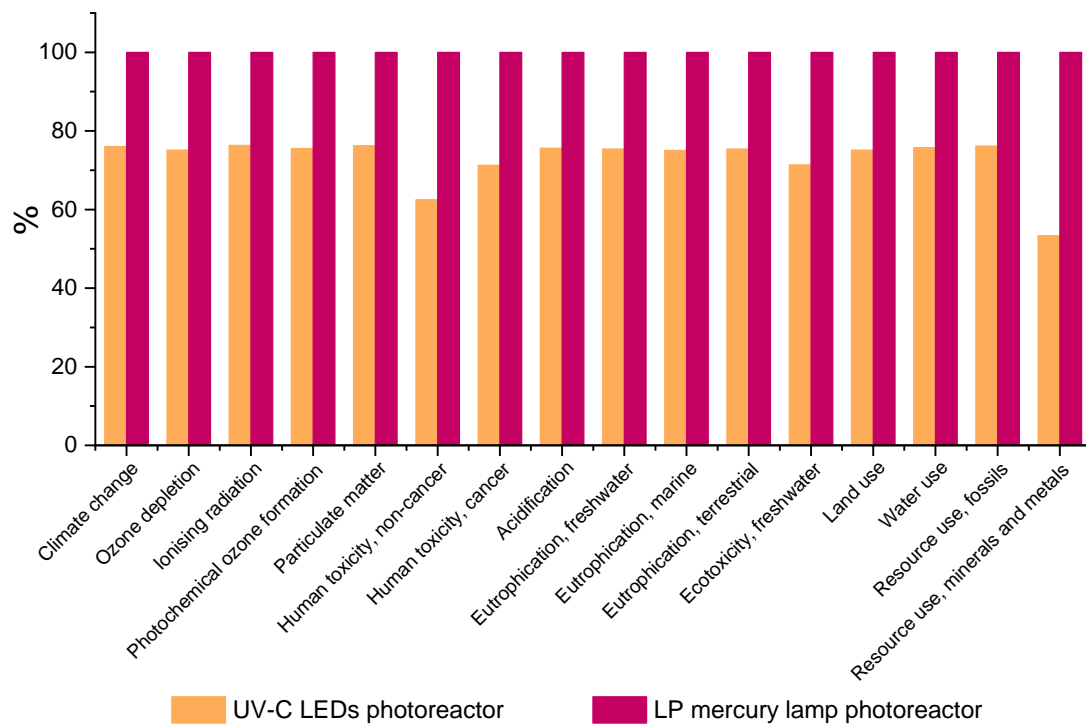


Figure 4.54. Relative impacts in percentage of the UV-C LEDs and the LP mercury lamp photoreactors referred to the FU on the 16 categories of the EF method.

It is noticeable that the LEDs system outperformed in all potential environmental impact categories, having around 25% less impact in almost all categories. The exceptions were “Human Toxicity, non-cancer” and “Resource use, minerals and metals”, where the impacts were even lower, 38% and 47%, respectively. These results are very promising for the wide implementation of LEDs in water treatments. However, they are mainly linked to the different times required to treat the solution and, therefore, the impacts of the energy related to the centrifugal pump and the magnetic stirrer. Even if the active volume in the mercury lamp photoreactor was larger, meaning less recirculation for volume treated, the time needed to degrade 90% of DCF was 1.5 times that of the LEDs photoreactor due to the lower efficiency at 254 nm and the lower irradiation energy. Therefore, the electricity used to light up the lamp, recirculate and stir the solution for a prolonged time was mainly responsible for the higher environmental impacts.

Unfavourable case

An unfavourable scenario for the UV-C LEDs photoreactor was evaluated by decreasing the LED lamp irradiation so that the electricity consumption for the pump and magnetic stirrer was similar between the two systems, as they are specific to the experimental assembly. In this way, the aim was to identify the influence on the potential environmental impacts of the UV source in water treatments while the other variables remained similar. The LEDs photoreactor operation time was redefined by considering the same irradiation as that of the mercury lamp photoreactor. Taking advantage of the linear relationship between LED lamp irradiance, DCF degradation, and lamp power, working at 150.70 W m^{-2} (68% lamp intensity) corresponded to an operation time of 43.38 min and a power input of 24.79 W. Under these conditions, the overall time in the two photoreactors was comparable since the lower efficiency of the 254 nm system was counterbalanced by its larger active volume given by the mercury lamp geometry. In this case, the energy inputs per FU for the LEDs photoreactor were 17.92 Wh for the lamp, 36.88 Wh for the centrifugal pump, and 32.54 Wh for the magnetic stirrer. Figure 4.55 shows the output in this unfavourable case.

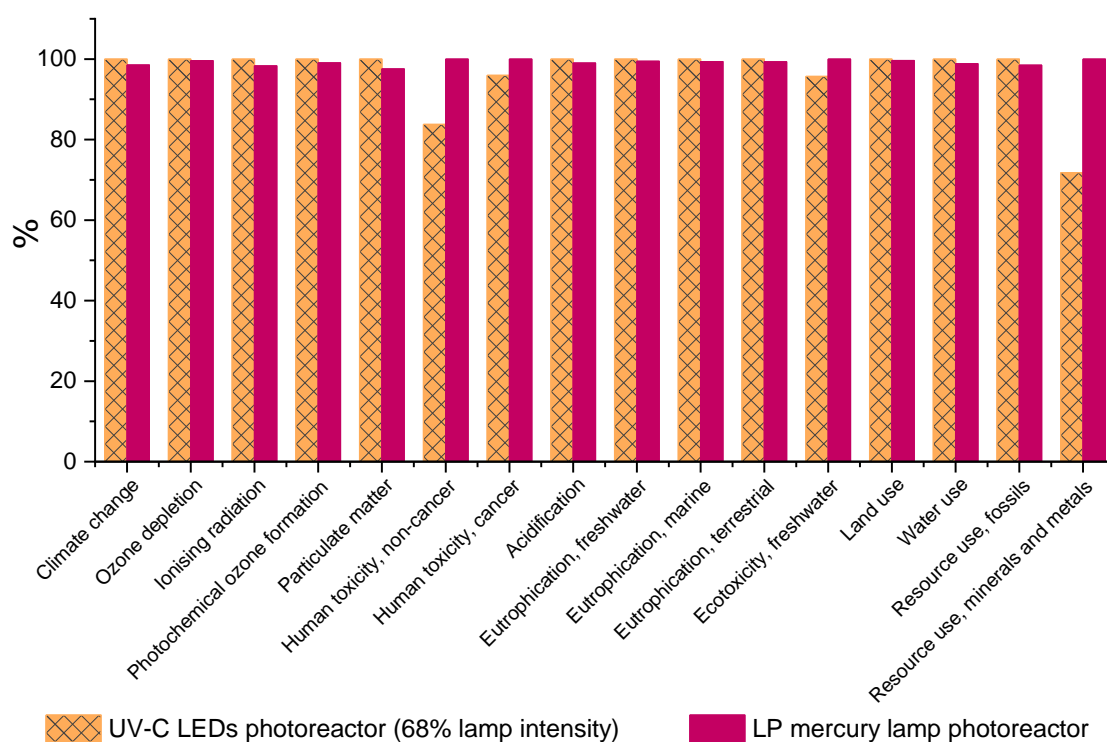


Figure 4.55. Relative impacts in percentage of the UV-C LEDs and the LP mercury lamp photoreactors when the lamps are emitting at the same irradiation. Results referred to the FU on the 16 categories of the EF method employed.

This time, the impacts are quite comparable, and it is less straightforward to state the overall best performance. In this case, the energy input for the centrifugal pump and the magnetic stirrer were quite similar, and therefore, it is highlighted the impact of the higher energy input needed by the LEDs lamp compared to the mercury lamps (17.92 Wh versus 12.19 Wh), which is expected given the fact that UV-C LEDs still are relatively inefficient and at the early stage of development. Even so, the categories mentioned earlier, “Human toxicity, non-cancer” and “Resource use, minerals and metals”, are still more affected by the mercury lamp photoreactor, where the LED system has 16% and 28% less impact, respectively. Additionally, the “Human toxicity, cancer” and the “Ecotoxicity, freshwater” categories were also more affected by the mercury lamp photoreactor, with a ~4% difference in both cases. All these categories were negatively affected by the higher environmental burden of the mercury lamps compared to the LEDs, mainly due to mercury production, which is found to release as emission to air 16% of mercury for each kg produced, according to the ecoinvent dataset [153]. For the rest of the categories, the differences were between 1-2% in favour of the mercury lamp, a percentage that can be considered inside the dataset’s uncertainty and is due to the higher energy inputs required for the UV-C LED lamp.

Given the similarities of the results in this case and the interest in understanding the hotspots of the systems, the individual percentage contributions for the three main parts: the UV source, the lab equipment, and the overall electricity employed during the treatment, were evaluated for the two photoreactors separately. Figure 4.56 shows the relative contribution of each part for “Climate change” and “Human toxicity, non-cancer”. These categories were chosen as representative of the entire dataset, other than being particularly important for decision-making. The contribution within “Climate change” highly resembles the contribution within most of the categories, while between “Human toxicity, non-cancer” and “Resource use, minerals and metals”, where the mercury lamp was remarkably more impactful than the UV-C LEDs, only the former was shown for discussion since they were showing similar results.

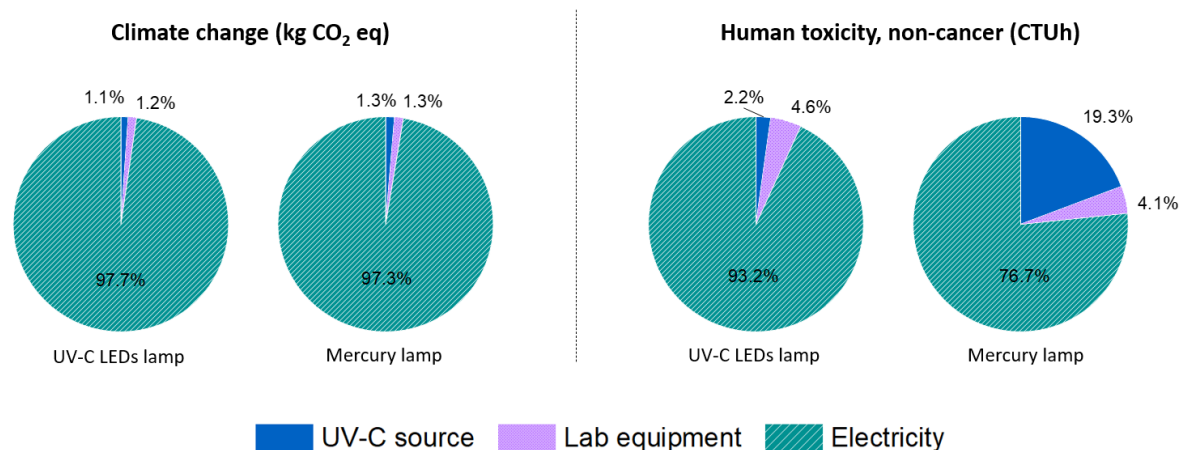


Figure 4.56. Percentage contributions referred to the FU of the individual components: UV-C source (blue), lab equipment (violet), and electricity (teal) for the impact categories: “Climate change” on the left side and “Human toxicity, non-cancer” on the right side.

It is clear that electricity is the main contributor in all categories. In the case of “Climate change”, in which the total values were 0.0352 and 0.0346 kgCO₂ equivalent for the UV-C LED and the mercury lamp, respectively, more than 97% was attributed to the energy consumption in both cases. On the other hand, for “Human toxicity, non-cancer”, with values respectively of $4.83 \cdot 10^{-10}$ and $5.77 \cdot 10^{-10}$ CTUh for the UV-C LEDs and the mercury lamp, the impact of the latter in percentage was more prominent given the toxicity of mercury, reaching almost one-fifth of the entire category, whereas, in the case of the UV-C LEDs, the impact was ten times less.

Favourable case

A second case, this time favourable for the UV-C LEDs photoreactor, was evaluated considering the predicted trend of the UV-C LEDs efficiency in the coming years. The power input for the UV-C LED lamp was assumed to be 20% lower, a value expected to be reached by 2030 [119], and considering that from 2019, when the UV-C LEDs were first chosen to build the lamp, the market has already seen considerable steps. Therefore, Figure 4.57 compares the mercury lamp photoreactor, which market can be considered stable [119], with the base case at 100% intensity of the UV-C LEDs and the unfavourable case when working at 68% of the LED lamp, both with 20% lower power inputs, therefore considering 28.92 and 19.83 W instead of 36.14 and 24.79 W, respectively.

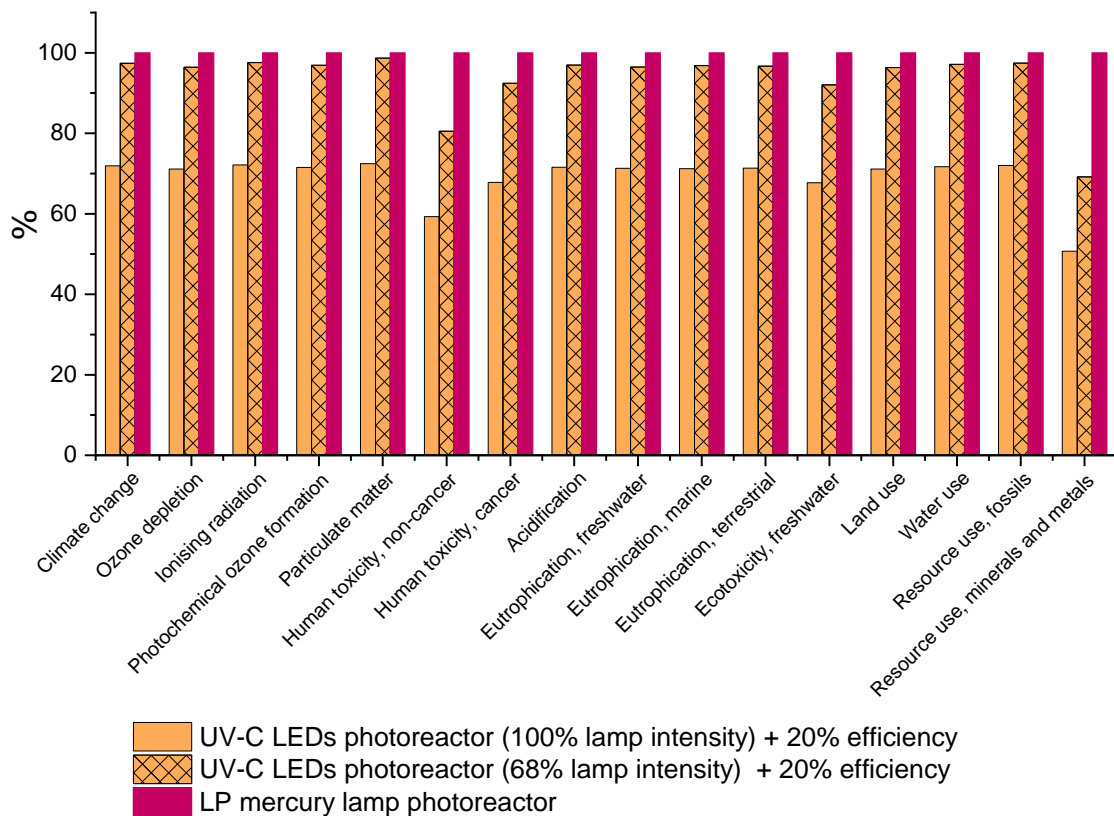


Figure 4.57. Relative impacts in percentage of the UV-C LEDs and the UV mercury lamp photoreactors assuming a 20% improvement in the energy efficiency of the UV-C LED lamp. The results refer to the FU on the 16 categories of the EF method employed.

With only 20% higher efficiency, UV-C LEDs performed better than mercury lamps in all categories, also when working at a lower intensity. The UV-C LEDs lamp at 68% had around 3% less impact in all categories, except for the ones it was already outstanding in the unfavourable case, where the impact was 20 and 30% lower. Whilst the UV-C LEDs lamp at 100% intensity had more than 27% less impact in all categories. Assuming that this higher efficiency will be reached in the next years, it can be concluded that the results are very promising for the implementation of the UV-C LED lamp in water treatment systems. However, for the system analysed, it is specifically recommended to prioritise working at a higher intensity and reduce the overall time of the treatment, whether possible.

4.5.6 Comparison between UV-C, UV-C/H₂O₂, and UV-C/FC

The addition of an oxidant also provides a strategy to reduce the required operation time. However, in this case, the contribution of the oxidant to the impact categories should also be considered. As mentioned, Pesqueira et al. [103] evaluated the sustainability of three oxidants, H₂O₂, PMS, and persulfate, and found the unsuitability of the last two even if shorter times and higher efficiencies were achieved. Therefore, in this section, the life cycle impacts of combining UV-C with H₂O₂ and FC were investigated with the same FU, where the UV source was the UV-C LEDs lamps at 265 nm, previously inventoried.

The operation times considered were taken from the experimental results carried out in this thesis, where 90% of the DCF removal was achieved at 0.50, 0.33, and 0.34 h for UV-C, UV-C/H₂O₂, and UV-C/FC, respectively. Indeed, while FC was more efficient in removing DCF when coupled with 285 and 310 nm, with the 265 nm lamp, the kinetic constants with the two oxidants were very similar. Within SimaPro modelling, the correspondingecoinvent datasets of the oxidants were added to the UV-C LEDs treatment inventory, in particular, “hydrogen peroxide, without water, in 50% solution state {RER}| market for | Cut-off, U” for UV-C/H₂O₂ and “sodium hypochlorite, without water, in 15% solution state {RER}| market for | Cut-off, U” for UV-C/FC, in the amount needed for a final concentration in solution of 20 mg L⁻¹, respectively 40 and 133.33 mg. Table 4.23 shows the different operation times and the electrical consumption for the three UV-C_{265nm} treatments.

Table 4.23. Electrical energy inputs by the three UV-C_{265 nm} LED treatment systems, referred to the FU.

Treatment type	Operation Time (h)	Input energy lamp (Wh)	Input energy pump (Wh)	Input energy stirrer (Wh)
UV-C	0.50	17.93	25.33	22.35
UV-C/H ₂ O ₂	0.33	11.73	16.56	14.61
UV-C/FC	0.34	12.15	17.15	15.14

According to the new operation times, the operation phase for the UV-C/H₂O₂ treatment required 4.1·10⁻⁵ p of UV-C LED lamp, 1.2·10⁻⁵ p of quartz tube, plastic tubes and plastic container, and 2.5·10⁻⁶ p of magnetic stirrer, magnetic bar, centrifugal pump, and aluminium

support base, while for the UV-C/FC treatment, it was needed $4.2 \cdot 10^{-5}$ p, $1.3 \cdot 10^{-5}$ p, and $2.6 \cdot 10^{-6}$ p, respectively. The results are finally shown in Figure 4.58.

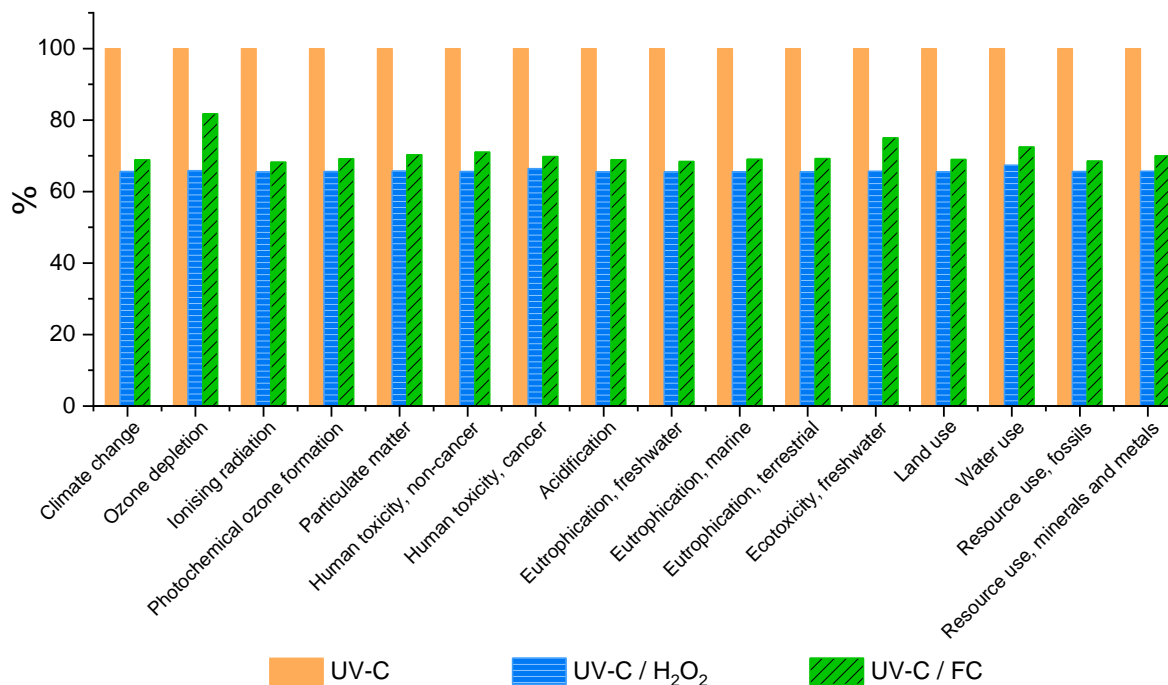


Figure 4.58. Relative impacts of the three UV-C_{265 nm} LED water treatments (UV-C, UV-C/H₂O₂, and UV-C/FC) for the removal of 90% of DCF on the 16 categories of the EF method.

The addition of H₂O₂ or FC led to an average reduction of around 35% and 30%, respectively, in all the impact categories. Therefore, the addition of the oxidants generated less impact on the environment than the additional electricity consumption required for longer times when no oxidant is added. However, when comparing the two UV-based AOPs with each other, H₂O₂ showed, on average, 5% lower impacts, except for “Ozone depletion” and “Ecotoxicity, freshwater”, where the impact difference was 19.5% and 12.5%, respectively, being these last two categories the most affected by the addition of sodium hypochlorite. Figure 4.59 shows the relative impacts of the oxidants, UV-C_{265nm} LED lamp, lab equipment, and electricity in the three cases for four selected categories: “Climate change” and “Human toxicity, non-cancer”, as previously selected and quite representative of the distribution in all the other categories, and “Ozone depletion” and “Ecotoxicity, freshwater” since the most affected by the oxidant selection. While H₂O₂ contribution to the

environmental impact is almost null at the concentrations employed (below 1% in all categories), the use of FC impacted in percentages respectively of 1.6%, 17%, 4.5%, and 9.6% in “Climate change”, “Ozone depletion”, “Human toxicity, non-cancer”, and “Ecotoxicity, freshwater”. The higher impacts were due to sodium hypochlorite production, which involved the releases in the water of 0.5 kg of chloride and 0.3 kg of sodium for each kg produced, according to the information provided in the ecoinvent dataset [153].

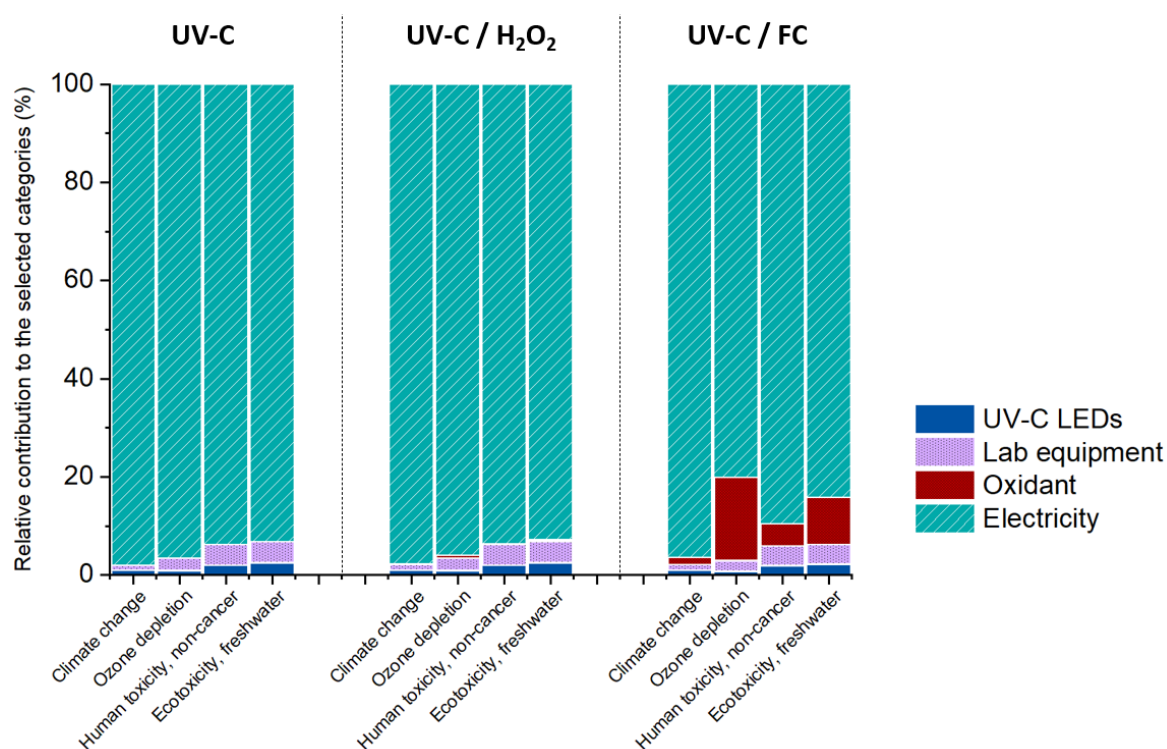


Figure 4.59. Relative contribution of the oxidant (red), UV-C_{265 nm} LED lamp (blue), lab equipment (violet), and electricity (teal) of the three UV-C water treatments per FU for the selected four categories. “Climate change”, “Human toxicity, non-cancer”, “Ozone depletion”, and “Ecotoxicity, freshwater”.

Therefore, among H₂O₂ and FC, the former is preferred when similar treatment times are required to achieve DCF degradation. However, the use of FC is still recommended in comparison to only photolysis, and if it achieves shorter treatment times compared to H₂O₂, like in the case of the 285 nm LED lamp, where the operation times were 12.36 min and 16.31 with FC and H₂O₂, respectively, and the corresponding extra electricity consumed would advantage the use of UV/FC. Since, in all cases, electricity is the main hotspot for this

technology in the experimental system studied; strategies to reduce its environmental burden are necessary.

4.5.7 Renewable electricity

The results of employing renewable energy sources to replace the selected average electricity mix for the European market have therefore been investigated. As a feasible option for countries like Spain that benefit from high solar exposition all year, the electricity from the photovoltaic energy source was selected from the ecoinvent database: “electricity, low voltage {ES}| electricity production, photovoltaic, 3 kWp slanted-roof installation, single-Si, panel, mounted | Cut-off, U”. Another feasible option for Spain [205], but also for other countries that do not benefit from so many hours of sun, such as Ireland [206], wind power was also considered, selected in the ecoinvent database: “electricity, high voltage {ES}| electricity production, wind, <1 MW turbine, onshore | Cut-off, U” for the Spanish market as well. For the comparison, the treatment with the 265 nm UV-C LED lamp without any oxidant and at 100% intensity was chosen, and the results referred to the FU are shown in Figure 4.60.

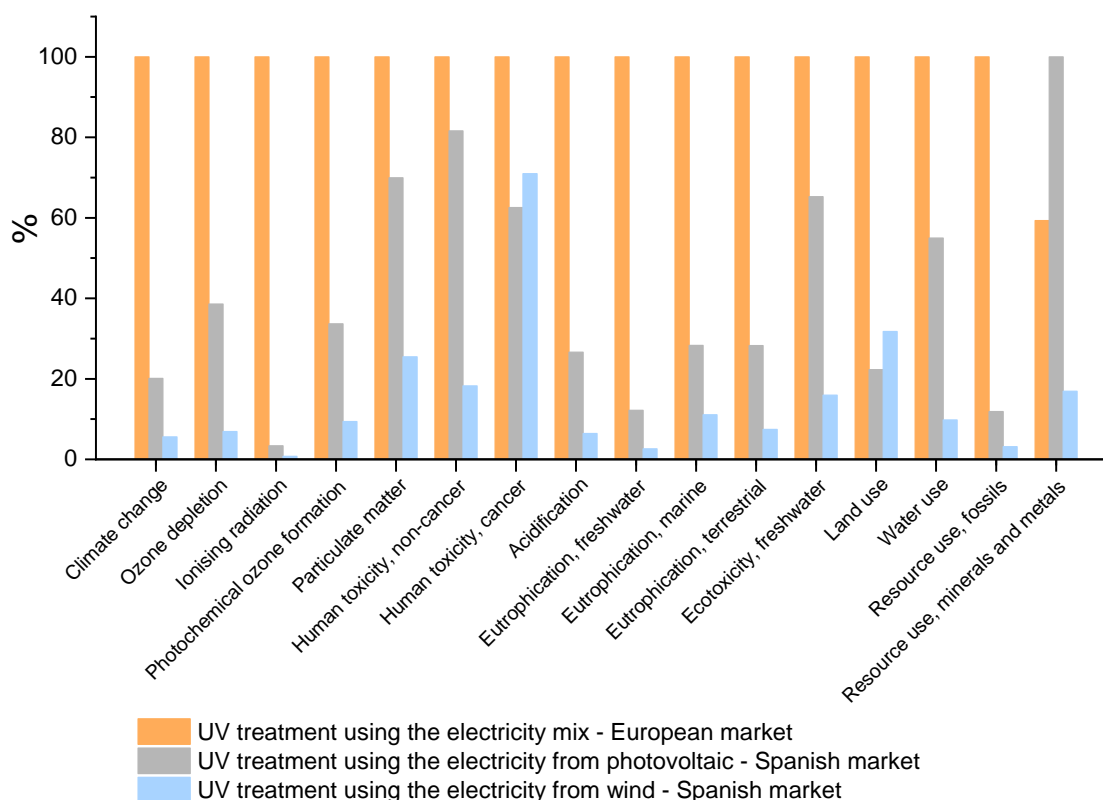


Figure 4.60. Relative impacts in percentage of the UV-C LED water treatment referred to the FU when employing the electricity mix of the European market and the electricity from photovoltaic or wind of the Spanish market. The results are shown for the 16 categories of the EF method employed.

All categories showed a middle to high impact reduction, except for the “Resource use, mineral and metals” in the case of photovoltaic. The latter saw an increase of 40% when employing electricity from solar energy compared to the European electricity mix, mainly due to the copper mine operation, followed by the silver-gold mine operation involved in the production of the solar panels, based on the information of the ecoinvent dataset [153]. In this regard, wind produced less impact in the resources categories compared to solar energy and achieved a reduction in all 16 categories ranging from 30% up to 99% compared to the European electricity mix. Compared to photovoltaic, wind energy had higher impacts only in “Human toxicity, cancer” and “Land use” of 12% and 30% due to the ferrochromium production for the wind turbine and the wind power plant construction, respectively. In all

other categories, the impacts were from 60% to 80% lower than photovoltaic according to the relative impacts of each clean energy source [207].

The use of photovoltaic and wind energy was also investigated for UV/H₂O₂ and UV/FC. By comparing only the “Climate Change” category, the reduction observed were respectively 80% and 93% when employing photovoltaic and wind energy instead of the electricity mix for both UV-based AOPs.

In conclusion, using cleaner sources during the UV-C LEDs and UV-C LEDs-based AOPs treatments can greatly improve the environmental sustainability of these processes, which can significantly enhance the quality of water for safe consumption in small- and large-scale applications.

5. CONCLUSIONS

5 Conclusions

The first part of the present thesis evaluated the most suitable commercial microfiltration membrane for developing an effective and low-cost technology for MPs removal. The main conclusions were:

- High mass removal efficiencies (above 94% for all cases) were achieved with all membranes, showing that, in general, microfiltration is a suitable low-cost process for MPs removal.
- Membrane abrasion and particles breaking down are potentially occurring during microfiltration in dead-end configurations. MPs particles in the range of 20-300 μm were detected passing through the membranes' pores nominally smaller (5 μm), but also the filtrate presented MPs particles smaller than the feed stream.
- Due to its hydrophobicity, PTFE requires a high working pressure, negatively affecting the pumping costs, without a tangible advantage for the MPs removal; therefore, it is unsuitable for this application.
- PC and CA membranes have similar behaviour during PA filtration. However, during PS filtration, CA allowed higher water flux. Furthermore, since CA has the lowest hardness, the impact of the particles with the membrane induced less breaking down; however, it seemed more prone to abrasion since bigger particles could pass through. The choice of membrane properties needs to compromise the risk of producing a higher amount of NPs or allowing the passage of bigger MPs particles.

CA membranes were the best or among the best in removing MPs both in terms of mass and number of particles, and they also achieved the best overall performance of TMP and water flux; therefore, CA membranes were chosen among the three membranes.

The second part of the thesis deeply analysed the kinetic and mechanistic aspects of CA membrane fouling by MPs and their interaction during the filtration run. The fouling mechanisms were sequentially modelled into complete pore blocking followed by cake layer formation, with a good agreement between the models and the experimental data. The

corresponding mechanisms' kinetic constants were studied at different operating conditions, varying MPs load and operating TMP. As a result:

- As the MPs load increased, the kinetic constants also increased. Both K_c and η_B followed a similar power-law relationship depending on $C^{2.3}$ for PS and $C^{1.4}$ for PA particles. A stronger correlation was observed in the case of PS, likely due to the larger particle size, which resulted in greater steric hindrance interactions compared to PA.
- Increasing the working TMP led to a threshold pressure value identified as the best operational condition, which is the right compromise between lowering the fouling and avoiding increasing the operational costs, other than limiting particle breakage and membrane abrasion. For PA particles, the optimal range was found to be between 0.3 and 0.5 bar, while for PS particles, it was found to be at 0.3 bar.
- The fouling was found to be higher after PA filtration due to various factors such as the higher hydrophobicity of PA particles, their neutral charge, and smaller particle size. These factors resulted in the formation of a denser cake layer due to interlaying and binding of particles during cake formation.
- Conversely, the PS particles' repulsive electrostatic interactions with the negatively charged CA membrane and their high shape irregularity formed a looser cake layer, also inducing great abrasion on the CA surface, which was confirmed by SEM images. This abrasion visibly reduced the selective layer and allowed more flux to pass through.
- The fouled membrane surface increase in hydrophobicity and roughness may also contribute to further fouling.
- Instead of relying on physical or cleaning methods to remove MPs in households or small drinking water treatments, an alternative approach could be directly replacing the fouled CA membranes. This approach enables the recovery and recycling of the particles while preventing secondary MPs pollution.

To conclude, modelling membrane fouling helped identify the optimal operating conditions based on the specific foulant present in the water to be treated and predict membrane replacement cycles, ultimately improving MPs removal efficiency.

The third part of the thesis aimed to tackle the problem of another concerning contaminant, DCF. The study explored the application of 265, 285, and 310 nm LED emitters via photolysis alone and combined with H₂O₂ or FC. The main conclusions were:

- Removal dependency on the wavelength was found in conformity with the absorption coefficient of the DCF and the oxidants. Therefore, the highest DCF degradation constants were achieved for the lamps at 265 and 285 nm. A synergistic effect was reached when coupling the UV treatment with the oxidants; in particular, the highest synergistic factors were achieved for 285 and 310 nm with FC, and 265 followed by 285 nm with H₂O₂, following the absorption trend of the oxidants. While no synergy was obtained with 310 nm/H₂O₂ since the absorption of the latter at that wavelength is nearly null.
 - Despite the higher degradation by UV-LED driven AOPs than photolysis alone, the overall treatments, considering only the photoreactor contact time, show similar electrical energy per order values due to the energy consumed to produce the oxidants.
 - The reaction mechanisms for UV/H₂O₂ and UV/FC were proposed, and a good fit between the experimental and simulated data was obtained with the estimated second-order kinetic constants $k_{HO} = 9.12 \cdot 10^9 \text{ M}^{-1} \text{ s}^{-1}$ for HO• with DCF and $k_{Cl} = 1.30 \cdot 10^{10} \text{ M}^{-1} \text{ s}^{-1}$ for Cl• with DCF.
 - Studies at different intensities, performed at 265 and 285 nm, highlighted a linear correlation with the time-based degradation constants, which is important, given a desired removal, for selecting the resident time or the irradiation intensity inside the reactor.
 - The dual-wavelength system (265 + 285 nm) alone and in combination with the oxidants did not show significant synergy ($p > 0.05$).
 - Regardless of the treatment, while the DCF was completely removed, the DOC decreased only partially by 20-30%, and the formation of stable dimers explained the limited DOC removal, which is confirmed by the yellowish colour formed after each photolysis process.
 - UV-based treatments are in general effective in decreasing toxicity towards bacteria, organisms and plants, although the optimal treatment time should be chosen accurately to prevent the occurrence of toxic and unstable by-products.
-

Overall, the results provide valuable evidence for the application of UV-B and UV-C LED emitters in water treatment plants, where factors like tuneable wavelength, instant on-off, and adjustable intensity can be positively exploited.

Finally, in the fourth part of the study, a comprehensive life cycle assessment of the UV-C LEDs photoreactor was conducted compared with a UV-C mercury lamp photoreactor for the degradation of 90% of DCF in water. Furthermore, the comparison between UV-C, UV-C/H₂O₂, and UV-C/FC while employing the 265 nm UV-C LEDs lamp was also assessed. The main results achieved were:

- Overall, the LEDs achieved higher performance, with lower impacts observed when working at higher lamp irradiation or assuming that the power efficiency will increase by 20% in the coming years. However, the impacts were similar when working at the same lamp irradiation and treatment time. It should be noted, however, that the LEDs employed in the lamp were chosen in 2019, and significant improvements in efficiency are already available in the market.
- The addition of H₂O₂ and FC reduced the total treatment time leading to a decrease of around 35% and 30% in all the impact categories compared to photolysis alone. Furthermore, for equal treatment time, the use of H₂O₂ is preferred between the two oxidants as it was found to be more environmentally sustainable.
- In all the cases studied, the main hotspot was electricity. Consequently, the use of the electricity mix for the European market during the operation phase of the treatment was compared to the use of photovoltaic and wind energy taken for the Spanish market as an example. Using photovoltaic energy lowered the impacts in all categories except one, while employing wind energy reduced the impacts in all 16 categories. Therefore, cleaner energy sources are highly encouraged to increase the overall sustainability.

To conclude, based on the ex-ante environmental LCA assessment, the applicability of the UV-C LED lamp looks very promising, and research towards scaling up these systems in real water treatment applications should be done, given the advantages over the mercury lamp. However, if electricity keeps being the main hotspot also in large-scale applications,

to decrease the environmental impacts, it is key to lower the treatment time by adding oxidants such as H₂O₂ and FC or to opt for clean energy sources.

Future work

Beyond the scope of the present PhD thesis, but given the interest in the topic, the following points have been identified as future work related to this thesis:

- Development of a hybrid system, integrating the UV-LED system with the filtration setup.
- Extend the modelling of membrane fouling to constant flow rate filtrations, which is also an important operational condition in domestic and industrial membrane treatments.
- A kinetic model that includes the effect of membrane abrasion and the particles' breakup, depending to some degree on the membrane's hardness value and the particles' type and shape, should be developed once robust data sets are available on the fouling mechanisms by MPs in water.
- Studies on NPs removal through UV-based AOPs. While UV/H₂O₂ and UV/FC were not suitable for MPs removal because of the enormous treatment times required for their complete degradation, the coupling of the membrane with UV treatment in this order would allow a first screen of bigger MPs particles, and UV-based AOPs can further tackle organic compounds together with NPs, which need shorter treatment times.
- This work was performed using solutions of MPs or DCF in distilled water not to have the influence of other fouling agents and scavengers affecting the results and not allowing to address the single mechanisms. However, real drinking water scenarios should be investigated in the same conditions to compare the results in more practical circumstances.
- Perform a social life cycle assessment to evaluate not only the environmental impacts but also the social impacts, which are also strictly connected with the SDGs and are found usually affected by new technologies.

Bibliography

Bibliography

- [1] European Water Charter of the Council of Europe, Strasbourg, 1968.
- [2] United nations on behalf of UN-Water, The United Nations world water development report: water and climate change, 2020.
- [3] European Union, Council Directive 91/271/EEC of 21 May 1991 concerning urban waste water treatment, 1991.
- [4] European Union, Council Directive 98/83/EC of 23 November 1998 on the quality of water intended for human consumption, 1998.
- [5] European Union, Directive 2000/60/EC of the European Parliament and of the Council of 23 October 2000 establishing a framework for Community action in the field of water policy, 2000.
- [6] European Environment Agency, European waters: Assessment of status and pressures, 2018.
- [7] C.M. Villanueva, M. Kogevinas, S. Cordier, M.R. Templeton, R. Vermeulen, J.R. Nuckols, M.J. Nieuwenhuijsen, P. Levallois, Assessing exposure and health consequences of chemicals in drinking water: Current state of knowledge and research needs, *Environmental Health Perspectives*. 122 (2014) 213–221.
- [8] B.S. Rathi, P.S. Kumar, P.L. Show, A review on effective removal of emerging contaminants from aquatic systems: Current trends and scope for further research, *Journal of Hazardous Materials*. 409 (2021) 124413.
- [9] PlasticsEurope, *Plastics - the Facts 2021*, an analysis of European plastics production, demand and waste data, 2021. <https://plasticseurope.org/knowledge-hub/plastics-the-facts-2021/> (accessed April 17, 2023).
- [10] R. Geyer, J.R. Jambeck, K.L. Law, Production, use, and fate of all plastics ever made, *Science Advances*. 3 (2017).
- [11] M. Wagner, S. Lambert, *Freshwater Microplastics*, 2018.
- [12] K. Novotna, L. Cermakova, L. Pivokonska, T. Cajthaml, M. Pivokonsky,

- Microplastics in drinking water treatment – Current knowledge and research needs, *Science of the Total Environment*. 667 (2019) 730–740.
- [13] I. Ali, T. Ding, C. Peng, I. Naz, H. Sun, J. Li, J. Liu, Micro- and nanoplastics in wastewater treatment plants: Occurrence, removal, fate, impacts and remediation technologies – A critical review, *Chemical Engineering Journal*. 423 (2021) 130205.
- [14] J. Sun, X. Dai, Q. Wang, M.C.M. van Loosdrecht, B.J. Ni, Microplastics in wastewater treatment plants: Detection, occurrence and removal, *Water Research*. 152 (2019) 21–37.
- [15] M. Enfrin, L.F. Dumée, J. Lee, Nano/microplastics in water and wastewater treatment processes – Origin, impact and potential solutions, *Water Research*. 161 (2019) 621–638.
- [16] H. Cai, M. Chen, Q. Chen, F. Du, J. Liu, H. Shi, Microplastic quantification affected by structure and pore size of filters, *Chemosphere*. 257 (2020) 127198.
- [17] J. Li, H. Liu, J. Paul Chen, Microplastics in freshwater systems: A review on occurrence, environmental effects, and methods for microplastics detection, *Water Research*. 137 (2018) 362–374.
- [18] Y. Picó, D. Barceló, Analysis and prevention of microplastics pollution in water: Current perspectives and future directions, *ACS Omega*. 4 (2019) 6709–6719.
- [19] J.P. Harrison, J.J. Ojeda, M.E. Romero-González, The applicability of reflectance micro-Fourier-transform infrared spectroscopy for the detection of synthetic microplastics in marine sediments, *Science of the Total Environment*. 416 (2012) 455–463.
- [20] A. Vianello, A. Boldrin, P. Guerriero, V. Moschino, R. Rella, A. Sturaro, L. Da Ros, Microplastic particles in sediments of Lagoon of Venice, Italy: First observations on occurrence, spatial patterns and identification, *Estuarine, Coastal and Shelf Science*. 130 (2013) 54–61.
- [21] M.G.J. Löder, M. Kuczera, S. Mintenig, C. Lorenz, G. Gerdtz, Focal plane array detector-based micro-Fourier-transform infrared imaging for the analysis of microplastics in environmental samples, *Environmental Chemistry*. 12 (2015) 563–
-

- 581.
- [22] L. Peng, D. Fu, H. Qi, C.Q. Lan, H. Yu, C. Ge, Micro- and nano-plastics in marine environment: Source, distribution and threats — A review, *Science of the Total Environment*. 698 (2020) 134254.
- [23] L.M. Rios Mendoza, H. Karapanagioti, N.R. Álvarez, Micro(nanoplastics) in the marine environment: Current knowledge and gaps, *Current Opinion in Environmental Science and Health*. 1 (2018) 47–51.
- [24] S.C. Gall, R.C. Thompson, The impact of debris on marine life, *Marine Pollution Bulletin*. 92 (2015) 170–179.
- [25] F. Ribeiro, J.W. O'Brien, T. Galloway, K. V. Thomas, Accumulation and fate of nano- and micro-plastics and associated contaminants in organisms, *TrAC - Trends in Analytical Chemistry*. 111 (2019) 139–147.
- [26] F. Wang, C.S. Wong, D. Chen, X. Lu, F. Wang, E.Y. Zeng, Interaction of toxic chemicals with microplastics: A critical review, *Water Research*. 139 (2018) 208–219.
- [27] S. Lambert, M. Wagner, *Freshwater Microplastics*, 2018.
- [28] O.H. Fred-Ahmadu, G. Bhagwat, I. Oluyoye, N.U. Benson, O.O. Ayejuyo, T. Palanisami, Interaction of chemical contaminants with microplastics: Principles and perspectives, *Science of the Total Environment*. 706 (2020) 135978.
- [29] L.H.M.L.M. Santos, S. Rodríguez-Mozaz, D. Barceló, Microplastics as vectors of pharmaceuticals in aquatic organisms – An overview of their environmental implications, *Case Studies in Chemical and Environmental Engineering*. 3 (2021) 100079.
- [30] T. Atugoda, H. Wijsekara, D.R.I.B. Werellagama, K.B.S.N. Jinadasa, N.S. Bolan, M. Vithanage, Adsorptive interaction of antibiotic ciprofloxacin on polyethylene microplastics: Implications for vector transport in water, *Environmental Technology & Innovation*. 19 (2020) 100971.
- [31] S. Perveen, C. Pablos, K. Reynolds, S. Stanley, J. Marugán, Microplastics in fresh- and wastewater are potential contributors to antibiotic resistance - A minireview,
-

-
- Journal of Hazardous Materials Advances. 6 (2022) 100071.
- [32] A.P. Periyasamy, A. Tehrani-bagha, A review on microplastic emission from textile materials and its reduction techniques, *Polymer Degradation and Stability*. 199 (2022) 109901.
- [33] P. Kay, R. Hiscoe, I. Moberley, L. Bajic, N. McKenna, Wastewater treatment plants as a source of microplastics in river catchments, *Environmental Science and Pollution Research*. 25 (2018) 20264–20267.
- [34] E.R. Zettler, T.J. Mincer, L.A. Amaral-Zettler, Life in the “plastisphere”: Microbial communities on plastic marine debris, *Environmental Science and Technology*. 47 (2013) 7137–7146.
- [35] Q. Zhang, E.G. Xu, J. Li, Q. Chen, L. Ma, E.Y. Zeng, H. Shi, A Review of Microplastics in Table Salt, Drinking Water, and Air: Direct Human Exposure, *Environmental Science & Technology*. 54 (2020) 3740–3751.
- [36] D. Santillo, K. Miller, P. Johnston, Microplastics as contaminants in commercially important seafood species, *Integrated Environmental Assessment and Management*. 13 (2017) 516–521.
- [37] M. Revel, A. Châtel, C. Mouneyrac, Micro(nano)plastics: A threat to human health?, *Current Opinion in Environmental Science and Health*. 1 (2018) 17–23.
- [38] C. Rubio-armend, S. Alejandro-vega, S. Paz-montelongo, Á.J. Guti, C.J. Carrascosa-iruzubieta, A.H. Torre, Microplastics as Emerging Food Contaminants : A Challenge for Food Safety, *Internation Journal of Environmental Research and Public Health*. 19 (2022).
- [39] M. Shen, B. Song, Y. Zhu, G. Zeng, Y. Zhang, Y. Yang, X. Wen, M. Chen, H. Yi, Removal of microplastics via drinking water treatment: Current knowledge and future directions, *Chemosphere*. 251 (2020) 126612.
- [40] O.M. Rodríguez-Narvaez, A. Goonetilleke, L. Perez, E.R. Bandala, Engineered technologies for the separation and degradation of microplastics in water: A review, *Chemical Engineering Journal*. 414 (2021) 128692.
- [41] A. Kundu, N.P. Shetti, S. Basu, K. Raghava Reddy, M.N. Nadagouda, T.M.
-

- Aminabhavi, Identification and removal of micro- and nano-plastics: Efficient and cost-effective methods, *Chemical Engineering Journal*. 421 (2021) 129816.
- [42] M.N. Nguyen, L.H. Nguyen, X.P. Nguyen, T.H. Le, V. Viet, A techno-environmental assessment from microplastic characterization to its removal by innovative technologies, *Journal of Mechanical Engineering Research and Developments*. 44 (2021) 55–68.
- [43] Y. Zhang, H. Jiang, K. Bian, H. Wang, C. Wang, A critical review of control and removal strategies for microplastics from aquatic environments, *Journal of Environmental Chemical Engineering*. 9 (2021) 105463.
- [44] M.R. Karimi Estahbanati, M. Kiendrebeogo, A. Khosravanipour Mostafazadeh, P. Drogui, R.D. Tyagi, Treatment processes for microplastics and nanoplastics in waters: State-of-the-art review, *Marine Pollution Bulletin*. 168 (2021) 112374.
- [45] B. Ma, W. Xue, C. Hu, H. Liu, J. Qu, L. Li, Characteristics of microplastic removal via coagulation and ultrafiltration during drinking water treatment, *Chemical Engineering Journal*. 359 (2019) 159–167.
- [46] B. Ma, W. Xue, Y. Ding, C. Hu, H. Liu, J. Qu, Removal characteristics of microplastics by Fe-based coagulants during drinking water treatment, *Journal of Environmental Sciences*. 78 (2019) 267–275.
- [47] W. Perren, A. Wojtasik, Q. Cai, Removal of Microbeads from Wastewater Using Electrocoagulation, *ACS Omega*. 3 (2018) 3357–3364.
- [48] J. Grbic, B. Nguyen, E. Guo, J.B. You, D. Sinton, C.M. Rochman, Magnetic Extraction of Microplastics from Environmental Samples, *Environmental Science and Technology Letters*. 6 (2019) 68–72.
- [49] Y. Tang, S. Zhang, Y. Su, D. Wu, Y. Zhao, B. Xie, Removal of microplastics from aqueous solutions by magnetic carbon nanotubes, *Chemical Engineering Journal*. 406 (2021) 126804.
- [50] S. Felsing, C. Kochleus, S. Buchinger, N. Brennholt, F. Stock, G. Reifferscheid, A new approach in separating microplastics from environmental samples based on their electrostatic behavior, *Environmental Pollution*. 234 (2018) 20–28.
-

- [51] L. Cai, J. Wang, J. Peng, Z. Wu, X. Tan, Observation of the degradation of three types of plastic pellets exposed to UV irradiation in three different environments, *Science of The Total Environment*. 628–629 (2018) 740–747.
- [52] P. Wang, Z. Huang, S. Chen, M. Jing, Z. Ge, J. Chen, S. Yang, J. Chen, Y. Fang, Sustainable removal of nano/microplastics in water by solar energy, *Chemical Engineering Journal*. 428 (2022) 131196.
- [53] S. Kim, A. Sin, H. Nam, Y. Park, H. Lee, C. Han, Advanced oxidation processes for microplastics degradation : A recent trend, *Chemical Engineering Journal Advances*. 9 (2022) 100213.
- [54] Z. Wang, T. Lin, W. Chen, Occurrence and removal of microplastics in an advanced drinking water treatment plant (ADWTP), *Science of the Total Environment*. 700 (2020) 134520.
- [55] R. Chen, M. Qi, G. Zhang, C. Yi, Comparative experiments on polymer degradation technique of produced water of polymer flooding oilfield, *IOP Conference Series: Earth and Environmental Science*. 113 (2018) 012208.
- [56] H. Hidayaturrehman, T.G. Lee, A study on characteristics of microplastic in wastewater of South Korea: Identification, quantification, and fate of microplastics during treatment process, *Marine Pollution Bulletin*. 146 (2019) 696–702.
- [57] H. Luo, Y. Zeng, Y. Zhao, Y. Xiang, Y. Li, X. Pan, Effects of advanced oxidation processes on leachates and properties of microplastics, *Journal of Hazardous Materials*. 413 (2021).
- [58] C. Scherer, N. Brennholt, G. Reifferscheid, M. Wagner, Feeding type and development drive the ingestion of microplastics by freshwater invertebrates, *Scientific Reports*. 7 (2017) 1–9.
- [59] J. Gong, T. Kong, Y. Li, Q. Li, Z. Li, J. Zhang, Biodegradation of Microplastic Derived from Poly(ethylene terephthalate) with Bacterial Whole-Cell Biocatalysts, *Polymers* 2018, Vol. 10, Page 1326. 10 (2018) 1326.
- [60] A.F. Herbort, M.T. Sturm, S. Fiedler, G. Abkai, K. Schuhen, Alkoxy-silyl Induced Agglomeration: A New Approach for the Sustainable Removal of Microplastic from
-

- Aquatic Systems, *Journal of Polymers and the Environment*. 26 (2018) 4258–4270.
- [61] Y. Zhang, H. Jiang, K. Bian, H. Wang, C. Wang, A critical review of control and removal strategies for microplastics from aquatic environments, *Journal of Environmental Chemical Engineering*. 9 (2021) 105463.
- [62] A. Adewuyi, A.J. Campbell, O.G. Adeyemi, The Potential Role of Membrane Technology in the Removal of Microplastics from Wastewater, *Journal of Applied Membrane Science & Technology*. 25 (2021) 31–53.
- [63] T. Poerio, E. Piacentini, R. Mazzei, Membrane Processes for Microplastic Removal, *Molecules*. 24 (2019).
- [64] M. Golgoli, M. Khiadani, A. Shafieian, T.K. Sen, Y. Hartanto, M.L. Johns, M. Zargar, Microplastics fouling and interaction with polymeric membranes: A review, *Chemosphere*. 283 (2021) 131185.
- [65] Y. Liao, C.H. Loh, M. Tian, R. Wang, A.G. Fane, Progress in electrospun polymeric nanofibrous membranes for water treatment: Fabrication, modification and applications, *Progress in Polymer Science*. 77 (2018) 69–94.
- [66] M.K. Selatile, S.S. Ray, V. Ojijo, R. Sadiku, Recent developments in polymeric electrospun nanofibrous membranes for seawater desalination, *RSC Advances*. 8 (2018) 37915–37938.
- [67] D. Barcelo, Y. Pico, Case Studies of Macro- and Microplastics Pollution in Coastal Waters and Rivers: Is There a Solution With New Removal Technologies and Policy Actions?, *Case Studies in Chemical and Environmental Engineering*. (2020) 100019.
- [68] M. Simon, N. van Alst, J. Vollertsen, Quantification of microplastic mass and removal rates at wastewater treatment plants applying Focal Plane Array (FPA)-based Fourier Transform Infrared (FT-IR) imaging, *Water Research*. 142 (2018) 1–9.
- [69] R. Singh, Introduction to membrane technology, in: *Hybrid Membrane System for Water Purification*, 2005: pp. 1–56.
- [70] M. Enfrin, J. Lee, P. Le-Clech, L.F. Dumée, Kinetic and mechanistic aspects of ultrafiltration membrane fouling by nano- and microplastics, *Journal of Membrane Science*. 601 (2020) 117890.
-

- [71] J. Li, B. Wang, Z. Chen, B. Ma, J.P. Chen, Ultrafiltration membrane fouling by microplastics with raw water: Behaviors and alleviation methods, *Chemical Engineering Journal*. 410 (2021) 128174.
- [72] R.J. LaRue, B. Patterson, S. O'Brien, D.R. Latulippe, Evaluation of Membrane Fouling by Microplastic Particles in Tertiary Wastewater Treatment Processes, *ACS Environmental Science and Technology Water*. 2 (2022) 955–966.
- [73] X. Xiong, T. Bond, M. Saboor, W. Yu, The stimulation of microbial activity by microplastic contributes to membrane fouling in ultrafiltration, *Journal of Membrane Science*. 635 (2021) 119477.
- [74] M.B. Tanis-Kanbur, N.R. Tamilselvam, H.Y. Lai, J.W. Chew, Impact of Particle Shape and Surface Group on Membrane Fouling, *Membranes*. 12 (2022) 403.
- [75] Y. Zhao, L. Ye, X.-X. Zhang, Emerging Pollutants–Part I: Occurrence, Fate and Transport, *Water Environment Research*. 90 (2018) 1301–1322.
- [76] J.C.G. Sousa, A.R. Ribeiro, M.O. Barbosa, C. Ribeiro, M.E. Tiritan, M.F.R. Pereira, A.M.T. Silva, Monitoring of the 17 EU Watch List contaminants of emerging concern in the Ave and the Sousa Rivers, *Science of the Total Environment*. 649 (2019) 1083–1095.
- [77] M.O. Barbosa, N.F.F. Moreira, A.R. Ribeiro, M.F.R. Pereira, A.M.T. Silva, Occurrence and removal of organic micropollutants: An overview of the watch list of EU Decision 2015/495, *Water Research*. 94 (2016) 257–279.
- [78] A.I. Stefanakis, J.A. Becker, A review of emerging contaminants in water: Classification, sources, and potential risks, *Impact of Water Pollution on Human Health and Environmental Sustainability*. (2015) 55–80.
- [79] M. Crane, C. Watts, T. Boucard, Chronic aquatic environmental risks from exposure to human pharmaceuticals, *Science of the Total Environment*. 367 (2006) 23–41.
- [80] L.H.M.L.M. Santos, A.N. Araújo, A. Fachini, A. Pena, C. Delerue-Matos, M.C.B.S.M. Montenegro, Ecotoxicological aspects related to the presence of pharmaceuticals in the aquatic environment, *Journal of Hazardous Materials*. 175 (2010) 45–95.
-

- [81] European Commission, Decision (EU) 2015/495 of 20 March 2015 establishing a watch list of substances for Union-wide monitoring in the field of water policy pursuant to Directive 2008/105/EC of the European Parliament and of the Council, 2015.
- [82] European Union, Directive 2013/39/EU of the European Parliament and of the Council of 12 August 2013 amending Directives 2000/60/EC and 2008/105/EC as regards priority substances in the field of water policy, 2013.
- [83] N. Vieno, M. Sillanpää, Fate of diclofenac in municipal wastewater treatment plant - A review, *Environment International*. 69 (2014) 28–39.
- [84] L. Lonappan, S.K. Brar, R.K. Das, M. Verma, R.Y. Surampalli, Diclofenac and its transformation products: Environmental occurrence and toxicity - A review, *Environment International*. 96 (2016) 127–138.
- [85] I. Alessandretti, C.V.T. Riguetto, M.T. Nazari, M. Rosseto, A. Dettmer, Removal of diclofenac from wastewater: A comprehensive review of detection, characteristics and tertiary treatment techniques, *Journal of Environmental Chemical Engineering*. 9 (2021) 106743.
- [86] M. Herrero-Villar, É. Delepouille, L. Suárez-Regalado, C. Solano-Manrique, C. Juan-Sallés, J.J. Iglesias-Lebrija, P.R. Camarero, F. González, E. Álvarez, R. Mateo, First diclofenac intoxication in a wild avian scavenger in Europe, *Science of the Total Environment*. 782 (2021) 146890.
- [87] T. Atugoda, M. Vithanage, H. Wijesekara, N. Bolan, A.K. Sarmah, M.S. Bank, S. You, Y.S. Ok, Interactions between microplastics, pharmaceuticals and personal care products: Implications for vector transport, *Environment International*. 149 (2021) 106367.
- [88] S. Liang, K. Wang, K. Wang, Y. Kou, T. Wang, C. Guo, W. Wang, J. Wang, Adsorption of Diclofenac Sodium by Aged Degradable and Non-Degradable Microplastics: Environmental Effects, Adsorption Mechanisms, *Toxics*. 11 (2023).
- [89] J. Li, X. Huang, Z. Hou, T. Ding, Sorption of diclofenac by polystyrene microplastics: Kinetics, isotherms and particle size effects, *Chemosphere*. 290 (2022) 133311.
-

- [90] O.M. Rodriguez-Narvaez, J.M. Peralta-Hernandez, A. Goonetilleke, E.R. Bandala, Treatment technologies for emerging contaminants in water: A review, *Chemical Engineering Journal*. 323 (2017) 361–380.
- [91] R. Baccar, M. Sarrà, J. Bouzid, M. Feki, P. Blázquez, Removal of pharmaceutical compounds by activated carbon prepared from agricultural by-product, *Chemical Engineering Journal*. 211–212 (2012) 310–317.
- [92] J. Yang, G. Lv, T. Li, S. Sun, X. Sun, Theoretical insight into the degradation of diclofenac by hydroxyl and sulfate radicals in aqueous-phase: Mechanisms, kinetics and eco-toxicity, *Journal of Environmental Chemical Engineering*. 10 (2022) 108311.
- [93] Q. Li, C. Lai, J. Yu, J. Luo, J. Deng, G. Li, W. Chen, B. Li, G. Chen, Degradation of diclofenac sodium by the UV/chlorine process: Reaction mechanism, influencing factors and toxicity evaluation, *Journal of Photochemistry and Photobiology A: Chemistry*. 425 (2022) 113667.
- [94] A. Sharma, J. Ahmad, S.J.S. Flora, Application of advanced oxidation processes and toxicity assessment of transformation products, *Environmental Research*. 167 (2018) 223–233.
- [95] A.K. Biń, S. Sobera-Madej, Comparison of the Advanced Oxidation Processes (UV, UV/H₂O₂ and O₃) for the Removal of Antibiotic Substances during Wastewater Treatment, *Ozone: Science and Engineering*. 34 (2012) 136–139.
- [96] E.M. Cuerda-Correa, M.F. Alexandre-Franco, C. Fernández-González, Advanced Oxidation Processes for the Removal of Antibiotics from Water. An Overview, *Water*. 12 (2019) 102.
- [97] M. Klavarioti, D. Mantzavinos, D. Kassinos, Removal of residual pharmaceuticals from aqueous systems by advanced oxidation processes, *Environment International*. 35 (2009) 402–417.
- [98] D.B. Miklos, C. Remy, M. Jekel, K.G. Linden, J.E. Drewes, U. Hübner, Evaluation of advanced oxidation processes for water and wastewater treatment – A critical review, *Water Research*. 139 (2018) 118–131.
- [99] J.R. Bolton, M.I. Stefan, Fundamental photochemical approach to the concepts of
-

- fluence (UV dose) and electrical energy efficiency in photochemical degradation reactions, *Research on Chemical Intermediates*. 28 (2002) 857–870.
- [100] G.Y. Lui, D. Roser, R. Corkish, N.J. Ashbolt, R. Stuetz, Point-of-use water disinfection using ultraviolet and visible light-emitting diodes, *Science of the Total Environment*. 553 (2016) 626–635.
- [101] J. Rodríguez-Chueca, S. Varella della Giustina, J. Rocha, T. Fernandes, C. Pablos, Á. Encinas, D. Barceló, S. Rodríguez-Mozaz, C.M. Manaia, J. Marugán, Assessment of full-scale tertiary wastewater treatment by UV-C based-AOPs: Removal or persistence of antibiotics and antibiotic resistance genes?, *Science of the Total Environment*. 652 (2019) 1051–1061.
- [102] Y. Feng, D.W. Smith, J.R. Bolton, Photolysis of aqueous free chlorine species (HOCl and OCl-) with 254 nm ultraviolet light, *Journal of Environmental Engineering and Science*. 6 (2007) 277–284.
- [103] J.F.J.R. Pesqueira, J. Marugán, M.F.R. Pereira, A.M.T. Silva, Selecting the most environmentally friendly oxidant for UVC degradation of micropollutants in urban wastewater by assessing life cycle impacts: Hydrogen peroxide, peroxymonosulfate or persulfate?, *Science of The Total Environment*. 808 (2022) 152050.
- [104] W.L. Wang, Q.Y. Wu, Z.M. Li, Y. Lu, Y. Du, T. Wang, N. Huang, H.Y. Hu, Light-emitting diodes as an emerging UV source for UV/chlorine oxidation: Carbamazepine degradation and toxicity changes, *Chemical Engineering Journal*. 310 (2017) 148–156.
- [105] G. Cerreta, M.A. Roccamante, P. Plaza-Bolaños, I. Oller, A. Aguera, S. Malato, L. Rizzo, Advanced treatment of urban wastewater by UV-C/free chlorine process: Micro-pollutants removal and effect of UV-C radiation on trihalomethanes formation, *Water Research*. 169 (2020) 115220.
- [106] H.D. Minh Tran, S. Boivin, H. Kodamatani, K. Ikehata, T. Fujioka, Potential of UV-B and UV-C irradiation in disinfecting microorganisms and removing N-nitrosodimethylamine and 1,4-dioxane for potable water reuse: A review, *Chemosphere*. 286 (2022) 131682.
- [107] W. Heering, UV-sources - Basics, Properties and Applications, International
-

- Ultraviolet Association. 6 (2004) 7–13.
- [108] G. Matafonova, V. Batoev, Recent advances in application of UV light-emitting diodes for degrading organic pollutants in water through advanced oxidation processes: A review, *Water Research*. 132 (2018) 177–189.
- [109] P. Palakornkitti, P. Pinyowiwat, S. Tanrattanakorn, N. Rajatanavin, P. Rattanakaemakorn, The effectiveness of commercial household ultraviolet C germicidal devices in Thailand, *Scientific Reports*. 11 (2021) 1–9.
- [110] H. Amano, R. Collazo, C. De Santi, S. Einfeldt, M. Funato, J. Glaab, S. Hagedorn, A. Hirano, H. Hirayama, R. Ishii, Y. Kashima, Y. Kawakami, R. Kirste, M. Kneissl, R. Martin, F. Mehnke, M. Meneghini, A. Ougazzaden, P.J. Parbrook, S. Rajan, P. Reddy, F. Römer, J. Ruschel, B. Sarkar, F. Scholz, L.J. Schowalter, P. Shields, Z. Sitar, L. Sulmoni, T. Wang, T. Wernicke, M. Weyers, B. Witzigmann, Y.-R. Wu, T. Wunderer, Y. Zhang, The 2020 UV emitter roadmap, *Journal of Physics D: Applied Physics*. 53 (2020).
- [111] M.A. Khan, N. Maeda, J. Yun, M. Jo, Y. Yamada, H. Hirayama, Achieving 9.6% efficiency in 304 nm p-AlGa_N UVB LED via increasing the holes injection and light reflectance, *Scientific Reports*. 12 (2022) 1–11.
- [112] Y. Gerchman, H. Mamane, N. Friedman, M. Mandelboim, UV-LED disinfection of Coronavirus: Wavelength effect, *Journal of Photochemistry and Photobiology B: Biology*. 212 (2020) 112044.
- [113] T.C. Hsu, Y.T. Teng, Y.W. Yeh, X. Fan, K.H. Chu, S.H. Lin, K.K. Yeh, P.T. Lee, Y. Lin, Z. Chen, T. Wu, H.C. Kuo, Perspectives on UVC LED: Its progress and application, *Photonics*. 8 (2021) 196.
- [114] U.S. Environmental Protection Agency, Ultraviolet disinfection guidance manual for the final long term 2 enhanced surface water treatment rule, 2006.
- [115] United Nations Environment Programme, Minamata Convention on Mercury, 2019.
- [116] O. Lawal, J. Cosman, J. Pagan, UV-C LED Devices and Systems: Current and Future State, *IUVA News*. 20 (2018).
- [117] K. Song, M. Mohseni, F. Taghipour, Application of ultraviolet light-emitting diodes
-

- (UV-LEDs) for water disinfection: A review, *Water Research*. 94 (2016) 341–349.
- [118] P. Jarvis, O. Autin, E.H. Goslan, F. Hassard, Application of Ultraviolet Light-Emitting Diodes, *Water*. 11 (2019) 1–15.
- [119] M. Martín-Sómer, C. Pablos, C. Adán, R. Van, J. Marugán, A review on led technology in water photodisinfection, *Science of the Total Environment*. 885 (2023) 163963.
- [120] International Organization for Standardization, ISO 14040:2006 Environmental Management - Life cycle assessment - Principles and Framework, 2006.
- [121] M.Z. Hauschild, R.K. Rosenbaum, S.I. Olsen, *Life Cycle Assessment: Theory and Practice*, Springer International Publishing, 2018.
- [122] S. Cucurachi, C. Van Der Giesen, J. Guinée, Ex-ante LCA of Emerging Technologies, *Procedia CIRP*. 69 (2018) 463–468.
- [123] International Organization for Standardization, ISO 16290:2013: Space systems - Definition of the Technology Readiness Levels (TRL) and their criteria of assessment, 2013.
- [124] European Commission, Technology Readiness Levels (TRL) - Commission Decision C(2014)4995, 2014.
- [125] S. Foteinis, A.G.L. Borthwick, Z. Frontistis, D. Mantzavinos, E. Chatzisyneon, Environmental sustainability of light-driven processes for wastewater treatment applications, *Journal of Cleaner Production*. 182 (2018) 8–15.
- [126] S.M. McKee, E. Chatzisyneon, Assessing the environmental sustainability of light emitting diodes and conventional blacklight lamps for the treatment of bisphenol-A in water, *Environmental Impact Assessment Review*. 97 (2022) 106886.
- [127] B. Notarnicola, G. Tassielli, P.A. Renzulli, R. Di Capua, F. Astuto, G. Mascolo, S. Murgolo, C. De Ceglie, M.L. Curri, R. Comparelli, M. Dell'Edera, Life Cycle Assessment of UV-C based treatment systems for the removal of compounds of emerging concern from urban wastewater, *Science of the Total Environment*. 857 (2023) 159309.
- [128] S.A. Popova, G.G. Matafonova, V.B. Batoev, Dual-wavelength UV degradation of
-

-
- bisphenol A and bezafibrate in aqueous solution using excilamps (222, 282 nm) and LED (365 nm): yes or no synergy?, *Journal of Environmental Science and Health - Part A*. 58 (2023) 39–52.
- [129] Z.C. Gao, Y.L. Lin, B. Xu, Y. Xia, C.Y. Hu, T.C. Cao, X.Y. Zou, N.Y. Gao, Evaluating iopamidol degradation performance and potential dual-wavelength synergy by UV-LED irradiation and UV-LED/chlorine treatment, *Chemical Engineering Journal*. 360 (2019) 806–816.
- [130] S. Sankaranarayanan, B. Likozar, R. Navia, Real-time Particle Size Analysis Using the Focused Beam Reflectance Measurement Probe for In Situ Fabrication of Polyacrylamide–Filler Composite Materials, *Scientific Reports*. 9 (2019) 1–12.
- [131] J.A. Calles, J. Dufour, J. Marugán, J.L. Peña, R. Giménez-Aguirre, D. Merino-García, Properties of Asphaltenes Precipitated with Different n -Alkanes. A Study To Assess the Most Representative Species for Modeling, *Energy & Fuels*. 22 (2008) 763–769.
- [132] E.J. Hukkanen, R.D. Braatz, Measurement of particle size distribution in suspension polymerization using in situ laser backscattering, *Sensors and Actuators, B: Chemical*. 96 (2003) 451–459.
- [133] Ministerio de Vivienda, Real Decreto 314/2006, de 17 de marzo, por el que se aprueba el Código Técnico de la Edificación. Reference: BOE-A-2006-5515., 2006.
- [134] K.J. Howe, M.M. Clark, Fouling of microfiltration and ultrafiltration membranes by natural waters, *Environmental Science and Technology*. 36 (2002) 3571–3576.
- [135] E. Abbasi-Garravand, C.N. Mulligan, C.B. Laflamme, G. Clairet, Investigation of the fouling effect on a commercial semi-permeable membrane in the pressure retarded osmosis (PRO) process, *Separation and Purification Technology*. 193 (2018) 81–90.
- [136] A. Grenier, M. Meireles, P. Aimar, P. Carvin, Analysing flux decline in dead-end filtration, *Chemical Engineering Research and Design*. 86 (2008) 1281–1293.
- [137] J. Hermia, Constant pressure blocking filtration laws: application to power-law non-newtonian fluids, *Transactions of the Institution of Chemical Engineers*. 60 (1982) 183.
- [138] R.W. Field, J.J. Wu, Modelling of permeability loss in membrane filtration: Re-
-

- examination of fundamental fouling equations and their link to critical flux, *Desalination*. 283 (2011) 68–74.
- [139] E. Iritani, N. Katagiri, Developments of blocking filtration model in membrane filtration, *KONA Powder and Particle Journal*. 2016 (2016) 179–202.
- [140] R.W. Field, D. Wu, J.A. Howell, B.B. Gupta, Critical flux concept for microfiltration fouling, *Journal of Membrane Science*. 100 (1995) 259–272.
- [141] T.A. Trinh, W. Li, J.W. Chew, Internal fouling during microfiltration with foulants of different surface charges, *Journal of Membrane Science*. 602 (2020) 117983.
- [142] C. Duclos-Orsello, W. Li, C.C. Ho, A three mechanism model to describe fouling of microfiltration membranes, *Journal of Membrane Science*. 280 (2006) 856–866.
- [143] W. Li, R. Wu, J. Duan, C.P. Saint, D. Mulcahy, Overlooked effects of organic solvents from sample preparation on reaction constants of micropollutants in UV-based advanced oxidation processes, *Chemical Engineering Journal*. 313 (2017) 801–806.
- [144] J.R. Bolton, M.I. Stefan, P.S. Shaw, K.R. Lykke, Determination of the quantum yields of the potassium ferrioxalate and potassium iodide-iodate actinometers and a method for the calibration of radiometer detectors, *Journal of Photochemistry and Photobiology A: Chemistry*. 222 (2011) 166–169.
- [145] F. Cataldo, Uridine As Photochemical Actinometer: Application To Led-Uv Flow Reactors, *European Chemical Bulletin*. 6 (2017) 405.
- [146] A.P. Uppinakudru, K. Reynolds, S. Stanley, C. Pablos, J. Marugán, Critical assessment of optical sensor parameters for the measurement of ultraviolet LED lamps, *Measurement*. 196 (2022) 111278.
- [147] G.M. Eisenberg, Colorimetric Determination of Hydrogen Peroxide, *Industrial and Engineering Chemistry - Analytical Edition*. 15 (1943) 327–328.
- [148] F. Ghanbari, Q. Wang, A. Hassani, S. Waclawek, J. Rodríguez-Chueca, K.Y.A. Lin, Electrochemical activation of peroxides for treatment of contaminated water with landfill leachate: Efficacy, toxicity and biodegradability evaluation, *Chemosphere*. 279 (2021) 130610.
- [149] C. Casado, J. Moreno-SanSegundo, I. De la Obra, B. Esteban García, J.A. Sánchez
-

-
- Pérez, J. Marugán, Mechanistic modelling of wastewater disinfection by the photo-Fenton process at circumneutral pH, *Chemical Engineering Journal*. 403 (2021) 126335.
- [150] International Organization for Standardization, ISO 14044:2006 Environmental Management - Life cycle assessment - Requirements and guidelines, 2006.
- [151] M.A. Curran, *Environmental life-cycle assessment*, Springer International Publishing, 1996.
- [152] J.F.J.R. Pesqueira, M.F.R. Pereira, A.M.T. Silva, Environmental impact assessment of advanced urban wastewater treatment technologies for the removal of priority substances and contaminants of emerging concern: A review, *Journal of Cleaner Production*. 261 (2020) 121078.
- [153] G. Wernet, C. Bauer, B. Steubing, J. Reinhard, E. Moreno-Ruiz, B. Weidema, The ecoinvent database version 3 (part I): overview and methodology, *International Journal of Life Cycle Assessment*. 21 (2016) 1218–1230.
- [154] M. Goedkoop, M. Oele, J. Leijting, T. Ponsioen, E. Meijer, *Introduction to LCA with SimaPro*, Pré, 2016.
- [155] A.S. Tagg, M. Sapp, J.P. Harrison, J.J. Ojeda, Identification and Quantification of Microplastics in Wastewater Using Focal Plane Array-Based Reflectance Micro-FT-IR Imaging, *Analytical Chemistry*. 87 (2015) 6032–6040.
- [156] G. Renner, T.C. Schmidt, J. Schram, *Characterization and Quantification of Microplastics by Infrared Spectroscopy*, Elsevier Ltd, 2017.
- [157] R. Paoli, M. Bulwan, O. Castaño, E. Engel, J.C. Rodriguez-Cabello, A. Homs-Corbera, J. Samitier, Layer-by-layer modification effects on a nanopore's inner surface of polycarbonate track-etched membranes, *RSC Advances*. 10 (2020) 35930–35940.
- [158] S. Azari, L. Zou, E. Cornelissen, Y. Mukai, Facile fouling resistant surface modification of microfiltration cellulose acetate membranes by using amino acid L-DOPA, *Water Science and Technology*. 68 (2013) 901–908.
- [159] W. Schützner, E. Kenndler, *Electrophoresis in Synthetic Organic Polymer*
-

- Capillaries: Variation of Electroosmotic Velocity and ζ Potential with pH and Solvent Composition, *Analytical Chemistry*. 64 (1992) 1991–1995.
- [160] Z. Jiang, J. Miao, Y. He, K. Tu, S. Chen, R. Zhang, L. Zhang, H. Yang, A novel positively charged composite nanofiltration membrane based on polyethyleneimine with a tunable active layer structure developed: Via interfacial polymerisation, *RSC Advances*. 9 (2019) 10796–10806.
- [161] C. Shang, D. Pranantyo, S. Zhang, Understanding the Roughness-Fouling Relationship in Reverse Osmosis: Mechanism and Implications, *Environmental Science & Technology*. 54 (2020) 5288–5296.
- [162] G. Renner, T.C. Schmidt, J. Schram, Analytical methodologies for monitoring micro(nano)plastics: Which are fit for purpose?, *Current Opinion in Environmental Science & Health*. 1 (2018) 55–61.
- [163] M. Enfrin, J. Lee, Y. Gibert, F. Basheer, L. Kong, L.F. Dumée, Release of hazardous nanoplastic contaminants due to microplastics fragmentation under shear stress forces, *Journal of Hazardous Materials*. 384 (2020) 121393.
- [164] M. Enfrin, J. Wang, A. Merenda, L.F. Dum, J. Lee, Mitigation of membrane fouling by nano / microplastics via surface chemistry control, *Journal of Membrane Science*. 633 (2021) 119379.
- [165] N. Yadav, M. Hakkarainen, Degradable or not? Cellulose acetate as a model for complicated interplay between structure, environment and degradation, *Chemosphere*. 265 (2021) 128731.
- [166] J. Puls, S.A. Wilson, D. Höltzer, Degradation of Cellulose Acetate-Based Materials: A Review, *Journal of Polymers and the Environment*. 19 (2011) 152–165.
- [167] H. Ding, J. Zhang, H. He, Y. Zhu, D.D. Dionysiou, Z. Liu, C. Zhao, Do membrane filtration systems in drinking water treatment plants release nano/microplastics?, *Science of The Total Environment*. 755 (2021) 142658.
- [168] Y.J. Liu, D.D. Sun, Particles size-associated membrane fouling in microfiltration of denitrifying granules supernatant, *Chemical Engineering Journal*. 181–182 (2012) 494–500.
-

- [169] X. Du, Y. Wang, G. Leslie, G. Li, H. Liang, Shear stress in a pressure-driven membrane system and its impact on membrane fouling from a hydrodynamic condition perspective: a review, *Journal of Chemical Technology and Biotechnology*. 92 (2017) 463–478.
- [170] M. Enfrin, J. Lee, A.G. Fane, L.F. Dumée, Mitigation of membrane particulate fouling by nano / microplastics via physical cleaning strategies, *Science of the Total Environment*. 788 (2021) 147689.
- [171] M. Enfrin, C. Hachemi, D.L. Callahan, J. Lee, L.F. Dumée, Membrane fouling by nanofibres and organic contaminants – Mechanisms and mitigation via periodic cleaning strategies, *Separation and Purification Technology*. 278 (2022) 119592.
- [172] J. Kromkamp, F. Faber, K. Schroen, R. Boom, Effects of particle size segregation on crossflow microfiltration performance: Control mechanism for concentration polarisation and particle fractionation, *Journal of Membrane Science*. 268 (2006) 189–197.
- [173] T.K. Dey, M. Jamal, Separation of microplastics from water - What next ?, *Journal of Water Process Engineering*. 44 (2021) 102332.
- [174] K. Lekkerkerker-Teunissen, M.J. Benotti, S.A. Snyder, H.C. Van Dijk, Transformation of atrazine, carbamazepine, diclofenac and sulfamethoxazole by low and medium pressure UV and UV/H₂O₂ treatment, *Separation and Purification Technology*. 96 (2012) 33–43.
- [175] S. Mozia, D. Darowna, J. Przepiórski, A.W. Morawski, Evaluation of performance of hybrid photolysis-DCMD and photocatalysis-DCMD systems utilizing UV-C radiation for removal of diclofenac sodium salt from water, *Polish Journal of Chemical Technology*. 15 (2013) 51–60.
- [176] Y. Huang, Y. Liu, M. Kong, E.G. Xu, S. Coffin, D. Schlenk, D.D. Dionysiou, Efficient degradation of cytotoxic contaminants of emerging concern by UV/H₂O₂, *Environmental Science: Water Research and Technology*. 4 (2018) 1272–1281.
- [177] R. Yin, L. Ling, C. Shang, Wavelength-dependent chlorine photolysis and subsequent radical production using UV-LEDs as light sources, *Water Research*. 142 (2018) 452–458.
-

- [178] S.R. Sarathy, M.M. Bazri, M. Mohseni, Modeling the Transformation of Chromophoric Natural Organic Matter during UV/H₂O₂ Advanced Oxidation, *Journal of Environmental Engineering*. 137 (2011) 903–912.
- [179] C.-H. Liao, M.D. Gurol, Chemical Oxidation by Photolytic, *Environmental Science & Technology*. 29 (1995) 3007–3014.
- [180] H. Yu, E. Nie, J. Xu, S. Yan, W.J. Cooper, W. Song, Degradation of Diclofenac by Advanced Oxidation and Reduction Processes: Kinetic Studies, Degradation Pathways and Toxicity Assessments, *Water Research*. 47 (2013) 1909–1918.
- [181] S. Ledakowicz, E. Drozdek, T. Boruta, M. Foszpańczyk, M. Olak-Kucharczyk, R. Zylla, M. Gmurek, Impact of hydrogen peroxide on the UVC photolysis of diclofenac and toxicity of the phototransformation products, *International Journal of Photoenergy*. 1155 (2019) 1086704.
- [182] D. Minakata, D. Kamath, S. Maetzold, Mechanistic Insight into the Reactivity of Chlorine-Derived Radicals in the Aqueous-Phase UV-Chlorine Advanced Oxidation Process: Quantum Mechanical Calculations, *Environmental Science and Technology*. 51 (2017) 6918–6926.
- [183] Y. Lei, S. Cheng, N. Luo, X. Yang, T. An, Rate constants and mechanisms of the reactions of Cl[•] and Cl₂^{•-} with Trace Organic Contaminants, *Environmental Science and Technology*. 53 (2019) 11170–11182.
- [184] W.L. Wang, Q.Y. Wu, N. Huang, T. Wang, H.Y. Hu, Synergistic effect between UV and chlorine (UV/chlorine) on the degradation of carbamazepine: Influence factors and radical species, *Water Research*. 98 (2016) 190–198.
- [185] P. Sun, W.N. Lee, R. Zhang, C.H. Huang, Degradation of DEET and caffeine under UV/Chlorine and simulated sunlight/Chlorine conditions, *Environmental Science and Technology*. 50 (2016) 13265–13273.
- [186] S.E. Beck, H. Ryu, L.A. Boczek, J.L. Cashdollar, K.M. Jeanis, J.S. Rosenblum, O.R. Lawal, K.G. Linden, Evaluating UV-C LED disinfection performance and investigating potential dual-wavelength synergy, *Water Research*. 109 (2017) 207–216.

- [187] P.O. Nyangaresi, Y. Qin, G. Chen, B. Zhang, Y. Lu, L. Shen, Effects of single and combined UV-LEDs on inactivation and subsequent reactivation of *E. coli* in water disinfection, *Water Research*. 147 (2018) 331–341.
- [188] Y. Kebbi, A.I. Muhammad, A.S. Sant’Ana, L. do Prado-Silva, D. Liu, T. Ding, Recent advances on the application of UV-LED technology for microbial inactivation: Progress and mechanism, *Comprehensive Reviews in Food Science and Food Safety*. 19 (2020) 3501–3527.
- [189] Y. Xiao, L. Zhang, J. Yue, R.D. Webster, T.T. Lim, Kinetic modeling and energy efficiency of UV/H₂O₂ treatment of iodinated trihalomethanes, *Water Research*. 75 (2015) 259–269.
- [190] Y. Peng, H. Shi, Z. Wang, Y. Fu, Y. Liu, Kinetics and reaction mechanism of photochemical degradation of diclofenac by UV-activated peroxymonosulfate, *RSC Advances*. 11 (2021) 6804–6817.
- [191] K. Fischer, S. Sydow, J. Griebel, S. Naumov, C. Elsner, I. Thomas, A.A. Latif, A. Schulze, Enhanced removal and toxicity decline of diclofenac by combining uva treatment and adsorption of photoproducts to polyvinylidene difluoride, *Polymers*. 12 (2020) 1–15.
- [192] P. Leydy Katherine Ardila, B.F. da Silva, M. Spadoto, B. Clarice Maria Rispoli, E.B. Azevedo, Which route to take for diclofenac removal from water: Hydroxylation or direct photolysis?, *Journal of Photochemistry and Photobiology A: Chemistry*. 382 (2019) 111879.
- [193] O.S. Keen, E.M. Thurman, I. Ferrer, A.D. Dotson, K.G. Linden, Dimer formation during UV photolysis of diclofenac, *Chemosphere*. 93 (2013) 1948–1956.
- [194] P. Iovino, S. Chianese, S. Canzano, M. Prisciandaro, D. Musmarra, Photodegradation of diclofenac in wastewaters, *Desalination and Water Treatment*. 61 (2017) 293–297.
- [195] X. Lu, Y. Shao, N. Gao, J. Chen, Y. Zhang, H. Xiang, Y. Guo, Degradation of diclofenac by UV-activated persulfate process: Kinetic studies, degradation pathways and toxicity assessments, *Ecotoxicology and Environmental Safety*. 141 (2017) 139–147.
-

- [196] M. Majewska, D. Harshkova, M. Guściora, A. Aksmann, Phytotoxic activity of diclofenac: Evaluation using a model green alga *Chlamydomonas reinhardtii* with atrazine as a reference substance, *Chemosphere*. 209 (2018) 989–997.
- [197] N.S. Podio, L. Bertrand, D.A. Wunderlin, A.N. Santiago, Assessment of phytotoxic effects, uptake and translocation of diclofenac in chicory (*Cichorium intybus*), *Chemosphere*. 241 (2020) 125057.
- [198] V. Naddeo, S. Meriç, D. Kassinos, V. Belgiorno, M. Guida, Fate of pharmaceuticals in contaminated urban wastewater effluent under ultrasonic irradiation, *Water Research*. 43 (2009) 4019–4027.
- [199] S.K. Alharbi, J. Kang, L.D. Nghiem, J.P. van de Merwe, F.D.L. Leusch, W.E. Price, Photolysis and UV/H₂O₂ of diclofenac, sulfamethoxazole, carbamazepine, and trimethoprim: Identification of their major degradation products by ESI–LC–MS and assessment of the toxicity of reaction mixtures, *Process Safety and Environmental Protection*. 112 (2017) 222–234.
- [200] A. Smaali, M. Berkani, F. Merouane, V.T. Le, Y. Vasseghian, N. Rahim, M. Kouachi, Photocatalytic-persulfate- oxidation for diclofenac removal from aqueous solutions: Modeling, optimization and biotoxicity test assessment, *Chemosphere*. 266 (2021) 129158.
- [201] European Commission, Recommendation (EU) 2021/2279 of 15 December 2021 on the use of the Environmental Footprint methods to measure and communicate the life cycle environmental performance of products and organisations, 2021.
- [202] S. Sala, F. Biganzoli, E. Sanye, M. Erwan, Toxicity impacts in the environmental footprint method: calculation principles, *The International Journal of Life Cycle Assessment*. 2013 (2022) 587–602.
- [203] European Commission - Joint Research Center - Institute for Environment and Sustainability, International Reference Life Cycle Data System (ILCD) Handbook - General guide for Life Cycle Assessment - Detailed guidance, 2010.
- [204] S. Sala, E. Crenna, M. Secchi, E. Sany, Environmental sustainability of European production and consumption assessed against planetary boundaries, 269 (2020) 110686.
-

- [205] F.G. Montoya, M.J. Aguilera, F. Manzano-Agugliaro, Renewable energy production in Spain: A review, *Renewable and Sustainable Energy Reviews*. 33 (2014) 509–531.
- [206] Sustainable Energy Authority of Ireland (SEAI), *Renewable energy in Ireland*, 2020.
- [207] A. Gargiulo, M.L. Carvalho, P. Girardi, Life cycle assessment of Italian electricity scenarios to 2030, *Energies*. 13 (2020) 3852.

List of Figures

List of Figures

Figure 2.1. Microplastic morphology types.....	13
Figure 2.2. Schematic representation of the sources of MPs and plastic waste pathways. .	17
Figure 2.3. Main engineered technologies for MPs separation and degradation in water treatments.....	19
Figure 2.4. Schematic of the main pressure-driven membrane processes for water treatment technologies. Adapted from [65,66].	22
Figure 2.5. Representative sources and paths of organic micropollutants in the environment.	27
Figure 2.6. Diclofenac chemical formula and structure.....	29
Figure 2.7. Photolysis and AOPs explored for the removal of DCF, adapted from [85]. Photolysis and Photolysis + Oxidants are boxed since chosen in this study.	31
Figure 2.8. Main advantages and disadvantages of UV mercury lamps and UV-B and UV-C LEDs.	36
Figure 2.9. Technology readiness levels adopted by the European Commission [124]......	38
Figure 2.10. Efficiency trend and projections for LP mercury lamps, UV-A and UV-C LEDs [119]......	41
Figure 2.11. Relation between the objectives and the results.	44
Figure 3.1. PS particles bigger than 300 μm reduced by cryogenic milling (a), PA and PS particles sieved between 20-300 μm before being employed.....	47
Figure 3.2. Schematic filtration setup system.....	52
Figure 3.3. Laboratory implementation of the MPs filtration system.....	52
Figure 3.4. Electronic scheme to work at constant pressure using Arduino.....	53
Figure 3.5 Logical flowchart diagram used in the Arduino code for the filtration system..	54
Figure 3.6. Scheme of the experimental setup coupled with the vacuum filtrations with the GFs to analyse the removal efficiencies.	55

Figure 3.7. Schematic GF after vacuum filtration of the water gathered from each membrane's filtration.....	56
Figure 3.8. Fouling mechanisms and their corresponding physical meaning. Adapted from [136].....	57
Figure 3.9. UV-B and UV-C LED photoreactor working in recirculation to evaluate DCF degradation through LED-driven AOPs. Schematic representation (a) and a picture of the photoreactor realised in the laboratory (b).....	62
Figure 3.10. Heads of the LED lamps.....	62
Figure 3.11. Electronic circuit implemented through Arduino Mega 2560 to work at a constant flow rate in recirculation or in the presence of external variation.....	63
Figure 3.12. Logical flowchart diagram used in the Arduino code for the filtration system.	64
Figure 3.13. Calibration line to obtain the relation between the absorption and the concentration.....	66
Figure 3.14. Actinometry sample, 1 L solutions irradiated by 265 nm lamp at 100% intensity.	67
Figure 3.15. Details of the experimental setup for the chemical actinometry measurement.	68
Figure 3.16. Diclofenac calibration line.	69
Figure 3.17. Calibration line for the quantification of H ₂ O ₂	70
Figure 3.18. Life Cycle Assessment Framework according to ISO 14040 and 14044.....	73
Figure 3.19. Input, output, and system boundaries of a generic product system [151].	74
Figure 4.1. ATR-FTIR spectra of the two MPs (PA and PS) and the four membranes (CA, PC, PTFE, GF) under study.	80
Figure 4.2. Reflectance micro-FTIR spectra of the MPs (PA and PS) and the membranes (CA, PC, PTFE, and GF).	81

Figure 4.3. Particle size distribution of PA particles measured by microscopic counting and FBRM technology. The short-dash dot curve in green represents the log-normal distribution fitting the histogram data.	82
Figure 4.4. Particle size distribution of PS particles measured by microscopic counting and FBRM technology (the grey curve). The short-dash dot curve in green represents the log-normal distribution fitting the histogram data.	83
Figure 4.5. Zeta potential curves as a function of pH of 500 mg L ⁻¹ of PA (black squares) and PS (red triangles) particles with sizes between 20-300 μm.	84
Figure 4.6. Picture of the microplastic suspensions in water over time.	85
Figure 4.7. SEM images of the particles of PA (a and b, with unit distance of 50 and 10 μm) and PS (c and d, with unit distance of 400 and 100 μm).	87
Figure 4.8. Surface morphology of the three membranes: PC (a and b), CA (c and d), and PTFE (e and f) under SEM with unit distance of 100 and 10 μm, respectively.	88
Figure 4.9. Water contact angle measured after 60 s on the PTFE membrane.	89
Figure 4.10. Results of TMP and flow rate for PC (a and b), CA (c and d), and PTFE (e and f) during the filtration of PA and PS, respectively. The black dash-dash curve for TMP and the red dash-dot curve for the flow rate represent the behaviour of the membranes when filtering distilled water. On the other hand, the blue dot-dot and green straight-line curves represent the membrane's TMP and flow rate when filtering water containing 100 mg L ⁻¹ of PA and PS, respectively.	92
Figure 4.11. Average TMP (a) and flux (b) after 10 minutes of 100 mg L ⁻¹ of PA and PS filtration with the three membranes.	94
Figure 4.12. Phenomena potentially occurring during the filtration in dead-end configuration.	96
Figure 4.13. Mass removal efficiency (<i>MRE%</i>) and particle number removal efficiency (<i>NpRE%</i>) of each membrane when filtering water with 100 mg L ⁻¹ of PA and PS.	98
Figure 4.14. Morphology of the cake layer on PC (a and d), CA (b and e), and PTFE (c and f) after PA and PS filtration, respectively. The pictures were captured with a phone camera.	99

Figure 4.15. Studies on membrane compaction. No significant changes in water flux were observed after 1 h of distilled water filtration. The figure represents the filtration at 0.3 bar.	101
Figure 4.16. Plot of V (L) versus t (s) in black dash-dotted line for PA and in red straight line for PS (a). Plot of d^2t/dV^2 versus dt/dV for the determination of n -mechanism, black squares for PA and red dots for PS (b). Both curves refer to a representative curve at 10 mg L ⁻¹ and 0.3 bar.	102
Figure 4.17. Comparison between <i>model 1</i> (when only cake formation occurs) and <i>model 2</i> (complete pore blocking followed by cake formation). The experimental curve represents the averaged value for PA filtrations (a) and PS filtration (b) at 10 mg L ⁻¹ and 0.3 bar.	103
Figure 4.18. Permeate flux decline after 1 h of PA (a) and PS (b) filtrations at different MPs loads. The solid line corresponds to the average of the replicates, while the colour band around it indicates the error experienced under that operating condition.	104
Figure 4.19. K_b (a) and η_B (b) for PA (black squares) and PS (red dots) at variable MPs load, both reported on the same scale.	105
Figure 4.20. K_c as a function of MPs load for PA (black squares) and PS (red dots) in the same scale (a) and a magnification of the two trends on two scales (b).	106
Figure 4.21. Images of the CA pristine membrane (a) and after 1 h filtration of 10 mg L ⁻¹ of PA (b) and PS (c) particles at 0.3 bar.	107
Figure 4.22. Main interactions occurring between MPs and MPs-membrane and affecting the fouling kinetic.	108
Figure 4.23. Permeate flux decline after 1 h of PA (a) and PS (b) filtrations at different working TMP. The solid line corresponds to the average of the replicates, while the colour band around it indicates the error experienced under that operating condition.	109
Figure 4.24. K_b (a) and η_B (b) for PA (black squares) and PS (red dots) as a function of TMP, represented on the same scale.	110

Figure 4.25. K_c (a) and η_c (b) for PA (black squares) and PS (red dots) as a function of TMP, represented on two different scales to appreciate the trends.....	110
Figure 4.26. Schematic forces acting on an MP particle fouling during dead-end filtration.	114
Figure 4.27. WCA measured before and after the filtration of MPs (10 mg L ⁻¹ at 0.3 bar).	115
Figure 4.28. Profilometry measured before and after the filtration of MPs (10 mg L ⁻¹ at 0.3 bar).	115
Figure 4.29. SEM image of the CA membrane after PS filtration: details of mean roughness evaluation. Unit distance of 100 μm	116
Figure 4.30. SEM images of the CA membrane surface (a) with unit distance of 40 μm and cross-section (b) with unit distance of 50 μm	117
Figure 4.31. SEM images of the membrane surface (a and c after PA and PS filtration) and cross-section (b and d after PA and PS filtration). All images display a unit distance of 10 μm	118
Figure 4.32. Lamps characterisation (a), horizontal (b) and vertical (c) profile.....	121
Figure 4.33. Linear correlation among the current values (a) and maximum irradiance values measured by the ILT radiometer (b) at different lamp intensities.	122
Figure 4.34. Absorbance of DCF (pH 7.2) (a), HOCl/OCl ⁻ (pH 8.5), and H ₂ O ₂ (pH 6.5) (b).	122
Figure 4.35. The degradation of DCF (20 mg L ⁻¹) versus the total operation time through photolysis alone (a), UV/H ₂ O ₂ oxidation with 20 mg L ⁻¹ of H ₂ O ₂ (b), and UV/FC oxidation with 20 mg L ⁻¹ of FC (c), where k is the time-based kinetic constant (expressed in min ⁻¹).....	124
Figure 4.36. DCF degradation (20 mg L ⁻¹) versus UV fluence through photolysis alone (a), UV/H ₂ O ₂ oxidation with 20 mg L ⁻¹ of H ₂ O ₂ (b), and UV/FC oxidation with 20 mg L ⁻¹ of FC (c), where k' is the UV fluence-based kinetic constant (expressed in mJ ⁻¹ cm ²).	126

Figure 4.37. Comparison among the time-based constant k by direct photolysis, dark oxidation and UV-driven AOPs (a), and values of the synergist factor (b)..... 127

Figure 4.38. Correlation between the experimental data (red triangles, black squares, and green dots at 265, 285 and 310 nm) and model predictions (red dashed-dotted, black solid, and green dotted lines at 265, 285 and 310 nm) for DCF (a) and H₂O₂ (b)..... 130

Figure 4.39. Correlation between the experimental data (red triangles, black squares, and green dots at 265, 285 and 310 nm) and model predictions (red dashed-dotted, black solid, and green dotted lines at 265, 285 and 310 nm) for DCF (a) and FC (b). 135

Figure 4.40. Time-based constants (a, c) and UV fluence-based constants (b, d) alone or coupled with H₂O₂ or FC at different lamp intensities. 136

Figure 4.41. Linear correlation between the time-based constants and the lamp intensity for UV alone (brown squares), UV/H₂O₂ (blue dots), and UV/FC (green triangles) for the two lamps: 265 nm (a) and 285 nm (b)..... 137

Figure 4.42. Incorporation of lamp 2 into the experimental setup, schematic representation (a) and laboratory image (b). 138

Figure 4.43. Time-based constants (a) and UV-based constants for the “observed” and “simulated” dual-wavelength irradiation. 139

Figure 4.44. The extent of synergy during the dual-wavelength irradiation. 139

Figure 4.45. Change in colour over the treatment time. The sample in the figure represents the solution irradiated by the 265 nm lamp at 100 % intensity. 144

Figure 4.46. Absorbance at 400 nm versus operation time..... 145

Figure 4.47. The colour at the naked eye (a) UV spectra in the range of 200-400 nm (b) after 60 min of operation time..... 145

Figure 4.48. The peaks occurring during the DCF degradation. The example shown was taken after 5 min of operation time at 265 nm..... 146

Figure 4.49. The trend of the DCF (yellow squares) and the DCF by-product (blue dots) peaks’ area during the treatment. The example shown was taken for the photolysis alone at 265 nm..... 146

Figure 4.50. DCF degradation compounds after exposure to UV fluence at 254 nm. Proposed chemical structures of the products by Keen et al. [193].....	147
Figure 4.51. Schematic representation of the two photoreactors: UV-C LEDs lamp (to the left side) and two LP mercury lamps (to the right side).	151
Figure 4.52. Scheme of the system boundaries for the two photoreactors.	152
Figure 4.53. Connection between the LCIA impact categories of the EF method with the SDGs. Adapted from [204].	158
Figure 4.54. Relative impacts in percentage of the UV-C LEDs and the LP mercury lamp photoreactors referred to the FU on the 16 categories of the EF method.	159
Figure 4.55. Relative impacts in percentage of the UV-C LEDs and the LP mercury lamp photoreactors when the lamps are emitting at the same irradiation. Results referred to the FU on the 16 categories of the EF method employed.	160
Figure 4.56. Percentage contributions referred to the FU of the individual components: UV-C source (blue), lab equipment (violet), and electricity (teal) for the impact categories: “Climate change” on the left side and “Human toxicity, non-cancer” on the right side.	162
Figure 4.57. Relative impacts in percentage of the UV-C LEDs and the UV mercury lamp photoreactors assuming a 20% improvement in the energy efficiency of the UV-C LED lamp. The results refer to the FU on the 16 categories of the EF method employed.	163
Figure 4.58. Relative impacts of the three UV-C _{265 nm} LED water treatments (UV-C, UV-C/H ₂ O ₂ , and UV-C/FC) for the removal of 90% of DCF on the 16 categories of the EF method.	165
Figure 4.59. Relative contribution of the oxidant (red), UV-C _{265 nm} LED lamp (blue), lab equipment (violet), and electricity (teal) of the three UV-C water treatments per FU for the selected four categories. “Climate change”, “Human toxicity, non-cancer”, “Ozone depletion”, and “Ecotoxicity, freshwater”.	166
Figure 4.60. Relative impacts in percentage of the UV-C LED water treatment referred to the FU when employing the electricity mix of the European market and the electricity	

from photovoltaic or wind of the Spanish market. The results are shown for the 16 categories of the EF method employed..... 168

List of Tables

List of Tables

Table 2.1 Overview of different categories of CECs, the associated health effects, and occurrence in the environment.....	10
Table 2.2. Summary of the main analytical techniques for MPs analysis. Adapted from [17].	14
Table 2.3. A list of plastic additives associated with their application.....	16
Table 2.4. Factors affecting the MPs removal by membrane processes.....	23
Table 2.5. Literature review on membrane fouling by MPs.....	25
Table 2.6. List of 10 substances/groups of substances (total of 17 organic compounds) included in the first EU <i>watch list</i>	28
Table 2.7. Comparisons of the UV sources for water disinfection and purification.	35
Table 2.8. LCA studies on UV water treatments where the UV source was clearly specified in the inventory.	39
Table 3.1. Fouling mechanisms for constant pressure filtrations.	59
Table 3.2. Effect of particle diameter versus membrane pore diameter.	59
Table 3.3. Solutions of known concentration of Fe ²⁺ to obtain the calibration line.....	66
Table 4.1. Water contact angle and roughness measurement.	90
Table 4.2. Average transmembrane pressure increase (Δ TMP) and flux (J) after 10 min of 100 mg L ⁻¹ of MPs filtration of the membranes under study.....	93
Table 4.3. Total number of unremoved microplastic particles per litre (NT _{MP}), average size of unremoved MPs (D _{MP}), mass removal efficiency ($MRE\%$) and particle number removal efficiency ($NpRE\%$) of each membrane when filtering water with 100 mg L ⁻¹ of PA and PS.....	95
Table 4.4. Averaged values for complete pore blocking, K_b , cake formation, K_c , and the coefficient of determination, R^2 applied between the model and the experimental data for PA and PS filtration at different feed concentrations.....	105

Table 4.5. Averaged values for complete pore blocking, K_b , cake formation, K_c , and the coefficient of determination, R^2 applied between the model and the experimental data for PA and PS filtration at different TMP.....	109
Table 4.6. Permeate flux, flow velocity, Reynolds number, and wall shear stress after PA filtration at the beginning of the run, J_0 , u_0 , Re_0 , τ_0 , and at the transition from complete pore blocking to cake formation $J_{b \rightarrow c}$, $u_{b \rightarrow c}$, $Re_{b \rightarrow c}$, $\tau_{wb \rightarrow c}$	112
Table 4.7. Permeate flux, flow velocity, Reynolds number, and wall shear stress after PS filtration at the beginning of the run, J_0 , u_0 , Re_0 , τ_0 , and at the transition from complete pore blocking to cake formation $J_{b \rightarrow c}$, $u_{b \rightarrow c}$, $Re_{b \rightarrow c}$, $\tau_{wb \rightarrow c}$	113
Table 4.8. Lamps' characterisation through the chemical actinometry and the ILT radiometer.	121
Table 4.9. Molar absorption coefficient for DCF (pH 7.2), HOCl/OCl ⁻ (pH 8.5), and H ₂ O ₂ (pH 6.5) measured in this study at the wavelengths of interest.	123
Table 4.10. Proposed mechanism for the UV/H ₂ O ₂ treatment.	128
Table 4.11. Proposed mechanism for the UV/FC treatment.	131
Table 4.12. Apparent quantum yields and the molar absorption coefficients for HOCl and OCl ⁻ at the wavelengths of interest.	132
Table 4.13. Current, irradiance, and total electric power at different intensities of the lamp at 265 and 285 nm.....	136
Table 4.14. Dual-wavelength irradiation.	138
Table 4.15. The electrical energy per order for DCF degradation during different photolysis processes, considering the photoreactor contact time.....	142
Table 4.16. The electrical energy per order for DCF degradation at different lamp intensities.	143
Table 4.17. DOC value and DOC removal after the selected treatments.	143
Table 4.18. Germination index (GI) for radish and tomato seeds after the selected treatments.	148
Table 4.19. Raw materials and processes input for 1 unit of the UV-C LEDs lamp.....	153

Table 4.20. Raw materials and processes input for 1 unit of an LP mercury lamp of 6 W (20 g).	154
Table 4.21. Raw materials and processes input for the lab equipment, which are equal for the two photoreactors.	154
Table 4.22. Electricity consumption referred to the FU during the operation phase for the two photoreactors.	156
Table 4.23. Electrical energy inputs by the three UV-C _{265 nm} LED treatment systems, referred to the FU.	164

List of Abbreviations

List of Abbreviations

AOP	Advanced Oxidation Process
ATR	Attenuated Total Reflection
BL	Blacklight fluorescent lamp
CA	Cellulose Acetate
CLD	Chord Length Distribution
CEC	Contaminant of Emerging Concern
DCF	Diclofenac
DF	Disk Filter
DOC	Dissolved Organic Carbon
DWTP	Drinking Water Treatment Plant
DM	Dynamic Membrane
EE/O	Electric Energy per Order
EF	Environmental Footprint
FBRM	Focus Beam Reflectance Measurement
FTIR	Fourier-Transform Infrared Spectroscopy
FC	Free Chlorine
FU	Functional Unit
GC	Gas Chromatography
GMO	Genetically Modified Organism
GI	Germination Index
GF	Glass microfibre Filter
HPLC	High-Performance Liquid Chromatography
ISO	International Organisation for Standardisation
LCA	Life Cycle Assessment
LCIA	Life Cycle Impact Assessment
LCI	Life Cycle Inventory
LED	Light-Emitting Diode
LOD	Limit of Detection
LOQ	Limit of Quantification
LP	Low-Pressure

MS	Mass Spectroscopy
MP	Medium-Pressure
MBR	Membrane Bioreactor
MSSA	Micro Steady State Approximation
MF	Microfiltration
MP	Microplastic
MWWTP	Municipal Wastewater Treatment Plant
NF	Nanofiltration
NP	Nanoplastic
NRMSE	Normal Root Mean Squared Error
PSD	Particle Size Distribution
PMS	Peroxymonosulfate
POP	Persistent Organic Pollutant
PA	Polyamide
PC	Polycarbonate
PCP	Personal Care Products
PE	Polyethylene
PET	Polyethylene Terephthalate
PP	Polypropylene
PS	Polystyrene
PSF	Polysulfone
PTFE	Polytetrafluoroethylene
PVDF	Polyvinylidene Fluoride
RO	Reverse Osmosis
SEM	Scanning Electron Microscope
SQP	Sequential Quadratic Programming
SSE	Sum of Squared Error
TRL	Technology Readiness Level
TMP	Transmembrane Pressure
UF	Ultrafiltration
UV	Ultraviolet
UWWTP	Urban Wastewater Treatment Plant

List of Abbreviations

VFD	Variable Frequency Driver
VRPA	Volumetric Rate of Photon Absorption
WWTP	Wastewater Treatment Plant
WCA	Water Contact Angle

Publications and Congresses

Publications and communications to congresses

Publications in Scientific Journals

1. Angela Raffaella Pia Pizzichetti, Cristina Pablos, Carmen Álvarez-Fernández, Ken Reynolds, Simon Stanley, Javier Marugán. Evaluation of membranes performance for microplastic removal in a simple and low-cost filtration system. *Case Studies in Chemical and Environmental Engineering*. 3 (2021) 100075.
<https://doi.org/10.1016/j.cscee.2020.100075>
2. A. Raffaella P. Pizzichetti, Cristina Pablos, Carmen Álvarez-Fernández, Ken Reynolds, Simon Stanley, Javier Marugán. Kinetic and mechanistic analysis of membrane fouling in microplastics removal from water by dead-end microfiltration. *Journal of Environmental Chemical Engineering*. 11 (2023) 109338-109352.
<https://doi.org/10.1016/j.jece.2023.109338>
3. Raffaella Pizzichetti, Ken Reynolds, Cristina Pablos, Cintia Casado, Eric Moore, Simon Stanley, Javier Marugán. Removal of Diclofenac by UV-B and UV-C Light-Emitting Diodes (LEDs) Driven Advanced Oxidation Processes (AOPs): Wavelength Dependence, Kinetic Modelling and Energy Consumption (submitted, under peer-review process). Available at SSRN: <https://ssrn.com/abstract=4414818> or <http://dx.doi.org/10.2139/ssrn.4414818>
4. Pizzichetti et al. Assessing the environmental impacts of light-emitting diodes versus mercury lamps for the degradation of diclofenac in water and the impacts of hydrogen peroxide versus free chlorine to fasten the treatment (in preparation).

Scientific congresses

1. R. Pizzichetti, C. Pablos, K. Reynolds, S. Stanley, J. Marugán. Membranes' performance assessment for microplastic removal – recovery and recycling perspectives. IWA Wastewater, Water and Resource Recovery (WWRR) Online Conference, 10th –13th April 2022. Poster presentation.
2. R. Pizzichetti, C. Pablos, K. Reynolds, S. Stanley and J. Marugán. Microfiltration membrane fouling by microplastics: kinetic and mechanistic aspects at different operating conditions. MICROPOL 2022, 12th Micropol & Ecohazard Conference. Santiago de Compostela, Spain, 6th-10th June 2022. Poster presentation.
3. R. Pizzichetti, C. Pablos, K. Reynolds, S. Stanley, E. Moore, J. Marugán. Removal of emerging contaminants by UVC and UVB-LEDs driven AOPs. 32nd Irish Environmental Researchers Colloquium, Belfast (UK), 20th – 22nd June 2022. Oral presentation.
4. R. Pizzichetti, C. Pablos, K. Reynolds, E. Moore, S. Stanley, J. Marugán. Degradation of diclofenac by UV-B and UV-C LED driven AOPs processes. WCCE11 – 11th World congress of Chemical Engineering, Buenos Aires (Argentina), 4th-8th June 2023. Poster presentation (Cristina Pablos presenting).
5. R. Pizzichetti, C. Pablos, K. Reynolds, S. Stanley, E. Moore, J. Marugán. Application of UV-B and UV-C light-emitting diodes (LEDs) for the removal of diclofenac in drinking water. EcoSTP2023. 6th IWA International Conference on eco-Technologies for Wastewater Treatment. Girona (Spain). 26th-29th June 2023. Short-oral presentation.